

CoCrMo alloys in hip and knee replacements application



Submitted for the Degree of Doctor of Philosophy

**By
Righdan Mohsen Namus**

Supervisor: Professor W. Mark Rainforth

Materials Science and Engineering Department

The University of Sheffield

September 2018

Declaration

This thesis has been composed by myself and has not been submitted or accepted in any previous degree application. The work has been carried out by myself, except where due acknowledgement has been given.

Part of the work has been published as a scientific journal paper:

R. Namus, P. Zeng, and W. M. Rainforth, “Correlation of the wear transition in CoCrMo alloys with the formation of a nanocrystalline surface layer and a proteinaceous surface film,” *Wear*, vol. 376–377, pp. 223–231, 2017.

Conferences

- Student conference 2016, Sheffield, UK, May 2016. Oral presentation.
- Nanobrücken 2017, Manchester, UK, April 2017. Oral presentation.
- EUROCORR 2017, Prague/Czech Republic, September 2017. Poster presentation.
- 2018 Scotland and North of England Electrochemistry Symposium (RSC Butler Meeting), Aberdeen, UK, April 2018. Poster presentation.
- Electrochemical method in corrosion research EMCR international conference, Cambridge, UK, July 2018. Oral presentation.
- International corrosion symposium, Leeds, UK, September 2018. Oral presentation.

Acknowledgements

Firstly, I would like to express my sincere gratitude to my supervisor Professor **W Mark Rainforth** for the continuous support of my Ph.D study and related research, for his patience, motivation, and immense knowledge. His guidance helped me in all the time of research and writing of this thesis. I could not have imagined having a better advisor and mentor for my Ph.D study. Besides my supervisor, I would like to thank all the people and technicians in Material science and engineering department in Sheffield university for their insightful comments and encouragement, but also for the hard question which incited me to widen my research from various perspectives.

I would like to give my biggest thank to The Higher Committee for Education Development in Iraq HCED for their funding my Ph.D and unlimited support throughout my studying. The thank is given to Waset university for all the support that I got from them in my Ph.D.

Last but not the least, I would like to thank my family: my parents and to my brothers and sister for supporting me spiritually throughout writing this thesis and my my life in general.

Abstract

CoCrMo alloys have been widely used in hip replacements. On the one hand, they have exhibited excellent long-term survival rates, but recently high failure rates have been observed, associated with adverse local tissue reactions. It is still a puzzle why CoCrMo alloys sometimes work very well, while at the other times the wear rate is unacceptably high. There have been several reports that the formation of a surface carbonaceous layer appears to reduce the wear rate. Equally, the formation of surface deformations and nanocrystalline layer has been observed, but it remains unclear whether this is a beneficial or detrimental phenomenon. The application of CoCrMo in hip joints results in mechanical aspects in term of wear and electrochemical aspects in term of corrosion in what is called tribocorrosion. Therefore, the current work was designed to carefully cover some factors that have not been well investigated in the literature using different approaches for data analysis. The study was divided into two major parts; tribological study and tribocorrosion study.

In the tribological study, a directly correlation was found between the surface deformation and the presence of a carbonaceous layer with the wear behaviour. The lowest specific wear rate was associated with the formation of a carbonaceous layer. A wear transition was observed at higher load, related to the loss of the carbonaceous layer and the formation of a thick subsurface nanocrystalline layer. The formation of the carbonaceous layer appeared to be associated with the removal of the surface protective oxide film. Additionally, it was shown that superior mechanical properties of a thick nanocrystalline sub-surface layer could not protect the surface from a high wear rate. Although the formation of a thick nanocrystalline subsurface layer resulted in the highest surface mechanical properties, it also coincided with the highest wear rate.

In tribocorrosion part of the study, the mechanical and electrochemical contributions in tribocorrosion were separated using synergistic and mechanistic approaches. The influence of load, load-potential dual effect and sliding speed-potential dual effect were all studied. The results showed a significant effect of repassivating the worn surfaces on the wear behaviour of the material. At low loads and slow sliding speed, the worn surfaces were able to repassivate at OCP which in turn had a significant

effect on the microstructure of these surfaces and consequently on the mechanical properties and the tribocorrosion behaviour. Furthermore, the results of load-potential, and sliding speed-potential showed a correlation between the mechanical contribution of tribocorrosion and the hardness of the worn surfaces that is the harder worn surfaces wear less mechanically at OCP. Such this correlation was not found at anodic potentials.

The results also showed that the surface carbonaceous layer did not form on the surfaces that were covered by an oxide layer and a high cathodic potential was needed to almost entirely remove the oxide film. This is in good agreement with the results of the tribological study of the work which pointed out a certain minimum load is necessary to totally remove the oxide layer and helped in the formation of a carbonaceous layer on the worn surfaces.

A correlation between the COF and the thermodynamic stability of the surface was observed. Throughout the whole study, whenever the system was able to establish new thermodynamic stability (at low load and slow sliding at OCP and at all tested anodic potentials), COF significantly decreased. The study defined two surface status, passivating worn surfaces (the surface tries to repassivate) with high COF, and passivated surfaces (already passivated) with low COF.

Contents

1	INTRODUCTION.....	11
2	LITERATURE REVIEW	14
2.1	FRICITION	14
2.2	WEAR	15
2.3	COCrMo ALLOYS.....	16
2.3.1	SOLIDIFICATION AND PHASES.....	16
2.3.2	TREATMENTS AND ENHANCE PROPERTIES OF COCrMo ALLOYS	18
2.3.3	MARTENSITIC TRANSFORMATION	21
2.3.4	GRAIN REFINEMENT:	25
2.3.5	THE INFLUENCE OF STACKING FAULT ENERGY ON MECHANICAL PROPERTIES.....	28
2.3.6	MICROSTRUCTURE’S CHANGES DURING WEAR	31
2.3.7	LUBRICATION IN ARTIFICIAL HIPS AND KNEES	36
2.3.8	CORROSION RESISTANCE	38
2.3.9	PROTEIN ADSORPTION AND ITS EFFECT ON CORROSION PROPERTIES	39
2.3.10	TRIBOCORROSION THE INTERACTION BETWEEN WEAR AND CORROSION.....	44
3	EXPERIMENTAL WORK.....	55
3.1	MATERIAL AND PREPARATION	56
3.2	TRIBOLOGICAL STUDIES	56
3.2.1	INITIAL CONTACT PRESSURE CALCULATION:	56
3.2.2	WORK PROCEDURE	57
3.3	CORROSION CHARACTERIZATION	58
3.3.1	WORK PROCEDURE	58
 ELECTROCHEMICAL IMPEDANCE SPECTROSCOPY EIS BACKGROUND	
	59
3.3.2	59
3.4	TRIBOCORROSION STUDY	64
3.4.1	LOAD AND LOAD-POTENTIAL DUEL EFFECT	64
3.4.2	SLIDING SPEED EFFECT	67
3.5	MECHANICAL PROPERTIES CHARACTERIZATION BY USING NANOINDENTATION	68
3.5.1	BACKGROUND.....	68
3.5.2	TESTS PROCEDURE	69
3.6	MICROSCOPIC AND RAMAN CHARACTERIZATION OF THE WORN SURFACES..	70
4	RESULTS.....	72
4.1	TRIBOLOGY PROPERTIES.....	72
4.1.1	STARTING SURFACE, FRICTION AND WEAR RATE	72
4.1.2	CHARACTERISATION OF THE WORN SURFACES.....	73
4.1.3	MECHANICAL PROPERTIES OF THE SURFACE	76
4.1.4	MICROSTRUCTURE AS A FUNCTION OF DEPTH BELOW THE WORN SURFACE	79
4.2	TRIBOCORROSION PROPERTIES	80
4.2.1	LOAD EFFECT (SYNERGISTIC APPROACH)	80
4.2.2	LOAD-POTENTIAL DUEL EFFECT	85
4.2.3	SUBSURFACE MICROSTRUCTURE:.....	115
4.2.4	SLIDING SPEED-POTENTIAL EFFECT:	117

<u>5</u>	<u>DISCUSSION.....</u>	<u>133</u>
5.1	TRIBOLOGY PROPERTIES:.....	133
5.2	TRIBOCORROSION PROPERTIES.....	135
5.2.1	LOAD EFFECT:	135
5.2.2	LOAD-POTENTIAL EFFECT:	140
5.2.3	SLIDING SPEED-POTENTIAL EFFECT:	144
<u>6</u>	<u>CONCLUSIONS.....</u>	<u>148</u>
6.1	TRIBOLOGICAL STUDY.....	148
6.2	TRIBOCORROSION STUDY	148
6.2.1	LOAD EFFECT	148
6.2.2	LOAD POTENTIAL DUAL EFFECT:.....	149
6.2.3	SLIDING SPEED EFFECT:	150
<u>7</u>	<u>FUTURE WORK:.....</u>	<u>152</u>
<u>8</u>	<u>REFERENCES.....</u>	<u>153</u>

Table of figures

FIGURE 2-1 STRIBECK CURVE	15
FIGURE 2-2 THE PHASE DIAGRAM OF Co-Cr SYSTEM [9].....	17
FIGURE 2-3 OPTICAL MICROSCOPIC IMAGE OF AS CAST CoCrMo ALLOY (ASTM F 75) [15]	18
FIGURE 2-4 BACKSCATTERED ELECTRON IMAGE OF DENDRITIC A-PHASE INSIDE LIQUID CARBIDES [21]	19
FIGURE 2-5 A AND B ARE SEM IMAGE OF RETRIEVED CAST ALLOY IMPLANT. FRACTURE OCCURRENCE IS CLEAR. C IS WROUGHT ALLOY AFTER 5 MILLION CYCLES SIMULATOR TEST [23].....	20
FIGURE 2-6 FORMING NANO-DEBRIS FROM MIXED PHASE CARBIDE [23]	20
FIGURE 2-7 FORMATION OF ISOTHERMAL MARTENSITE PHASE AT 1150°C FOR 1H + 850°C FOR 3H IN AS CASTE CoCrMo ALLOY, A AND B REPRESENT DIFFERENT MAGNIFICATIONS [25]	21
FIGURE 2-8 THE EFFECT OF TIME AND TEMPERATURE OF SOLUTION TREATMENTS ON HCP VOLUME FRACTION FOR 5 HOURS OF ISOTHERMAL AGEING AT 800°C [9]	22
FIGURE 2-9 TTT DIAGRAM FOR ISOTHERMAL MARTENSITIC TRANSFORMATION IN THE AS-CAST CoCrMoC ALLOY [27].....	23
FIGURE 2-10 SIT E-MARTENSITE APPEARS AS STRIATIONS (A) 10% DEFORMATION, (B) 20% DEFORMATION [29]	24
FIGURE 2-11 EFFECT OF STRAINING FOLLOWED BY AGING AT 800°C ON THE VOLUME FRACTION OF HCP PHASE IN THE MICROSTRUCTURE. (A) 0%, (B) 5% (C) 10% AND (D) 20% STRAINING [29].....	24
FIGURE 2-12 THE EFFECT OF ZENER–HOLLOMON PARAMETER ON DRX [32]	26
FIGURE 2-13 TRUE STRESS-TRUE STRAIN CURVES AND THE DEPENDENCE OF THE RATE OF STRAIN HARDENING ON THE FLOW STRESSES FOR MATERIALS WITH DIFFERENT SFE (Cu IS THE HIGHEST SFE) [41]	29
FIGURE 2-14 FOUR DISTINCT STAGES FOR STRAIN HARDENING IN LOW SFE MATERIALS. THE STRAIN HARDENING IS NORMALISED BY G [41]	29
FIGURE 2-15 THE DEPENDENCE OF (Σ TWIN- Σ 0)/G ON THE AVERAGE OF HDZ LENGTH OF TWINING INITIATION [43].....	31
FIGURE 2-16 THE ALTERATION OF HALL-PETCH RELATION THROUGH DIFFERENT GRAIN SIZES [45]	31
FIGURE 2-17 A: RHOMBIC CELLS; B: FORMING NANOPARTICLES IN THE VERY CLOSED SURFACE LAYER [2]	33
FIGURE 2-18 FORMING METALLO-ORGANIC NANOSTRUCTURE COMPOSITE [48].....	34
FIGURE 2-19 WEAR'S DEBRIS OF CoCrMo ALLOY [49].	34
FIGURE 2-20 A: DEFECTS IN THE SUBSURFACE; B: NANOPARTICLES [49]	35
FIGURE 2-21 WORN SURFACE OF CoCrMo ALLOY [49].....	35
FIGURE 2-22 TRIBO-CORROSION EFFECT [76].	44
FIGURE 2-23 EVANS DIAGRAMS REPRESENTING THE EFFECT OF RUBBING ON ELECTRODE POTENTIAL, A BEFORE RUBBING, B AND C ARE EXPLAINED IN THE TEXT [3].....	45
FIGURE 2-24 THE EFFECT OF RUBBING ON FLOWING ANODIC CURRENT [79].....	47
FIGURE 2-25 THE EFFECT OF NORMAL LOAD (A) ANGULAR VELOCITY (B) HEAD DIAMETER (C) AND RIDIAL CLEARANCE ON MECHANICAL, CHEMICAL AND TOTAL WEAR. [82]	49
FIGURE 2-26 CONTRIBUTION OF MECHANICAL AND ELECTROCHEMICAL WEAR AT THREE DIFFERENT POTENTIALS: CATHODIC POTENTIAL (CATH), LOW PASSIVATION POTENTIAL (PL) AND HIGH PASSIVATION POTENTIAL (PH) [79].....	49
FIGURE 2-27 UNIFORM GROWTH MODEL UG AND LATERAL GROWTH MODEL LG FOR PASSIVE FILM [80].....	50
FIGURE 2-28 THE HARDNESS AND WEAR VOLUME [84].....	51
FIGURE 2-29 TRIBO-CORROSION TEST FOR CoCrMo ALLOY (A) WITHOUT CP (B) WITH CP [85].....	51
FIGURE 2-30 SYNERGISTIC EFFECT OF WEAR AND CORROSION FOR THREE DIFFERENT MATERIALS IN THREE DIFFERENT BIOLOGICAL MEDIA [86]	52
FIGURE 2-31 FACTORS AFFECT TRIBOCORROSION [87].	52
FIGURE 3-1 CORROSION AND TRIBOCORROSION USED IN THIS WORK.	58
FIGURE 3-2 NYQUIST PLOT	62
FIGURE 3-3 RANDES CELL	62
FIGURE 3-4 BODE PLOT	63
FIGURE 3-5 BODE PLOT PHASE SHIFT.....	63
FIGURE 3-6 BODE PLOT (ON THE LEFT) AND 3D PLOT FOR NYQUIST PLOT AND BODE LOT (ON THE RIGHT)	64
FIGURE 3-7 WORK PROCEDURE FOR LOAD-POTENTIAL DUAL EFFECT	66
FIGURE 3-8 WORK PROCEDURE FOR SLIDING SPEED EFFECT	67
FIGURE 3-9 NANOINDENTATION CURVE [111]	69
FIGURE 4-1 ION CHANNELLING CONTRAST IMAGE FOR STARTING SURFACE.	72

FIGURE 4-2 SPECIFIC WEAR RATE, K, AS A FUNCTION OF LOAD.	73
FIGURE 4-3 SECONDARY ELECTRON SEM IMAGES FOR (A) 5N, (B) 10N, (C) 20N, (D) 40N, (E) 60N, AND (F) 80N WEAR TEST LOAD. (G) AND (H) ARE HIGHER MAGNIFICATION IMAGES FOR POINTED AREAS IN 60N AND 80N WEAR TEST LOAD RESPECTIVELY.	74
FIGURE 4-4 RAMAN SPECTRA SHOWS TWO PEAK D AT 1383 cm^{-1} AND PEAK G AT 1567 cm^{-1} FOR 40N AND 60N TEST LOAD.	75
FIGURE 4-5 OPTICAL IMAGES FOR (A) 40N, AND (B) 60N LOAD.	75
FIGURE 4-6 TYPICAL NANOINDENTATION LOADING-UNLOADING CURVES FOR ALL TESTED LOADS. THE PARTIAL UNLOAD FUNCTION HAS BEEN USED TO CHARACTERIZE THE MECHANICAL PROPERTIES FOR THE SUCCESSIVE LAYERS OF THE SURFACE.	76
FIGURE 4-7 SECONDARY ELECTRON SEM IMAGE FOR ONE OF THE INDENTS SHOWS SINK-IN EVENTS AND EXTRUSION ON ONE SIDE OF THE INDENT.	76
FIGURE 4-8 NANOINDENTATION RESULTS SHOW THE ALTERATION IN MECHANICAL PROPERTIES OF THE SURFACE WITH TESTING LOAD. THE LAST SEGMENT OF THE PARTIAL UNLOAD FUNCTION HAS BEEN USED TO EXTRACT THESE VALUES.	77
FIGURE 4-9 THE HARDNESS FOR THE SUCCESSIVE LAYER OF THE SURFACE FOR ALL TESTED LOAD. 0N REFERS TO STARTING SURFACE.	79
FIGURE 4-10 ELECTRON CHANNELLING CONTRAST IMAGES FOR (A) 20 N, (B) 40 N, (C) 60 N, AND (D) 80 N WEAR TEST LOAD. TAKEN BY DR PENG ZENG (SORBY CENTRE, THE UNIVERSITY OF SHEFFIELD) AND PUBLISHED IN [113].	80
FIGURE 4-11 COF AND K FOR TRIBOCORROSION TESTS AT OCP	81
FIGURE 4-13 TOTAL AND SYNERGISM MATERIAL LOSS RATE VS. LOAD.	83
FIGURE 4-14 SLIDING POTENTIAL FOR WIDE RANGE OF LOAD AT OCP	84
FIGURE 4-15 THE EFFECT OF APPLYING PULSE POTENTIAL IN THE MIDDLE OF TRIBOCORROSION TEST	84
FIGURE 4-16 POLARIZATION CURVE FOR COCrMo ALLOY IN 25 VOL.% BS IN PBS AT 37°C.....	85
FIGURE 4-17 EQUIVALENT CIRCUITS FOR EIS DATA MODELLING	87
FIGURE 4-18 NYQUIST PLOT FOR (A) -0.9V, (B) -0.7V, AND -0.5V (C) OCP AND ANODIC POTENTIAL	90
FIGURE 4-19 POTENTIAL VS. COF AND CURRENT (OR OCP) AT 4 N LOAD AND DIFFERENT POTENTIALS	92
FIGURE 4-20 COF AND I VERSUS TIME AT 8 N LOAD.....	93
FIGURE 4-21 COF AND I VERSUS TIME AT 16 N LOAD.....	94
FIGURE 4-22 COF AND K VS. POTENTIAL FOR 4N, 8N, AND 16N WEAR TEST LOADS	97
FIGURE 4-23 CONTOUR GRAPH FOR V_{TOTAL} OVER TESTED LOADS AND POTENTIALS.....	98
FIGURE 4-24 V_{TOTAL} , V_{CHEM} , AND V_{MECH}	100
FIGURE 4-25 ANODIC CURRENT CURVES AFTER SUBTRACTION OF THE BASELINES. V_{CHEM} RATE IS ADDED TO THE RIGHT	102
FIGURE 4-26 V_{CHEM} RATE AFTER AND BEFORE CURRENT DROP.....	103
FIGURE 4-27 SEM IMAGES FOR ALL TRIBOCORROSION TESTS	104
FIGURE 4-28 SEM IMAGES FOR 8N WEAR TEST LOAD AT DIFFERENT APPLIED POTENTIALS	105
FIGURE 4-29 SEM IMAGES FOR 16N WEAR TEST LOAD AT DIFFERENT APPLIED POTENTIALS	106
FIGURE 4-30 WORN SURFACE AT -0.9V POTENTIAL TEST.....	107
FIGURE 4-31 SEM IMAGES FOR 8N WEAR TEST LOAD AT -0.9V APPLIED POTENTIAL	107
FIGURE 4-32 SEM IMAGES FOR 16N WEAR TEST LOAD AT -0.9V APPLIED POTENTIAL	108
FIGURE 4-33 TYPICAL RAMAN SPECTRUM WITH GAUSSIAN PEAK FITTING FOR -0.9V AT 4N, 8N, AND 16N, AND OCP 8N	109
FIGURE 4-34 MICROSTRUCTURE REVEALING VIA SEM IMAGING FOR WORN SURFACES AT OCP AND DIFFERENT LOADS	110
FIGURE 4-35 MICROSTRUCTURE REVEALING VIA SEM IMAGING FOR WORN SURFACES AT DIFFERENT ANODIC POTENTIALS AND LOADS.....	111
FIGURE 4-36 NANOINDENTATION HARDNESS FOR WORN SURFACES AT DIFFERENT LOAD AND POTENTIAL	113
FIGURE 4-37 H FOR THE SUCCESSIVE LAYER OF THE SURFACE FOR -0.9V TEST.	114
FIGURE 4-38 MODULUS MAPPING FOR THE VERY EDGE OF THE WEAR TRACH AT -0.9V TEST.....	115
FIGURE 4-39 BACK SCATTERED ELECTRON IMAGES FROM FIB CROSS SECTIONS (A) -0.9V, (B) -0.7V, (C) OCP, AND (D) 0V. THE MAGNIFICATION IS 5000X. TAKEN BY DR PENG ZENG (SORBY CENTRE, THE UNIVERSITY OF SHEFFIELD)	116
FIGURE 4-40 SUBSURFACE MICROSTRUCTURE FOR 0V 4N WORN SURFACE. TAKEN BY DR PENG ZENG (SORBY CENTRE, THE UNIVERSITY OF SHEFFIELD)	117
FIGURE 4-41 SLIDING SPEED EFFECT ON SLIDING POTENTIAL AT 400, AND 500 MPA INITIAL CONTACT PRESSURE	117
FIGURE 4-42 COF AND THE CURRENT VERSUS TIME FOR ALL TESTED SLIDING SPEEDS AT CATHODIC POTENTIAL.....	118
FIGURE 4-43 COF AND THE POTENTIAL VERSUS TIME FOR ALL TESTED SLIDING SPEEDS AT OCP TESTS.....	119
FIGURE 4-44 COF AND ANODIC CURRENT VERSUS TIME FOR ALL TESTED SLIDING SPEEDS AT ANODIC POTENTIAL	120
FIGURE 4-45 SLIDING POTENTIAL FOR TWO DIFFERENT TESTS FOR 1 HZ SLIDING SPEED AT OCP	121

FIGURE 4-46 COF AGAINST POTENTIAL BEFORE AND AFTER THE TRANSITION IN OCP OR THE ANODIC CURRENT	122
FIGURE 4-47 SPECIFIC WEAR RATE K AT DIFFERENT POTENTIALS AND SLIDING SPEEDS	122
FIGURE 4-48 SLIDING SPEED EFFECT ON TRIBOCORROSION PROPERTIES OF CoCrMo ALLY IN 25 VOL.% BS IN PBS AT 37°C	124
FIGURE 4-49 SLIDING CURRENT AFTER SUBTRACT BASELINE	124
FIGURE 4-50 VOLUME OF MATERIAL LOSS AT ANODIC POTENTIAL	125
FIGURE 4-51 V_{CHEM} VS. NUMBER OF CYCLES AT ANODIC POTENTIAL	125
FIGURE 4-52 CHANGING IN V_{CHEM} AFTER AND BEFORE THE DROP DOWN IN CURRENT	126
FIGURE 4-53 SEM IMAGES FOR WORN SURFACES AT CATHODIC POTENTIAL AT DIFFERENT SLIDING SPEEDS	127
FIGURE 4-54 SEM IMAGES FOR WORN SURFACES AT OCP AT DIFFERENT SLIDING SPEEDS	128
FIGURE 4-55 SEM IMAGES FOR WORN SURFACES AT ANODIC POTENTIAL AT DIFFERENT SLIDING SPEEDS	129
FIGURE 4-56 MICROSTRUCTURE OF THE WORN SURFACES AT OCP WITH DIFFERENT SLIDING SPEEDS	131
FIGURE 4-57 H FOR WORN SURFACES AFTER DIFFERENT TESTED POTENTIALS AND SLIDING SPEED	132
FIGURE 5-1 C_w , W_c , AND H VS. LOAD	140
FIGURE 5-2 SCHEMATIC DIAGRAM ILLUSTRATES THE IMPACT OF FORMING A GALVANIC COUPLE AT DIFFERENT POTENTIALS .	144
FIGURE 5-3 H, MECHANICAL WEAR, AND ELECTROCHEMICAL WEAR VS. SLIDING SPEED AT OCP AND ANODIC POTENTIAL ...	147

List of tables

TABLE 3-1 CHEMICAL COMPOSITION OF THE MATERIAL	56
TABLE 3-2 EQUIVALENT CIRCUIT ELEMENTS.....	60
TABLE 4-1 VOLUME OF MATERIAL LOSS, AND WEAR RATE	72
TABLE 4-2 MECHANICAL PROPERTIES OF ALL TESTED SAMPLES FROM THE NANOINDENTATION EXAMINATION.	77
TABLE 4-3 COF AND K FOR TRIBOCORROSIONAL TESTS AT DIFFERENT LOADS.	81
TABLE 4-4 RATE OF MATERIAL LOSS OF LOAD EFFECT TRIBOCORROSION TESTS. A PREVIATION: TSA: TOTAL SYNERGISTIC FACTOR, CAF: CORROSION AUGMENTATION FACTOR, WAF: WEAR AUGMENTATION FACTOR.	82
TABLE 4-5 CORROSION PARAMETERS EXTRACTED FROM TAFEL CURVE	85
TABLE 4-6 EIS RESULTS AT DIFFERENT POTENTIALS	89
TABLE 4-7 TRIBOCORROSION PARAMETERS FOR LOAD-POTENTIAL DUEL EFFECT TESTS	96
TABLE 4-8 THE REPRODUCIBILITY OF THE DATA FOR TWO DIFFERENT SAMPLES	98
TABLE 4-9 V_{CHEM}/S AT ANODIC POTENTIALS IN MM^3/S	101
TABLE 4-10 SURFACE ROUGHNESS FOR WORN SURFACES AT 4N LOAD.	108
TABLE 4-11 MECHANICAL PROPERTIES FOR WORN SURFACES.....	112
TABLE 4-12 NANO HARDNESS OF THE SUCCESSIVE LAYER OF -0.9V TEST WORN SURFACE	114
TABLE 4-13 TRIBOCORROSION TESTS RESULTS FOR SLIDING SPEED EFFECT STUDYING	120
TABLE 4-14 PENETRATION RATES IN TRIBOCORROSION TESTS IN MM/Y	123
TABLE 4-15 V_{CHEM} PER CYCLE FOR ANODIC CURRENT AT DIFFERENT SLIDING SPEEDS. CALCULATED FROM THE SLOPE OF THE LINES IN FIGURE 4-51	126
TABLE 4-16 THE ROUGHNESS OF THE WORN SURFACES.....	129
TABLE 4-17 THE MECHANICAL PROPERTIES AS MEASURED BY NANOINDENTATION FOR THE WORN SURFACES SOR SLIDING SPEED EFFECT STUDYING	132

1 Introduction

According to the American Academy of Orthopedic Surgeons, the primarily hip replacements in 2003 were 220000 in the US. It is expected to rise to 572000 in 2030. With younger patients who need these surgeries, the researches should focus not only on the longevity of these implants but also on improving the function of them [1].

The high wear rate in the polymer on metal PoM replacement ($<500\mu\text{m/a}$) was significantly reduced by using hard on hard couples like ceramic on ceramic or metal on metal MoM joints. It is believed that the later attains the lowest wear rate at steady state ($1\text{-}5\ \mu\text{m/a}$) after intensive running-in wear ($35\ \mu\text{m/a}$) [2].

CoCrMo components have been used as successful MoM replacements for a long time. They have excellent mechanical properties, biocompatibility and good corrosion resistance. The second generation of these components was developed in the 1990 with better clearance leading to better lubrication condition in comparison with the first generation. Interestingly, some of these implants survived up to 15 years while others failed within the first 5 years of the service. Additionally, the presence of nano-debris and ion release in both surrounding tissue and remote location in the body of the patients with the failed implant was reported. It has been pointed out that cobalt and chromium ions are considered to be toxic or even carcinogenic [3]. Therefore, agencies in the US (FDI) and the UK (MHRA) recently issued alerts for using MoM hip replacement leading to significant drop in their use [4]. Nevertheless, there is a large number of people still have these implants in their body.

Many changes at the surface and in the subsurface of CoCrMo alloys have been revealed in both in-vivo and in-vitro materials such as forming a carbonaceous layer on the surface and forming nanocrystalline and strain induced transformation from FCC to HCP in the subsurface. However, the effect of these phenomena on the wear behaviour of these alloys is not well understood.

Tribocorrosion is such a complicated phenomenon. It includes many factors like the worn surface microstructural changes and its effect on mechanical properties and repassivation process of the worn surfaces which in turn might be extremely important in the whole wear process. The formation of a carbonaceous layer on the worn surfaces in the protein content solution, like the one used in this work, adds another complexity. Throughout many testing procedures, the current work tried to add valuable knowledge and to improve our understanding of tribocorrosion. It is well

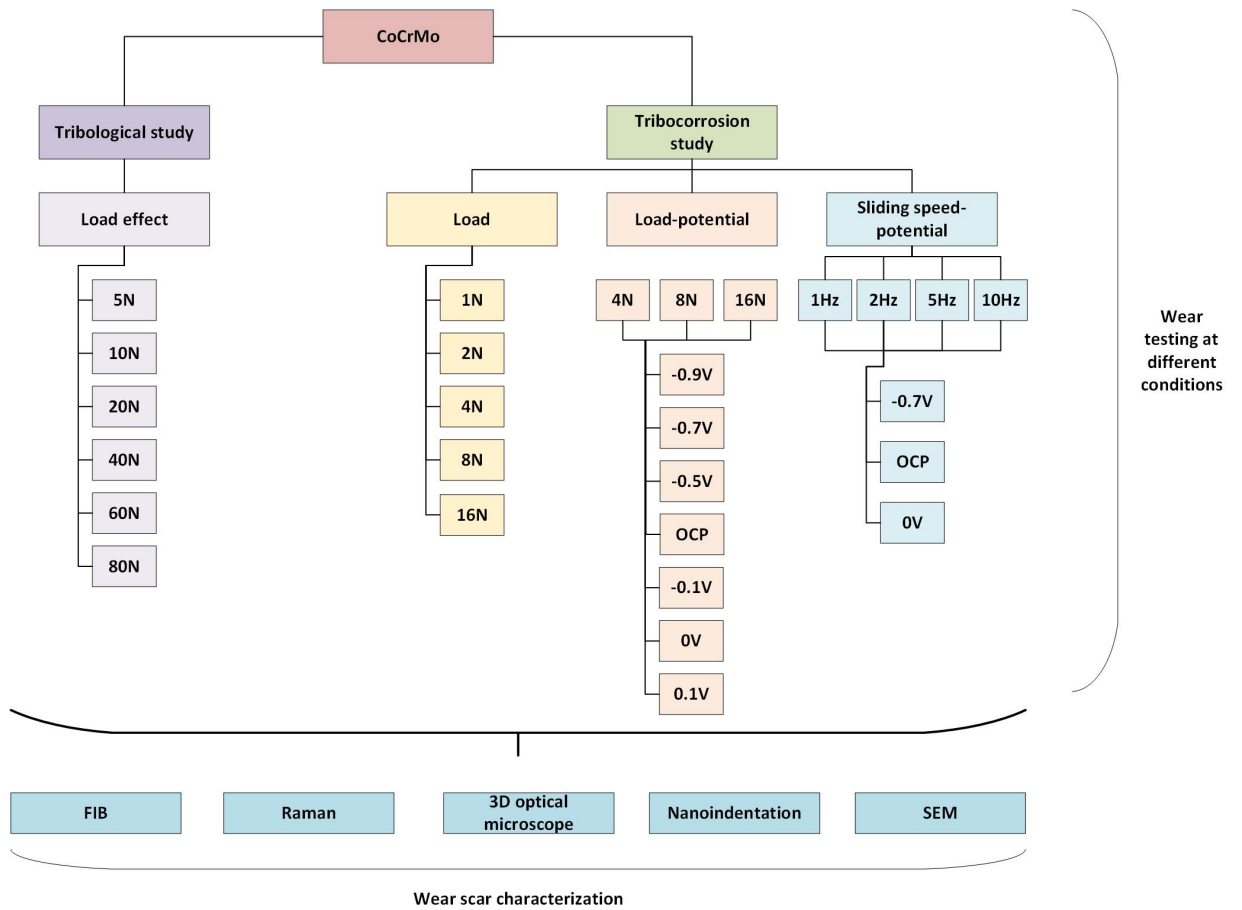
known that wear is a system property, not a material property, therefore, every effort was made to simulate the service conditions of the human body by choosing the protein concentration in the solution (15.5 g/L within the range in the body fluid of healthy human), the temperature (37°C), the pH (7.4), and wide range of load, sliding speeds and potentials to cover the variety of human activities.

Thus, the work was designed as a systematic consequence to study CoCrMo biomedical grade alloy as follow:

1. Tribological study: The work included an extended range of load (5-80 N) to totally cover the influence of the microstructural changes on the formation of the nanocrystalline subsurface layer and the formation of the carbonaceous layer on the worn surfaces. It also aimed to understand the effect of these events on the wear behaviour of this alloy.
2. Tribocorrosion behaviour: This was done by using synergistic and mechanistic approaches and subdivided to:
 1. Load effect: The work is based on synergistic approach. The material was subjected to a range of loads (1-16 N) to study the tribocorrosion behaviour.
 2. Load-Potential dual effect: It is based on a hybrid synergistic and mechanistic approaches. Wide range of cathodic and anodic electrode potentials were chosen (-0.9, -0.7, -0.5, OCP, -0.1, 0, 0.1 V vs. Ag/AgCl RE) at three loads (4, 8, 16 N). The work aimed to understand the effect of the interaction between load and potential on the tribocorrosion behaviour of the material being studied.
 3. Sliding speed-Potential dual effect: Different sliding speeds were chosen (1, 2.5, 5, 10 Hz reciprocating speed) to be tested at cathodic, OCP and anodic electrode potentials. The goal was to improve our understanding of the effect of walking fast, slow, or even running on the behaviour of this alloy.

In all mentioned above works, the state-of-the-art techniques were successfully employed to produce accurate data. All wear tests were done on UMT wear rig with high stability and reproducibility. Optical profilometry was used to accurately calculate the volume of material loss. SEM and FIB were successfully employed to image the worn surfaces and subsurfaces. Nanoindentation was extremely useful in determining the mechanical

properties of the worn surfaces as well as the starting surface. Raman spectroscopy was also used to detect the carbonaceous layer on the worn surfaces. The figure below shows the map of the work.



2 Literature review

2.1 Friction

When two surfaces come into contact and move laterally over each other, there is resistance to this motion called the friction force. It is essential to spend some work to initiate and maintain this motion. Some of this work wastes as heat. In some engineering application when this phenomenon is harmful, the design should be made in such a way that reduces this energy waste as much as possible.

Friction includes load-controlled contribution and adhesion-controlled contribution. The first one is determined depending on the topography of the surface and defined by friction coefficient μ . It is assumed to be the same everywhere on the surface. So, for the multiple contacts:

$$F = \sum_n \mu \left(\frac{L}{n} \right) = \mu L$$

Where F is friction force, L is normal load and n is number of contacts. This means that this term does not depend on real contact area. On the other hand adhesion-controlled contribution does depend on real contact area and can be determined as:

$$F = \sum_n \sigma A_n$$

Where σ is shear stress.

Therefore, the total friction force is:

$$F_{\text{total}} = \mu L + \sum_n \sigma A_n$$

It is necessary to distinguish between the force needed to initiate the lateral motion and the one needed to maintain it. Friction coefficient during sliding is called kinetic friction coefficient. It is generally lower than static coefficient of friction [5].

Dry sliding always gives high friction coefficient and consequently high-energy dissipation. Inserting a material that has low shear stress (lubricant) between solid surfaces in contact effectively reduces coefficient of friction to acceptable engineering

values. Depending on the thickness of lubricant layer compared with surface roughness there are four different lubrication regimes. In hydrodynamic lubrication the two surfaces completely separated from each other. Elastohydrodynamic EHL lubrication regime refers to high local pressure and very thin lubrication film that elastic deformation of the surfaces cannot be neglected. With thinner lubrication film boundary lubrication is entered and finally the solid lubrication regime. It has been shown that there is a relation between applied normal load L , lubricant viscosity η and sliding velocity V on one hand and friction coefficient on the other hand. Figure 2-1 shows this relation and the Stribeck curve. Decreasing the term z ($\eta V/L$) leads to a decrease in the friction coefficient through hydrodynamic and EHL regions until it reaches a minimum value in EHL region and then increases rapidly indicating boundary and solid lubrication regions. The Stribeck curve has a special importance as it gives a clear idea about friction of certain material in certain lubricant [6].

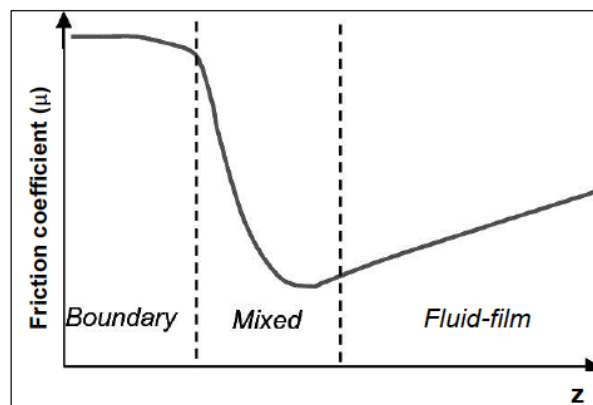


Figure 2-1 Stribeck curve

2.2 Wear

Wear can be defined as a removal of material from its surface under mechanical effect of another surface. Sliding wear therefore is kind of wear when the material is removed under sliding conditions. Abrasive wear on the other hand is a wear when one surface is much harder than other (two body abrasion) or when there are hard particles trapped between the surfaces (three body abrasion). These particles form either by detachment from the surfaces (debris) or from the presence of a third body. Detachment of particles from two sliding bodies is most likely to occur. Thus, there is no clear boundary between

different kinds of wear.

Mathematically wear can be explained by using Archard equation, which presumes a direct proportionality between wear rate Q and normal load L:

$$Q = K \frac{L}{H}$$

Where K is dimensionless coefficient of wear and H is the hardness of the softer surface. Wear rate Q here is volume of debris per unit distance. In engineering application, it is more useful to replace the quantity K/H by another one called k. The latter quantity is known as dimensional wear coefficient and measured in volume of debris (mm³) per unit load (N) per unit distance (m) [6], [4].

2.3 CoCrMo alloys

2.3.1 Solidification and Phases

Cobalt is a tough metal with an appearance that resembles nickel and iron. Utilizing their corrosion resistance, wear resistance and biocompatibility, the usage of some Co-based alloys has prompted in orthopaedic implant applications [8].

Historically, Elwood Haynes was the first person who discovered the high strength and stainless nature of cobalt-chromium alloys and later he identified both tungsten and molybdenum as good strengthening agents. The main purpose of having Mo in such these alloys is to participate in forming carbides and reduces chromium's consumption in like this process, which in turn keeps chromium in solid solution and retains high corrosion resistance [8].

The phase diagram of Co-Cr system is shown in Figure 2-2 [9]. It shows the existence of three main phases, α -FCC phase, ϵ -HCP phase, and σ -intermetallic component with approximate chemical composition Co₂Cr₃. This phase diagram, as well known, is for the alloy during extremely slow cooling rate. The real casting, however, does not offer this kind of cooling. Add to this the sluggish nature of the FCC to HCP phase transformation. Thus, as cast CoCrMo alloys naturally have α -FCC phase with a small fraction of ϵ -HCP. It is also reported that at a temperature below 600°C, the intermetallic component σ phase starts to precipitate.

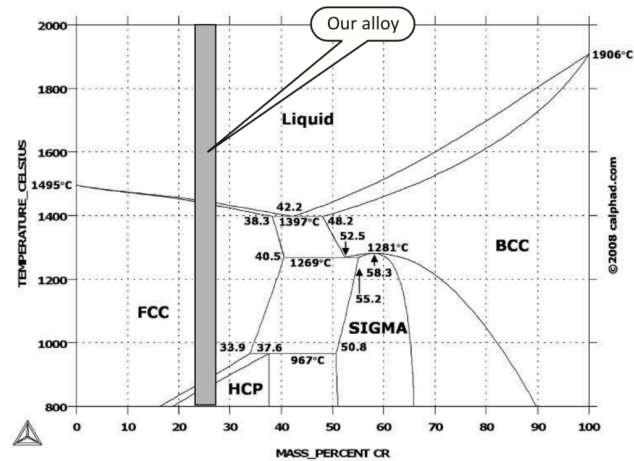


Figure 2-2 the phase diagram of Co-Cr system [9]

As cast Co₂₉Cr₆Mo alloy has α -FCC, and ϵ -HCP phases. The properties of the alloy strongly depend on the ratio of these phases. The ductility of the alloy increases with more α -FCC phase fraction [10], [11]. Whereas, corrosion and wear resistance enhance with ϵ -HCP phase fraction increasing [12].

Because of the low workability of CoCrMo alloys, they are often made by using investment casting (as this method gives nearly final dimensional products). The solidification of CoCrMo alloys starts with a dendritic growth of α -FCC crystals. With decreasing temperature precipitates of secondary phases formed in grain boundaries and interdendritic zones. The first secondary phase to appear is sigma σ intermetallic compound [13]. According to global reaction $\sigma + C = M_{23}C_6$, carbides form with further cooling. It has been also reported that there are some metastable carbides form during solidification process in limited range of temperatures like M_7C_3 and $M_{12}C$ [13], [14].

$M_{23}C_6$ carbides exist in two different morphologies, a blocky type and pearlite type (Figure 2-3). The latter one forms at 990°C once the solidification has completed under slow cooling rate [15].

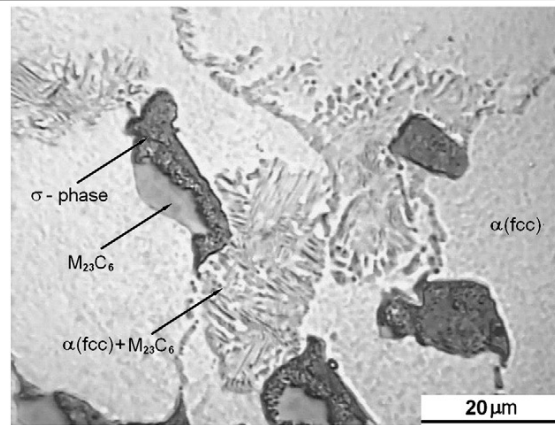


Figure 2-3 optical microscopic image of as cast CoCrMo alloy (ASTM F 75) [15]

It has been stated that the volume fraction of both the eutectoid phase and blocky carbides significantly increases with carbon content. However, the cooling rate does not have a considerable effect on the volume fraction of blocky carbide [16].

2.3.2 Treatments and Enhance Properties of CoCrMo alloys

As is clearly known, the as-cast alloys have many kinds of defects like porosity, large grain size, inhomogeneous chemical composition and precipitates at the grain boundary and interdendritic zones [17].

For the sake of removing casting defects and improving mechanical properties, as cast CoCrMo alloys are subjected to different kinds of treatments.

Forming carbides is the main strengthening mechanism in as-cast alloys. Nevertheless, precipitation of these carbides at the grain boundary is responsible for the reduction in mechanical properties. Treatments of these materials include hot isotactic pressing (hipping), conventional solution or homogenization treatment and carbides refining by using additives [10]. Clemow et al. [18] studied the solution treatment of CoCrMo alloy in a range of temperature between 1185-1270°C to improve ductility. This treatment included incipient melting, the transformation of $M_{23}C_6$ to M_6C and σ -phase formation. They found that the optimum treatment temperature is 1220°C. It has been shown that a fully solution treatment gave a good improvement in ductility at the expense of other mechanical properties due to the dissolution of precipitates at the grain boundaries [19]. It was also proved that partially solution treated alloys exhibited an excellent combination of mechanical properties without influencing corrosion resistance [19]. Giacchi et al. [20] examined the solution treatment of ASTM F-75 alloys for different times. They came to

find that the most detrimental phases, which are σ -phase and lamellar structure, are dissolved in the earlier stage of treatment. They also reported carbides transformation according to $M_{23}C_6 = M_6C$ in some alloys during this treatment.

Mancha et al. [21] suggested a multistage mechanism for $M_{23}C_6$ dissolution during heat treatment. According to this mechanism, dissolution occurs in the following consequence:

1. Solid-state diffusion of the elements forming carbides. It was noted that lamellar carbides dissolved faster than blocky ones because of better diffusion conditions provided by these structures.
2. Fusion and complete melting of carbides. After starting fusion serrated interface forms as it is more thermodynamically favored.
3. The growth of solid internal phase. The growth of the solid phase inside liquid carbide has been observed (Figure 2-4). Close examination of this phase showed that it has a dendritic shape and chemical composition similar to that of matrix α -phase.

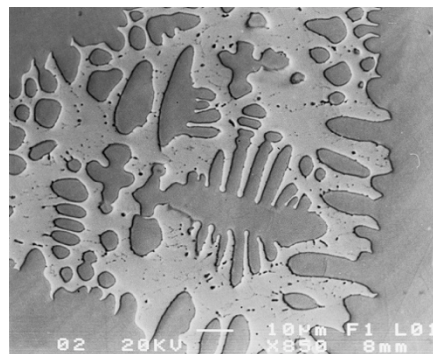


Figure 2-4 backscattered electron image of dendritic α -phase inside liquid carbides [21]

CoCrMo alloys include two main different types, cast alloys (ASTM F-75) and wrought alloys. It has been reported that latter alloys have superior crevice corrosion and better mechanical properties [22].

According to Liao et al. [23], the structure of carbides is different in these two types alloys. The carbides in cast alloys are mixed-phase and consist of fine grains of about 100 nm in size. This kind of carbide is found to be a stable phase and formed under low cooling rate conditions. Furthermore, it comprises of three phases (FCC phase similar to the matrix phase, Co-rich carbide and Mo-rich carbide). On the other hand, wrought alloys have single-phase fine carbide, which is a metastable phase and needs a high

cooling rate to form. Despite the same crystallographic structure, these carbides have a different chemical composition and mechanical properties. Single-phase carbide is twice as hard as mixed phase carbide, which directly reflects on the final mechanical properties of the alloys. The occurrence of fractures in mixed phase carbide (Figure 2-5) and forming nano-debris (Figure 2-6) have also been reported [22].

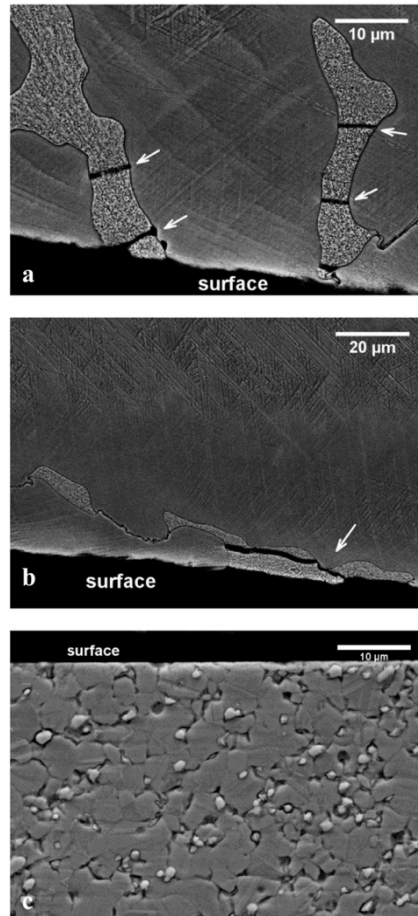


Figure 2-5 a and b are SEM image of retrieved cast alloy implant. Fracture occurrence is clear. c is wrought alloy after 5 million cycles simulator test [23]

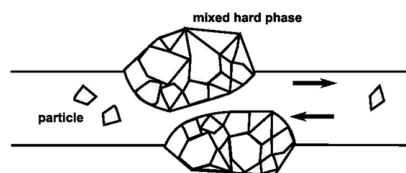


Figure 2-6 forming nano-debris from mixed phase carbide [23]

It was shown that minimum wear loss could be achieved by self-mating these alloys with HCP structure. In contrast, maximum wear loss was when self-mating them with FCC

structure. An intermediate value was found when matting FCC with HCP. This was attributed to the higher plastic deformation that FCC structure experiences [24].

2.3.3 Martensitic Transformation

Under normal cooling conditions, the structure of CoCrMo alloys at room temperature mainly includes metastable FCC phase and a few amounts of HCP phase (less than 4%). The complete extinction of the latter phase has been noticed after 1 h homogenization [25].

Quenching and ageing are found to promote FCC to HCP martensitic transformation. Figure 2-7 shows that the nucleation of HCP phase starts as fine plates close to precipitated carbide while it is long straight intragranular plates across the dendrite arms [25]. Different behavior has been reported in the case of wrought alloys. HCP starts to nucleate as pearlite form in the grain boundaries of these alloys [25].

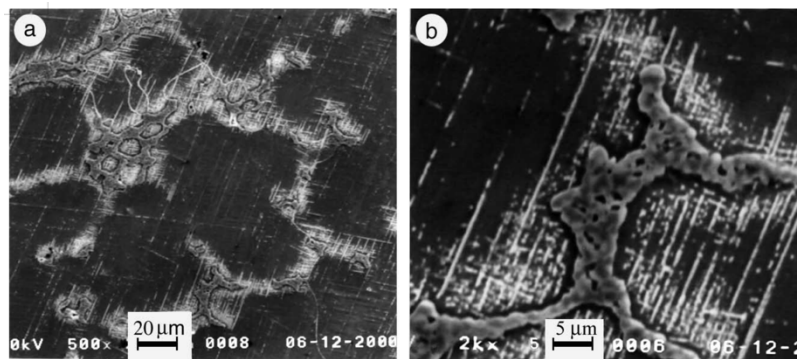


Figure 2-7 formation of isothermal martensite phase at 1150°C for 1h + 850°C for 3h in as cast CoCrMo alloy, a and b represent different magnifications [25]

Martensitic transformation of FCC to HCP in these alloys is rather sluggish due to weak chemical driving force under normal conditions. However, this transformation can be promoted by quenching from a temperature above T_C (athermal martensite) and ageing (isothermal martensite) [9]. It has been shown that the amount of athermal ϵ -martensite increases with increasing the temperature of solution treatment. In contrast, the amount of isothermal ϵ -martensite during ageing at 800°C decreases with increasing both time and temperature of prior solution treatment (Figure 2-8) [9].

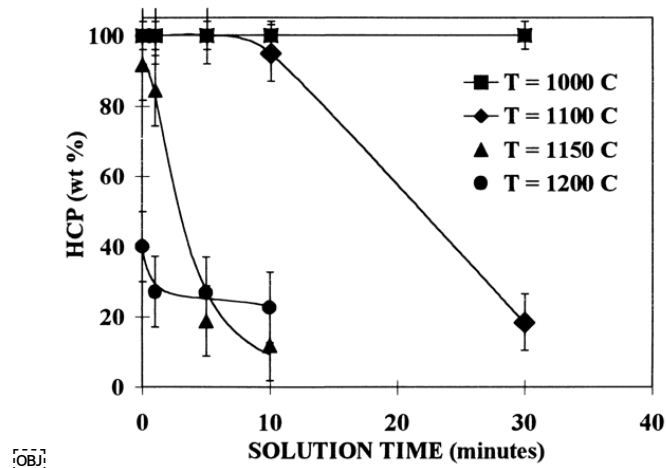


Figure 2-8 the effect of time and temperature of solution treatments on HCP volume fraction for 5 hours of isothermal ageing at 800°C [9]

García et al. [9] indicated that quenching from 1150°C to room temperature retards FCC to HCP transformation during subsequent ageing up to one order of magnitude in time compared with material aged without quenching. They attributed this retardation to the decreasing the number of HCP embryos as a result of local plastic deformation due to transformational, and thermal stresses occur over quenching.

Stacking faults consider to be nuclei for the HCP phase since the forming and moving of Shockley partial dislocation in FCC structure give rise to change stacking from FCC to HCP. It is well known that in FCC structure when stacking fault energy γ is small; the dislocations tend to dissociate themselves into partial dislocations leading to form stacking faults. The width of the stacking fault has an inverse proportionality with γ [26]. It has been reported that in some CoCrMo alloys stacking fault energy falls to almost zero promoting the splitting of dislocations into infinitely separated partial dislocations [27]. Lopez et al. [27] studied isothermal martensitic transformation and established C-curve for as-cast CoCrMoC alloy (Figure 2-9). They noticed two individual ϵ -martensite phases as well. The first one is pearlite like forms close to coarse carbide due to multiple nucleation events. While the other one forms in the matrix dendrite arms and has a straight plates shape. The energy barrier for martensitic transformation in the regions nearby coarse carbide or dendritic boundaries is found to be less than that in bulk dendrites matrix regions, which suggests the strong effect of segregation. Carbon content increases the SFE and consequently decrease FCC to HCP transformation, which explains the multi-nucleation events close the carbides.

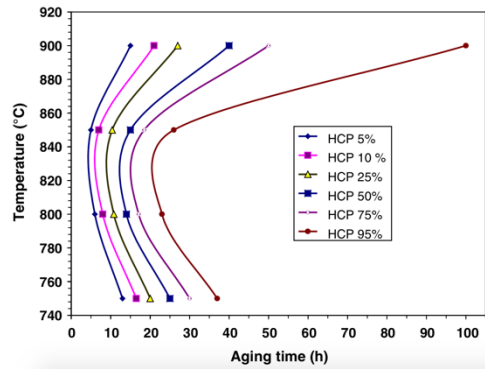


Figure 2-9 TTT diagram for isothermal martensitic transformation in the as-cast CoCrMoC alloy [27]

Martensitic transformation can be promoted through plastic straining in a process called strain induced transformation SIT. Lashgari et al. [28] compared the occurrence of martensitic transformation in as-cast CoCrMo alloy while ageing for two groups of samples with and without pre-straining. Their results showed that for these samples without pre-straining the α to ϵ isothermal transformation was not completed even after 24 h at 850°C ageing. In contrast, this transformation accelerated and completed after just 8 h under the same conditions for pre-strained samples.

It has been found that for wrought, and quenched CoCrMo alloy F75 ASTM, plastic straining gives martensitic SIT rise, which appears as intragranular striations (Figure 2-10). The density of these striations increases with increasing plastic strain [29]. Figure 2-11 illustrates the influence of ageing time at 800°C on the volume fraction of HCP phase in the structure of specimens for different percentage of plastic straining for wrought CoCrMo alloy. It was noticed that in the case of absence of pre-straining, a complete α to ϵ transformation is obtained after 3h. In contrast, in the rest of the specimens, it can be readily recognized two transformation stages. In the first hour, there is an initial increase in ϵ -martensite followed by plateau [29]. This behaviour explained as following. The stresses occurred during quenching are enough to restrict the growth of ϵ -martensite embryos, which in turn limits the amount of ϵ -martensite phase. However, the plastic straining after quenching activates some of these embryos leading to increasing the amount of HCP phase at the first stage. Moreover, ageing at a suitable temperature gives rise to more α to ϵ transformation. Throughout the first period of ageing internal stresses are relaxed, and potential ϵ -martensite embryos are exhausted. This synchronizes with the creation of new nuclei of ϵ -martensite. In the second stage of ageing some incubation time is needed for the new nuclei to grow up. Importantly, they pointed out that the HCP phase fraction mainly affects the plastic behaviour of the material.

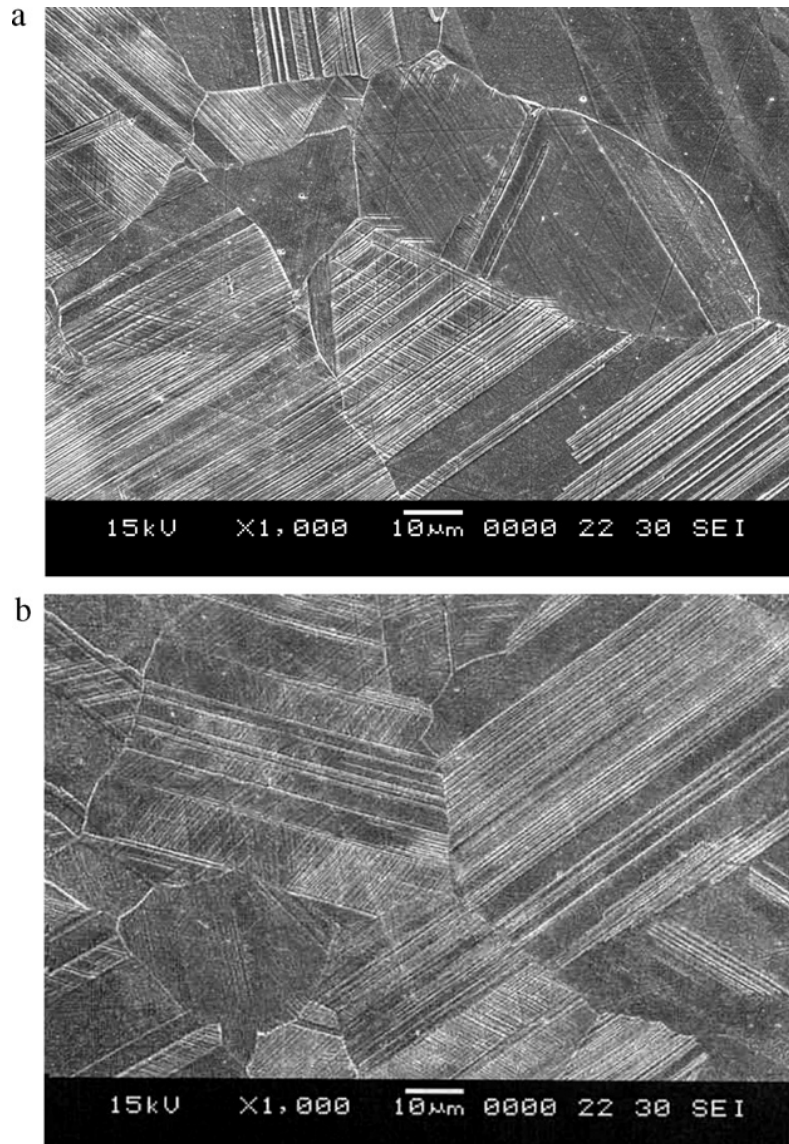


Figure 2-10 SIT ϵ -martensite appears as striations (a) 10% deformation, (b) 20% deformation [29]

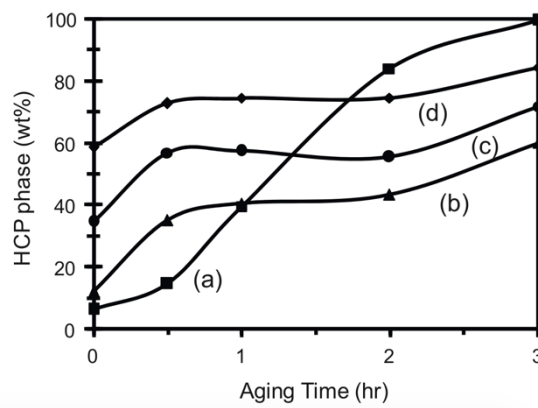


Figure 2-11 Effect of straining followed by aging at 800°C on the volume fraction of HCP phase in the microstructure. (a) 0%, (b) 5% (c) 10% and (d) 20% straining [29]

2.3.4 Grain Refinement:

Different approaches have been used by many researchers like Hall and Petch, Cottrell, Li and others to estimate a relationship between grain size and mechanical properties. These studies, however, have agreed that with reducing grain size yield stress increases [26], [30].

Severe plastic deformation (SPD) in which significant plastic strain is imposed to materials structure is a vital and efficient way to produce ultra-fine grains UFG microstructure. High-pressure torsion (HPT), accumulative roll bonding (ARB) and equal channel angular pressing (ECAP) are just examples of this process. Nevertheless, these processes are high-energy consumer and the strain required is much higher than that in the large-scale production [31].

As an alternative method, combining of phase transformation and plastic deformation has been reported to obtain UFG microstructure. Three different sequences have been reported in this context: plastic deformation of the initial phase before phase transformation, plastic deformation after phase transformation and repeating plastic deformation and phase transformation several times [32].

In general, there are two types of recrystallization: static recrystallization SRX and dynamic recrystallization DRX. In the former one, the nucleation of embryos occurs during deformation as a result of the orientation gradient while their growth occurs in the annealing process. The new embryos need to have two conditions to be able to grow up rather than shrink and diminish, which are: having a size larger than critical size and high angle boundaries [33]. Additionally, the migration of grain boundaries during growth is affected by their structure and existence of solute atoms. For instance, the presence of solute atoms hinders their migration and having a particular structure like coincident sites boundaries increases GBs mobility [30], [33]. It has been reported that all kinds of boundaries including incidence dislocation boundaries IDBs and geometrical necessary dislocation boundaries GNBs tend to rotate and increase their misorientation under deformation [33].

In contrast, in dynamic recrystallization DRX both nucleation and growth occur during deformation at high temperature. Since high storage energy particles, which form in cold working and grow during annealing (SRX process) do not readily form under the high

temperature of DRX, it has been proposed that primary mechanism of nucleation is particle stimulated nucleation PSN, the details of PSN is provided elsewhere [34].

It has been reported that in DRX the grain size reduces with increasing Zener–Hollomon parameter:

$$Z \cong \dot{\epsilon} \exp\left(\frac{Q}{RT}\right)$$

where $\dot{\epsilon}$ is strain rate, Q is deformation activation energy at high-temperature R gas constant and T is absolute temperature. This means the final grain size depends on both T and $\dot{\epsilon}_0$. Nevertheless, getting full recrystallization needs high strain rate [32]. Figure 2-12 shows this effect.

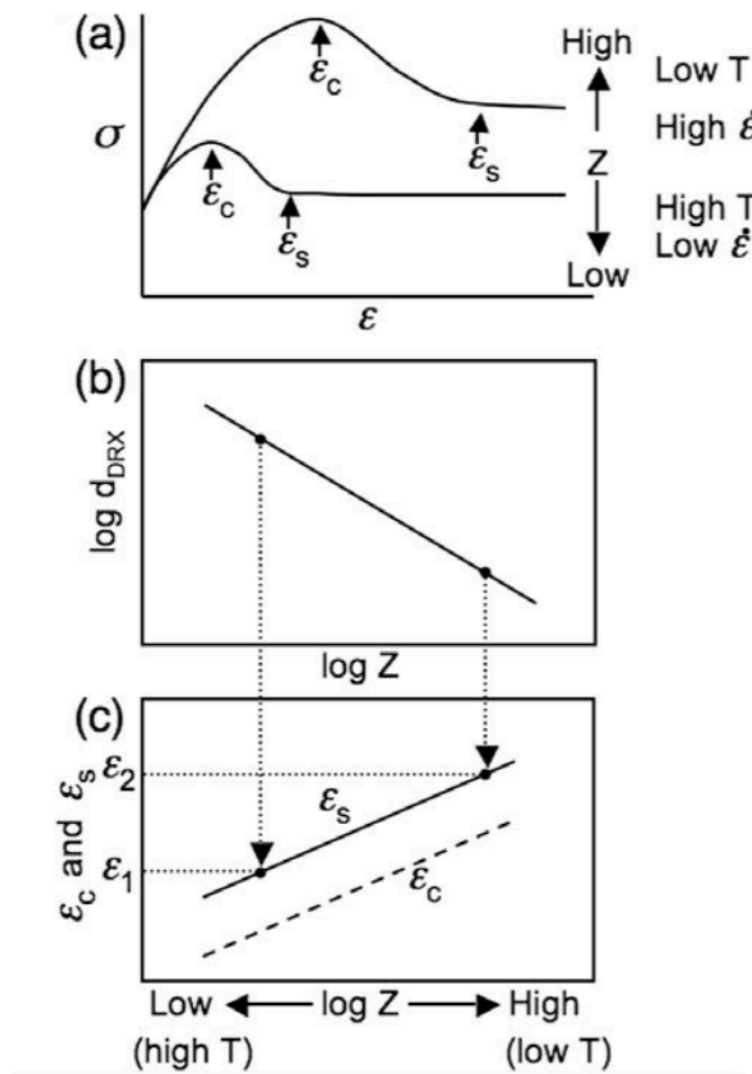


Figure 2-12 the effect of Zener–Hollomon parameter on DRX [32]

Yamanaka et al. [35] investigated DRX to produce UFG structure of CoCrMo alloy. They carried out their work using a range of strain rate and temperature ($\dot{\epsilon}$: 10^{-3} to 10 s $^{-1}$ and T: 1050 to 1200°C). Although their results show a good agreement with d-Z relation, the grains were coarser than expected by this relation at high strain rate (1 and 10 s $^{-1}$ strain rates). They also noticed a considerable local misorientation in nonrecrystallized regions. This misorientation has been attributed to low SFE, that these alloys have, promoting forming geometrical necessary dislocation GND, which in turn consider being the driving force of nucleation.

It has been shown that hot deformation [35] and nitrogen addition [36] remarkably reduce the fraction of athermal and strain induced martensite phase in CoCrMo alloys. Sigma phase has not been detected in both cases as well. The significant grain refinement during hot deformation hinders the formation of martensite.

The mechanical properties of UFG structure of Co₂₉Cr₆Mo alloy with and without nitrogen addition has been studied [36]. It has been identified that the strength of this alloy drastically enhances with decreasing grain size. However, the elongation could not be improved without adding nitrogen. Nitrogen here works as α phase stabilizer. Therefore, it eliminates athermal and strain induced ϵ phase that in turn increases work hardening and prevents the instability in plastic deformation [36]. The mechanism of α phase stabilizing cannot explain by thermodynamic stability terms. Instead, it is ascribed to suppressing α to ϵ martensite transformation.

The effect of nitrogen in Co₂₉Cr₆Mo alloy has been studied systemically [37], [38]. It has been revealed that as nitrogen concentration increases the volume fraction of athermal ϵ -martensite dramatically decreases up to 0.10 wt% N. This transformation is entirely suppressed when nitrogen concentration exceeds this weight per cent. It also appears that both strength and elongation are significantly enhanced. The inhibition of forming athermal ϵ phase was attributed to precipitate nanoparticles of Cr₂N on {111} planes of the α phase. These nanoparticles work as obstacles prevent forming Shockley partial dislocations, which means the suppressing of martensitic transformation.

Kurosu et al. [39] used reverse transformation as an effective way of grain refinement for Co₂₇Cr₅Mo_{0.16}N. They reported that grain size could be reduced one-tenth the initial grain size. Solution treatment followed by aged treatment were used to obtain completed lamellar structure of ϵ phase and Cr₂N. These lamellar blocks are surrounded by HABs and divided into small colonies by LABs. After reverse transformation, numerous

nucleation events could happen at both HABs and LABs leading to a refined structure. They also revealed that the final structure after reverse transformation can be α -FCC single phase or nanoparticles of Cr_2N distributed in α -FCC depending on the temperature of reverse treatment.

2.3.5 The influence of stacking fault energy on mechanical properties

In FCC metals, dislocations tend to decompose themselves into partial dislocations during their moving to reduce the energy needed for this motion. The separation between partial dislocations depends on stacking fault energy SFE as describe in the equation below:

$$\gamma_{\text{SF}} = \frac{Gb^2}{2\pi d}$$

Where γ_{SF} is stacking fact energy, b is burger's vector and d is the separation between partial dislocations. Hence, d decreases with increasing γ_{SF} . SFE has a direct effect on dislocations movement and consequently on plastic deformation. Smaller d facilitates pinching of partial dislocation and consequently easier cross slip. The dislocations in high SFE materials tend to rearrange themselves in dislocations cells (slip and cross slip) where the majority of them resides in cell's walls. On the other hand, at low SFE materials, dislocations organize themselves in planner ways (no cross slip) forming more uniform distribution. Stacking fault energy is very sensitive for adding alloying elements, for example, adding aluminum to copper drops it to about one ordered of magnitude [30].

It is also shown that SFE drastically affects plastic deformation mode. Remy and pineal [40] studied the influence of SFE on deformation mode in Co-Ni alloys with different composition (different SFE) at room temperature. Their results suggest the occurrence of strain induced transformation (γ to ϵ) in range of 0 to near 20 mJ/m^2 SFE. At around 20 mJ/m^2 SFE twining occurs under small strain. Between 20-50 mJ/m^2 twining and dislocations cells occur concurrently. Whereas, in higher SFE the deformation mode is only by dislocations cells. They proposed a parabolic relation between SFE and deformation twinning. High strain hardening rate was also reported for low SFE materials.

Asgari et al [41] conducted compression test for three FCC polycrystalline materials with different SFE Copper, α -brass and MP35N ((35% Ni, 35% Co, 10% Mo, 20% Cr). True stress- true strain curves and the dependence of the rate of strain hardening on the flow stresses are shown in Figure 2-13.

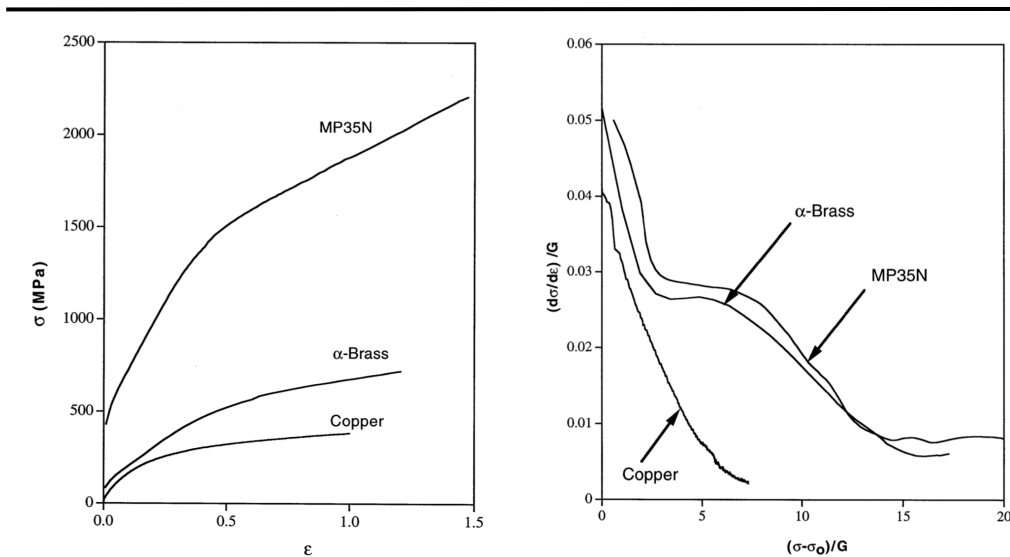


Figure 2-13 True stress-true strain curves and the dependence of the rate of strain hardening on the flow stresses for materials with different SFE (Cu is the highest SFE) [41]

They detected four distinct strain hardening stages for low SFE materials. They labelled them as A, B, C, and D as shown in Figure 2-14. Strain hardening rate decreased with a strain in stages A, and C and it is almost constant in stages B, and D. Stage A corresponded to dynamic recovery, and saturation stresses stage in higher SFE materials. Stage B was correlated with the onset of primary deformation twins. In stage C the fall in strain hardening rate was attributed to severe inhomogeneous deformation and misorientation between twin/matrix interface and $\{111\}$ plans in the matrix that were developed in most grains. Therefore, the coherency is lost between twin/matrix interface and the matrix. Extensive secondary twins were found in stage D that intersect primary twins and gives constant strain hardening.

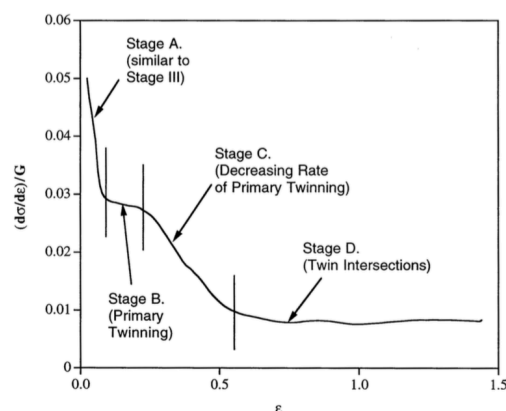


Figure 2-14 four distinct stages for strain hardening in low SFE materials. The strain hardening is normalised by G [41]

Rohatgi et al [42] put forward a modification for Hall-Petch relation for low SFE FCC metals. Their modification uses inter-twin spacing as effective grain size that is HallPetch can be rewrite as following:

$$\sigma_{total} = (\sigma_0 + kd_{untwinned}^{-1/2}) \times (1 - f_{twinned}) + (\sigma_0 + kd_{twinned}^{-1/2}) \times f_{twinned}$$

Where: σ_{total} is total flow stresses, $d_{untwinned}$ is actual grain size, $d_{twinned}$ is inter-twin spacing, $f_{twinned}$ is fraction of grains that exhibit deformation twinning. They also revealed that low SFE materials are not as much sensitive for strain rate as high SFE materials. Increasing strain rate was reported to increase strain hardening rate for high SFE materials. This has been attributed to the delay in the dynamic recovery. In contrast, in low SFE materials, the dynamic recovery process is inherently inhibited. Therefore, the strain hardening rate for these materials is not sensitive to strain rate.

On the other hand, El-Danaf et al. [43] reported indirect dependence of deformation twinning on SFE. They showed that dislocation density and the homogeneous slip length are more relevant variables affect twinning stress. The low SFE has two main effects on plastic behaviour of materials. First, it significantly promotes strain hardening due to the inhibition of dynamic recovery, i.e. cross slip. Secondly, it hinders the development of in-grain misorientation allowing slip length to be almost as same as the grain size up to the onset of twins. They presented their results in a plot (Figure 2-15) and proposed a criterion for deformation twinning initiation stress for polycrystalline FCC material at near room temperature as following:

$$\frac{(\sigma_{twin} - \sigma_0)}{G} = C \left(\frac{d}{b}\right)^A$$

Where d is the average of homogeneous deformation zone HDZ, b is Burger's vector, C and A are fitting parameters. Homogeneous deformation zone HDZ parameter has been created in this study and defined as the area that homogeneously deformed inside the grain. It is also revealed that the smaller grain size, the more difficult to attain this criterion (more difficult to attain critical deformation needed for deformation twinning onset). In other words, it is possible to inhibit deformation twinning even for low SFE material by reducing the grain size.

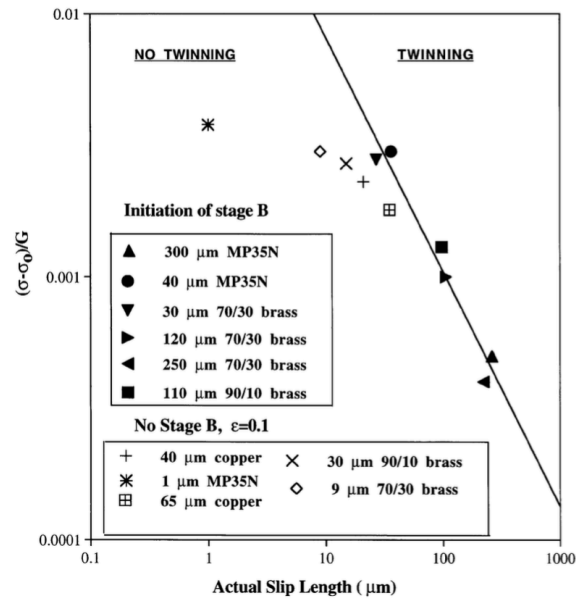


Figure 2-15 the dependence of $(\sigma_{twin} - \sigma_0)/G$ on the average of HDZ length of twinning initiation [43].

2.3.6 Microstructure's Changes During Wear

According to the Hall-Petch relationship, it is well known that hardness increases with grain size reduction [30] [20]. However, it has been reported that this relation breaks down in nanocrystalline [44]. It is also revealed that low temperature and high strain rate among other factors are regarded as a favourable condition for forming nanocrystalline. Figure 2-16 shows the alteration of the mechanical properties dependence on grain size in nanoscale. It can be clearly noticed the breakdown of Hall-Petch relationship in the range between 10-100 nm. Moreover, the relation becomes inversed in the range less than 10 nm grain size [45].

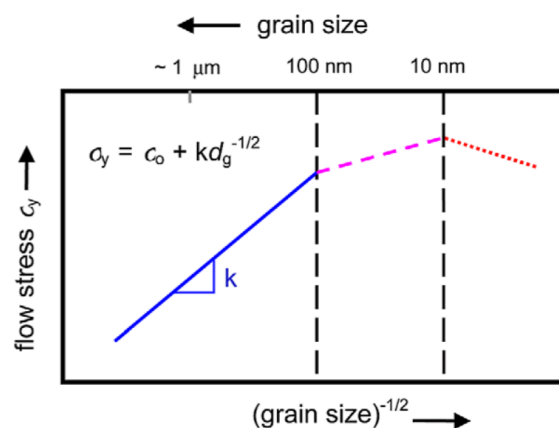


Figure 2-16 the alteration of Hall-Petch relation through different grain sizes [45]

The inverse of the Hall-Petch relationship has been ascribed to the significant increase in grain boundary region compared with conventional materials [46]. It has supposed that

the stresses needed to propagate shear in the boundary region is less than that needed in the case of the crystalline matrix that leads to inverse Hall-Petch relationship.

Buscher and Fischer [2] studied both in vivo and in-vitro tested CoCrMo alloys. The microstructure of both samples (laboratory sample after wear test and retrieval one) was almost the same. They recognized three distinct microstructural zones with respect to the worn surface. At a depth of about 30 μm , the structure includes stacking fault and needles like ϵ -martensite. Closer to the worn surface when the shear strains increase these defects interact with each other forming rhombic cells as shown in Figure 2-17a. In the distance between 10 to 1 μm , no clear microstructure can be identified. Finally, in last 1 μm nanocrystalline was observed (Figure 2-17b). The hardness was found to increase towards the worn surface. Since most of the nanoparticles were more than 10 nm in size, no reverse Hall-Petch relationship has been detected. The increase in hardness was ascribed to the dramatic reduction in grain size, which reaches to 20 k times in retrieval sample and forming rhombic cells.

This astonishing reduction in grain size was attributed to DRX (or in situ recrystallization as it is called by some authors) and explained as follows: in the low SFE materials cyclic shear stresses bring about plastic deformation along discrete sliding planes where neither cross slip nor climb, occurs. On each sliding plane, SF and consequently ϵ -martensite needles form and react with each other forming rhombic cells with size ranging between 100-500 nm. These cells block any further deformation of the incorporated lattice. Toward the surface when the shear stresses increase, these cells sheared and divided into smaller grains. This effect exaggerates with an even further increase in shear stresses (closer to the surface) reaching to the size when these cells are not able to be further refined, resulting in rotation and removal of the texture. This scenario explains the unclear structure in the range of 10-1 μm . However, a kind of recrystallization could occur very close to the surface (1 μm and less) due to mechanically mixed and material transfer layers [6] [34]. Even for self-mating surfaces there is a high probability of having oxides or organic materials on the surface.

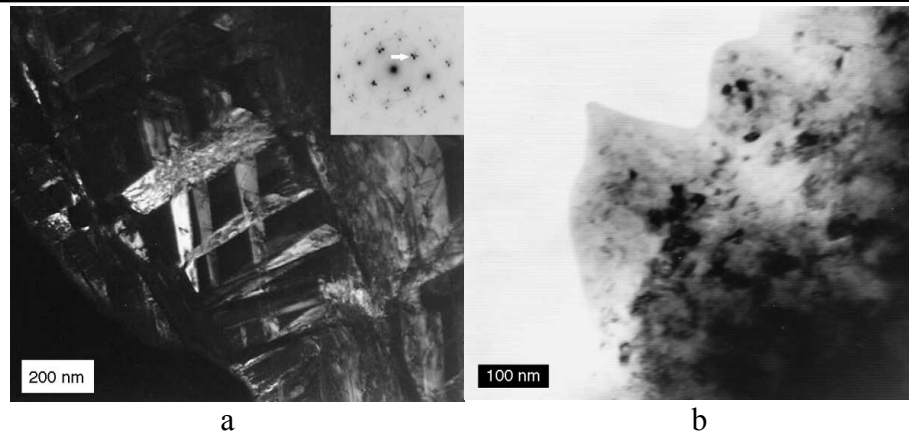


Figure 2-17 a: rhombic cells; b: forming nanoparticles in the very closed surface layer [2]

Wimmer et al. [47] used forty-two retrieved McKee–Farrar prostheses specimens to compare with in vitro specimens. The results showed that 93% of cups and 83% of heads of retrieval samples exhibit the same macroscopic and microscopic layers as in vitro samples. It has been shown that the tribological layers of denatured proteins are formed at the contact spots due to high pressure and flashing temperature (60°C). It has also been suggested that the formation of this layers has a significant influence on the wear behaviour due to prevent direct contact and provide solid lubricant layer.

Fischer [48] identified two distinct regions in both laboratory and retrieved samples of CoCrMo metal on metal hip replacement joints. In the first 200 nm with respect to the worn surface, the region consists of nanocrystalline and interfacial medium (proteins) followed by another nanocrystalline layer but this time consists of just based material. It has been suggested that the cyclic nature of sliding wear and ratcheting behaviour of materials under fatigue loading and fluctuation of friction force leading to increase stresses in the surface and subsurface zones that consequently bring about the formation of different kinds of defects like SF, twins, and strain-induced martensitic transformation. Mechanical mixing, which occurs in the outermost surface layer (<200 nm) between the metal and any substance might exist at the surface is responsible for forming metallo-organic nanostructure composite (Figure 2-18).

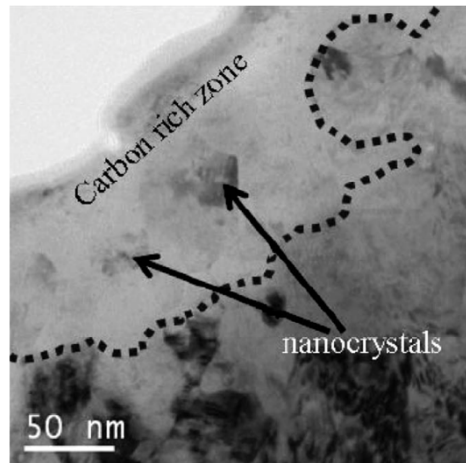


Figure 2-18 forming metallo-organic nanostructure composite [48]

To have a better understanding of the wear mechanism for MoM articulation, Buscher et al [49] investigated the wear debris and their formation for both in-vitro and in vivo samples. There were no significant differences between these samples. Two groups of debris were identified, globular and needle-like. Both of them were less than 100 nm in size (

Figure 2-19). Significant changes again have been detected like stacking fault formation and strain-induced martensite in the subsurface (Figure 2-20a) and nanocrystalline in the outermost surface layer (Figure 2-20b)

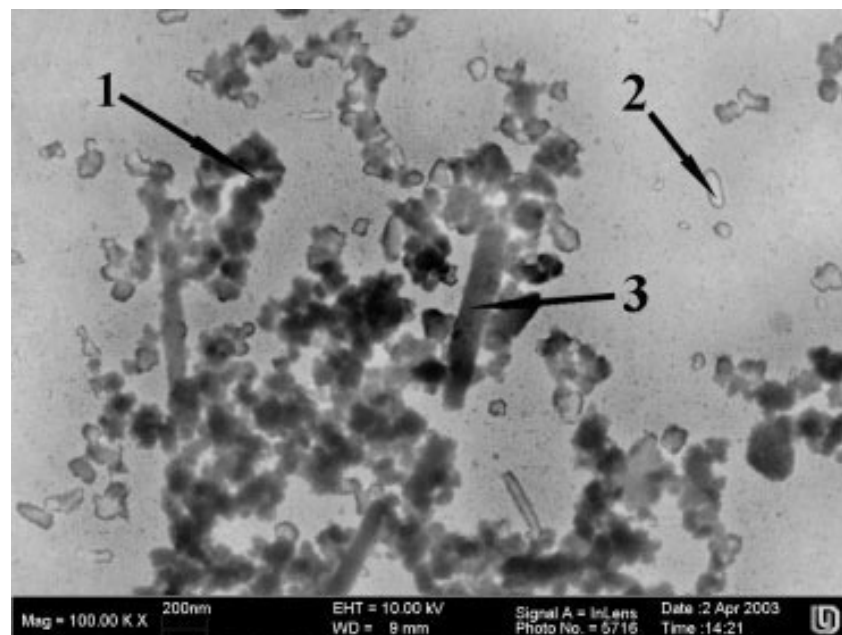


Figure 2-19 wear's debris of CoCrMo alloy [49].

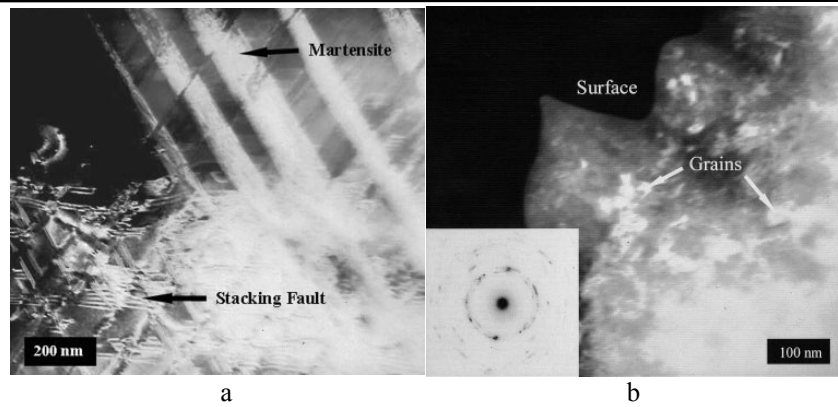


Figure 2-20 a: defects in the subsurface; b: nanoparticles [49]

The worn surface has also been examined (Figure 2-21). It is easy to recognize the existence of grooves parallel to the sliding direction. Most of them are smooth referred to as microploughing (zone 2), but there are some sharp edges that referred to as microcutting (zone 1). Forming tribolayer is noticeable as well (zone 3). Closer examination of the wear debris showed that it consists of crystalline and amorphous structures, and they are either global or needle-like.

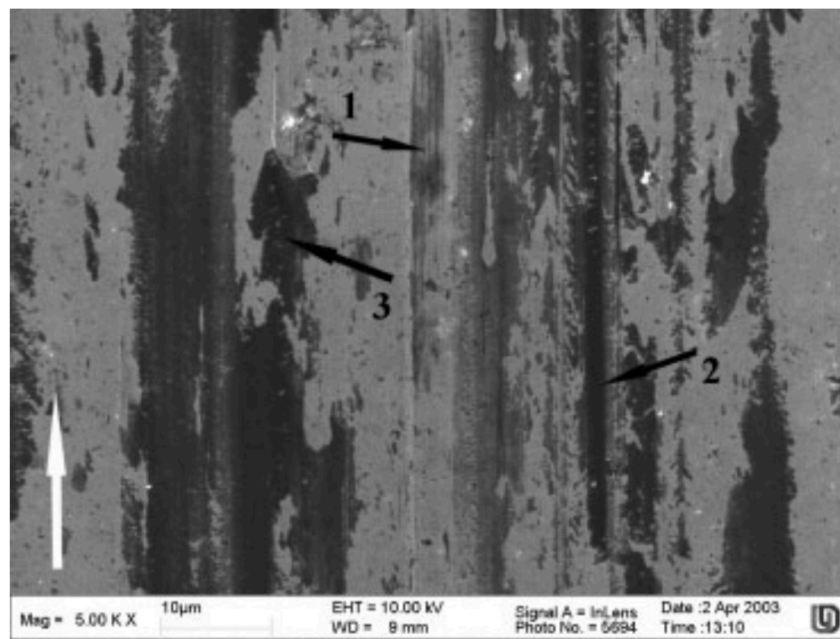


Figure 2-21 worn surface of CoCrMo alloy [49]

The appearance of the worn surface reveals that the dominant wear mechanism is abrasion. Like this mechanism, however, should bring about the formation of either flake-like or chip-shape debris. Microploughing and microcracking are regarded as submechanism for the former while microcutting is the submechanism for the later. On the other hand, self-matting surfaces tend to adhere and form micrometer-sized particles.

Additionally, forming tribilayers and tribochemical reactions are a continuous formation of amorphous particles [6], [50]. All mentioned mechanisms are not valid here since the wear debris is less than 100 nm in size and it has amorphous and crystalline structures. Therefore, it is clear that the changes in surface and subsurface have led to change wear mechanism in such a way that brings about the generation of like this wear debris. The formation of globular debris was attributed to the formation of the nanoparticles on the surface, detached them under cyclic strain, compact them under the effect of their high surface energy and cold sintering. Whereas, needle-like debris was described as a just detachment of needle-like martensitic particle from the surface. Thus, it was suggested that the wear mechanism is surface fatigue within the nanolayer.

Low SFE of CoCrMo alloys, which prevents dislocation cross slip and climbing and consequently the formation of dislocation cells has a dramatic effect on the wear behavior of these materials.

Pourzal et al. [51] used 28 mm CoCrMo alloy femoral head and acetabular cup to analyze primary wear zone, stripe wear zone, and non-contact zone, They reported forming nanocrystalline structure in all these three zones but with different thickness and average grain size. Carbon and oxygen content was reported to increase toward the worn surface proving the occurrence of mechanical mixing. They emphasized that the occurrence of mechanical mixing and particles detachment must take place just within the peaks (the asperities) of the surfaces. Significant microstructure differences have been reported depending on sample preparation technique. The sample prepared by using Focus Ion Beam FIB exhibits double or triple larger grain size in the outermost subsurface compared with others prepared by common cross section preparation.

2.3.7 Lubrication in Artificial Hips and Knees

Hertzian contact theory calculation for Metal on Metal (MOM) total hip replacement shows that the elastic deformation is in order of several micrometre. On the other hand, the theoretical minimum film thickness is reported to be in order of nanometers or tens of nanometers. Therefore, the elastic deformation of these implants is hundred to thousand times larger than film thickness. Additionally, water, serum, and synovial fluid are little affected by pressure. Therefore, it is concluded that MOM joints would work in elastohydrodynamic-isoviscous regime [52].

Dowson et al. [52] have showed theoretically and experimentally that mixed lubrication regime in MOM hip replacement can be achieved by increasing the diameter as much as possible and make the clearance as low as it could be practically. They revealed that the lambda λ rises from less than unity for smaller diameter to up to 3 for the larger diameter. This increasing includes the transition from boundary lubrication regime to elastohydrodynamic EHL one.

The minimum film thickness for the hip joint can be calculated by using the following equation [53]:

$$h_{min} = 0.66685d^{2.19}c_d^{-0.77}\eta^{0.65}\Omega^{0.65}w^{-0.12}E'^{-0.44}$$

where: d: head diameter in m, c_d : the clearance in m, Ω : angular velocity in Rad/s, η : lubricant viscosity in Pa.s, w: load in N, E' : equivalent elastic modulus in Pa.

The equivalent elastic modulus can be calculated by:

$$\frac{2}{E'} = \frac{1 - \nu_1^2}{E_1} + \frac{\nu_2^2}{E_2}$$

E and ν are the elastic modulus and poisson's ratio for the head and cup [54].

It is worth here to define lambda ratio λ which is the ratio between minimum film thickness and composite surface roughness R_{com} in the elastohydrodynamic regime.

$$\lambda = \frac{h_{min}}{R'}$$

$$\text{and } R' = (R_{head}^2 + R_{cup}^2)^{0.5}$$

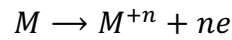
where R is the r.m.s. for the head and cup.

The value of λ provides a measurement of severity of contact between surfaces. If $\lambda \geq 3$ the continues lubricant film will separate the surfaces. For $\lambda \leq 1$ severe contact between surfaces occurs. The regime $1 \geq \lambda \geq 3$ termed mixed EHL when some asperities come into contact. Therefore, the best way to put any regime in mixed EHL for a particular material is by reducing the surface roughness to the minimum [6], [50], [53].

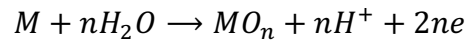
The breakdown of lubricant film in MOM replacement is widely believed to be the reason of failure of McKee–Farrar implants after only a few years while other survive for 20 or even 30 years. It is worth to mention what McKee wrote: “It is very important that the two components are correctly lapped in, so that they articulate freely without any binding, and they are paired and numbered to ensure this accuracy of fit” [55].

2.3.8 Corrosion Resistance

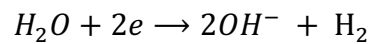
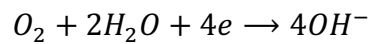
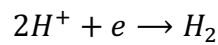
Corrosion is an electrochemical process includes oxidation reaction of active metals to form metal's ions M^{+n} and electrons ne :



Some metals are passive that is they can form a protective oxide layer over their surface and suppress further corrosion. The oxidation reaction for these metals is:



The transferred electrons are consumed either by releasing hydrogen gas (in acidic solutions) or by oxygen reduction (in aerated solution) or water reduction according to following equations:



Under normal corrosion conditions, the corrosion rate of metals depends on oxidation reaction that in turn depends on many factors like temperature, type of electrolyte, availability of corrosive species close to the surface, forming oxides over the surface and forming a galvanic couple. Metals can be in kinetic equilibrium with the surrounding environment at a certain potential called electrode potential or open circuit potential OCP [56].

Although the excellent mechanical properties and high corrosion resistance that CoCrMo alloys have, it was reported that Co, Cr and Mo ions are released to the implant surrounding tissue. It was also reported that Cr and Co are toxic ions [57]. The passive behaviour of CoCrMo alloys was shown to be due to the formation of the oxide film that mainly consists of Cr_2O_3 . This film thickens with increasing time and potential for all anodic potentials except for transpassive ones. Furthermore, the most element to be dissolved is cobalt apart from in transpassive region where all elements are dissolved depending on the alloy's composition. Therefore, the passive behaviour of these alloys is strongly influenced by element chromium, and the dissolution behaviour is mainly affected by element cobalt [58]. Cobalt presents mainly as CoO and Molybdenum as MoO_3 . The distribution of these oxides through the surface layer appears to be nonhomogeneous as the cobalt oxide lays close to the oxide/metal interface and chromium and molybdenum oxides concentrate at the outermost part of the layer [59].

Hsu et al [60] studied the corrosion behaviour of CoCrMo alloys in different biological fluids including urine, serum, and joint fluid by using potentiodynamic scan, cyclic voltammetry and AC impedance spectroscopy. They came to find that these alloys exhibit a larger passive region in urine in comparison to serum and joint fluid. The hysteresis cyclic loop of cyclic voltammetry test in serum and joint fluid were larger which means higher local corrosion resistance in these electrolytes. It is also pointed out that the corrosion resistance of the alloy in joint fluid and serum is slightly higher than in urine. It has been reported that small amount of σ intermetallic phase (<0.6% area fraction) precipitated at the grain boundary does not affect the formation and the breakdown of the oxide layer of Co-29Cr-6Mo alloy in saline solution. However, the quantity of released Cr, Mo, and Ni ions increases with area fraction of σ intermetallic phase. Co ions reported to be the same for different area fraction of σ intermetallic phase [12].

The influence of crystal structure on the corrosion resistance has been studied concern cobalt alloys [61], [62]. These studies have concluded that FCC crystal structure exhibits better corrosion resistance than HCP crystal structure. Any alloying element stabilizes FCC structure would improve corrosion resistance. Xiaoqing Zhang et al [63] studied the corrosion resistance of CoCrMo alloy in 2 wt% H₂SO₄ with different crystal structure. They have noticed different open circuit potential OCP but, same anodic behavior for both FCC and HCP within the passive and transpassive regions. However, they pointed out that the precipitation of σ phase and/or Mo-rich phase on the grain boundary of HCP structure results a heterogeneous microstructure which might act as preferential sites for oxide layer breakdown in the transpassive region. It is also noticed that despite the important role of Cr in forming the oxide layer in passive region, Mo effectively inhibits the dissolution in the transpassive region by attaching to the outermost layer of the oxide film.

2.3.9 Protein adsorption and its effect on corrosion properties

Unsaturated bonded atoms at the surface of the materials attract the active species in the surrounding gas or liquid media in a process called adsorption. It is quite possible that this phenomenon significantly influences the corrosion process by affecting either cathodic reaction or anodic dissolution or even passive film formation. In the centre of the interest of the adsorption phenomenon for the biometallic material is protein adsorption since the implants are always surrounded by protein-rich body fluids. When the protein adsorb on the implant surface it will forms a pocket between the surface and

surrounding tissue. This pocket provides a good environment for bacterial and viral infections which in turn causes increasing in corrosion rate as a result of bacterial metabolic products formation and variation of the pH. Such a complex phenomenon thought to be influenced by many factors including the surface properties of the sorbent, the structural stability of protein, ionic strength, and the pH of the solution [64].

Chemical structure, surface topography, and hydrophobicity among other surface properties of the sorbent play an important role in the adsorption process. Generally, hydrophobic surfaces have more affinity to adsorb protein than hydrophilic ones because of the lack of repulsive forces come from bonded water on these surfaces [64]. However, many researchers [65], [66] have reported no dependence of adsorption on hydrophobicity and surface roughness for passive materials. Clarke et al. [65] showed that the chemical composition of the surface oxide layer has a direct relation to the adsorption of protein on nitinol (50% nickel and 50% titanium). With increasing nickel content and decreasing oxygen content, the adsorption increases. They have reported no dependence on roughness and hydrophobicity. Cai et al. [66] have grown the same chemical composition oxide layer on pure titanium but with different roughness (2- 21 nm RMS) to build a model for studying the roughness effect on protein adsorption. No statistically significant dependence has been observed as well.

The primary structure of the protein and having active sites are another important factors because these are the sites that interact with the surface of the sorbent [64]. In the same context, the pH of the solution plays a role since it changes the protein charges. In acidic solution, the protein gets positive due to the change of $-NH_2$ group to $-NH_3^+$. Conversely, carboxyl group $-COOH$ in the protein loses H to be $-COO^-$ in alkaline solutions.

The influence of adsorption of biological molecules on the corrosion behaviour of biometallic material can be summarized as [64], [67]:

1. Altering the availability of anions on the interface causing cathodic reaction modification.
2. Covering the surface by a compacted layer which consequently affects the diffusion of cations (metals ions).
3. Binding to metal's ions forming organometallic complexes and move them away from the metal/solution interface. Thus, enhancing further dissolution.

The adsorption equilibria can be described by using different isotherms in which the adsorbate coverage has been treated differently. These models are summarized here [64]:

1. Langmair isotherm:

The model assumes single monolayer homogenously covers the surface. Thus, a saturation point can be reached at equilibrium when there is no further adsorption/desorption. In other words, there is a threshold after which no further adsorption occurs. Mathematically, it can be expressed as:

$$\Gamma = \frac{B_{ADS}\Gamma_{max}c}{1 + B_{ADS}c}$$

Simplified to $\frac{c}{\Gamma} = \frac{1}{B_{ads}\Gamma_{max}} + \frac{c}{\Gamma_{max}}$

in which Γ is the concentration of adsorbed protein on the surface in (mol/cm²), B_{ads} is the affinity of the adsorbate molecules toward the adsorption surface in (cm³/mol), Γ_{max} is the maximum value of Γ , and c is the bulk solution concentration in (mol/cm³).

It has repeatedly been reported that this isotherm successfully describes protein adsorption on biometallic surfaces i.e. CoCrMo, titanium, and austenitic stainless steel) [68]–[71].

2. Freundlich isotherm:

This isotherm proposes increasing in adsorption with solution bulk concentration. Thus, infinite adsorption might occur.

$$\Gamma = B_F c^{\frac{1}{n}}$$

simplified to: $\ln\Gamma = \ln B_F + \frac{1}{n} \ln c$

where B_F and n are constants. B_F represents the quantity of adsorbed protein for a unit equilibrium concentration. The isotherm is used to describe heterogeneous adsorption of protein like that on ultrahigh molecular polyethylene UHMPE or on nanoparticles. The line slop $1/n$ is ranging from 0 to 1 when the lower value refers to higher heterogeneity.

3. Temkin isotherm:

This isotherm uses binding energies approach and assumes a uniform distribution of these energies. The mathematical form of this isotherm is:

$$\Gamma = \Gamma_T(1 + B_T c)$$

Γ_T is the differential capacity of the surface for adsorbed protein per unit binding energy. B_T is equilibrium binding constant which is:

$$B_T = e^{\frac{\Delta G_{max}}{RT}}$$

The isotherm parameters (Γ_T , and B_T) are determined by nonlinear regression via a computer software.

The corrosion rate of austenitic stainless steel was reported to be increased significantly when protein exists in the solution. The polarization resistance decreases with protein concentration followed by plateau after a threshold (Langmuir isotherm) at 299-343 K temperature range. The mechanism of adsorption was proposed as the interaction of the negatively charged carboxylate group of the protein with austenitic stainless steel involving charge transfer and thus strong adsorption (chemisorption) [69], [70]. The influence of bovine serum albumin and fibrinogen in buffered saline solution on corrosion rate for aluminium, copper, titanium, nickel, cobalt, chromium, molybdenum, and CoCrMo cast alloy has been studied [72]. With adding protein, highly passivated metals like aluminium and titanium do not exhibit any change in their corrosion rate while the corrosion resistance of nickel and chromium slightly decreases to about two- to fourfold. Copper and cobalt, however, showed a significant increase in the corrosion rate to 30-40 times in comparison with free protein solution. It is also noticed that cobalt and molybdenum probably selectively dissolve from CoCrMo alloy leaving chromium-rich surface layer. The differences in the corrosion behaviour have been attributed to the stability of the oxide film in case of titanium and aluminium when the corrosion rate has not changed that much. Protein might work as a catalyst on cobalt and copper enhancing corrosion rate. The possibility of oxide film breakdown was also proposed in case of cobalt and copper.

The adsorption of fibrinogen and BSA on commercial pure titanium over a range of temperature (295-343 K) and protein bulk solution concentration (0-0.4 g/L) has been studied [71]. Direct relation between charge transfer and protein surface concentration has been shown indicating that the process is chemisorption. The two proteins showed different adsorption isotherm. BSA exhibits bimodal isotherm, whilst fibrinogen revealed single saturation plateau with twice higher affinity for adsorption. The process of protein adsorption appears to be endothermic and entropically controlled. The pseudocapacitance measured by EIS was in good agreement with charge transfer measured by cyclic voltammetry and well related to protein surface adsorption like charge transfer.

Valero Vidal et al [68] successfully used EIS to investigate the effect of BSA adsorption on CoCrMo alloys. Charge transfer resistance is found to be very sensitive to amount of

protein adsorption. Corrosion activation energy was reported to decrease with protein adsorption till a particular point (500 mg/L) where it significantly increases. The inhibition behaviour of protein at relatively high solution bulk protein concentration was rationalized to the covering the surface by protein which blocks, to somehow, mass transport of corrosion products and/or oxygen. The entropically control nature was also reported to be dominated as a thermodynamic driving force for the adsorption of protein on CoCrMo alloys exactly as is noticed on autunitic stainless steel [70] and titanium [71]. The obvious gain in entropy clearly unveils conformational changes of adsorbed protein which could arise from protein structural unfolding on the adsorbate.

The adsorption of bovine serum albumin on CoCrMo alloy is reported to be sensitive for surface passivation. Increasing OCP time and applying passive potential both have led to reduce the amount of adsorbed protein. The deliberately passivated surfaces adsorb less BSA compared to those surfaces that have not developed stable oxide layer [73]. Ann Igual and Stefano Mischler [74] suggested competitive adsorption mechanism of phosphate buffered saline PBS ions and albumin on the surface on CoCrMo alloy. They tested the adsorption at OCP and passive potential in different solutions (NaCl, and PBS. with and without albumin). At passive potential, the oxide layer's chemical composition and thickness have not been affected by the solution chemistry. However, the adsorbed layer resistance and capacitance show a significant dependence on solution composition. The extreme case was at PBS solution that has given highest adsorbed layer resistance. This resistance was even higher than oxide layer resistance making the adsorbed layer is the kinetics limiting factor in the corrosion process. This has been attributed to the very compacted detected phosphate ions layer that covers the surface and probably efficiently blocks mass transport. Like this compacted layer cannot be achieved with giant molecules like albumin. The presence of albumin has the same effect but to less extent where oxide layer still the most important factor in blocking mass transport. Conversely, at OCP the nature of the passive film has been modified by composition of the solution. The formation condition of the oxide layer is thought to be the reason behind this. The fast growth of the oxide layer at passive potential could limit the interfere of phosphate ions and albumin to the process which is not the case at OCP where this growth is relatively slow.

2.3.10 Tribocorrosion the interaction between wear and corrosion

According to ASTM International tribocorrosion is defined as “a form of solid surface alteration that involves the joint action of relatively moving mechanical contact with chemical reaction in which the result may be different in effect than either process acting separately” [75]. This phenomenon can be explained by assuming a hard and inert ball is sliding over a passive metal under F_n load and v_s speed (Figure 2-22) [76].

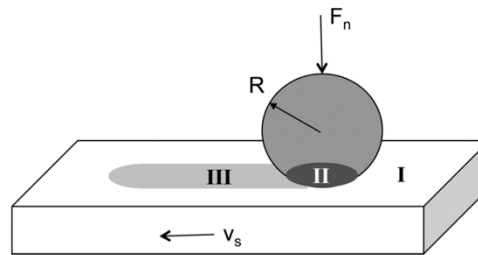


Figure 2-22 Tribo-corrosion effect [76].

Three different zones with three different degradation mechanisms can be recognized. The first zone is a mechanically unaffected zone (zone I). Although this zone never comes into contact with the ball, rubbing effect might change degradation mechanism, as one of the polarization mechanism depends on mass transfer of corrosive species (concentration polarization) [77] and directly affected by rubbing. It has been reported that this stirring effect enhances oxide film dissolving in tungsten exposed to sulfuric acid [78]. Forming a galvanic couple between wear track and this zone which changes the potential of both zones considers as another crucial factor leads to alter degradation mechanism in this zone. It is worth noting that changing potential for passive metals may put them in the active region rather than in the passive one.

In zone II, mechanical wear is the dominant degradation mechanism. Nevertheless, air may enter this zone leading to corrosion reaction. Zone III represents bare metal after removing oxides under mechanical effect.

Using electrochemical methods in tribological studies provides two important advantages. Firstly, one can precisely study the effect of corrosive environment just by varying the applied potential. Secondly, they are used to know the amount of dissolved metal simply by using current measurement [79].

In the example that shown in Figure 2-22, the potentials of zone I and zone III are changed due to rubbing because of forming a galvanic cell between bare metal (zone III) and passive metal (zone I). This effect can be well visualized using Evans diagrams (Figure 2-23). These diagrams illustrate anodic and cathodic current as a function of electrode

potential. Figure 2-23a represents the situation before rubbing starts. E_{corr} corresponds to the intersection between cathodic and anodic reactions. Rubbing mixes it up by forming two different areas with two different potentials, one corresponds to the active state and other to the passive state. In the ideal conditions, these two potentials would move toward one potential lays somewhere in the middle between the two potentials. However, and due to the ohmic resistance of the electrolyte, a certain potential is maintained between active and passive areas. This potential is given by the product of anodic current I_a times resistance R (Ohmic drop iR) and leads to attaining E_a and E_c for anodic and cathodic potentials in Figure 2-23c respectively [3]. It is known that with increasing potential for passive metals, current decreases due to building up of a passive film [80]. This means that the net potential is a result of both ionic resistance of the electrolyte (although it is small in biological fluids) and the interruption of oxide film formation. It also means that actual electrode potential might vary with time in tribocorrosion even if the applied potential is constant.

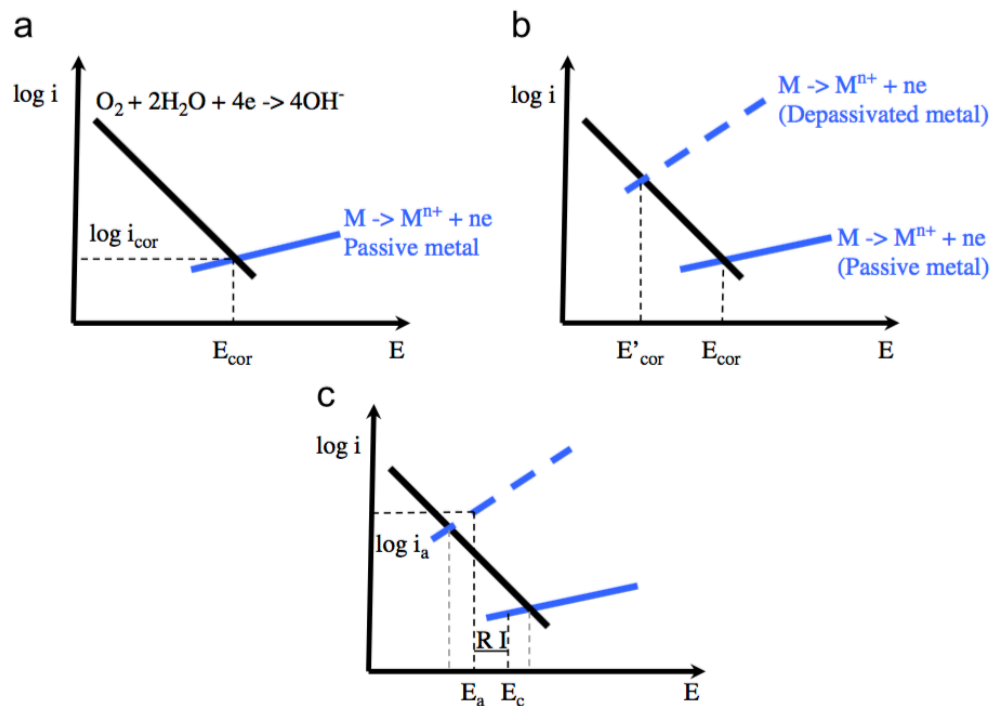


Figure 2-23 Evans diagrams representing the effect of rubbing on electrode potential, a before rubbing, b and c are explained in the text [3].

A theoretical model has been developed by Vieira et al. [81] to describe passive surface potential E_a and depassivated one E_c as following:

$$E_a = E_c - R_{ohm}I_a$$

R_{ohm} is the electrolyte resistance. Derived from the linear part of cathodic branch in Tafel extrapolation to find a relation between cathodic potential and current density and combine it with previous equation yield:

$$E_c = E_{corr} + a_c - b_c \log i_a - b_c \log \frac{A_a}{A_c}$$

Where: a_c and b_c are constants, and E_{corr} is the corrosion potential of the passive metal. This equation shows that cathodic potential in galvanic couple forms in tribocorrosion mainly depends on anodic current and the ratio of anodic to cathodic areas. For determining the excess anodic current due to rubbing two main scenarios of sliding have been proposed. The first one supposes sliding of two surfaces with comparable roughness. Therefore, the interaction occurs between asperities (quite similar to the assumption of classical wear theory) leading to deform and depassivate them. The second scenario is when an asperity moves over flat leaving a track of depassivated metal. In both cases the excess current can be calculated by [79]

$$I_p = Kv \left(\frac{F}{H} \right)^{1/2} Q$$

K is proportionality factor, v is sliding velocity Q is charge density needed for passivation, F is the load and H is the hardness of the softer metal.

Depending on the nature of the protective oxide film and its adhesion to the surface, two limiting galvanic couple cases might arise. The first one is when the wear track is completely depassivated. This case is likely to occur when the film is weak and not strongly adheres to the surface. The anodic area is the area of the wear track while the cathodic area is the passive area surrounding it. In this case, the anodic area and consequently A_a/A_c is continuously increases in the course of the experiment and depends on the normal load. The second scenario occurs when the film strongly adheres to the surface, therefore, not the whole wear track is depassivated. Galvanic couple, thus, forms between depassivated and passive areas inside the wear track. Here it is supposed that A_a/A_c remains constant in the course of the experiment and does not depend on normal load as long as the contact pressure is high enough to provoke depassivation and plastic deformation [81].

Figure 2-24 shows the effect of rubbing on measured current for 430 stainless steel in sulfuric acid. The alumina pin was rubbed against anodically polarized stainless steel at 1 Hz frequency. This rubbing included stopping the end of each stroke for 0.2 s as

illustrated in the figure. The current increases during rubbing due to depassivation and removing of the oxide layer under the mechanical effect [79].

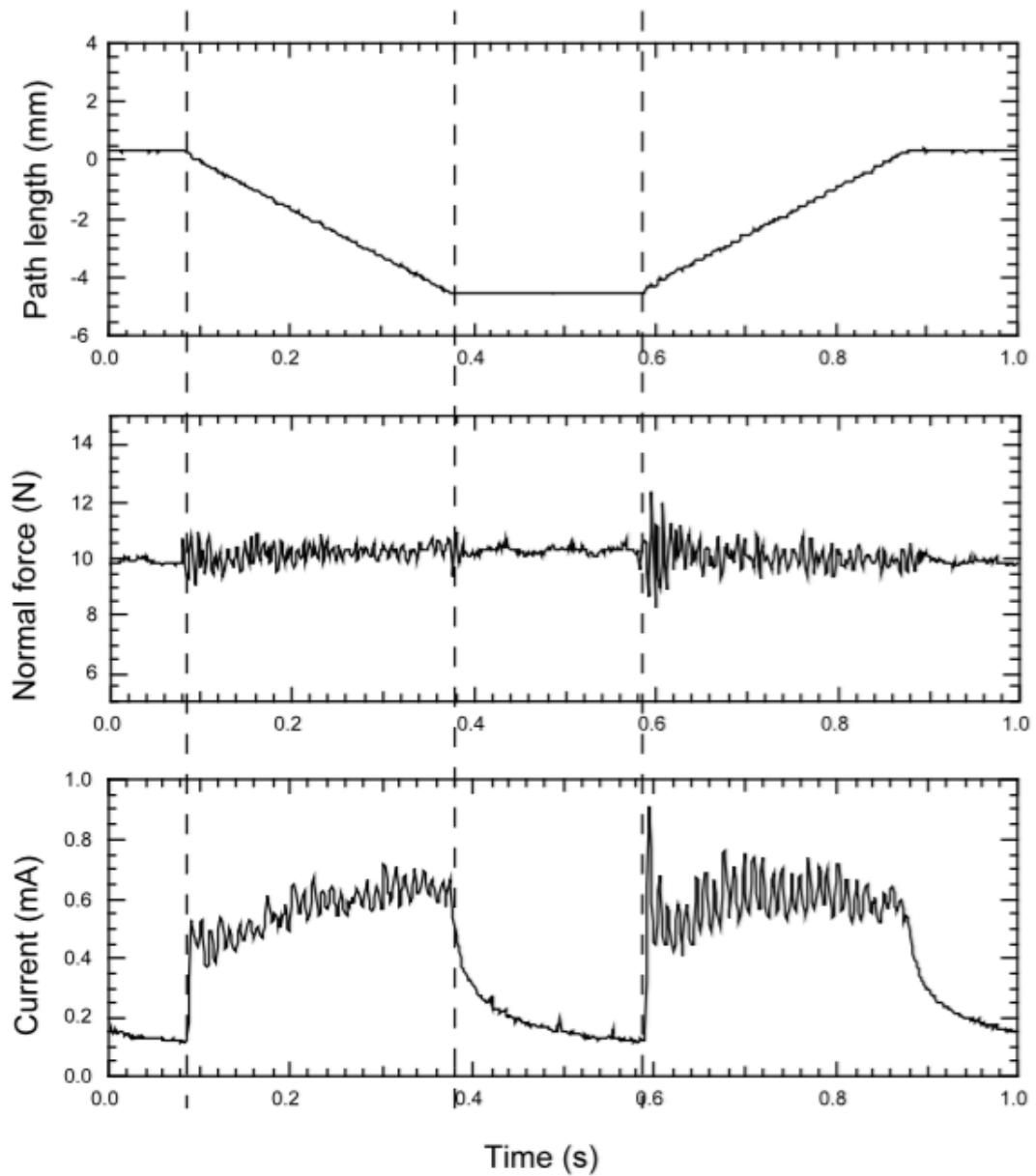


Figure 2-24 the effect of rubbing on flowing anodic current [79]

Total wear volume V_t is the sum of mechanical V_{mech} and electrochemical V_{chem} wear volume,

$$V_t = V_{mech} + V_{chem}$$

Electrochemical contribution of wear at anodic potentials can be determined by using Faraday's law [56], [79]:

$$V_{chem} = \frac{I_p M}{nF\rho}$$

Where: I_p is excess passive current, M is the equivalent atomic mass, ρ is the density and F is Faraday's constant (96500 C/mol). Furthermore, it was proposed [82]:

$$V_{chem} = \frac{K v \left(\frac{F}{H}\right)^{0.5} Q_p M}{n F \rho}$$

Where: K is proportionality factor and Q_p is passivation charge. This equation was developed for boundary lubrication regime when lubricant film does not provide any load bearing in the contact area. In the design of artificial joints, however, a lot of efforts have been spent to ensure that mixed elastohydrodynamic lubrication regime is achieved.

Shoufan et al [82] presented a predictive wear model for MOM artificial hip joints based on tribocorrosion and lubrication approached. They calibrated their model depending on the literature data for tribocorrosion experiments for CoCrMo alloys in 0.5 M H_2SO_4 and tested it for the data of other tribocorrosion sets (CoCrMo in 0.14 M NaCl).

$$V_{tot} = 0.01363 \frac{E'^{(0.6556)}}{\eta^{0.9685}} \times \frac{F_n^{1.3129} v^{0.0315}}{R'^{(1.1473)}} + 750.35 \frac{M Q_p E'^{(0.3278)}}{\eta^{0.4843}} \times \frac{F_n^{0.6565} v^{0.5158}}{R'^{0.5737} H^{0.5}}$$

The model involves number of material (E' , M and H), mechanical (F_n , v and η) and electrochemical (Q_p) factors and was in good agreement with literature data. The differences were rationalized to the determination of exact passivation charge density.

Figure 2-25 shows the prediction of mechanical, chemical and total wear rate for some parameters by using this model. Figure 2-25a shows relation between the normal load and wear rate. It is clear that chemical contribution is higher than mechanical one. Figure 2-25b indicates that the angular velocity has a great influence on chemical wear as it increases the total distance while it has little effect on mechanical wear since it leads to increase the lubricated film thickness. Figure 2-25c and d clarify the effect of head radius and radial film thickness. In general, wear rate decreases with increasing head diameter and reduce clearance. This is not always the case, however, as it is shown in Figure 2-25c, in 20 mm head radius, the chemical wear becomes dominated and the total effect of this parameter becomes less.

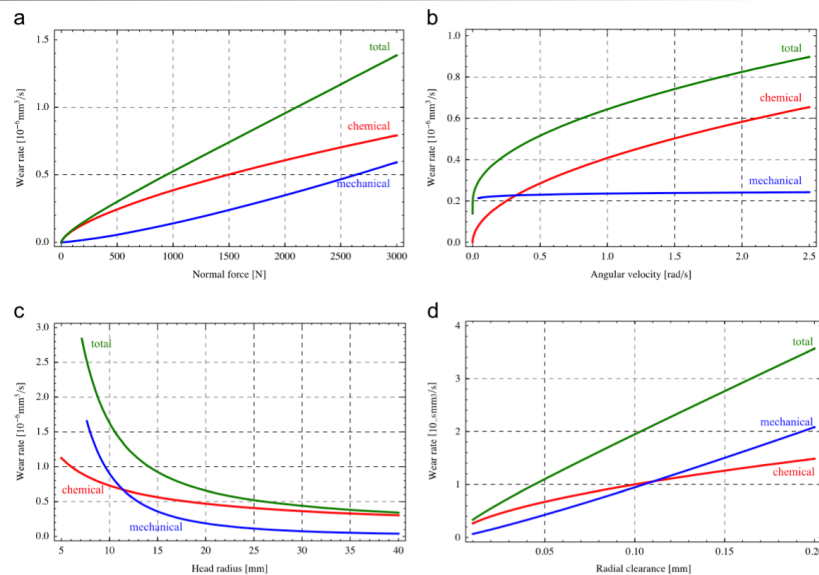


Figure 2-25 the effect of normal load (a) angular velocity (b) head diameter (c) and radial clearance on mechanical, chemical and total wear. [82]

Figure 2-26 shows the contribution of both V_{mech} and V_{chem} for 403 stainless steel in 0.5 M H_2SO_4 at different potentials. Obviously, it is possible to eliminate electrochemical contribution under cathodic potential. However, over-potential should be avoided to prevent hydrogen embrittlement in acidic solutions [83]. While in low and high passive potentials both mechanical and electrochemical wear work, their contribution directly depends on valence number. As it is not easy to identify the valence for some metals and alloys, the calculation of V_{chem} always includes some uncertainty.

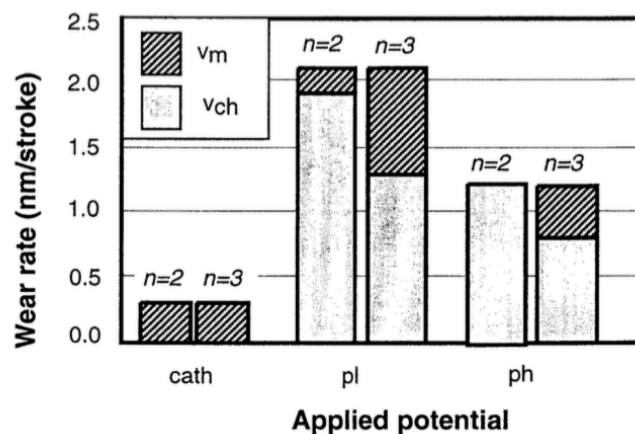


Figure 2-26 contribution of mechanical and electrochemical wear at three different potentials: cathodic potential (cath), low passivation potential (pl) and high passivation potential (ph) [79]

Jemmely et al. [80] developed a theoretical model to describe the current transients in tribocorrosion for iron-chromium alloy AISI 430. They took passive film growth kinetic and ohmic resistance between the anode (wear scare) and a reference electrode in their

account. This model is in good quantitative agreement with experimental results as it can draw the shape of current transients. However, the quantitative prediction could not have been achieved. They attributed quantitative discrepancies to some mechanical and electrochemical factors that they did not take in their account like third body effect and the prevailing electrochemical conditions in the contact zone.

Two passive film growth models were proposed, lateral growth LG and uniform growth UG (Figure 2-27). According to the lateral growth model, the oxide film grows laterally until covers the entire surface when the dissolution is blocked and the current drops down abruptly. This model was in a clear disagreement with experimental results. In contrast, the second model supposes uniform growth of passive film, which is in qualitative agreement with experiments observation. The surface has to be covered with contiguous passive layer before uniform growth can occur. This possibly means that LG occurs in the initial phase followed by UG.

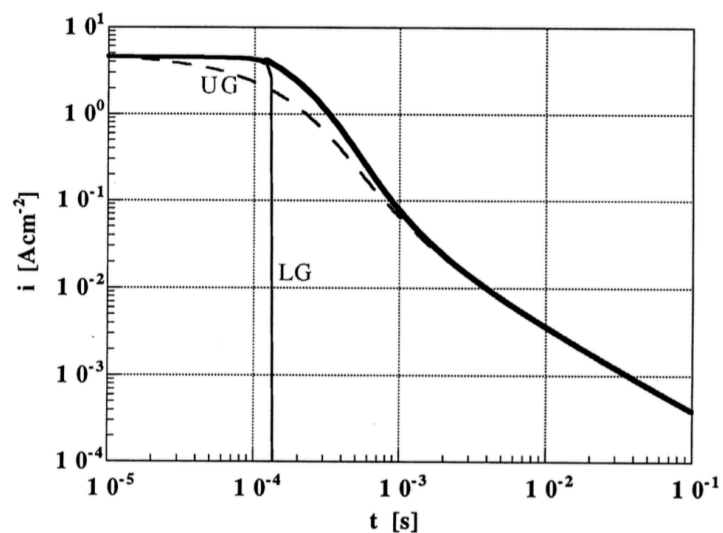


Figure 2-27 uniform growth model UG and lateral growth model LG for passive film [80]

In tribocorrosion conditions, the wear mechanism might vary depending on applied potential. Mischler et al. [84] revealed that hardness does not play the same role under cathodic and anodic potentials as it is showed in Figure 2-28. Surprisingly mechanical wear for all steel samples at anodic polarization was higher than that at cathodic polarization. Additionally, this was more pronounced with higher hardness steel. Based on SEM imaging, they attributed this behavior to the wear mechanisms that work under particular potential. At cathodic potential wear's debris form a compact layer over the surface which was periodically removed under sliding effect. At anodic polarization, on

the other hand, the wear mechanisms were fatigue cracking and abrasion characterized by local disruption (cracks) and scratches respectively. This strongly suggests that applying potential does affect both mechanical and electrochemical wear.

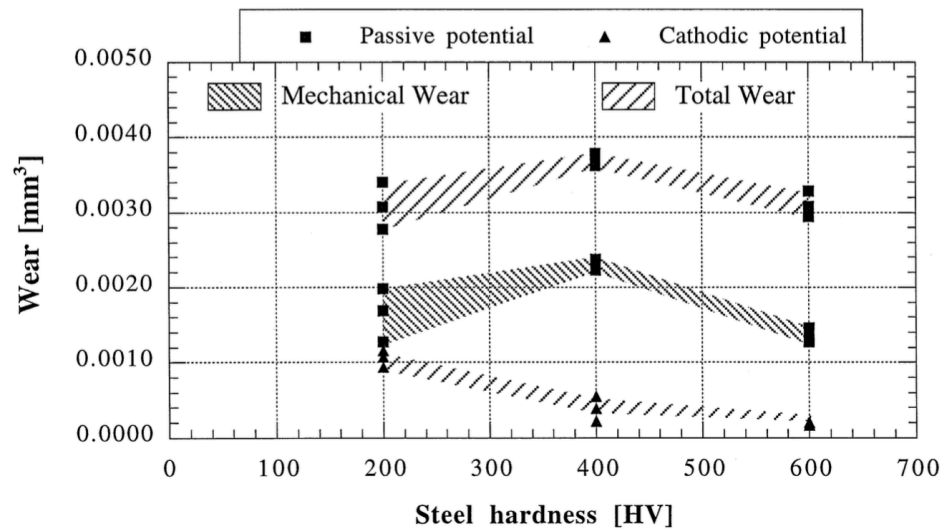


Figure 2-28 The hardness and wear volume [84]

It has also been revealed that applying cathodic protection CP to eliminate the effect of corrosion on wear has led to significant enhancement in wear scar appearance by preventing adhesion wear and delamination (Figure 2-29) [85].

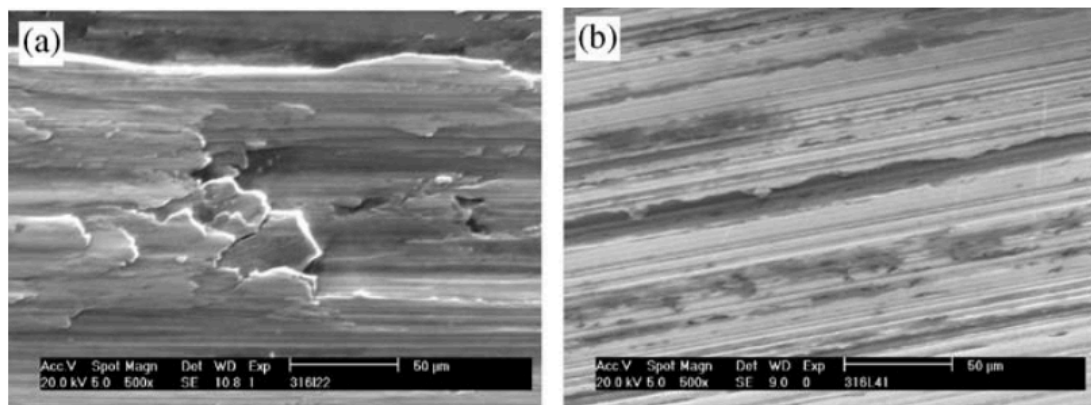


Figure 2-29 tribo-corrosion test for CoCrMo alloy (a) without CP (b) with CP [85]

Some studies have been carried out [85], [86] to understand how can the synergistic effect of the mechanical loading and chemical reaction influences wear and corrosion rate. It has been shown that between 22% to 50% of the damage in different biological media is rationalized to synergistic effect as can be seen in Figure 2-30.

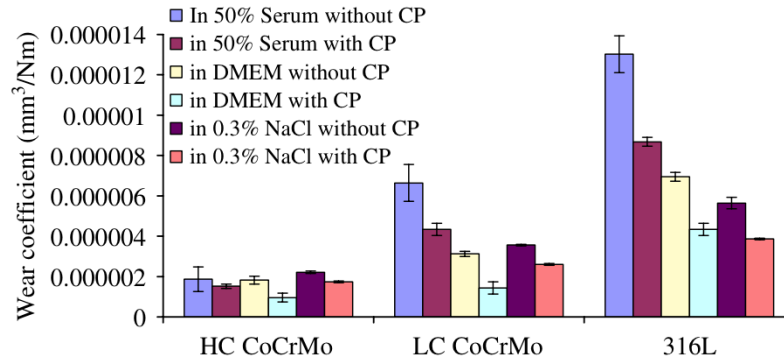


Figure 2-30 synergistic effect of wear and corrosion for three different materials in three different biological media [86]

Mathew et al [87] classified tribocorrosion. According to this classification, tribocorrosion is the interaction of corrosion with one or more of following:

- Abrasion
- Fretting
- Erosion
- Sliding wear

They identified four different main groups as factors affect tribocorrosion. These groups are (as shown in Figure 2-31): materials, solution, operational and electrochemical.

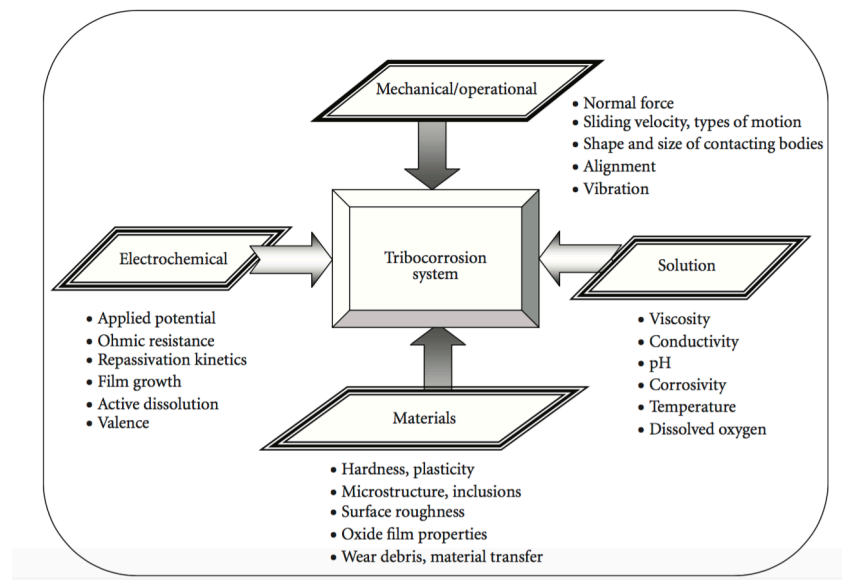


Figure 2-31 factors affect tribocorrosion [87].

It has been found that the coefficient of friction varies with electrode potential, and it can be recognized three different stages. In the first stage, the protective layer is removed under the mechanical effect. Thus, the ions start to release rapidly and interact with proteins forming organo-metallic complex. This complex provides efficient solid

lubricant, which consequently reduces the friction force. Further increase in potential leads to breakdown of this protective layer and thus increasing friction force again.

Rapid formation of nano-crystalline layer right below the worn surface at the passive potentials compared with cathodic potentials has been reported for the stainless steel in sulfuric acid [88], [89]. This was attributed to the mismatch of elastic properties between oxide layer and the metallic surface itself which consequently interferes generation and inhalation of dislocations in the subsurface region.

Igual and Mischler [90] compared high and low carbon CoCrMo alloys corrosion and tribocorrosion behaviour in different kinds of body fluid (NaCl and PBS with and without albumin). They came to find that in general LC alloys exhibit higher corrosion resistance in most used solutions and using PBS solution enhances corrosion resistance of HC alloy. In PBS solution it has found that adding albumin increases current densities in HC alloy. Indeed corrosion resistance depends on alloy composition and microstructure, and environment and chemical composition of the used lubricant (electrolyte). In NaCl and NaCl + albumin solutions it seems that the dominated controlling factor is the composition of the alloy. Obviously, in HC alloy, a significant part of chromium goes to form chromium carbide leaving behind the matrix with less chromium and more prone to corrosion [8]. Therefore the dissolution rate of LC alloy is lower than that of HC alloy. In PBS solution, the phosphate ions are adsorbed on the surface of CoCrMo alloys and work as corrosion inhibitors. However, adding albumin to this solution effectively reduces this inhibition effect since it forms complex metallic ions, which are adsorbed on the surface, but its anodic catalytic effect is higher than the inhibition effect of it and phosphate ions together. The dominant wear mechanism was three body abrasive wear. In the presence of albumin, agglomerations of small particles have been noticed showing the binding effect of protein, which reported by others researchers [91], [92] as well.

The effect of thermal treatment of as-cast HC CoCrMo alloy in simulated body fluid (NaCl, NaCl + Bovine Serum Albumin BSA, and Bovine Serum BS) on tribocorrosion behaviour has been studied [93]. The thermal treatment has decreased carbide amount and increased grain size area. Generally, high carbide volume fraction generates lower wear coefficient while less grain boundary leads to decrease anodic current. The existence of protein has a direct effect on wear mechanism and the appearance of wear debris. Forming a tribolayer on the surface (in the case of protein existence) and repeated load stimulate nano-debris to agglomerate under the consequence agglomeration-compaction-

cold sintering. The later entrapped in wear track especially in grooves providing a protection against further abrasion. This conclusion is supported by Radice and Mischler [94] who studied using alumina nanoparticles suspension as a lubricant in 316L steel-alumina reciprocal sliding wear experiment. They found that this decreases the coefficient of friction by 40-50% and wear accelerated corrosion by one order of magnitude. They attributed this to the formation of adhered third body layer on the surface.

3 Experimental work

The tribological and tribocorrosion behaviour of CoCrMo biomedical grade alloy was investigated in details. The tribological testing covered a wide range of load to figure out the load effect on the microstructure, mechanical properties and consequently on the wear behaviour of the alloy.

Depending on the results of this investigation, a range of load was chosen to be examined under tribocorrosion condition.

The cathodic polarization of the metallic surface in bioapplications is likely to occur. When a small part of the surface gets scratched, the potential of the surface inside this scratch is bare metal with much lower cathodic potential. Thus, the whole system is cathodically polarized. It is also likely for this to maintain for a while when it occurs during walking or running. The severity of this polarization depends among others on kind, numbers and position of these scratches. Interestingly, the potential effect on the mechanical and chemical material loss for *in vitro* tribocorrosion testing has not been covered well in the literature. Thus, realistic selective cathodic potentials were chosen to be studied as well as the normal case at open circuit potential. Three anodic potentials were added to the work to get a better understanding for the tribocorrosion behaviour of the material being investigated.

Additionally, the sliding speed effect was poorly tackled in the literature despite being an important factor in orthopedic implants. Therefore, a range of reciprocating sliding speeds was examined. The range covers the real sliding speeds in the hip joint and two slower sliding speeds to find out the possibility of enhancing the performance of CoCrMo alloy by simply changing the design.

Throughout the entire work, the authors tried to mimic the real application conditions by pragmatic choosing of the investigated parameter. However, the loads were selected to be much higher than that at real hips and knees. This is for many reasons. First, the work is targeting the worst scenario in the application, and secondly, it has been reported that local contact pressure in the hips could reach a higher than expected value [95].

3.1 Material and preparation

The chemical composition of the as cast low carbon CoCrMo alloy, supplied in 20 mm diameter bar form, is shown in Table 3-1. Samples were sectioned into 3 mm thick discs. All samples were mechanically ground in the standard manner, finishing with 1 μm diamond and Silco™ to ensure the best possible surface finish with the minimum residual surface damage. Optical profilometry (ContourGT 3D Optical Microscope, Bruker) was used to measure the surface roughness of the samples after polishing, which was less than 10 nm R_a for all starting surfaces.

Table 3-1 chemical composition of the material

Element	Co	Cr	Mo	Mn	Fe	Si	Ni
%	64.91	27.48	5.25	0.45	0.32	0.42	0.16

Ion channelling contrast imaging for polished surface was used to calculate the grain size of starting surface. The imaging was done by FEI (Quanta 200 3D FIB, SEM). The current was 30 pA and the scan rate was 0.5 ms.

3.2 Tribological studies

3.2.1 Initial contact pressure calculation:

The configuration of all wear tests in this work was ball on flat. Under this configuration, the initial shape of contact is circular with contact radius calculated depending on Hertz contact theory as follows [96]:

$$a = \left(\frac{3Wr}{4E^*} \right)^{1/3}$$

where W is the normal load, r is the ball radius, E* is reduced modulus. E* can be calculated as follows:

$$\frac{1}{E^*} = \frac{1 - \nu_B^2}{E_B} + \frac{1 - \nu_M^2}{E_M}$$

E and ν are the modulus of elasticity and Poisson's ratio and the subscription B and M refer to the ball and the material respectively. The maximum contact pressure is in the centre of this contact shape and is given by:

:

$$P_{max} = \frac{3}{2}P_{mean}, \quad P_{mean} = \frac{W}{A} = \frac{W}{\pi a^2}$$

$$\rightarrow P_{max} = \frac{3}{2} \frac{W}{\pi a^2} = \frac{3W}{2\pi \left(\frac{3Wr}{4E^*}\right)^{2/3}} = \frac{1}{\pi} \left(\frac{6WE^{*2}}{r^2}\right)^{1/3}$$

The shear stress of this configuration is [50]

$$\tau = \frac{P_{max}}{3.3} = 0.3P_{max}$$

3.2.2 Work procedure

Reciprocating sliding wear tests were carried out by using a Bruker UMT Multi-Specimen Test System (Bruker, UK). A ball on plate configuration, which conformed to ASTM G133, was used. The counterpart was an alumina ball with 4 mm diameter and 99% purity (Oakwase Ltd., UK). An alumina ball was used to have an inert counterface and to be able to compare the data with tribocorrosion tests. To simulate body fluids, new born calf bovine serum (First Link (UK) Ltd.) was diluted and buffered to 25 vol.% in an aqueous solution of phosphate buffer saline PBS (Sigma-Aldrich). Ultrapure water (Alfa Aesar) was used in the preparation of the solution. 1 wt.% sodium azide (99% extra pure (Arcos Organics) was added to the solution to avoid bacterial growth. This gave a solution with a protein content of 15.8 g/L. The pH of the solution is 7.4. For reciprocating testing, a 10 mm stroke length and constant reciprocating speed of 10 Hz (0.2 m/s) was used. Although this speed is faster than in normal hip articulation (0.02-0.05 m/s) it was chosen to ensure a continuous removal of the oxide layer so that wear was dominated by the mechanical effect. A test duration of 3 h was used in all cases (which is equivalent to 108000 cycles and 2.16 km sliding distance). A wide range of normal loads were used, namely, 5, 10, 20, 40, 60, and 80 N. Two tests were undertaken for each load, and the wear results were found to be very consistent.

The wear volume was determined by using a 3D optical microscopy. A series of images along the wear track were taken and stitched together to get precise and statistically meaningful wear volume from the wear tracks. A total length of 11 mm was analyzed, with each image overlapped by 20%. The specific wear rate K in mm³/N.m was calculated using the standard formula [97]:

$$K = \frac{V}{dL}$$

where V is the wear volume of material loss in mm^3 ; L is normal load in N and d is the total sliding distance in m.

3.3 Corrosion characterization

3.3.1 Work procedure

Corrosion characterization of the starting surface was carried out by using a corrosion and tribocorrosion cell with no rubbing (showed schematically in Figure 3-1). It is three electrodes traditional cell which has Ag/AgCl wire in 1 M KCl as a reference electrode (its potential vs. SHE is 0.235 V), a platinum wire as a counter electrode, and the material being tested as working electrode. The cell also has a heater and temperature sensor to control the test temperature. The volume of the cell is about 100 mL. The cell is connected to Bruker UMT Multi-Specimen Test System to control the temperature and record F_z , F_x and COF (in the case of tribocorrosion test) and to VersaSTAT 3F Potentiostat Galvanostat (Princeton Applied Research) to control the potential.

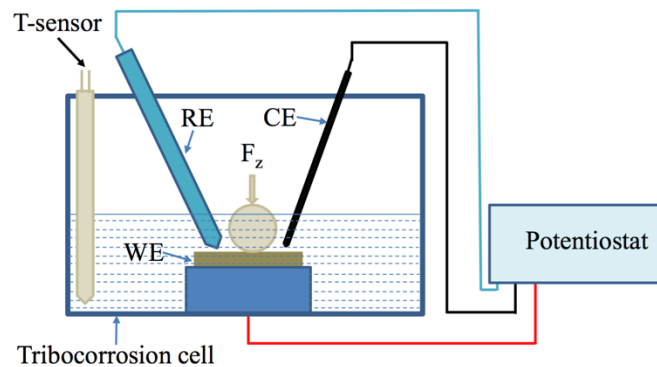


Figure 3-1 corrosion and tribocorrosion used in this work.

Potentiodynamic curve were carried out from ± 0.25 V vs OCP at 0.16 mV/s scan rate. Corrosion parameter like corrosion current density i_{corr} , corrosion potential V_{corr} and anodic and cathodic slopes (β_a , β_c respectively) were calculated by using CView software.

Polarization resistance R_p was calculated using Stern-Geary relation:

$$i_{corr} = \frac{B}{R_p}$$

B is Stern-Geary constant in (V) calculated from polarization curve as following [98]:

$$B = \frac{\beta_a \beta_c}{2.3(\beta_a + \beta_c)}$$

Penetration corrosion rate in mm/y was calculated as [98]:

$$CR = K \frac{i_{corr}}{\rho} M$$

i_{corr} is in $\mu\text{A}/\text{cm}^2$, K is a constant (3.27×10^{-3}) given in $\text{mm.g}/\mu\text{A.cm.year}$. M is the equivalent weight (24.17 g/mol).

EIS was employed to investigate the status of the oxide layer and the polarization resistance R_p of the starting surface and surfaces at different cathodic and anodic potentials namely (-0.9V cathodic, -0.7V cathodic, OCP, and 0 anodic). The frequency range was 100 kHz to 15 mHz in perturbation amplitude 10 mV at 10 points per frequency decade. ZView software was used to model the data with appropriate equivalent circuit.

3.3.2 Electrochemical impedance spectroscopy EIS background

Electrochemical impedance spectroscopy is a powerful technique used in many applications. The use of the technique in corrosion studies is growing because it gives a detailed investigation of the corrosion behaviour and the nature of the oxide layer. The technique perturbs the surface by a very small potential (potentiostatic EIS) or current (galvanostatic EIS) AC amplitude. Although the amplitude must be small enough to keep the linearity between potential and current, it should be large enough to reduce the signal noise to a minimum.

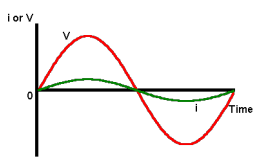
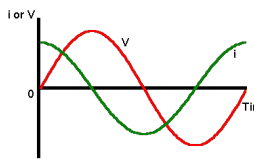
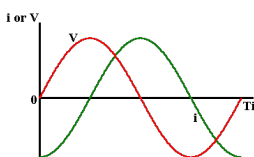
When the current flows in an electrical circuit, it is impeded by the impedance Z of the circuit. The relation between the current I and the potential V is:

$$E = IZ$$

When the frequency is zero the circuit is DC and Z is called resistor R (Ohm's law). Otherwise, it is an AC circuit and Z is the impedance.

Depending on the circuit element, there are different real and imaginary components of the impedance. The impedance of the resistor has no imaginary component and the phase shift between the potential and current is zero degree. In other words, the current and potential are in-phase and there is no frequency dependence. In a capacitor, there is no real component of the impedance, the phase shift is 90 degrees with the current leads the potential. At high frequencies, the capacitor behaves as short circuit with zero impedance, while, at low frequencies it acts as an open circuit with infinity impedance. The third passable element is an inductor. Like a capacitor, the inductor has only an imaginary component, but in the opposite direction. The current lags the potential by 90-degree phase shift. The inductor is open circuit at high frequencies and short circuit at low frequencies. Table 3-2 shows the impedance for each circuit element.

Table 3-2 equivalent circuit elements

The element	Mathematical expression	Waveform
Resistor	$Z = R$	
Capacitor	$Z = \frac{-j}{\omega C}$, $\omega = 2\pi f$	
Inductor	$Z = j\omega L$	

In many cases in corrosion studies, the capacitor is replaced by another element called the constant phase element CPE. This is because the capacitance of the surface layer is not perfect. It is affected by the solid surface roughness and inhomogeneity of the surface layer. The mathematical expression of this element is:

$$Z = \frac{-j}{\omega C^n}$$

Where the power n is 1 for a perfect capacitor and 0.5 for a diffusion element. The capacitance can be calculated from CPE in some cases as follows [99]:

$$C = \frac{(CPE \times R)^{1/n}}{R}$$

EIS data can be plotted in different format each one of them has some advantages. A Nyquist plot (Figure 3-2) plots the imaginary component Z_i against the real component Z_r . The simplest corrosion system is modelled by Randles cell (Figure 3-3) where the solution resistance R_s is in series with a parallel combination of charge transfer resistance R_{ct} and the capacitance of the double layer C_{dl} . At high frequencies, the capacitor acts as a short circuit that effectively cancels R_{ct} . Therefore, the semi-circle intersects the real axis at value equal to R_s . At low frequencies, on the other hand, the capacitor acts as an open circuit blocking the current flow through it. Thus, the semi-circle intersects the real axis again at value (R_s+R_{ct}) . Between these two extremes, there are different contributions of the resistor and the capacitor form the shape of the semi-circle.

The other format to represent EIS data is the Bode plot (Figure 3-4) where the magnitude of impedance $|Z|$, which is the length of the vector, is plotted against the frequency in a log scale to allow wide range of data. The plot is used to diagnose the system as it shows the frequency dependence. Figure 3-4 shows a schematic diagram for the Bode plot for Randles cell. At high and low frequencies, the horizontal line represents R_s and $R_s+ R_{ct}$ respectively. At intermediate frequencies, the curve is also a straight line with -1 slope. Extrapolating this line to intersect $|Z|$ axis can yield the value of the C_{dl} as shown in the figure.

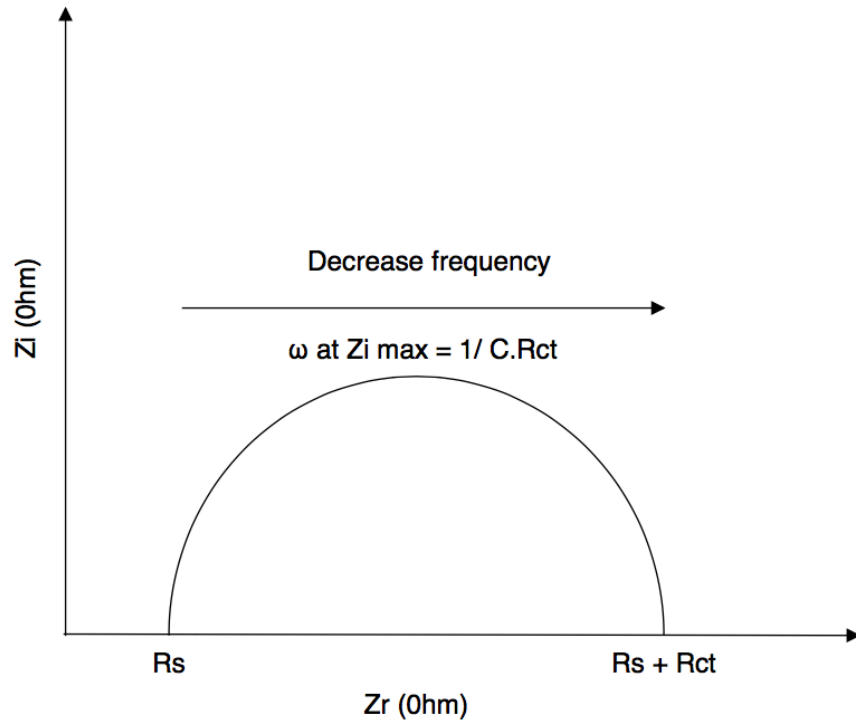


Figure 3-2 Nyquist plot

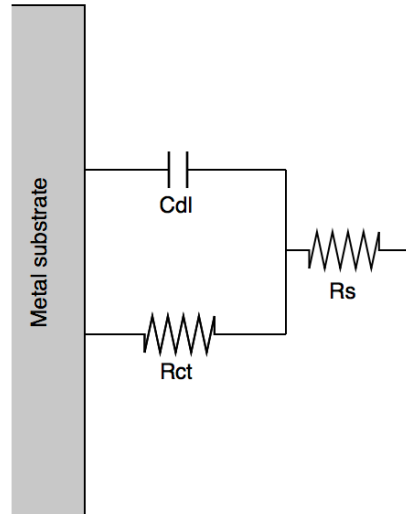


Figure 3-3 Randles cell

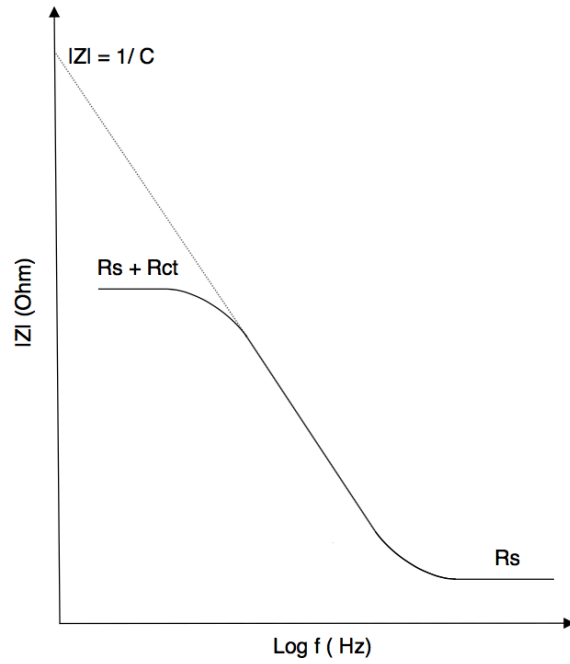


Figure 3-4 Bode plot

The Bode plot phase shift format (Figure 3-5) shows the phase angle in degrees. At high and low frequencies, the phase angle is zero showing the resistance behaviour of the Randles cell. At intermediate frequencies, the curve beaks as the imaginary component of the impedance increases [99].

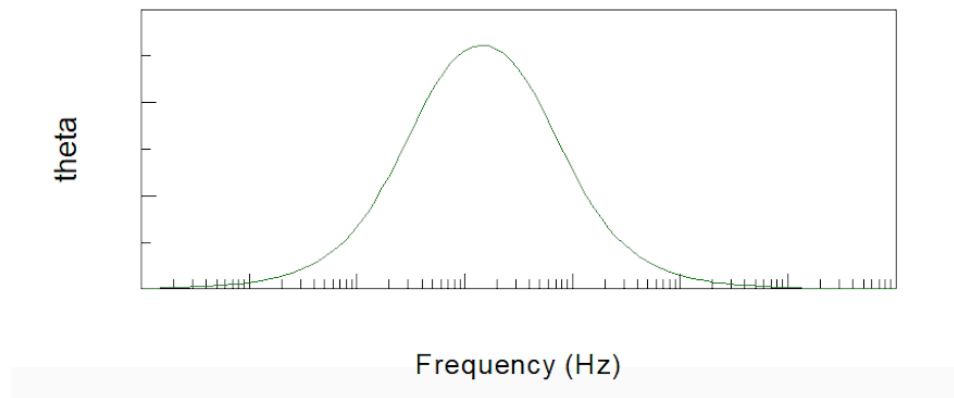


Figure 3-5 Bode plot phase shift

Figure 3-6 shows bode plot and 3D Nyquist plot and bode plots for a typical Randle cell consist of $20 \Omega R_s$, $10 \mu\text{F } C_{dl}$, and $10 \text{K}\Omega R_{dl}$.

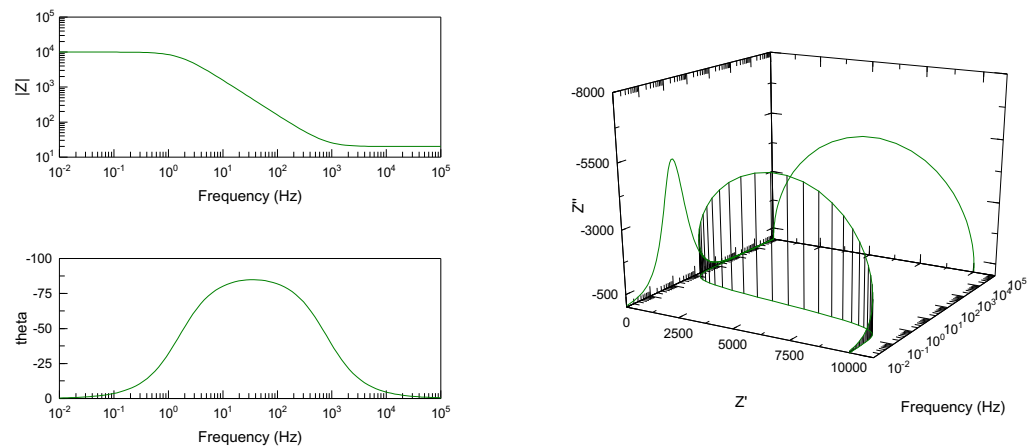


Figure 3-6 Bode plot (on the left) and 3D plot for Nyquist plot and bode lot (on the right)

3.4 Tribocorrosion study

3.4.1 Load and load-potential duel effect

The effect of load on the mechanical properties, microstructure, and consequently the wear behaviour of the material was studied using the synergistic approach conformed to ASTM standard G119.09. Thus, a range of loads namely (1, 2, 4, 8, and 16N) were covered. The wear test duration was 3 h at 37°C in 25 vol.% BS in PBS gives 15.8 g/L total protein content. The sliding speed was fixed to 5 Hz for this work. For this sliding speed and 2 mm stroke length, the linear sliding velocity is 20 mm/s. The wear tests were done at open circuit potential OCP and at -0.9 V cathodic potential.

In tribocorrosion experimentation, the material loss rate in mm/year is described depending on the way how it is generated as follows:

- The material loss rate due to pure corrosion C_0 . This has been calculated from Tafel extrapolation. C_0 is quite small for CoCrMo alloys in the testing solution. Thus, it can be neglected.
- Material loss rate due to pure mechanical wear without corrosion W_0 . The material loss volume is directly measured by using 3D optical microscope for the wear test at -0.9V cathodic potential.
- Material loss rate due to wear accelerated corrosion C_w . The driving force for this material loss is the galvanic couple that forms between the depassivated surface

(wear track) and the still passivate one (the rest of the surface). Espallargas et al. [100] suggested a new experimental set to calculate this effect using zero-resistance ammeter (ZRA). Because of the current lack of this configuration in our laboratory, the galvanic coupling model suggested by Vieira et al. [81], and applied for different material by Papageorgiou and Mischler [101], was employed to calculate the current flows from wear track (i_{wt}) as the following:

$$\log i_{wt} = \frac{\left(E_{corr} - E_{wt} + a_c - b_c \log \left(\frac{A_{wt}}{A_p} \right) \right)}{b_c}$$

where: E_{wt} is sliding potential, a_c, b_c are Tafel constants measured from the cathodic branch of the potentiodynamic curve (-1.26, 0.46 respectively) [76].

- The total material loss rate due for both corrosion and wear T. The material loss volume is directly measured by using 3D optical microscopy for the wear test at OCP.

Wear rate in mm/y was calculated by using the following formula [102]:

$$WR = \frac{8760V}{SA \cdot t}$$

V and SA are the volume and the surface area of the wear scare, t is the time in h.

Thus, total material loss T in mm/year is:

$$T = W_0 + C_0 + S$$

where S is the synergistic effect which is:

$$S = \Delta W_c + \Delta C_w$$

ΔW_c and ΔC_w are the enhancement of wear due to corrosion (synergistic effect) and the enhancement of corrosion due to wear (additive effect) respectively. Furthermore, the total contribution of wear in the process is:

$$W_c = W_0 + \Delta W_c$$

and the total contribution of corrosion is:

$$C_w = C_0 + \Delta C_w$$

To study the dual effect of potential and load on mechanical properties, microstructure and wear behaviour of the worn surfaces, three different loads were used (4, 8, and 16 N) at a wide range of cathodic and anodic potentials namely (-0.9, -0.7, -0.5, OCP, -0.1, 0, and 0.1V vs. RE). Both COF and current (or potential in case of OCP test) were recorded along the tests. The potential had been applied before rubbing started for 10 min. Figure 3-7 shows the work procedure for load-potential dual effect.

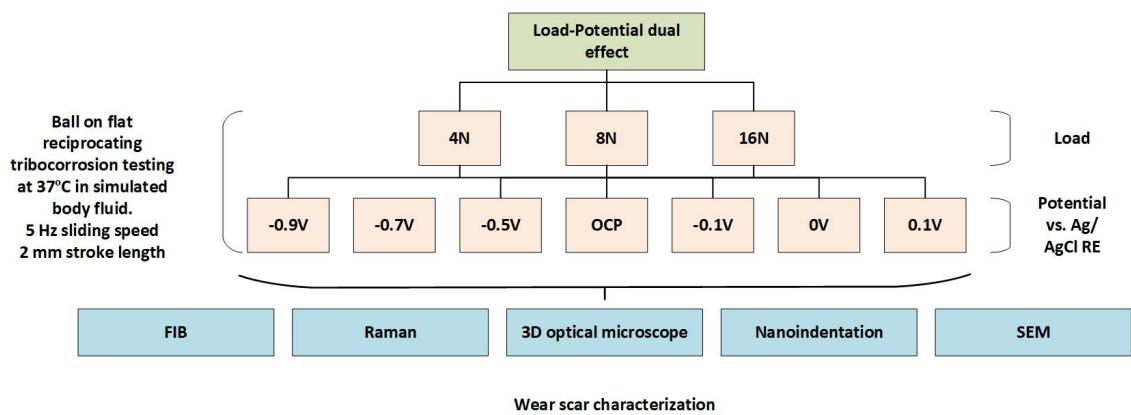


Figure 3-7 work procedure for load-potential dual effect

The wear volume was determined by using a 3D optical microscope in the same manner described in section 3.2.2. The total volume of material loss V_{total} at anodic potentials is the summation of the volume of the material loss due to corrosion V_{chem} and due to mechanical wear V_{mech} (mechanistic approach) [103]:

$$V_{total} = V_{chem} + V_{mech}$$

V_{chem} at anodic potential is calculated using Faraday's law:

$$V_{chem} = \frac{MQ}{nF\rho}$$

F is Faraday's constant, and ρ is the material density (8.3 g/cm³); Q the charge released (C) due to rubbing. For anodic tests, Q is the area under the current curve after subtracting the background current [104].

3.4.2 Sliding speed effect

The effect of sliding speed on the mechanical properties, microstructure, and consequently the wear behaviour of the material was studied using a ball on plate configuration, which conformed to ASTM G133 and tribocorrosion synergistic approach conformed to ASTM G119.09 standard. The same corrosion and tribocorrosion cell, wear rig, and potentiostat explained previously in section 3.2 were used in this work. The counterface, testing electrolyte, and testing temperature were kept the same as in section 3.4.1. Four reciprocating sliding speeds were chosen at 2 mm stroke length namely 1, 2.5, 5, 10 Hz which give 4, 10, 20, and 40 mm/s linear sliding speed respectively and 0.5, 0.2, 0.1, and 0.05 s latent time (the time between two successive contact events). The work was done at -0.7 V cathodic potential, and OCP. -0.7 V cathodic potential was chosen depending on the results of the work in section 3.4.1 to avoid the interruption that might occur due to the formation of carbonaceous layer at -0.9 V cathodic potential. The sliding distance was fixed to 72 m to make the results comparable. Thus, the test times were 5, 2, 1, 0.5 h for 1, 2.5, 5, and 10 Hz reciprocating sliding speed respectively. Figure 3-8 shows the work procedure. Anodic potential at 0 V with the same sliding conditions was added to get a better understanding for sliding speed effect.

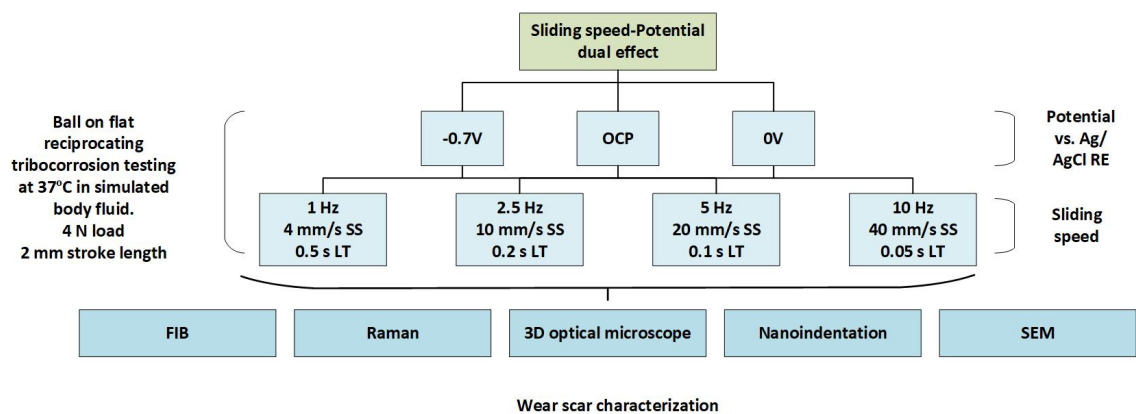


Figure 3-8 work procedure for sliding speed effect

The samples were placed in the electrolyte at the testing temperature and left for some time waiting for OCP to be stabilised. The test potential was applied for 10 minutes followed by applying load and rubbing. F_x , F_z , and the current (or sliding potential) were continuously recorded throughout the tests.

3.5 Mechanical properties characterization by using nanoindentation

3.5.1 Background

Instrumented indentation testing or nanoindentation test, is a continuous recording of the applied load and resulting penetration depth throughout the entire loading and unloading cycle. The technique can be done with full control of force or displacement. It allows determination of hardness, elastic modulus, and many other mechanical properties without the need of any further imaging.

Figure 3-9 shows the typical curve for controlled loading-unloading cycle. For the loading part of the curve, the relation between P and h is described by Kick's law [105]:

$$P = Ch^2$$

C is material constant that is independent on the indentation depth.

The contact depth as proposed by Oliver and Pharr [106] is:

$$h_c = h_{max} - \omega \left(\frac{P_{max}}{S} \right)$$

Where ω is geometrical parameter, it is 1 for flat punch, 0.75 for cone and Berkovich tip.

The hardness of the material can be found as [107]:

$$H = \frac{P_{max}}{A}$$

A is the projected area which is function of contact depth. For a Berkovich tip it is:

$$A = 24.5h_c^2$$

The stiffness of the material S is extracted from loading-unloading curve as the initial slop of the unloading curve. Having both A and S one can determine the reduced modulus E_r depending on the elastic part of deformation as following [107]:

$$E_r = \frac{\sqrt{\pi} \cdot S}{2\beta\sqrt{A}}$$

Where β is constant depends on the indenter geometry, it is 1.034 for a Berkovich tip.

Detailed calculations for elasto-plastic properties of the material by using nanoindentation can be found elsewhere [108][109][110].

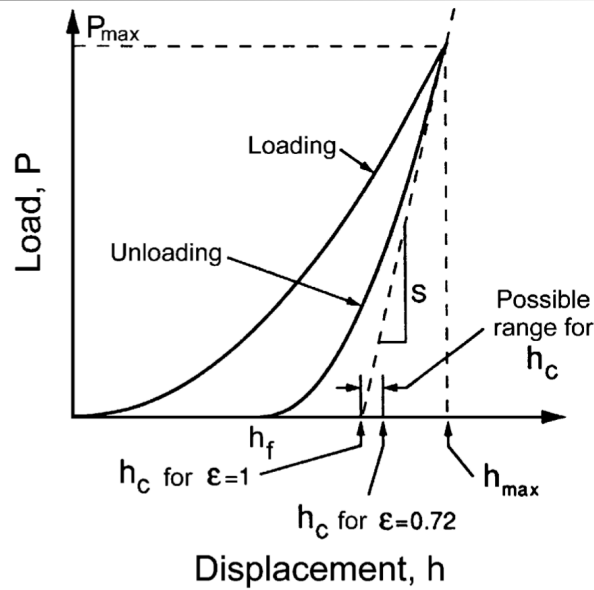


Figure 3-9 nanoindentation curve [111]

3.5.2 Tests procedure

Nanoindentation (Hysitron, TI Premier, USA) was employed to study the local mechanical properties of the starting and worn surfaces. A Berkovich three-sided pyramidal indenter was used, with 65.3° face angle with different work procedure depending on the test as follows:

3.5.2.1 Tribology tests

The partial unload function was used to characterize the mechanical properties of the worn surface as a function of depth. This function consists of 15 successive cycles, each of which includes loading, holding, and partial unloading to the half of the load. At the end of each cycle, there was 2 s hold. The indent began with a $100 \mu\text{N}$ load, which was incrementally increased up to a maximum load of $10000 \mu\text{N}$. 20 points were chosen on the central line of each wear track. Individual indent results were analysed, but also the average of all 20 indents was used to present the mechanical properties of the worn surface. The distance between each two indents was $5 \mu\text{m}$ to cover $95 \mu\text{m}$ distance in total for each wear track. The instrument allows calculation of the hardness (H), the reduced modulus (E_r), the contact stiffness (S), the surface area of the contact (A) and the yield strength (σ_y). Details of how these are calculated are given elsewhere [108] [112].

3.5.2.2 Tribocorrosion tests

The trapezoid load function was used to characterize the mechanical properties of the worn surfaces of all tribocorrosion tests. The function is loading to 10000 μN in 5 s, holding for 2 s, and unloading in 5 s. 30 points were chosen on the central line of each wear track. Individual indent results were analyzed, but also the average of all 30 indents was used to determine the mechanical properties of the worn surface. The distance between each two indents was 5 μm to cover 145 μm distance in total for each wear track. The instrument allows calculation of the hardness (H), the reduced modulus (E_r), contact stiffness (S), and the surface area of the contact (A).

Further mechanical investigation was conducted for -0.9 V potential and 4 N load sample in section 3.4.1. The partial unload function was used to characterize the mechanical properties of the worn surface as a function of depth because the worn surface was covered by a relatively thick tribolayer. The function consists of 15 successive cycles, each of which includes loading, holding, and partial unloading to the half of the load. At the end of each cycle, there was 2 s hold. The indent began with a 200 μN load, which was incrementally increased up to the maximum load of 13000 μN . 20 points were chosen on the central line of each wear track. The distance between each two indents was 5 μm to cover 95 μm distance in total.

Modulus mapping technique was also used to show the difference in modulus on the edge of the wear track of -0.9 V and 4 N tribocorrosion test. 15 μm^2 area was chosen in the very edge of wear track. The area was carefully chosen in such a way that the height difference is minimum (200 nm). The frequency was 300 Hz and the setpoint was 6 μN with load amplitude 5 μN .

3.6 Microscopic and Raman characterization of the worn surfaces

The general morphology of the wear track was characterised by SEM (FEI, Inspect F50, the Netherlands). The presence of a proteinaceous layer on the wear track was investigated using Raman spectroscopy (inVia Renishaw, UK) in spectrum range 1000-2000.

Focused ion beam milling (FIB) was undertaken to investigate the damage accumulation mechanisms below the worn surface. FIB milling was undertaken using a FEI Helios G4

Nanolab (FEI, the Netherlands). Platinum deposition was applied on the region of interest to prevent Ga⁺ implantation and sputter erosion of the top portion of the surface. Various Ga⁺ ion beams (65 nA – 2.5 nA) were used for rough milling with a 790 pA Ga⁺ ion beam finishing. SEM images of the subsurface microstructures were recorded using mirror (in lens) high energy electron detector, with a 52° angle between the electron beam and the subsurface cross-sectional planes. The FIB work was done by Dr Peng Zeng in Sorby centre, The University of Sheffield.

4 Results

4.1 Tribology properties

4.1.1 Starting surface, friction and wear rate

Figure 4-1 shows an ion channelling contrast image for the starting surface. The linear intercept method was used to measure the average grain size, measured at a diameter D of $7.4 \mu\text{m}$.

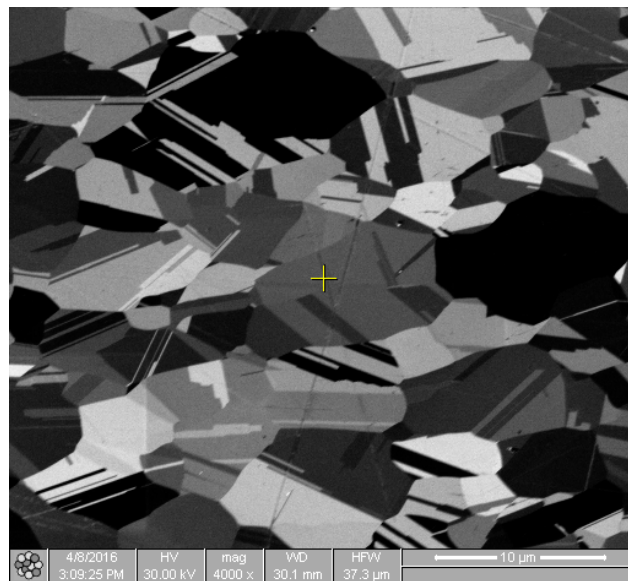


Figure 4-1 Ion channelling contrast image for starting surface.

The volume of the material loss, specific wear rate K , and wear rate Q are tabulated in table Table 4-1.

Table 4-1 volume of material loss, and wear rate

Load (N)	Wear Volume (mm^3)	K ($\text{mm}^3/\text{N.m}$)
5	0.046	4.26E-06
10	0.05	2.31E-06
20	0.059	1.37E-06
40	0.08	9.26E-07
60	0.103	7.95E-07
80	2.0	1.16E-05

The specific wear rate is plotted against load in Figure 4-2. Interestingly, the specific wear rate exhibited a decrease with load up to around 40 N, and was then constant at 60 N, but showed a wear transition at 80 N with an increase in the specific wear rate in excess of an order of magnitude.

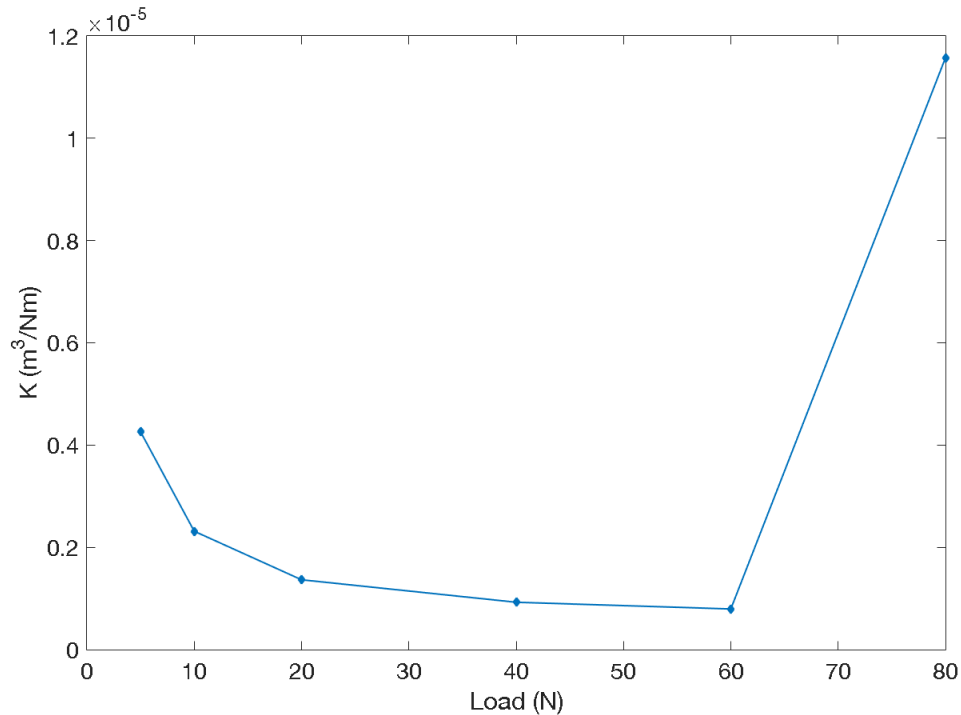


Figure 4-2 specific wear rate, K , as a function of load.

4.1.2 Characterisation of the worn surfaces

SEM images of the worn surface, Figure 4-3, show that the surface was relatively smooth after testing at loads for 5, 10 and 20 N, but with occasional grooves also present (e.g. see Figure 4-3 4c for the 20 N test). Interestingly, the surface became smoother at 40 N (Figure 4-3 d). As detailed later, this coincided with the formation of a carbonaceous layer on the worn surface. The worn surface was rougher at 60 N test load compared to 40 N with evidence of microscale gouging of the surface (Figure 4-3 e). Moreover, there was evidence of wear debris agglomerated on the surface as shown in Figure 4-3 g. The wear track also exhibited sharp edges resulting from microcutting in the area close to the agglomerated wear debris. The wear track at 80 N was quite different compared to that at lower loads, exhibiting severe ploughing, again with agglomerated wear debris on the surface (Figure 4-3 f and h).

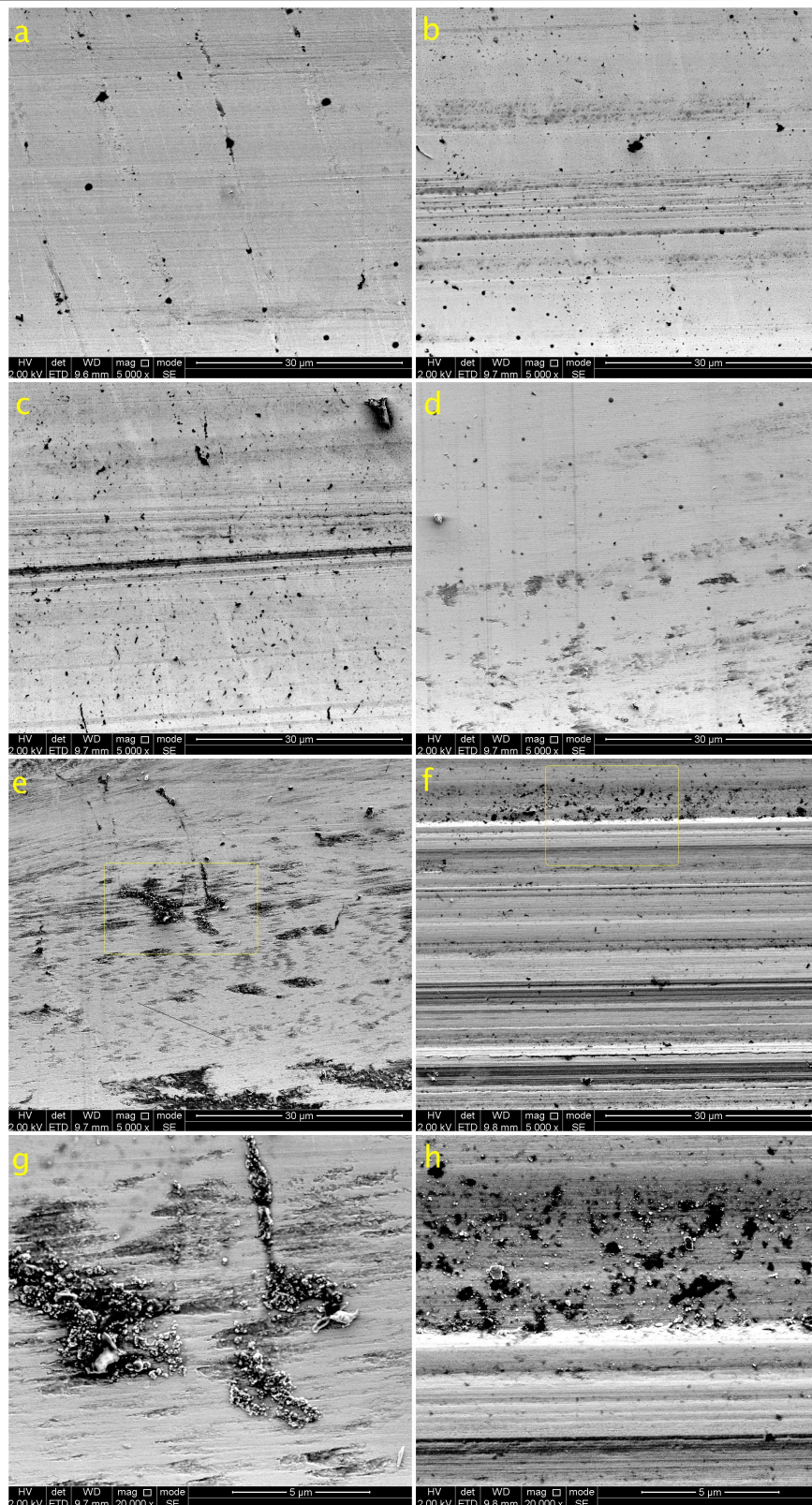


Figure 4-3 secondary electron SEM images for (a) 5N, (b) 10N, (c) 20N, (d) 40N, (e) 60N, and (f) 80N wear test load. (g) and (h) are higher magnification images for pointed areas in 60N and 80N wear test load respectively.

All wear tracks were examined by Raman spectroscopy to determine the presence of a carbonaceous layer. No signal was observed at 5, 10, 20 and 80 N, indicating that the surface was free from any carbonaceous layer. However, at 40 and 60 N, D and G Raman bands at 1383 and 1567 cm^{-1} were observed from spectra taken inside the wear track, Figure 4-4 indicating the presence of a carbonaceous layer on the surface of the wear track. Optical microscopy of the wear tracks from the 40 and 60 N wear tests (Figure 4-5) showed the location of this carbonaceous layer, which was constrained to inside the wear track. The carbonaceous layer appeared to cover a wider area at 60 N load than at 40 N.

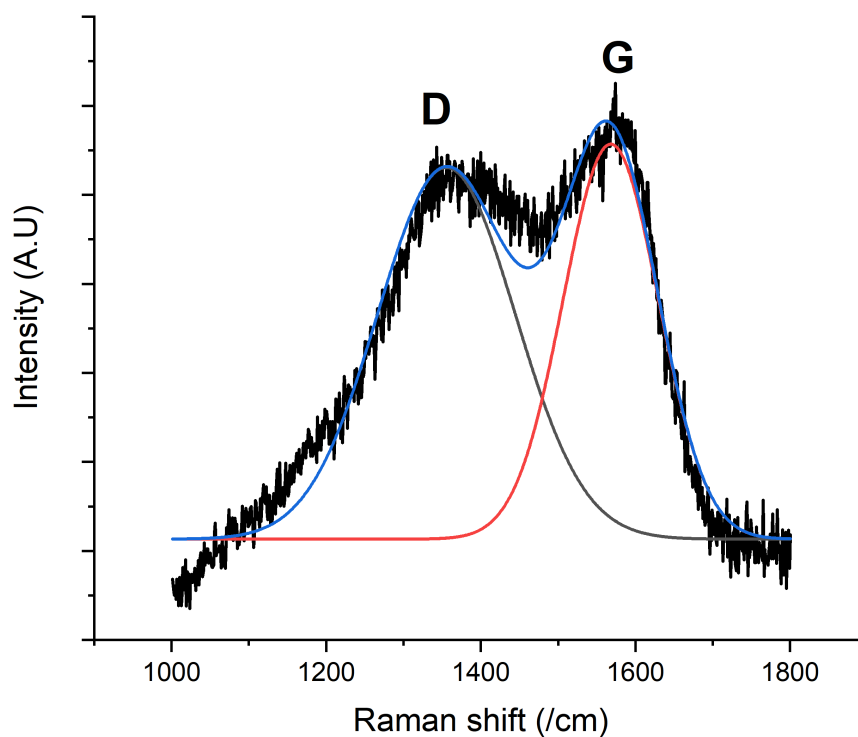


Figure 4-4 Raman spectra shows two peak D at 1383 cm^{-1} and peak G at 1567 cm^{-1} for 40N and 60N test load.

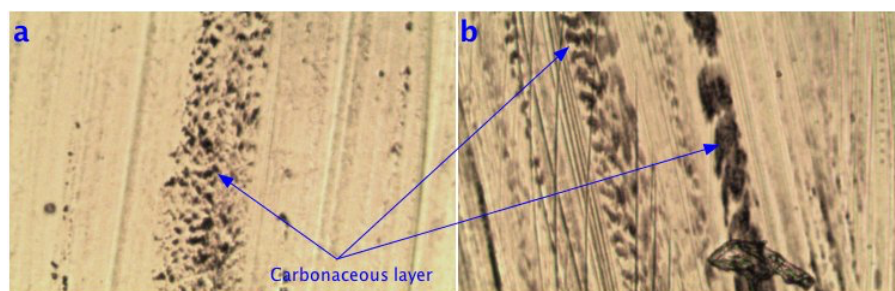


Figure 4-5 Optical images for (a) 40N, and (b) 60N load.

4.1.3 Mechanical properties of the surface

The mechanical properties of the worn surface of all wear tracks as well as the starting surface were measured using nanoindentation. Figure 4-6 shows typical loading-partial unloading curves for all tested surfaces (these are selected curves from the 20 recorded for each wear scar). The curves show clear differences in h_r and h_{max} . The ratio of h_r/h_{max} was less than 0.875 in all cases, indicating that sink-in events occurred around the indenter, as shown in Figure 4-7. Such sink-in events are typical of metals with low stacking fault energy and high strain hardening.

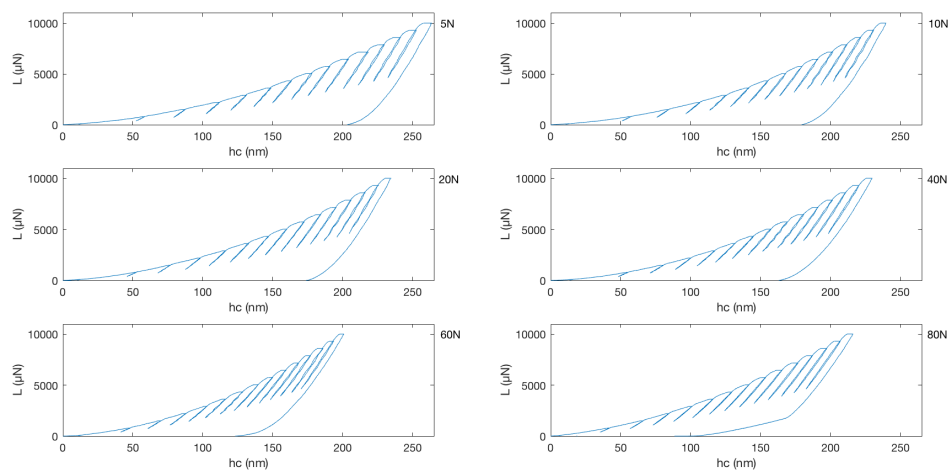


Figure 4-6 typical nanoindentation loading-unloading curves for all tested loads. The partial unload function has been used to characterize the mechanical properties for the successive layers of the surface.

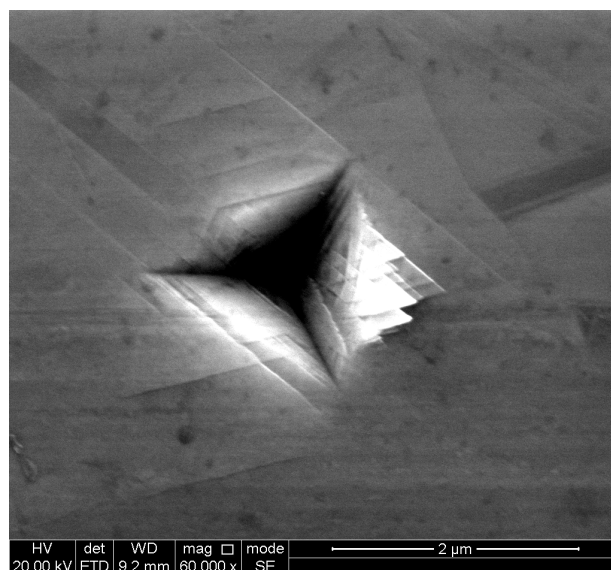


Figure 4-7 Secondary electron SEM image for one of the indents shows sink-in events and extrusion on one side of the indent.

Figure 4-8 and Table 4-2 show the values of H , A , E_r , S , A and σ_y that were calculated from the final loading-unloading cycle of the curves shown in Figure 4-6. The hardness of the wear track was greater than the starting surface by a significant amount for all loads. The hardness of the starting surface was 6.53 GPa, which increased approximately linearly to 8.4 GPa for the 10 N test, with a slower increase in hardness up to 11.2 GPa for the 60 N test. Interestingly, the average hardness of the surface of the 80 N test, 11.5 GPa, was about the same as the 60 N test.

Table 4-2 Mechanical properties of all tested samples from the nanoindentation examination.

Load	h_r/h_{max}	A (nm ²)	S (μ N/nm)	E_r (GPa)	H (GPa)	σ_y
0	0.76	1531752	260.0	186.1	6.53	550
5	0.78	1415673	273.3	203.6	7.08	683
10	0.76	1196707	273.7	221.7	8.38	787
20	0.75	1150627	264.4	218.5	8.72	820
40	0.71	1023747	252.9	221.6	9.79	921
60	0.68	899084	231.0	216.3	11.20	1058
80	0.68	909301	222.7	210.2	11.48	1087

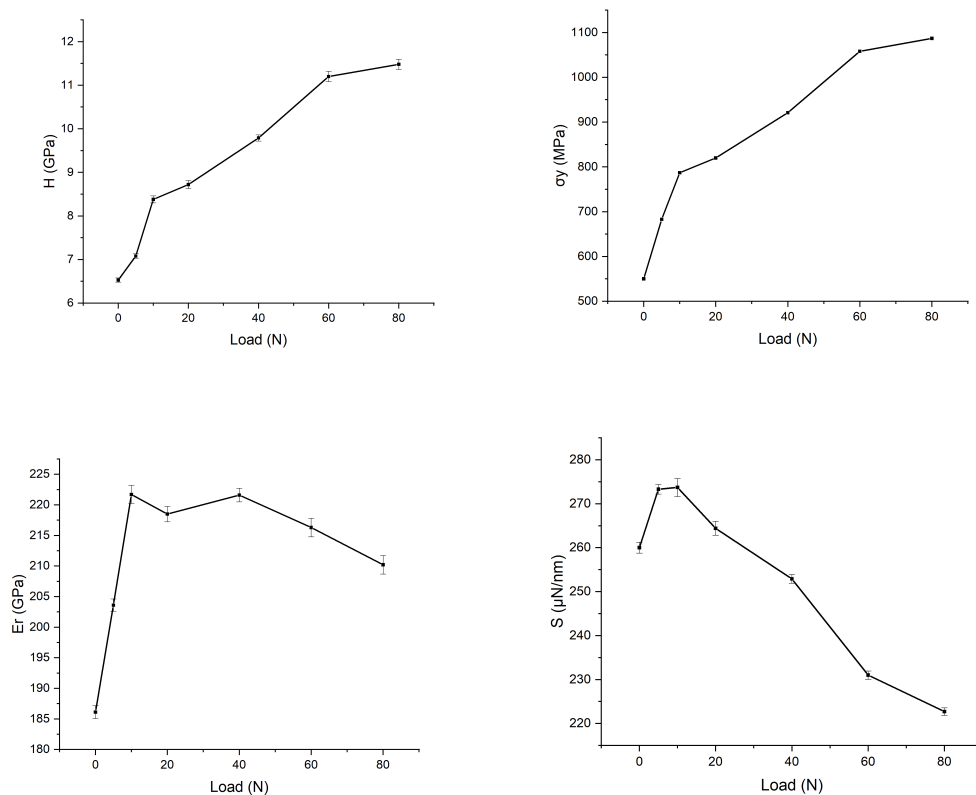


Figure 4-8 Nanoindentation results show the alteration in mechanical properties of the surface with testing load. The last segment of the partial unload function has been used to extract these values.

The reduced modulus of elasticity, E_r , increased linearly from the starting surface up to 10 N. For higher loads the values of E_r was approximately constant. The contact stiffness, S , broadly followed a similar trend to the reduced modulus of elasticity, but with some significant differences. For the low load test, the stiffness increased from 260 $\mu\text{N}/\text{nm}$ for the starting surface to 273 $\mu\text{N}/\text{nm}$ at 5 N wear test load. The value was similar for the 10 N wear test load, but then showed a reduction at higher loads, reducing to the lowest value (223 $\mu\text{N}/\text{nm}$) at 80 N. The difference between the trend in E and S can be explained by the trend in the surface area of the indent, A .

The yield stress of the starting surface was 550 MPa. The yield stress of the worn surface increased with load up to 60 N, reaching a value of 1058 MPa, and then showed a small increase to 1087 MPa at 80 N. Thus, as expected, the yield stress follows a similar trend to the hardness of the surface.

The nanoindentation curves shown in Figure 4-6 can be used to look at the mechanical properties of the surface as a function of depth. Figure 4-9 shows the hardness of the worn surface for all wear tracks as a function of the indentation depth. The data presented are an average of 20 indents. At the lowest load the displacement was around 50 nm for all indents. Thus, all of them were considered as they are greater than one third of the indenter radius. Generally, the hardness of the surface increased with the load for all sampled depths. The hardness of the worn surface decreased with depth below the surface in all cases except for the 60 N test, which appeared to increase with depth. The hardness of starting surface was close to that at 5N test worn surface. The 80N surface showed the maximum hardness at all depths.

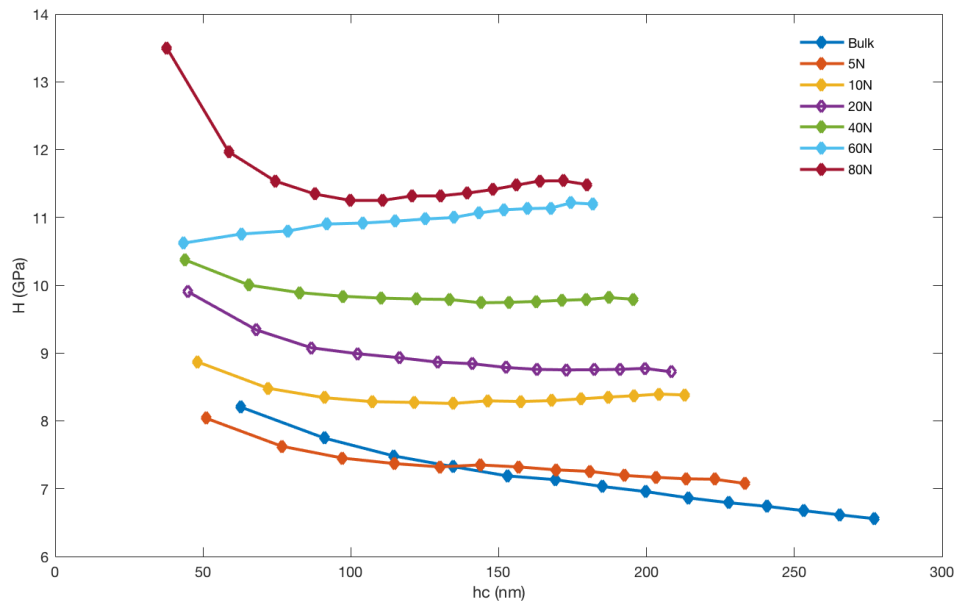


Figure 4-9 The hardness for the successive layer of the surface for all tested load. 0N refers to starting surface.

4.1.4 Microstructure as a function of depth below the worn surface

Figure 4-10 a, b, c and d show back scattered electron images from FIB cross-sections of the surface for 20, 40, 60, and 80 N tests. Each section was taken longitudinally at the base of the wear scar. For the 20 N test, martensite laths can clearly be seen. The laths extended to random depths, typically 1-3 grain depths (note that care must be taken in differentiating the martensite laths from the recrystallisation twins). In addition, a very thin layer of nanocrystals could just be detected at 20 N. At 40 N, the nanocrystalline layer was clearly visible, which extended 60-130 nm below the worn surface. The martensite laths do not appear particularly different to those observed at 20 N, although the density was probably higher. At 60 N, a thicker nanocrystalline layer can clearly be seen, with a thickness in the range ~ 3 to 5 μm . Note that nanocrystalline layer has a rather abrupt interface with the substrate and is of variable thickness. In addition, at 60 N many more martensite laths can be seen. At 80 N, a very substantial nanocrystalline layer was observed, with average thickness of more than 10-16 μm . The size of the subgrains in the nanocrystalline layer was a function of depth below the surface, with the finest subgrains appearing at the surface itself. Locally, the nanocrystalline layer penetrated further into the substrate in narrow bands typically angled at 40-60° to the worn surface. The martensite laths dominate the microstructure below the nanocrystalline layer.

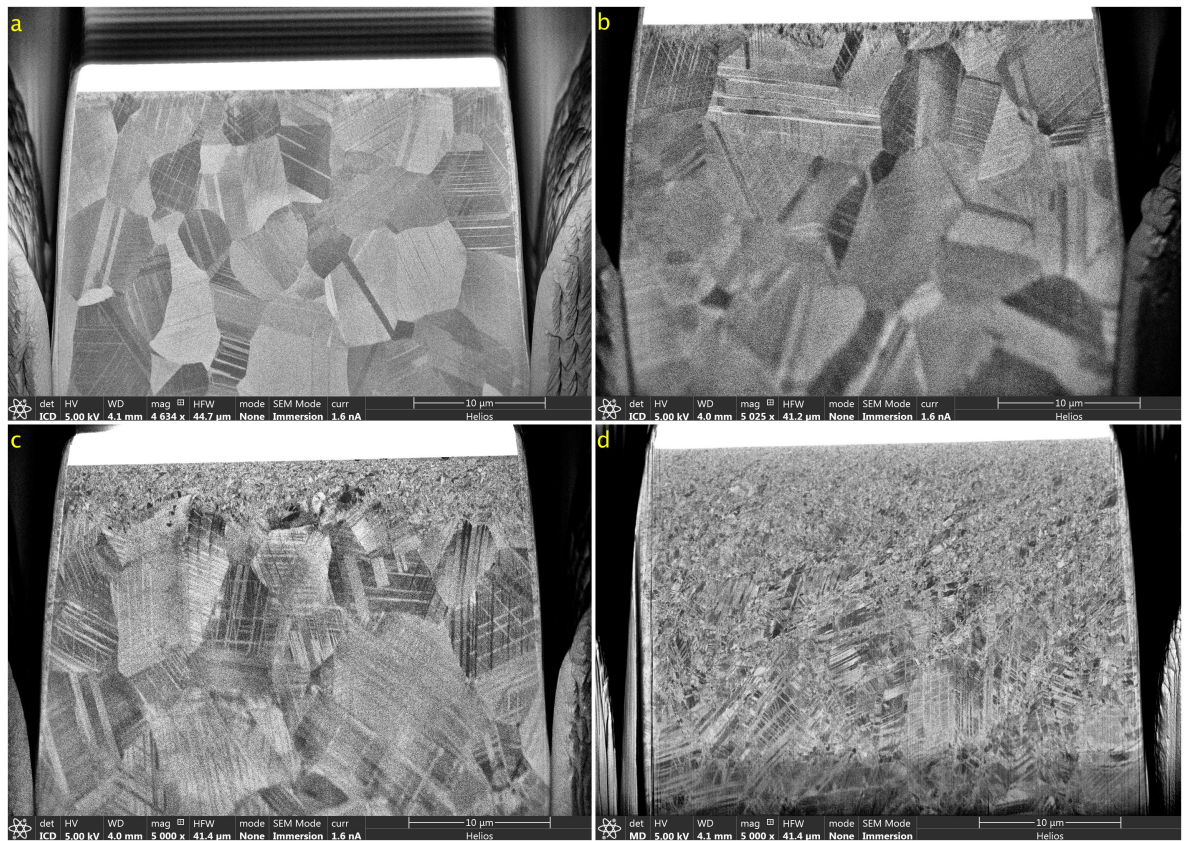


Figure 4-10 electron channelling contrast images for (a) 20 N, (b) 40 N, (c) 60 N, and (d) 80 N wear test load. Taken by Dr Peng Zeng (Sorby centre, The university of Sheffield) and published in [113]

4.2 Tribocorrosion properties

4.2.1 Load effect (synergistic approach)

Table 4-3 and Figure 4-11 show the coefficient of friction, COF, and the specific wear rate, K , at open circuit potential OCP and at -0.9 V cathodic potential for all loads. The test follows ASTM standard G119.09. COF for OCP tests peaks at 2 N load followed by a continuous decrease with further load. K shows the same value at 1 N, and 2 N. It increased with load to peak at 8 N load followed by reducing again at 16 N. This wear behavior can be attributed to the microstructural changes in the worn surfaces as will be explained later.

Table 4-3 COF and K for tribocorrosional tests at different loads.

L (N)	Potential	COF	V (mm ³)	K (mm ³ /N.m)
1	OCP	0.184	2.56E-04	1.41×10 ⁻⁶
	Cathodic	0.127	7.80E-05	1.8×10 ⁻⁷
2	OCP	0.28	5.36E-04	1.48×10 ⁻⁶
	Cathodic	0.131	1.79E-04	4.14×10 ⁻⁷
4	OCP	0.182	2.80E-03	3.77×10 ⁻⁶
	Cathodic	0.125	2.80E-04	3.86×10 ⁻⁷
8	OCP	0.148	9.98E-03	5.78×10 ⁻⁶
	Cathodic	0.134	8.33E-04	5.07×10 ⁻⁷
16	OCP	0.128	9.70E-03	2.84×10 ⁻⁶
	Cathodic	0.124	3.39E-03	1×10 ⁻⁶

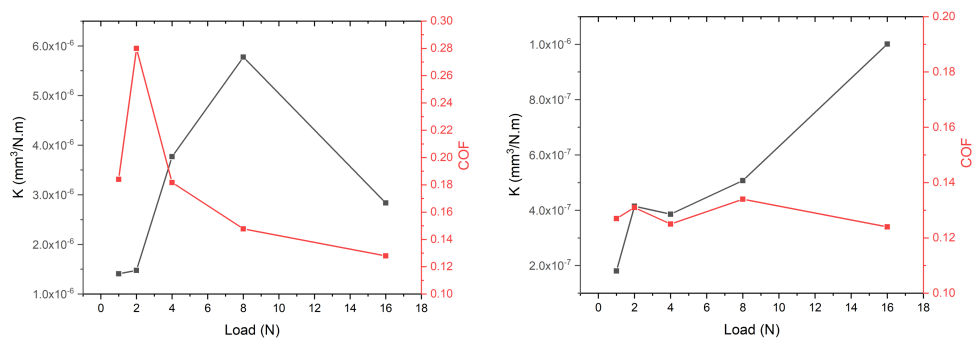


Figure 4-11 COF and K for tribocorrosion tests at OCP

At -0.9 V cathodic potential, COF showed no change with load, whereas K increases to more than double at 2 N compared to 1 N load. At 2, 4, and 8 N, K approximately plateaus.

However, the specific wear rate doubled again at 16 N load test. This is possibly because of the formation of a carbonaceous layer on the worn surface as will be explained later.

Table 4-4 and Figure 4-12 give the tribocorrosion tests results. The material loss due to pure mechanical effect, W_0 , almost linearly increased with load. The total material loss T exhibited a sharp increase with load to the maximum at 8 N load. In spite of doubling the load to 16 N, T did not increase, rather it slightly decreased. Interestingly, wear accelerated corrosion C_w shows a plateau at 4, 8, and 16 N. The plateau comes after a sudden jump at 2 N load. At lower test loads, C_w shows a slightly increase with load. Corrosion accelerated wear W_c , on the other hand, increased with load up to 8 N where it shows a plateau with further increased load. It is clear from these results that at up to 4 N load, corrosion and mechanical wear equally contributed in tribocorrosion process. Whereas, at higher load, the mechanical wear represented by W_c was the dominant tribocorrosion mechanism.

Table 4-4 rate of material loss of load effect tribocorrosion tests

L (N)	W₀ (mm/y)	C₀ (mm/y)	T (mm/y)	S (mm/y)	C_w (mm/y)	W_c (mm/y)	ΔW_c (mm/y)	ΔC_w (mm/y)	C_w/T
1	1.20	4×10 ⁻⁴	2.89	1.37	1.63	1.26	-0.24	1.61	0.56
2	2.26	4×10 ⁻⁴	4.72	2.45	1.92	2.81	0.54	1.90	0.41
4	3.00	4×10 ⁻⁴	17.53	14.51	9.43	8.10	5.10	9.41	0.54
8	5.45	4×10 ⁻⁴	33.28	27.81	9.13	24.14	18.69	9.12	0.27
16	16.00	4×10 ⁻⁴	30.65	14.64	8.15	22.50	6.50	8.13	0.27

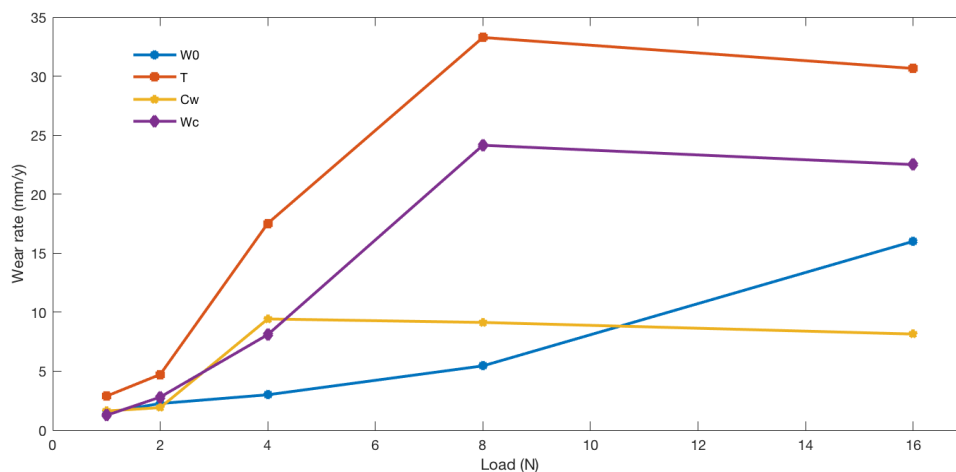


Figure 4-12 total and synergism material loss rate vs. load.

Figure 4-13 shows the sliding potential profile for a wide range of loads at OCP. The sliding potential shows a strong load dependence behaviour. At loads of 1 and 2N, rubbing resulted in a decrease in potential by about 50 and 110 mV loads, respectively. The sliding potential showed a significant recovery after about 1000 s. No change in potential was observed at 1N load when rubbing was stopped. However, there was a small recovery in the potential to a more noble value of about 10 mV when rubbing was stopped at 2 N. The application of higher loads resulted in a sharper reduction in sliding potential, compared to the OCP, to ~180 mV at 4 and 8N, and ~230 mV at 16N. Note that these measured potentials are the mixed potential, i.e. a combination of the potential of the active (scratched) surface and the rest of the surface which is cathodically polarized.

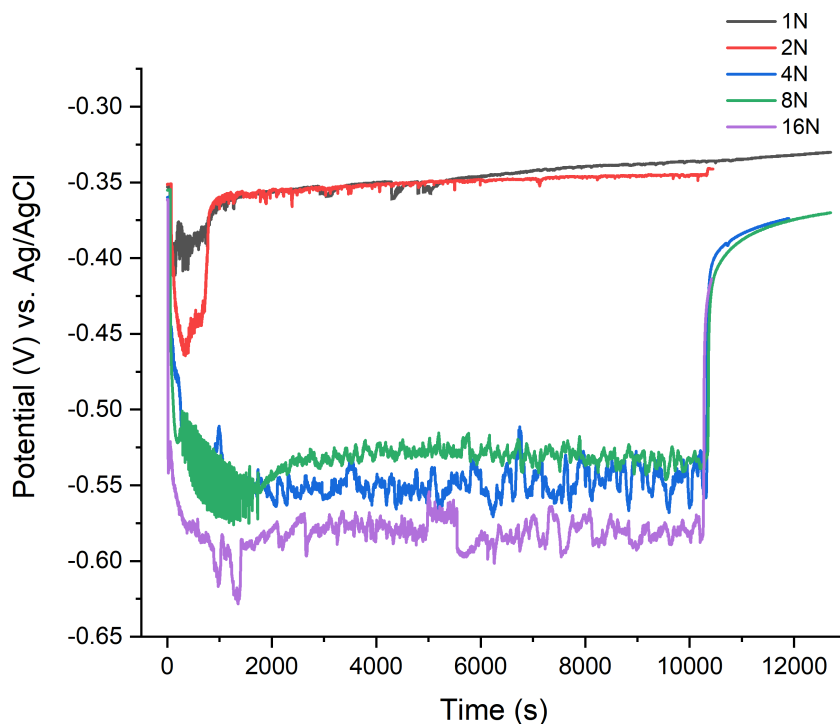


Figure 4-13 sliding potential for wide range of load at OCP

For further investigation of the dependence of sliding potential on load, two extra tests were conducted at 8 and 16 N load, shown in Figure 4-14. The potential pulse applied for 10 mins in the middle of the test was at the OCP. The 8 N test shows a change in sliding potential by +140 mV after applying this potential. In contrast, when sliding at 16 N load the potential returned to the value it had before after the application of this pulse.

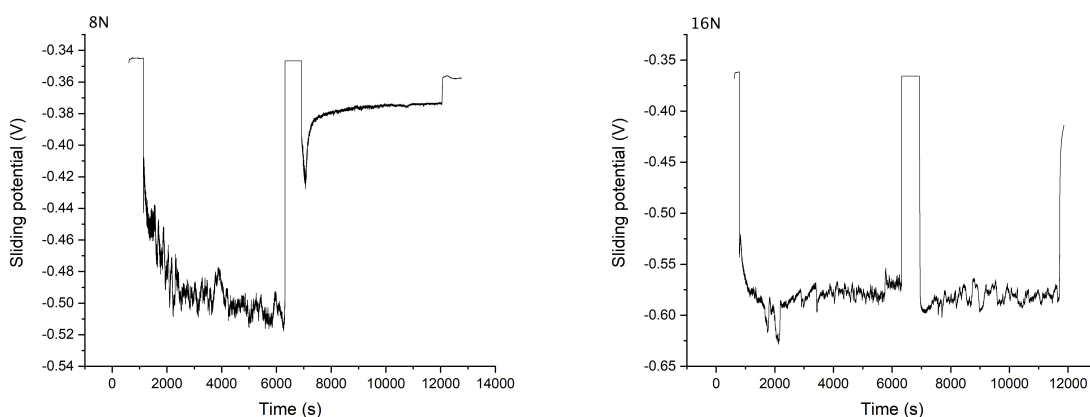


Figure 4-14 the effect of applying pulse potential in the middle of tribocorrosion test

4.2.2 Load-potential duel effect

4.2.2.1 Electrochemical investigation:

Figure 4-15 shows tafel curve of CoCrMo biomedical grade alloy in 25 vol.% BS in PBS at 37°C. All corrosion parameters extracted from Tafel curve for starting surface were tabulated in Table 4-5. The corrosion rate of the material is quite low in the testing solution and temperature. Thus, it is neglected in tribocorrosion calculations. Several potentials were chosen around OCP in cathodic and anodic domains for tribocorrosion testing.

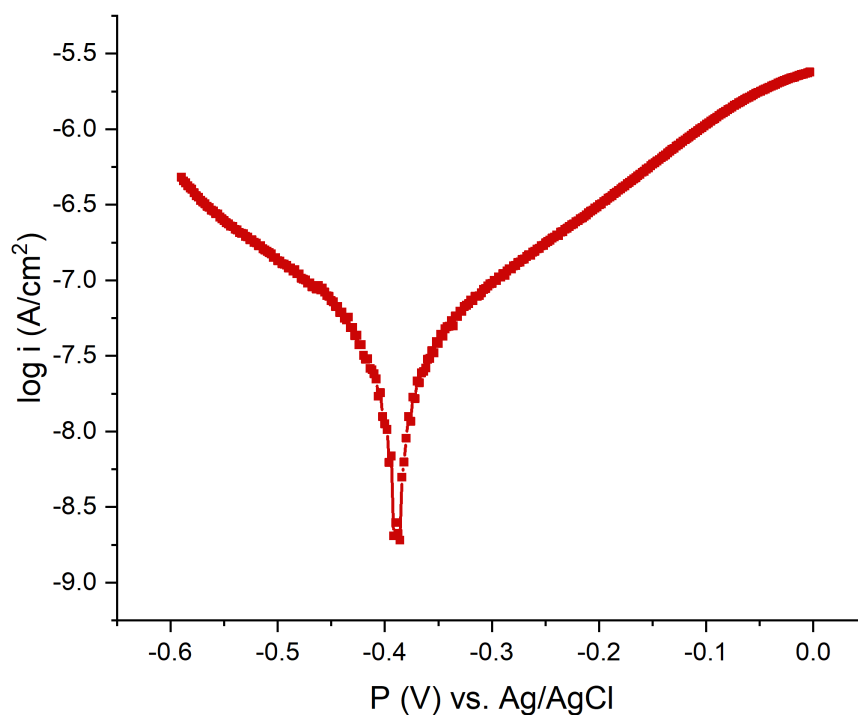


Figure 4-15 polarization curve for CoCrMo alloy in 25 vol.% BS in PBS at 37°C

Table 4-5 corrosion parameters extracted from Tafel curve

β_a (mV)	β_c (mV)	i_{corr} (A/cm ²)	E_{corr} (V)	B (mV)	CR (mm/y)	R_p (k Ω)
434	458	3.3×10^{-8}	-0.38	96	3.1×10^{-4}	290

The oxide film at the selected potentials was characterized by using the EIS technique. For all tests, the Nyquist plots shows a semicircle with centre depressed below the x-axis, clearly revealing the non-perfect capacitive behavior of the surface layer. The semicircles

intersect the x-axis at high frequencies giving the solution resistance R_s . At very low frequencies (which cannot be reached experimentally) the semicircle should intersect the x-axis again to give (R_s+R_{ct}) . At intermediate frequencies, the imaginary part starts to increase indicating the capacitive behavior of the surface. A Bode plot shows that material exhibits a plateau at high and low frequencies giving the solution resistance R_s and solution resistance plus total surface resistance (R_s+R_{ct}) respectively. At intermediate frequencies, the curve is a straight line with a slope close to -1 in all cases, indicating the capacitive behavior of the material. The phase shift gives the same indication as it is close to zero at both high and low frequencies, while it peaks at intermediate frequencies as the imaginary component of the impedance increases.

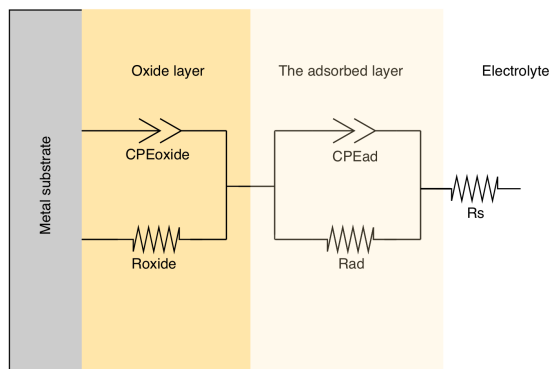
The equivalent electric circuits for modeling the EIS data is shown in Figure 4-16. At OCP and anodic potentials the circuit (Figure 4-16a) is solution resistance R_s in series with parallel combination of constant phase element CPE_{ad} and the resistance R_{ad} of the surface adsorbed layer which is in turn in series with another same combination for the oxide layer (R_{oxide} and CPE_{oxide}). For -0.7 V, and -0.5 V cathodic potentials, the equivalent circuit in Figure 4-16b was used. In the later circuit, the parallel combination of the resistance R_{bo} and CPE_{bo} of the barrier oxide is in series with another combination of the resistance of the pores R_{pl} of the porous oxide layer and the CPE_{pl} of this layer.

At -0.9V cathodic potential, the oxide layer lost its protection nature. Thus, the equivalent circuit shown in Figure 4-16c was used. The circuit is the combination of the resistance R_{ad} and CPE_{ad} of the adsorbed protein layer in parallel with short Warburg element W_s . The models were chosen to meet the following criteria:

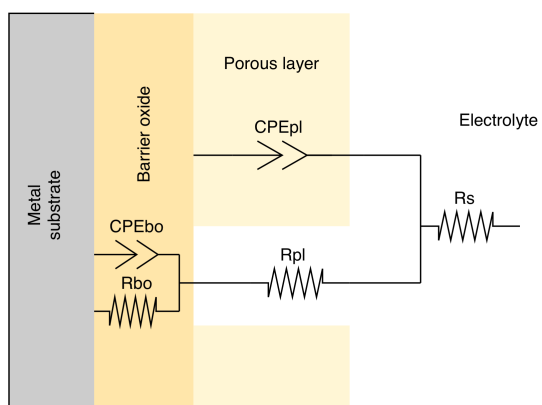
- Physically acceptable and meaningful.
- As simple as possible.
- Gives good fitting.

All the modeling results shown in Table 4-6. The capacitance of the surface layer is broadly related to CPE as in the following formula [114]:

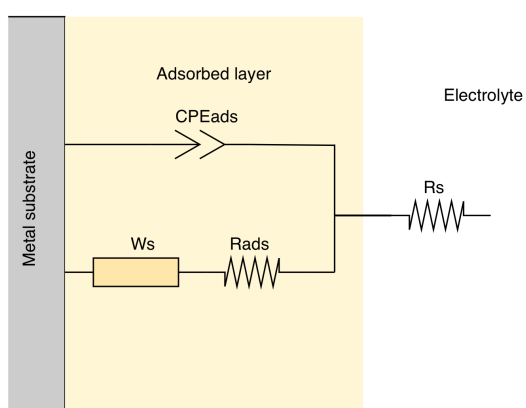
$$C = \frac{(CPE \times R)^{1/n}}{R}$$



a



b



c

Figure 4-16 equivalent circuits for EIS data modelling

The cathodic potential -0.9 V is sufficient to damage the protection nature of the oxide layer. Thus, the semicircle in Figure 4-17 is attributed to the adsorbed layer [115].

The Nyquist plot for -0.7 V, and -0.5 V (Figure 4-17b) shows a flattening at low frequencies which probably means that the oxide layer is porous in its outermost layer. This effect looks clearer at -0.7 V. The resistance of the barrier oxide R_{bo} for -0.7 V decreased by 60% compared to -0.5 V. The thickness of the oxide layer is correlated to its capacitance by the following formula [73]:

$$C = \varepsilon \cdot \varepsilon_0 \cdot \frac{A}{d}$$

d denotes the film thickness, A is the active area, ε is the film dielectric constant of the oxide layer (roughly taken as 12.5 for chromium oxide [116]), and ε_0 vacuum permittivity (8.85×10^{-14} F/cm). This suggests a reverse relation between the capacitance of the layer and its thickness. The capacitance of the oxide layer decreases with increasing cathodic polarization potential. All these indicate that the thickness of this layer decreases with increasing cathodic potential. However, the results do not show differences in the capacitance of the porous layer C_{pl} and its resistance R_{pl} .

The material at OCP, on the other hand, exhibits typical behaviour of the passive alloy with $537 \text{ K}\Omega \cdot \text{cm}^2$ oxide film resistance. The wide peak in phase Bode plot clearly indicates overlapping of two-time constants; one is for the oxide layer at high and intermediate frequencies and the other is for the surface adsorbed layer at low frequencies. This high oxide film resistance becomes even higher ($655 \text{ K}\Omega \cdot \text{cm}^2$) at 0 V anodic potential. No obvious change in the resistance of the adsorbed layer has been observed since the surface condition (surface passivation) keeps the same at OCP and anodic potentials. Nevertheless, the CPE of the adsorbed layer at anodic potential is higher meaning that the adsorbed layer gets thinner at this potential.

Table 4-6 EIS results at different potentials

P (V)	Chi-Sqr ($\times 10^{-3}$)	R_s (Ω)	CPE_{ad-T} ($\times 10^{-4}$) ($Fcm^{-1}s^{(\alpha-1)}$)	CPE_{ad-P}	R_{ads} ($\Omega.cm^2$)	$CPE_{oxide-T}$ ($\times 10^{-5}$) ($Fcm^{-1}s^{(\alpha-1)}$)	$CPE_{oxide-P}$	R_{oxide} ($k\Omega.cm^2$)
0	1.82	24.47	1.65	0.94	9304	2.82	0.95	655
OCP	3	25.22	1.09	0.95	11153	3.25	0.95	537
	Chi-Sqr ($\times 10^{-3}$)	R_s (Ω)	CPE_{pl-T} ($\times 10^{-5}$)	CPE_{pl-P}	R_{pl} ($\Omega.cm^2$)	CPE_{bo-T} ($\times 10^{-6}$)	CPE_{bo-P}	R_{bo} ($\Omega.cm^2$)
-0.5	1.62	23.83	5.38	0.89	1255	4.8	0.99	31008
-0.7	2.83	21.29	5.03	0.89	1414	5.67	0.99	19633
	Chi-Sqr ($\times 10^{-3}$)	R_s (Ω)	CPE_{ad-T} ($\times 10^{-5}$)	CPE_{ad-P}	R_{ad} ($\Omega.cm^2$)	W-R (Ω)	W-P	
-0.9	0.38	25.12	4.66	0.87	644.8	978.3	0.48	

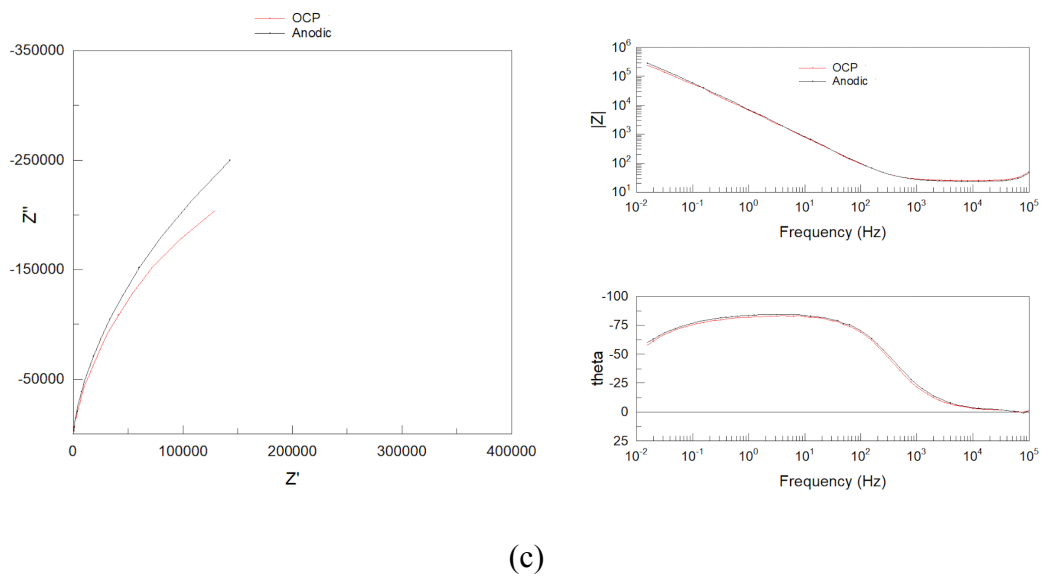
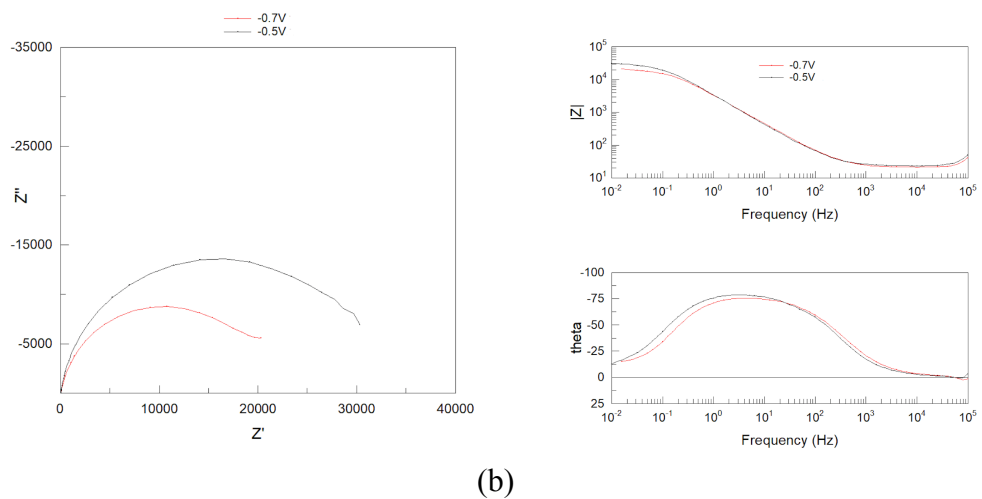
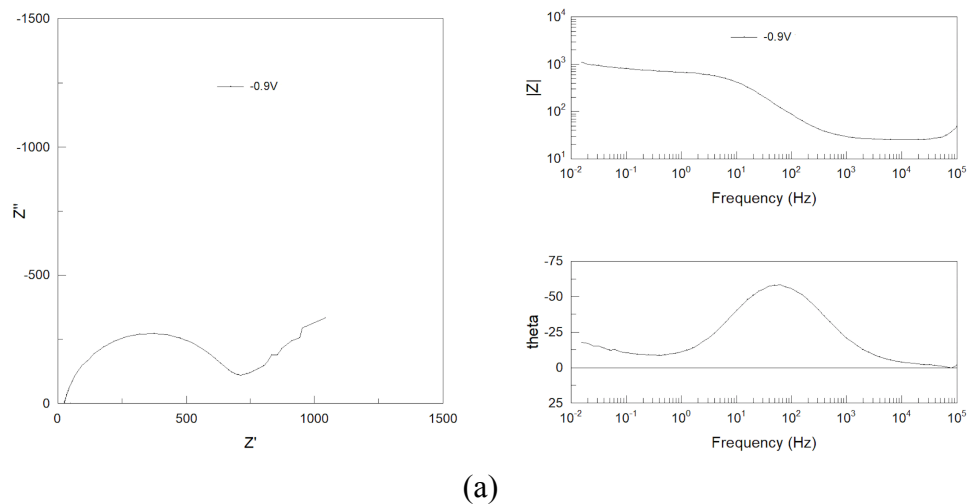


Figure 4-17 Nyquist plot for (a) -0.9V, (b) -0.7V, and -0.5V (c) OCP and anodic potential

4.2.2.2 Tribocorrosion behaviour

Figure 4-18, Figure 4-19 and Figure 4-20 show the current (or the potential P at OCP test) and the coefficient of friction COF versus time for 4, 8 and 16 N wear test load. shows all tribocorrosion parameters for load-potential duel effect.

At all loads, applying a cathodic potential (-0.9 V, -0.7 V, -0.5 V) had a direct effect on the flowing cathodic current in such a way that it increases with higher cathodic potential. The negative current at these potentials comes from the reduction of oxidizing species in the electrolyte. This current increases with higher applied cathodic potential. The average COF at these potentials for all tested loads remained more or less the same at around 0.125. However, it is always higher at the beginning of the tests. Importantly, load has no obvious influence on both COF and current at these potentials.

At OCP, rubbing causes a sharp drop in potential by more than 150 mV at all loads. The potential remains around this value during the entire rubbing. When rubbing stopped, the sliding potential jumps up in about 3.5 mV/s repassivation rate followed by much slower repassivation. The OCP recovered to close to its original value (the value before applying rubbing) within about 800 s after rubbing has been stopped. The average COF was higher than at cathodic potential at 4N load. Nevertheless, it gets closer to the cathodic value at 8N and 16N load (see Figure 4-21). The COF shows a strong load dependence at OCP tests. 4N OCP test shows the highest COF in all tests.

At anodic potentials, when rubbing was just initiated, the flowing anodic current shows a high value at all loads and anodic potentials. This was followed by a sudden drop in the first quarter of the test time. The current was stable after this drop- throughout the remainder of the test. Interestingly, the trend in the COF follows these events showing a high value when the current was high and a reduction when the current reduced. Increasing anodic potential does not exhibit an influence on COF within the same load.

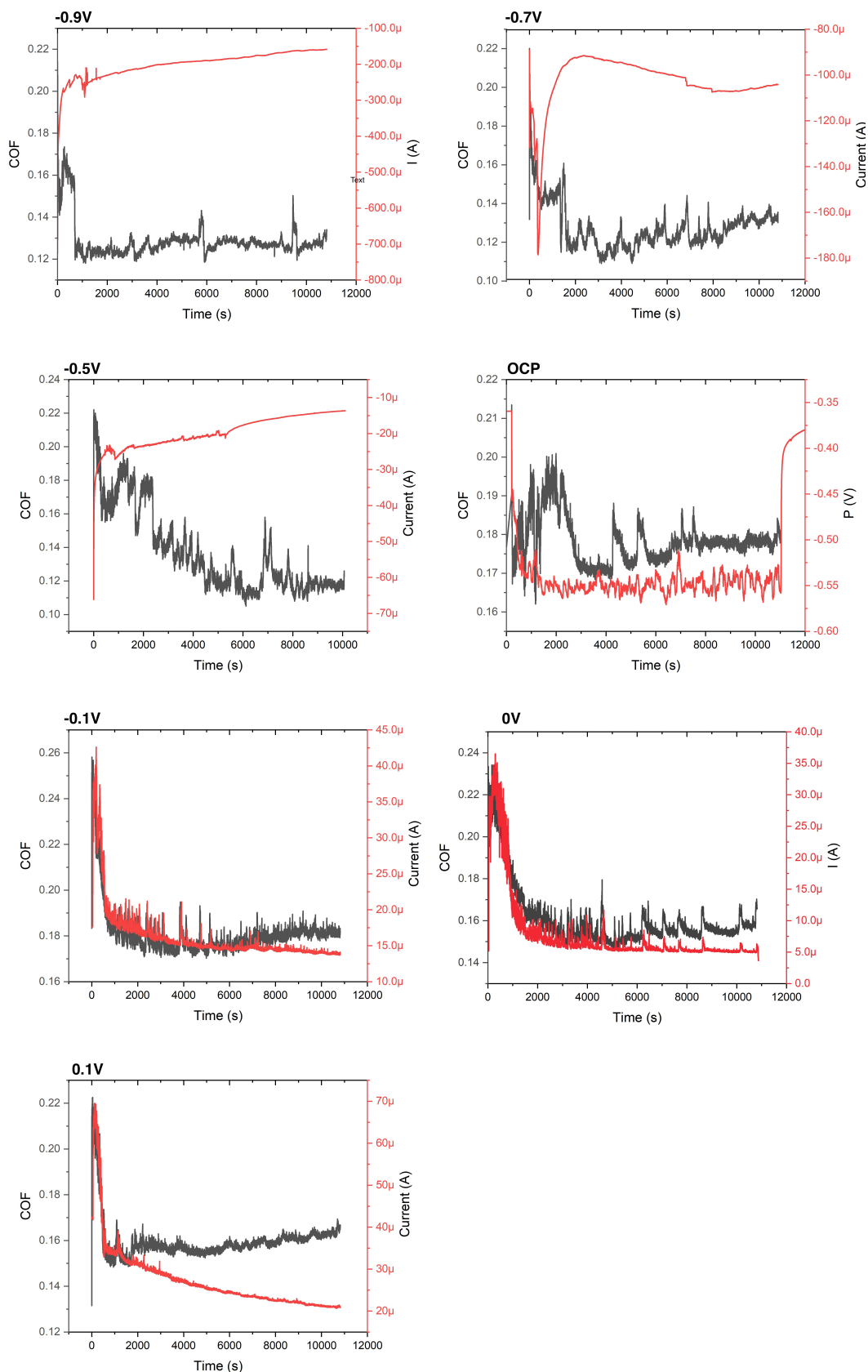


Figure 4-18 potential vs. COF and current (or sliding potential P) at 4 N load and different potentials

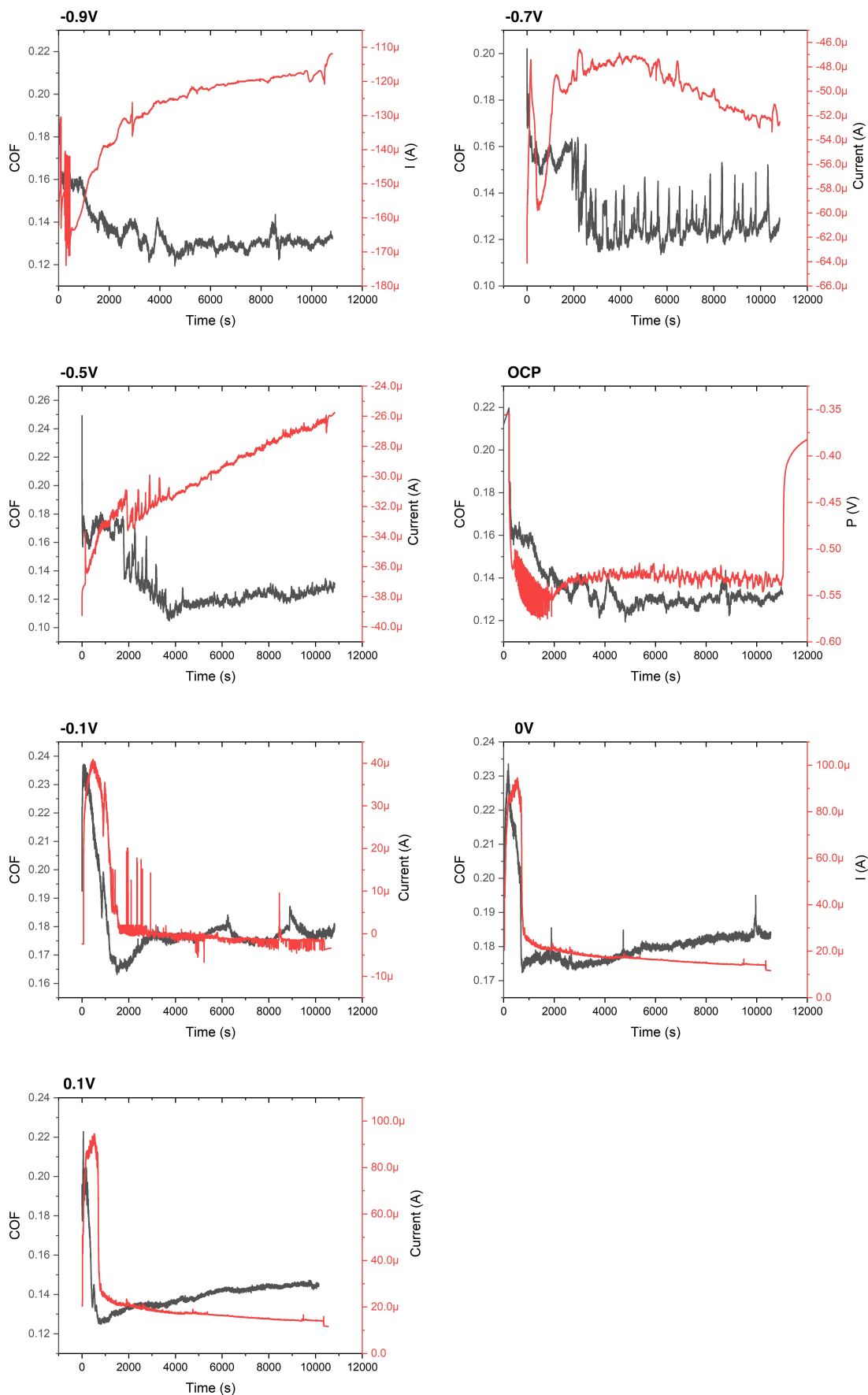


Figure 4-19 COF and I (or sliding potential P) versus time at 8 N load

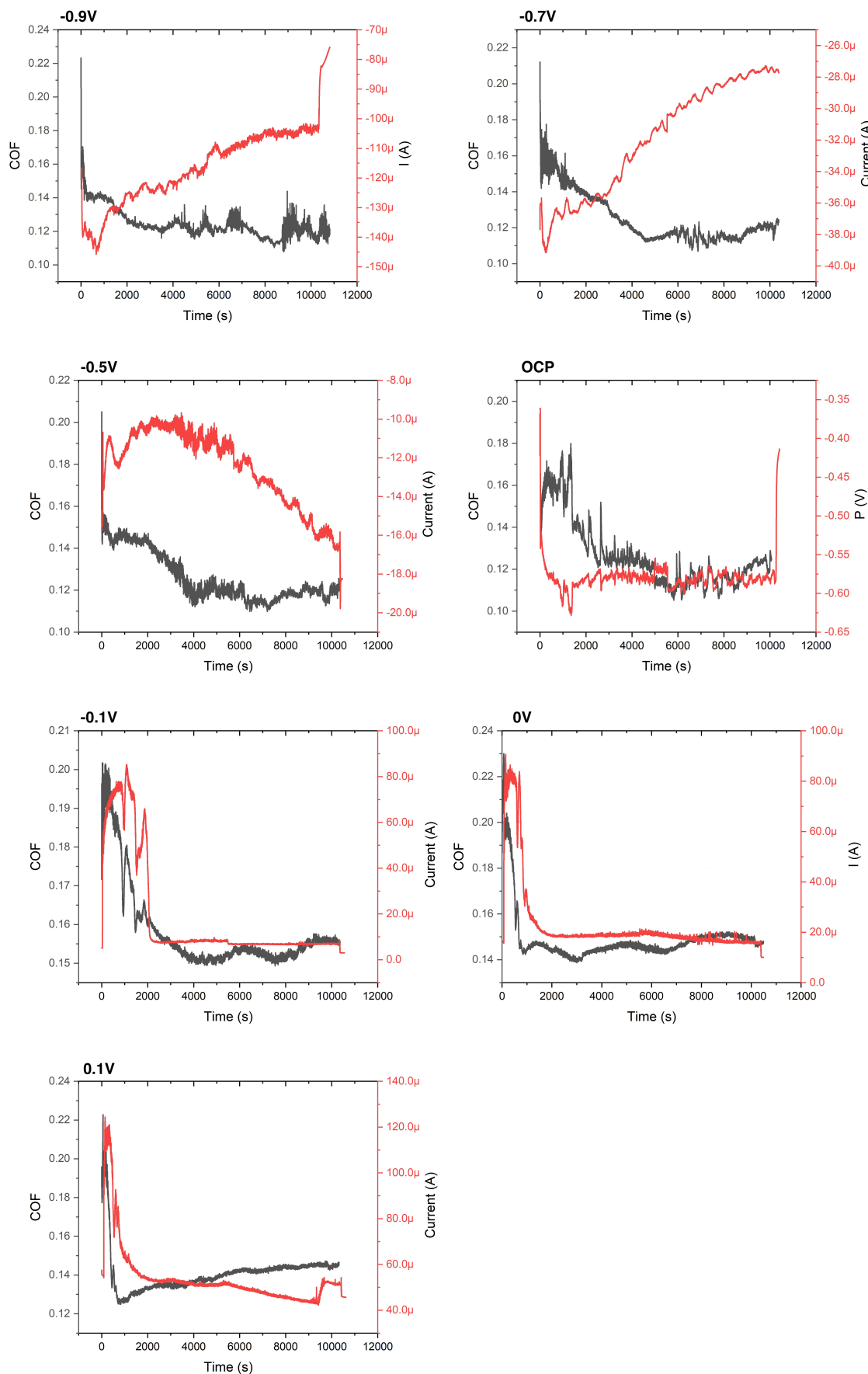


Figure 4-20 COF and I (or sliding potential P) versus time at 16 N load

Figure 4-21 shows the specific wear rate and COF versus potential for 4 N, 8 N and 16 N for a wide range of cathodic and anodic potentials as well as at the OCP. Interestingly, the highest K is almost always at the OCP. At cathodic potentials, K exhibited a linear increase with decreasing cathodic potential toward the OCP. The highest K was 5.7×10^{-6} mm³/N.m at 8 N OCP test, while the lowest was 3.86×10^{-7} mm³/N.m at 4 N -0.9V. Cathodic potential reduces or even stops the corrosion influence on the total tribocorrosion process. Thus, all tested cathodic potentials show lower specific wear rate than OCP or anodic potentials. As expected from Archard's law, K increases with load for each particular cathodic potential. At the OCP and further anodic potentials, the corrosion contribution became significant. As mentioned earlier, the highest K was at 8 N OCP, which dropped down at 16 N OCP to even less than that at 4 N OCP. Further anodic potential brought K down at all test loads. There was one exception to this case noticed at 16 N -0.1 V anodic potential, where K was the same as at the OCP. Figure 4-21 clearly shows that any polarization of the surface whatever cathodic or anodic it is, led to lower K and it was, in most cases, quite significant.

The COF was always lower at cathodic potentials compared to the other potentials. However, the COF was load and potential dependant at the OCP and under anodic conditions. At 4 N load it peaked at the OCP followed by a reduction at anodic potentials. At 8 N it increased at the OCP and further anodic potentials. The COF peaked at -0.1 V and 16 N load and then reduced with increasing anodic potential.

Table 4-7 tribocorrosion parameters for load-potential duel effect tests

Load (N)	Potential (V)	COF	K (mm³/N.m)×10⁻⁶	Q (C) ×10⁻²	V_{total} (mm³) ×10⁻³	V_{chem}(mm³) ×10⁻³	V_{mech} (mm³) ×10⁻³	V_{chem}/V_{total}
4	-0.9	0.125	0.38	---	0.28	---	---	---
	-0.7	0.120	0.51	---	0.37	---	---	---
	-0.5	0.119	1.26	---	0.86	---	---	---
	OCP	0.182	3.77	---	1.52	---	---	---
	-0.1	0.169	2.6	1.7	1.72	0.26	1.72	0.13
	0	0.164	1.95	1.6	0.83	0.46	0.83	0.36
	0.1	0.162	1.96	1.9	1.1	0.16	1.1	0.13
8	-0.9	0.134	0.5	---	0.83	---	---	---
	-0.7	0.131	0.79	---	1.3	---	---	---
	-0.5	0.130	1	---	1.72	---	---	---
	OCP	0.148	5.78	---	8.84	---	---	---
	-0.1	0.179	3.1	6.3	4.50	0.8	4.5	0.15
	0	0.182	2.31	5.8	2.98	1	2.98	0.26
	0.1	0.180	2.72	5.7	3.38	1.32	3.38	0.28
16	-0.9	0.124	1	---	3.39	---	---	---
	-0.7	0.125	1.26	---	4.34	---	---	---
	-0.5	0.126	1.52	---	5.15	---	---	---
	OCP	0.128	2.84	---	8.03	---	---	---
	-0.1	0.158	2.91	15.1	8.09	1.91	8.1	0.19
	0	0.149	2.27	11.1	6.42	1.38	6.42	0.18
	0.1	0.141	2.1	6.3	6.7	0.5	6.7	0.07

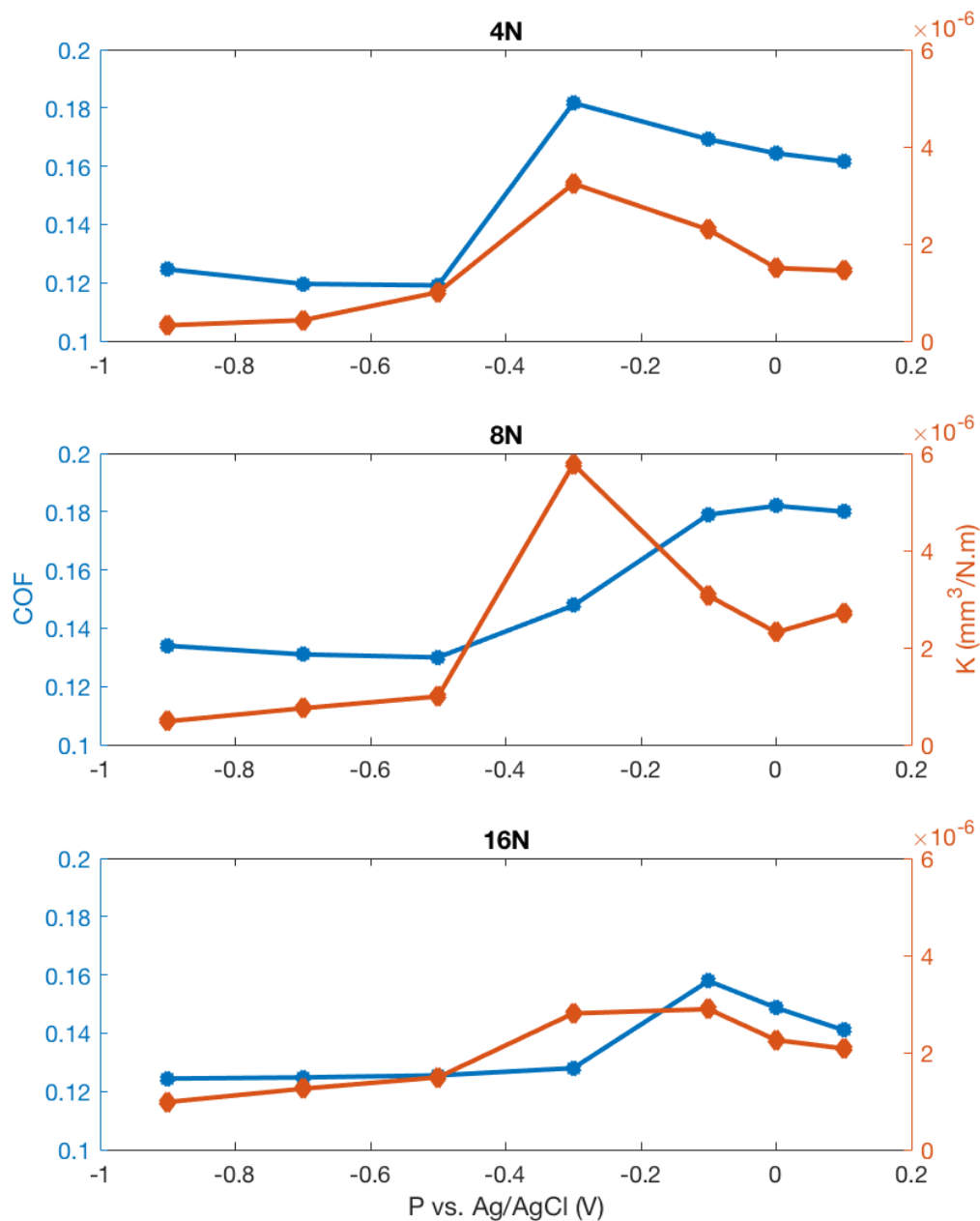


Figure 4-21 COF and K vs. potential for 4N, 8N, and 16N wear test loads

The reproducibility of the data was checked for many samples. An example is shown in Table 4-8.

Table 4-8 the reproducibility of the data for two different samples

Potential (V)	COF		V (mm ³)	
	Sample 1	Sample 2	Sample 1	Sample 2
-0.9	0.122	0.124	3.5×10^{-4}	2.8×10^{-4}
OCP	0.17	0.181	2.7×10^{-3}	2.8×10^{-3}
0	0.157	0.164	1.9×10^{-3}	1.3×10^{-3}

Figure 4-22 shows the total material loss V_{total} contour graph for the load-potential tests. V_{total} shows both a load and potential dependence. The volume of material loss at cathodic potentials for all tested loads were always less than that at OCP and anodic potentials. Nevertheless, it increased as the cathodic applied potential decreased towards the OCP. The graph clearly shows that the total material loss was always the highest at the OCP for all loads. V_{total} shows load and potential dependence. Applying cathodic or anodic potential decreased the V_{total} . On the other hand, load had a direct effect on V_{total} over the tested potential range. However, the influence of load on V_{total} was affected by the electrode potential. At OCP, V_{total} continuously increased with load up to 8 N followed by a plateau at further load. This behaviour can be explained depending on the microstructure and the galvanic couple forms in tribocorrosion tests as will be discussed later.

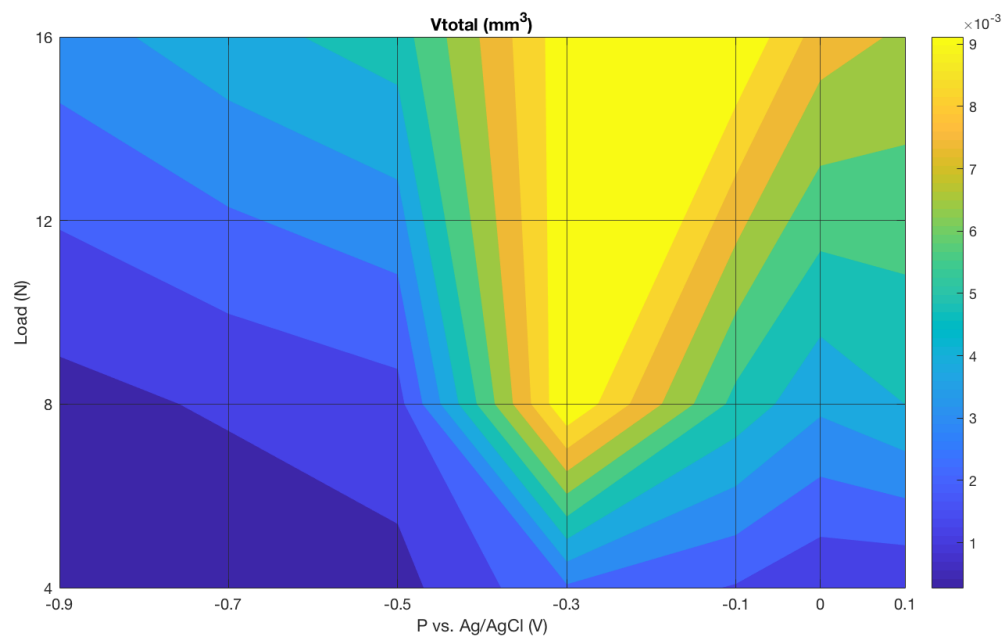


Figure 4-22 contour graph for V_{total} over tested loads and potentials

To get a better understanding of the tribocorrosion material loss mechanisms, further analysis for anodic electrode potential was undertaken. V_{chem} , which is the area under anodic current curves, was accurately calculated by creating a baseline for the current curve at anodic electrode potentials. The baseline represents the background current which should be removed. This baseline was subtracted from the anodic current curves and shown in Figure 4-24. Load at anodic potentials (within the passive domain) does not have the same effect on V_{chem} for the three tested loads (Figure 4-23 and). At 4 N, increasing anodic potential from -0.1 V to 0 V led to an increase in V_{chem} . However, further anodic potential (0.1 V) decreased V_{chem} . The figure is different at 8 N where there was a continuous increase in V_{chem} with anodic potential. At 16 N, on the other hand, the corrosion contribution, V_{chem} , was positively enhanced by further anodic potential, being about one quarter at 0.1 V compared to -0.1 V.

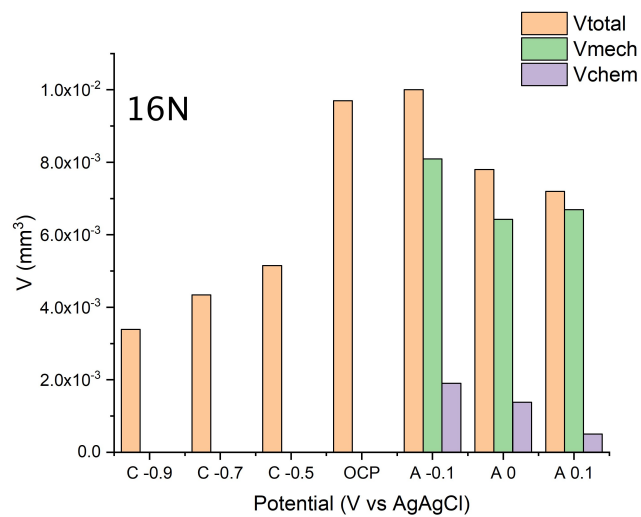
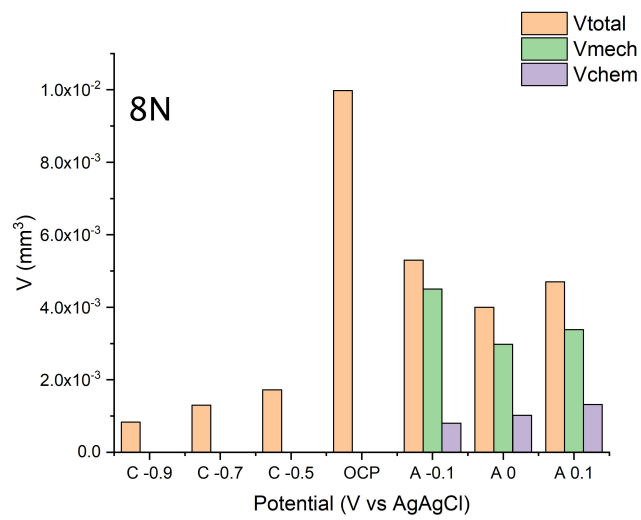
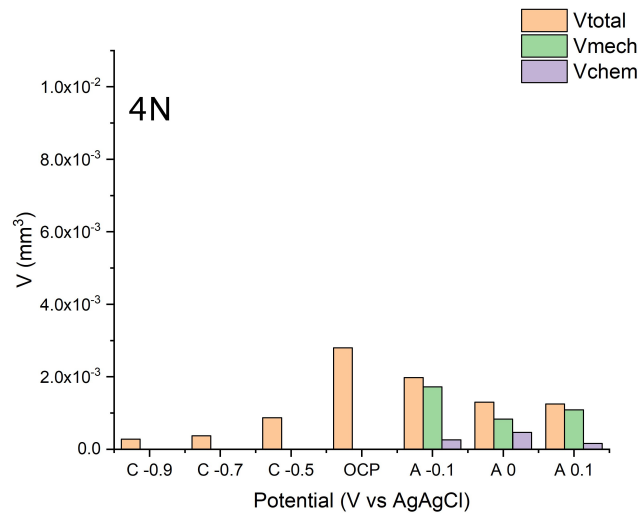


Figure 4-23 V_{total}, V_{chem}, and V_{mech}

V_{chem} starts with high rate at all tests followed by significant reduction which comes instantaneous with the drop down in the anodic current. Figure 4-25 and Table 4-9 show the V_{chem} rates before and after the current drop. This rate significantly decreased after this transition. V_{chem}/s started with 10^{-7} mm^3/s and reduced more than one order of magnitude after the current transition. Before the current drop at -0.1 V anodic potential, the relationship between the load and V_{chem}/s was linear, whereas, it showed an increase at 8 N and 16 N followed by slightly decrease at 0 V, and 0.1 V. In contrast, after the current drop, the linearity between V_{chem}/s and load was at -0.1 V, 0 V anodic potentials. Nevertheless, V_{chem}/s at 0.1 V exhibited a quite low value at 16 N load (8.12×10^{-10} mm^3/s).

Table 4-9 V_{chem}/s at anodic potentials in mm^3/s

Load (N)	-0.1 V		0 V		0.1 V	
	Before $\times 10^{-7}$	After $\times 10^{-8}$	Before $\times 10^{-7}$	After $\times 10^{-8}$	Before $\times 10^{-7}$	After $\times 10^{-8}$
4	2.97	1.14	3	1.98	2.9	0.25
8	4.73	2.71	8.78	4	8	4.9
16	8.29	5	7.92	8.34	7.17	0.081

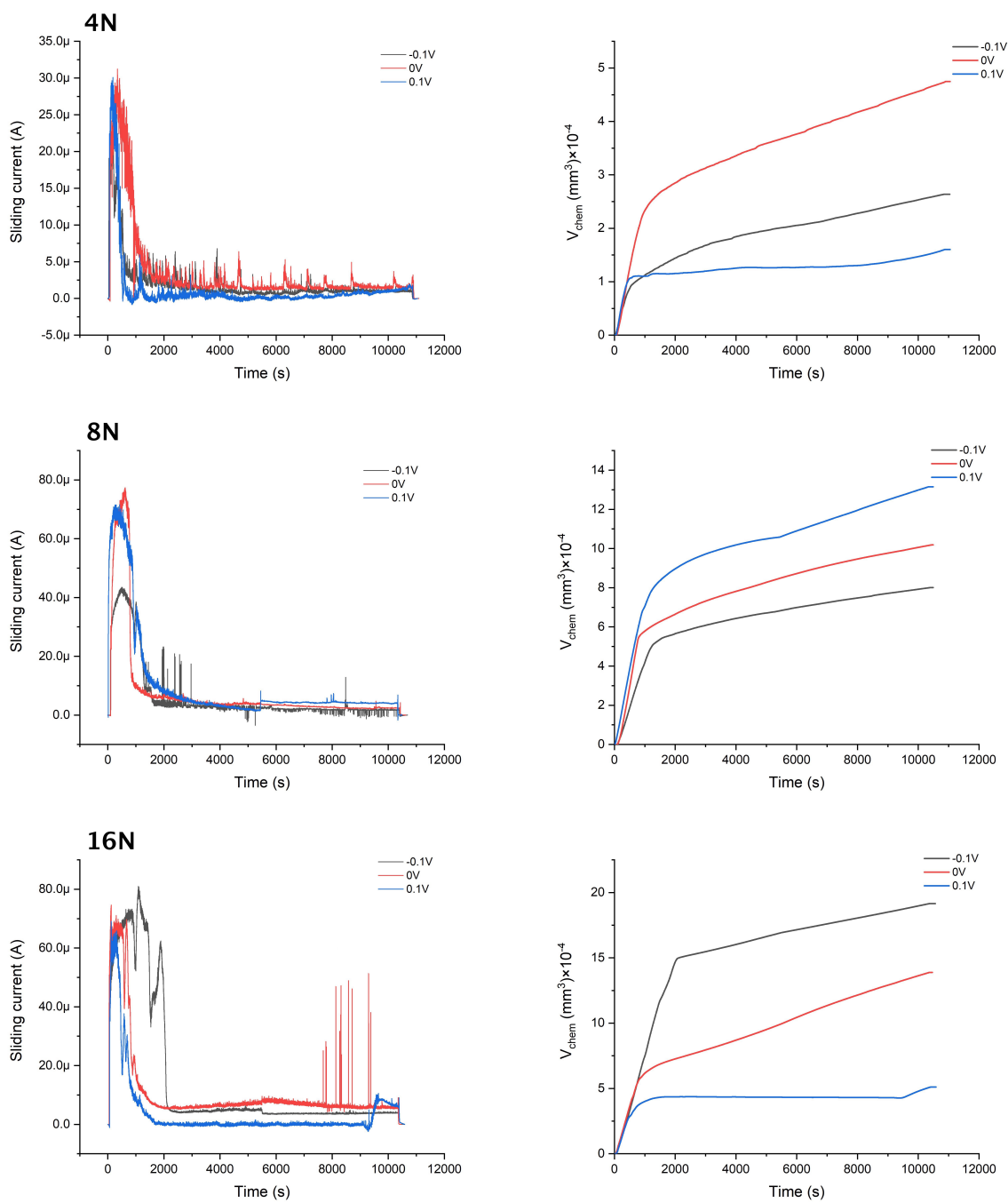


Figure 4-24 anodic current curves after subtraction of the baselines. V_{chem} rate is added to the right

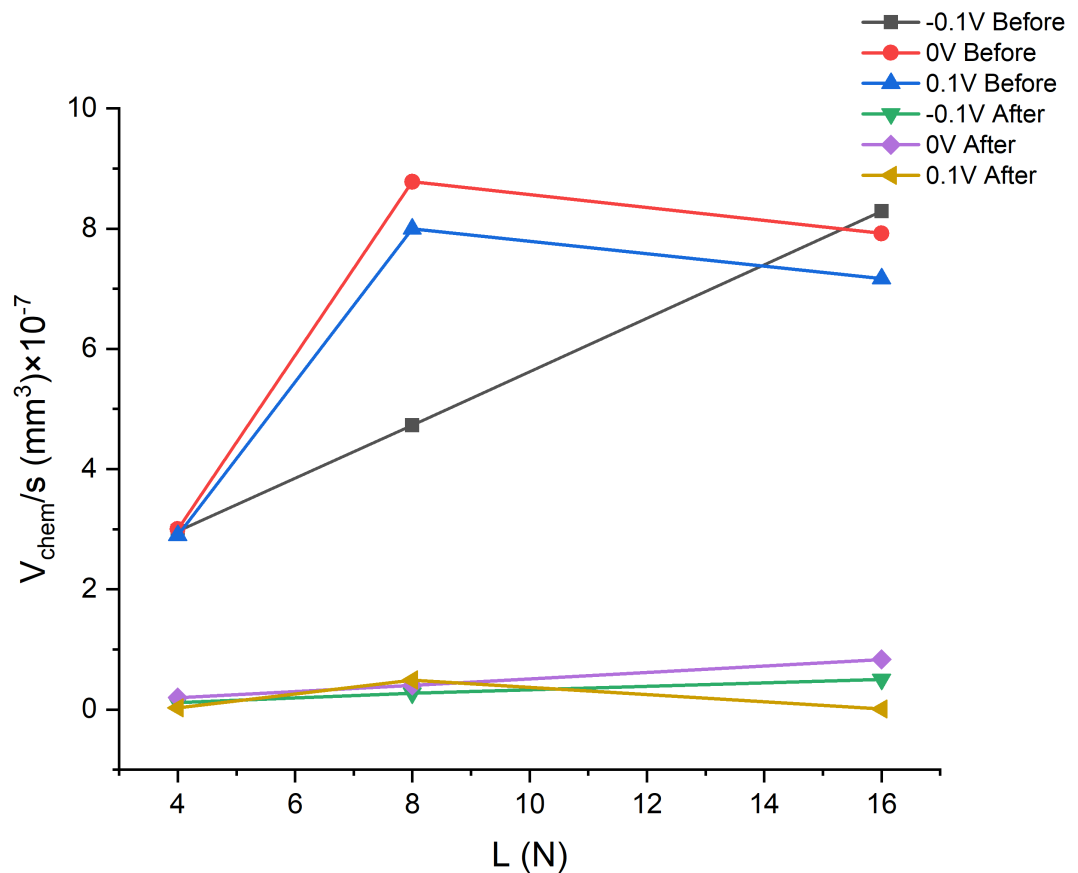


Figure 4-25 V_{chem} rate after and before current drop

4.2.2.3 Characterization of the worn surfaces:

Figure 4-26, Figure 4-27 and Figure 4-28 are SEM images for the worn surfaces for 4, 8, and 16 N at -0.7 V, -0.5 V, OCP, -0.1 V, 0 V, and 0.1V. The potential effect on the morphology of the worn surfaces and wear mechanism is quite obvious. The images show that the wear mechanism at cathodic potential was abrasive grooving wear gets more severe with increasing load and cathodic potential. The formation of wear debris due to this mechanism can clearly be seen at -0.7 V for 8 N and 16 N loads. A smoother surface at OCP and anodic potential conditions reflects a change in the wear mechanism to a hybrid abrasive-corrosive mechanism. Corrosion in combination with two-body (or probably three-body) abrasion increases the wear rate particularly at OCP. Doubling the load from 8 N to 16 N resulted in the formation of a surface carbonaceous layer (as will be confirmed later by Raman testing) at OCP and even anodic potential.

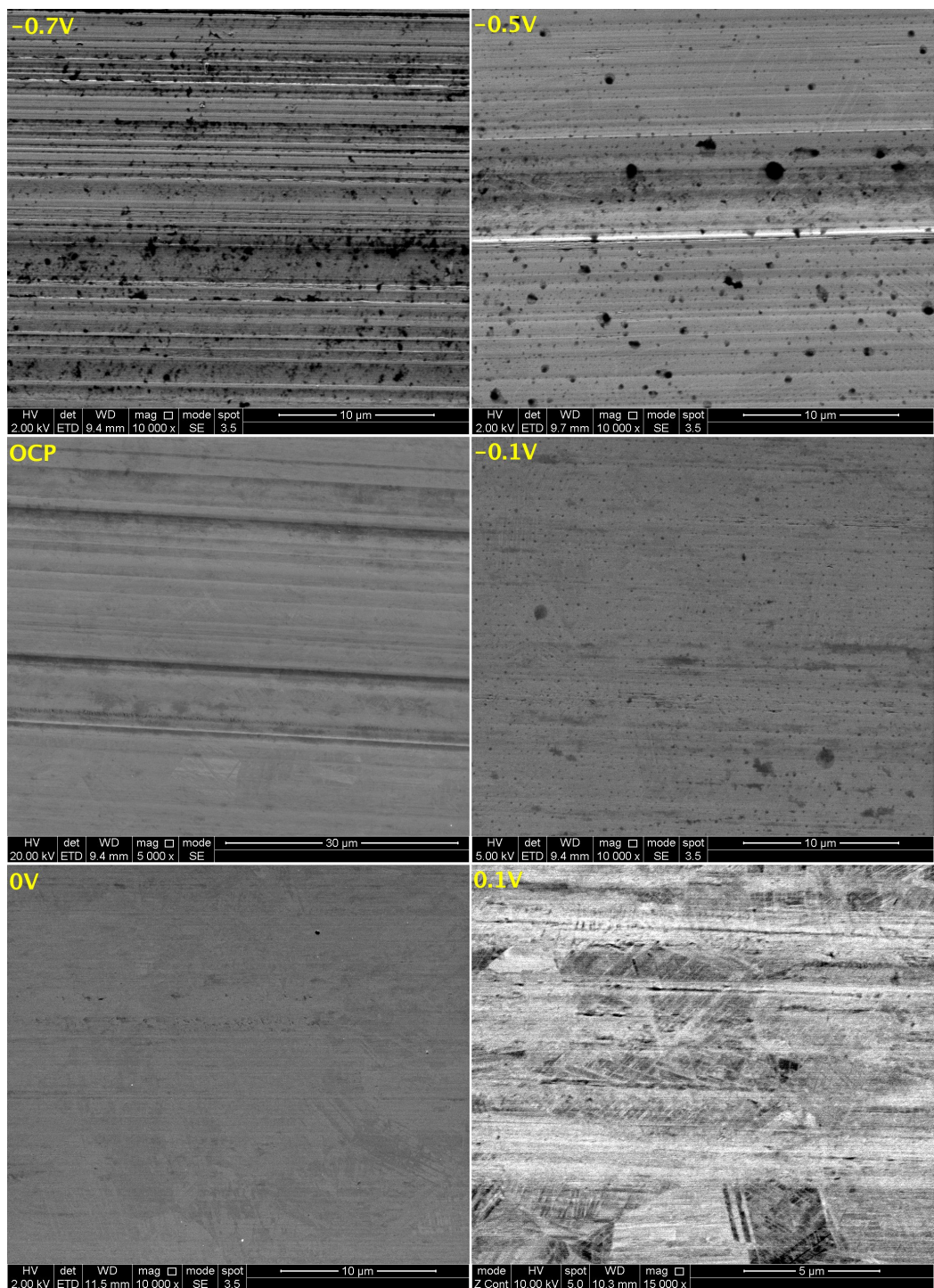


Figure 4-26 SEM images for all tribocorrosion tests

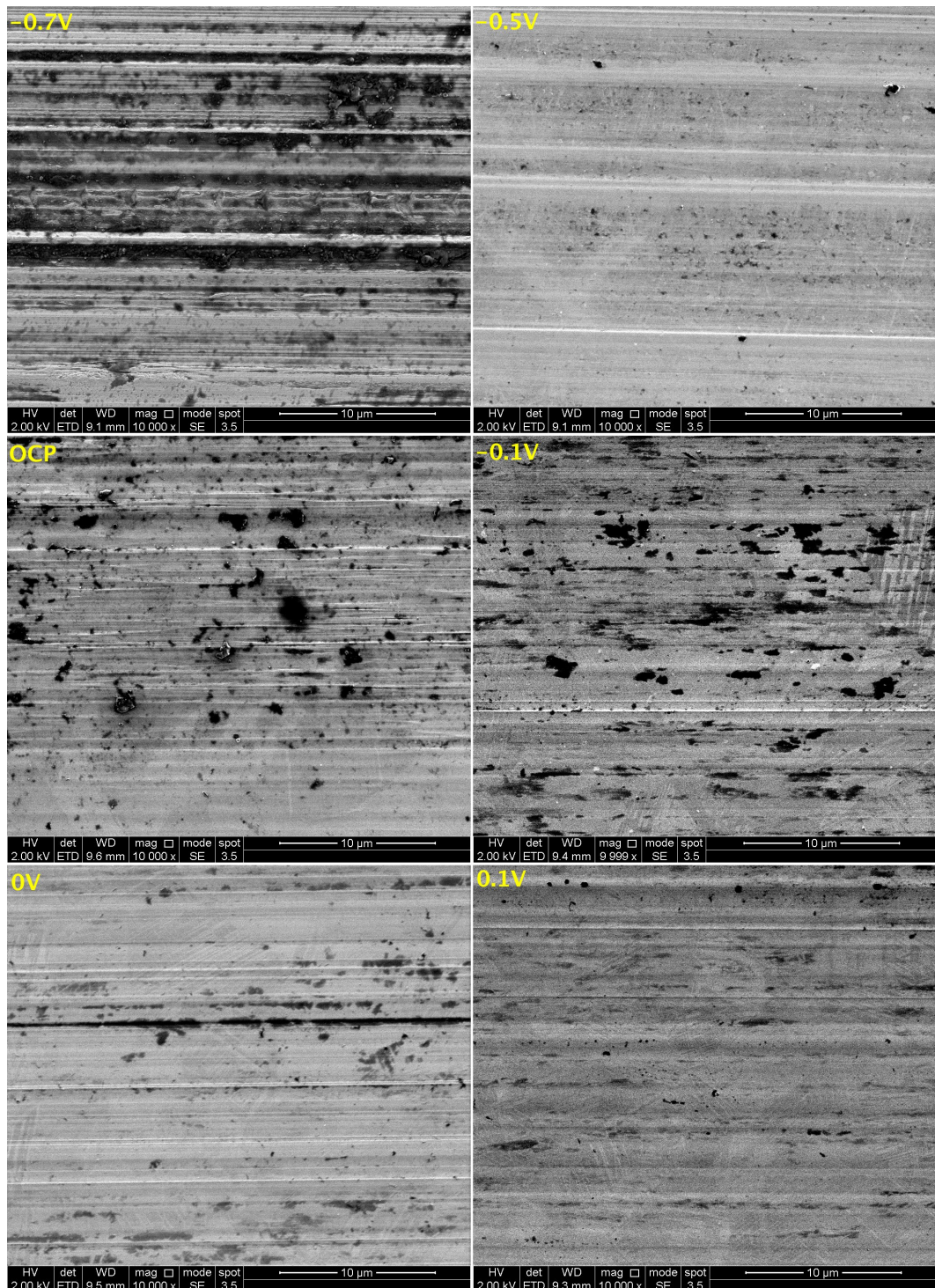


Figure 4-27 SEM images for 8N wear test load at different applied potentials

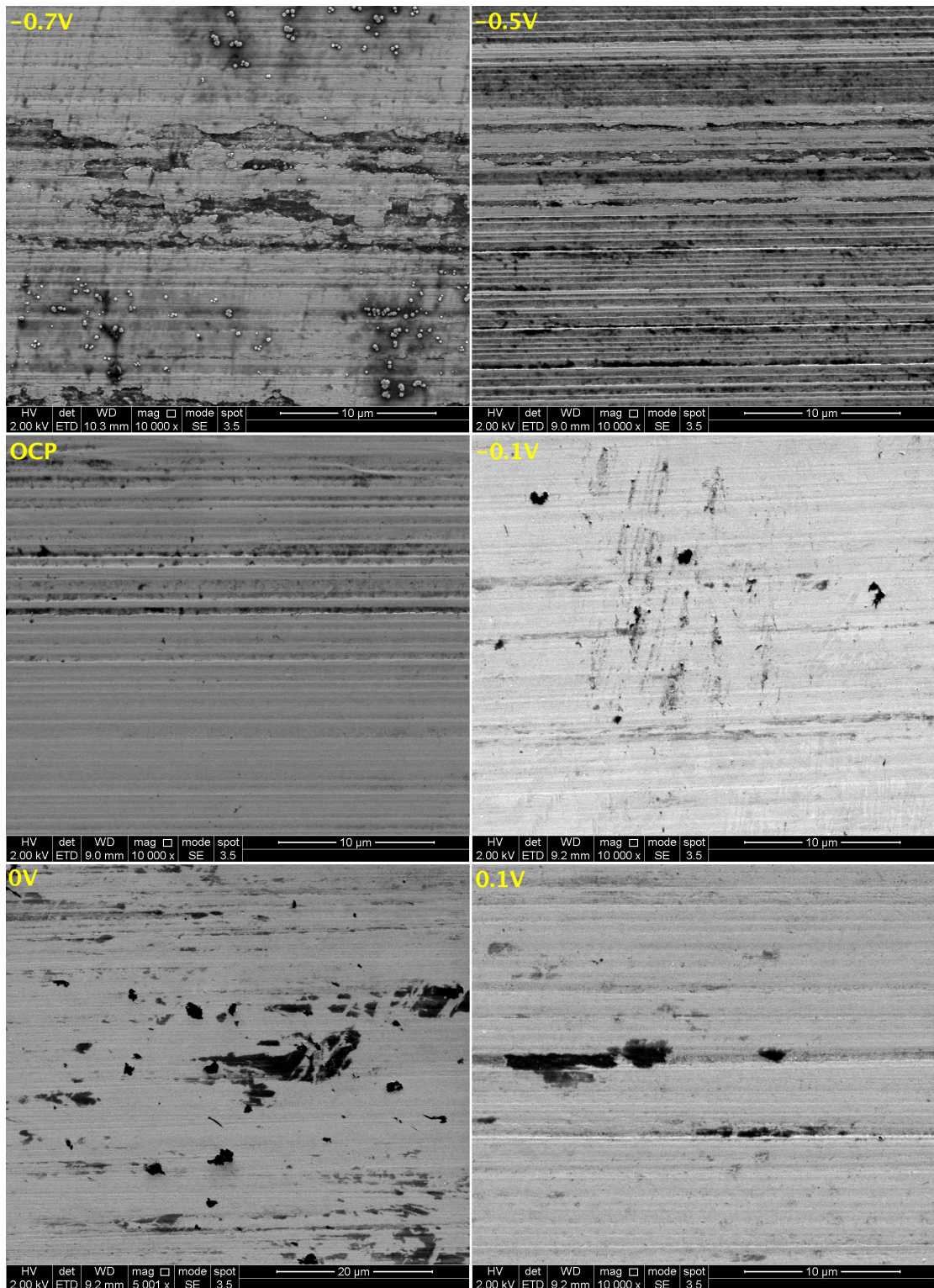


Figure 4-28 SEM images for 16N wear test load at different applied potentials

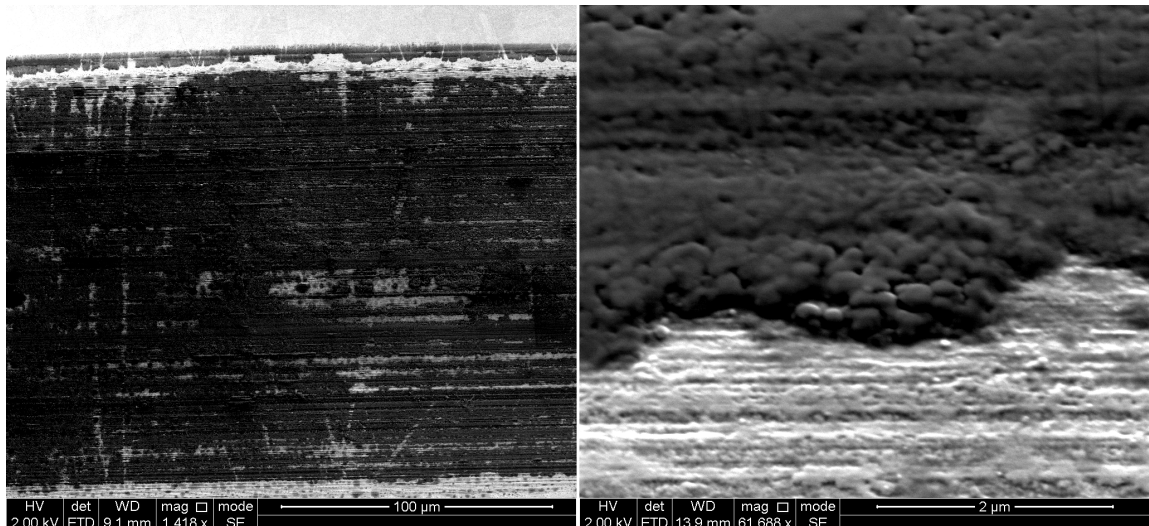


Figure 4-29 worn surface at $-0.9V$ potential test.

Figure 4-29 and Figure 4-30 are SEM images for the worn surface of 4 and 8 N at $-0.9V$ at different magnifications. The tribolayer can be seen to cover the entire surface at 4 N. The worn surface is heavily deformed as a result of dominant mechanical effect. It is evident that there is a surface layer deposited just next to both sides of the wear scar edges at 8 N. Note that like this layer is also present at 4 N $-0.9V$ (Figure 4-29), but it is much less narrow. Higher magnification SEM image for 8 N worn surface shows a deposited surface layer with a morphology similar to that deposited on 4 N. However, it covers much less of the wear scar.

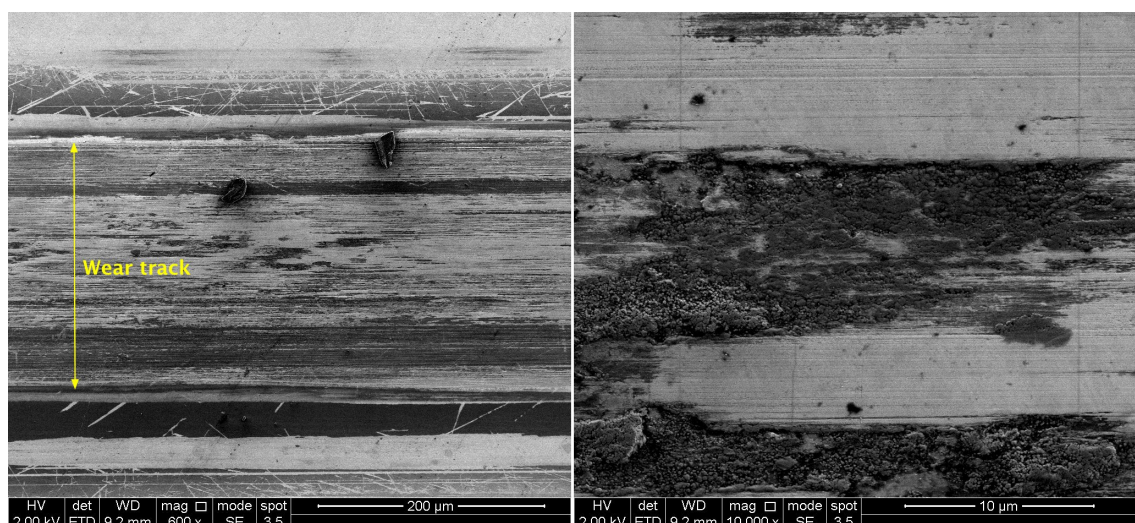


Figure 4-30 SEM images for 8N wear test load at $-0.9V$ applied potential

The worn surface of 16 N -0.9 V is shown in Figure 4-31. Regions exhibiting darker contrast cover much of the wear scar. Furthermore, there is a surface carbonaceous layer on some of these darker areas. The morphology of the carbonaceous layer looks somewhat different from that which formed on the 4 N -0.9 V and 8 N -0.9 V, with some nano-debris present.

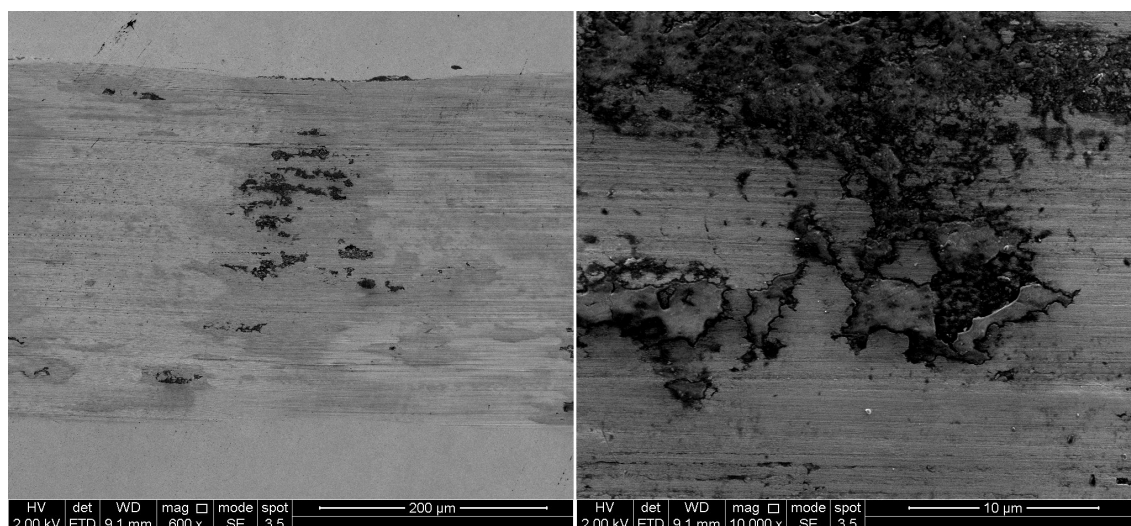


Figure 4-31 SEM images for 16N wear test load at -0.9V applied potential

The roughness of the worn surfaces at 4 N load was examined using 3D optical profilometry and the results are tabulated in Table 4-10. The roughness of the worn surfaces at cathodic potentials was twice that at OCP and anodic potentials.

Table 4-10 surface roughness for worn surfaces at 4N load.

Potential (V)	R _a (μm)	R _q (μm)
-0.9	0.083	0.105
-0.7	0.091	0.127
OCP	0.043	0.057
0	0.04	0.049
0.1	0.039	0.046

All wear tracks were examined by Raman spectroscopy to determine the presence of an organic layer. At -0.9 V of 4, 8 and 16 N load, D and G Raman bands at 1350 and 1566 cm⁻¹ were observed (Figure 4-32) indicating the presence of a carbonaceous layer on the surface of the wear track. The position of the G peak indicates that this layer was a mixture

of amorphous and nanocrystalline graphite [117]. Although SEM imaging suggests the presence of such a layer on the some of other worn surfaces, it could not have been detected it by Raman spectroscopy probably because of its morphology which was small separated spots or because of the thickness of this layer.

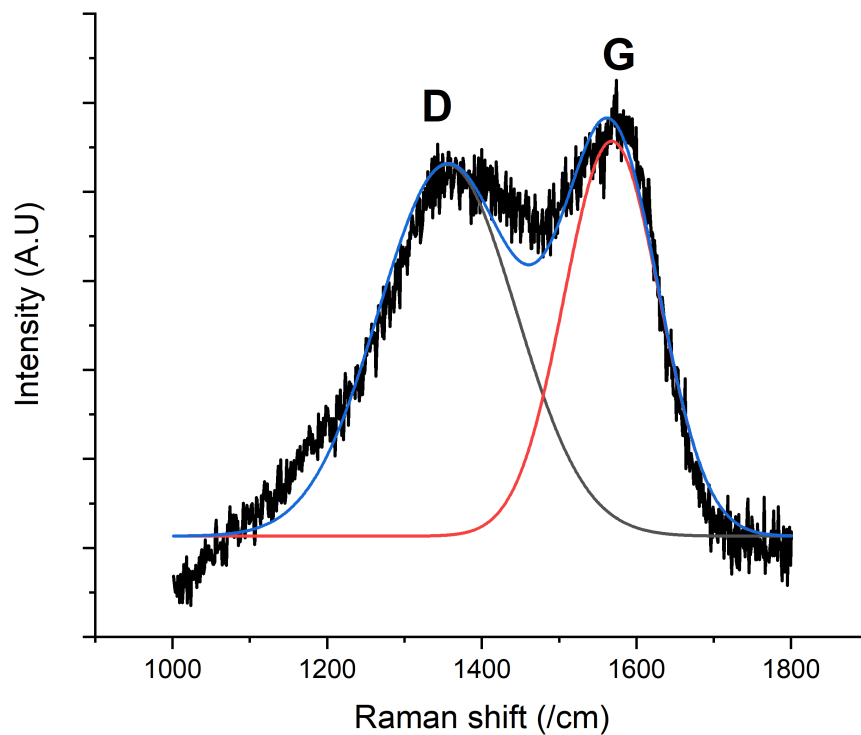


Figure 4-32 Typical Raman spectrum with Gaussian peak fitting for -0.9V at 4N, 8N, and 16N, and OCP 8N

The microstructure of the worn surfaces at OCP for 2, 4, 8 and 16 N load are shown in Figure 4-33. Martensitic laths and twins can be easily observed at 2 N load. These deformation features disappeared at 4, and 8 N loads, with a microstructure that was very close the starting surface (Figure 4-1). Dense martensitic laths appeared again at 16 N.

Figure 4-34 reveals the microstructure of the worn surfaces of the 4, and 8 N tested at anodic potentials. Twins started to form on the worn surfaces at -0.1 V. The density of these twins significantly increased at 0 V. At 0.1 V, an extensive net of martensitic laths covered almost the entire worn surface and intersected to form rhombic cells. No nanocrystalline layer could be revealed by SEM imaging. This microstructure is

consistence with hardness increase at anodic potentials for 4, and 8 N loads (Figure 4-35). At 16 N and an anodic potential, the worn surface microstructure could not be revealed indicating the highly deformed worn surfaces.

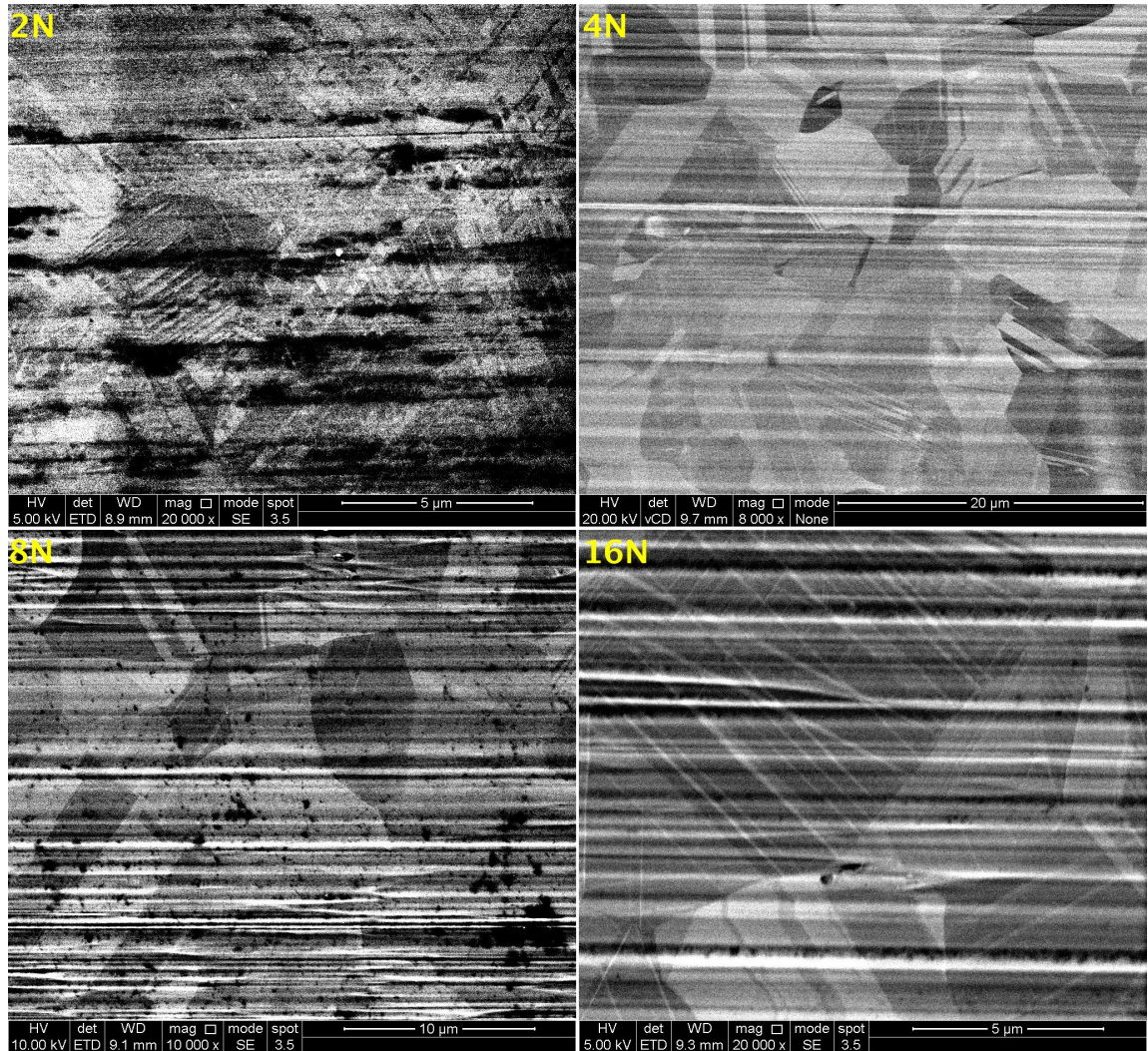


Figure 4-33 microstructure revealing via SEM imaging for worn surfaces at OCP and different loads

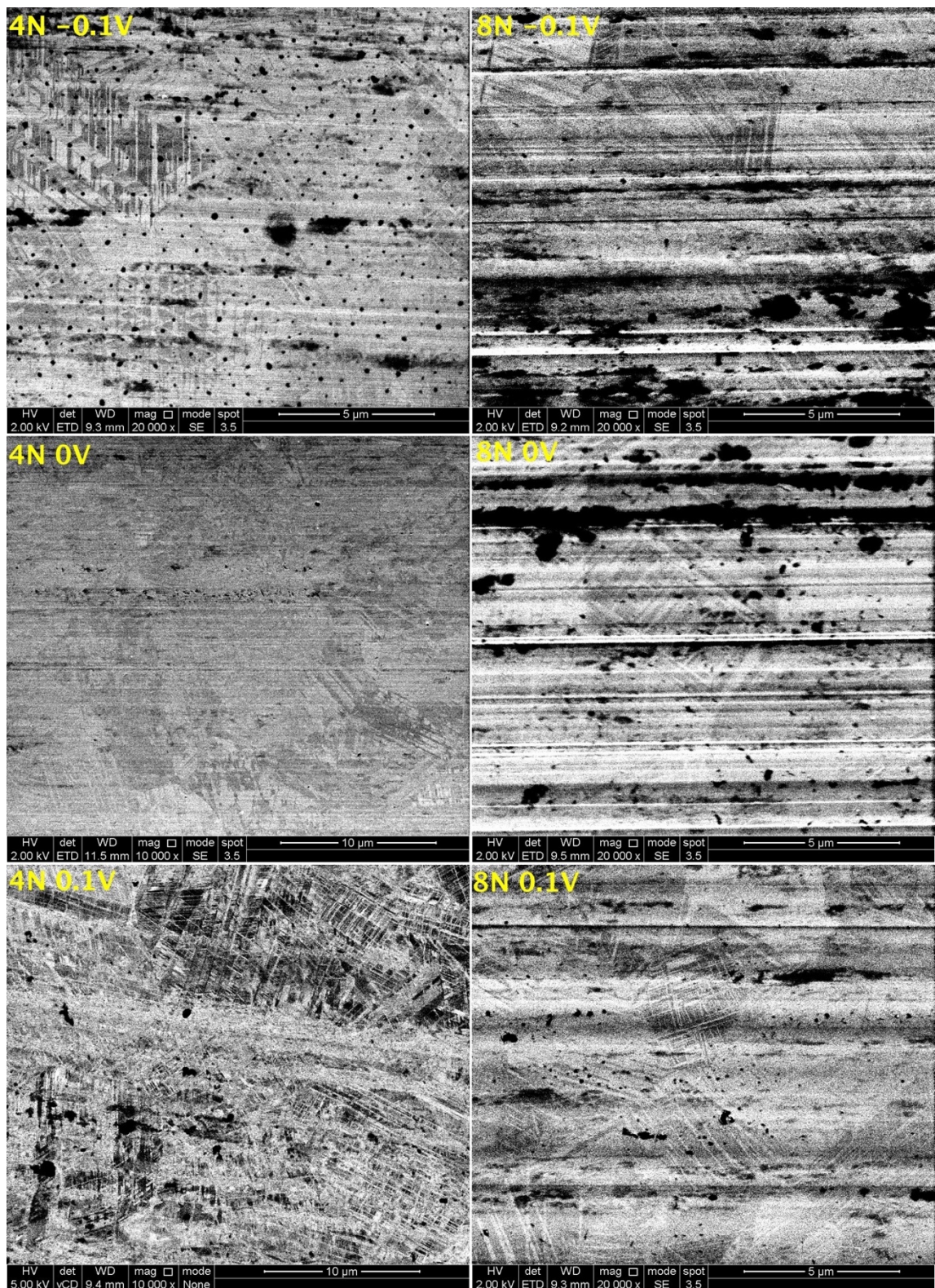


Figure 4-34 microstructure revealing via SEM imaging for worn surfaces at different anodic potentials and loads

4.2.2.4 Nanomechanical testing for worn surfaces:

The nano-hardness and reduced modulus for the worn surfaces at all tested potentials and loads are tabulated in Table 4-11. Figure 4-35 shows the variation in nano-hardness with potential and load for the worn surfaces. The worn surfaces for the material being tested experience strain induced phase transformation depending on load and applied potential as shown in section 4.2.2.3. Nanoindentation testing in this work was done inside the wear track. Therefore, the test was restricted to 20 points on a central straight line in the middle of the wear scar. These number of points are not enough to produce an accurate average reduced modulus. However, the test is good enough to get a precise nano-hardness because the scattering of the hardness data was acceptable.

Table 4-11 mechanical properties for worm surfaces

	4N		8N		16N	
Potential	E _r (GPa)	H(GPa)	E _r (GPa)	H(GPa)	E _r (GPa)	H(GPa)
-0.9	193.0	7.78	204.7	8.00	174.4	7.21
-0.7	218.8	8.81	183.9	7.40	200.6	7.84
-0.5	182.2	6.96	195.9	7.49	188.5	8.39
OCP	202.2	6.32	171.4	6.28	195.0	7.43
-0.1	205.0	6.69	189.2	7.07	189.2	7.09
0	169.4	6.51	171.6	6.80	185.5	6.92
0.1	169.1	6.53	205.8	7.13	182.7	7.71

Applying anodic or cathodic potentials led to an increase in hardness at 4, and 8 N tribocorrosion test loads. The lowest hardness at these two loads was at the OCP. Interestingly, load had no effect on hardness in this load range at the OCP. Nevertheless, the worn surface at 16N OCP exhibited higher hardness compared to the previous tested loads at the same potential. In the range of anodic potentials, load evidently influences nano-hardness that is the hardness increases with load. The same effect of load on hardness has been observed at the lowest tested cathodic potential (-0.5 V). The hardness does not show a clear correlation with load at higher cathodic potentials (-0.7, and -0.9V). This is probably because of the interference of the carbonaceous layer on the worn surfaces. At -0.9 8N the worn surface was less covered by the carbonaceous layer in comparison to 4N -0.9V one, so it was harder. At -0.9 V, and 16 N the worn surface showed a decrease in hardness compared to 4, and 8 N at the same potential. This will be explained in the discussion chapter.

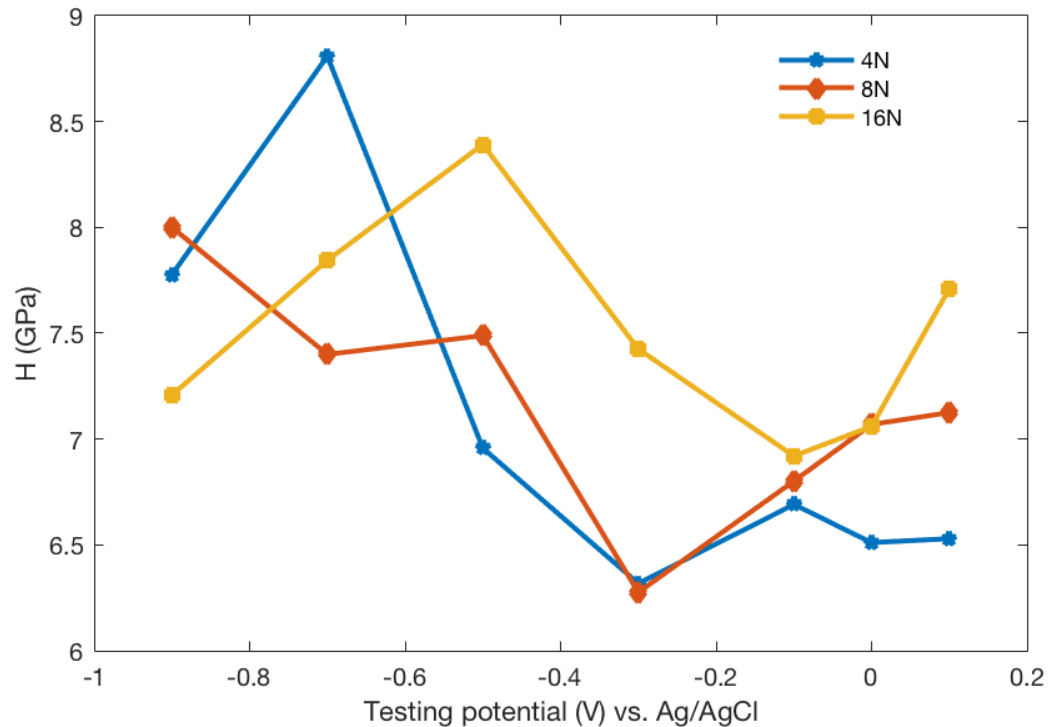


Figure 4-35 nanoindentation hardness for worn surfaces at different load and potential

At -0.9 V 4 N test the worn surface was almost entirely covered by a rich carbon layer (Figure 4-29). It is possibly worth to examine the mechanical properties of this relatively thick layer. Thus, partial unload function and modulus mapping techniques have been employed. Table 4-12 and Figure 4-36 show the hardness of the successive layer of the surface for -0.9 V 4 N worn surface. Hardness increases with depth starting from 5.74 GPa at 30 nm depth going up to 8.62 GPa at 200 nm depth to show a plateau there indicating the end of the tribolayer layer. This is consistency with SEM imaging (Figure 4-29) and the subsurface microstructure examination (section 4.2.3).

Table 4-12 nanohardness of the successive layer of -0.9V test worn surface

$h_{max}(nm)$	H (GPa)	h_f/h_{max}
30	5.74	0.42
34	5.84	0.52
50	6.02	0.48
60	6.42	0.57
74	6.78	0.61
88	7.12	0.66
103	7.39	0.65
118	7.78	0.67
136	8.05	0.65
155	8.28	0.65
176	8.49	0.65
200	8.62	0.65
225	8.66	0.66
252	8.61	0.67

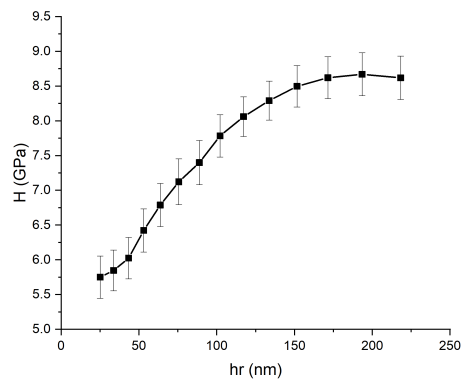


Figure 4-36 H for the successive layer of the surface for -0.9V test.

Figure 4-37 gives the modulus mapping for the very edge of the worn surface for the -0.9 V 4 N test. The area was carefully chosen to ensure that the height differences is minimum (here it is less than 200 nm). This height difference does not affect the accuracy of measured modulus. The aim of this test is to study the elastic properties of the tribolayer formed on the metallic worn surface. The figure clearly reveals that the complex modulus of this layer is far from that of the starting surface with a difference of more than 100 GPa. Nevertheless, the tribolayer does not show damping properties as the loss modulus is nearly the same everywhere.

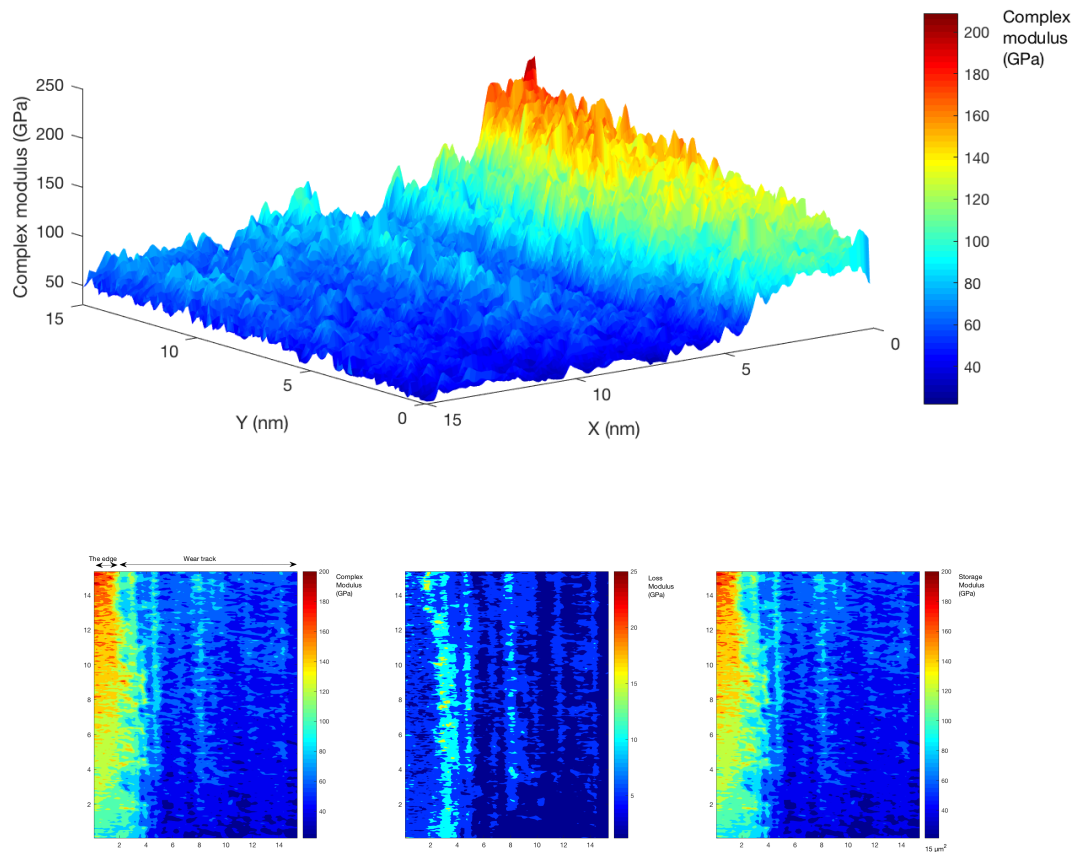


Figure 4-37 modulus mapping for the very edge of the wear track at -0.9V test.

4.2.3 Subsurface microstructure:

Figure 4-38 a, b, c and d show back scattered electron images from FIB cross sections of the subsurface taken longitudinally on the central line of worn surfaces in the middle of the wear track for 4 N load at -0.9 V, -0.7 V, OCP and 0 V tests respectively. The figure shows that the highest microstructural deformation was at cathodic potentials. Martensitic laths and relatively heavy deformation at the outermost subsurface can be seen at these

potentials. It is also clear that the worn surfaces at -0.9 V is covered by a relatively thick surface layer.

In contrast, the subsurface was only slightly damaged at the OCP. The examined subsurface microstructure confirms the important effect of corrosion on the mechanical deformation of the worn surfaces. A closer look at the subsurface microstructure of the worn surface at anodic potential (Figure 4-39) clearly shows the existence of martensitic laths and nano-twins.

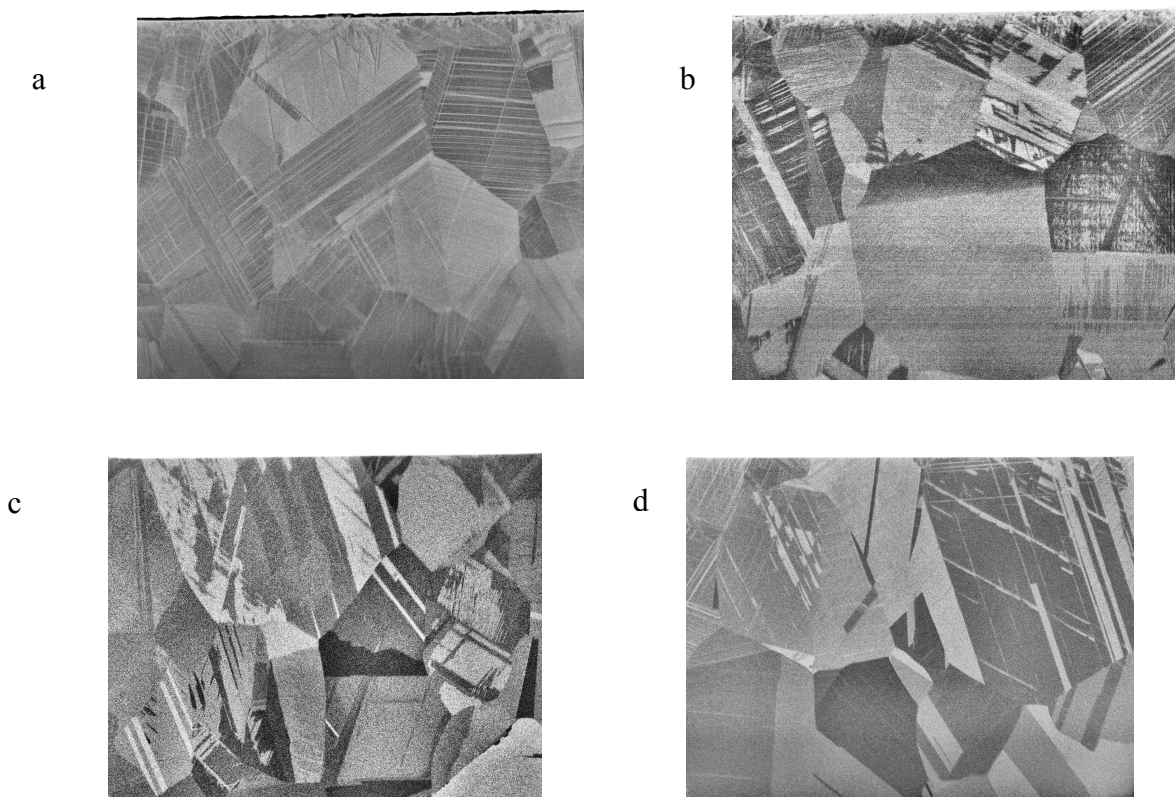


Figure 4-38 back scattered electron images from FIB cross sections (a) -0.9V , (b) -0.7V , (c) OCP, and (d) 0V . The magnification is $5000\times$. Taken by Dr Peng Zeng (Sorby centre, The university of Sheffield)

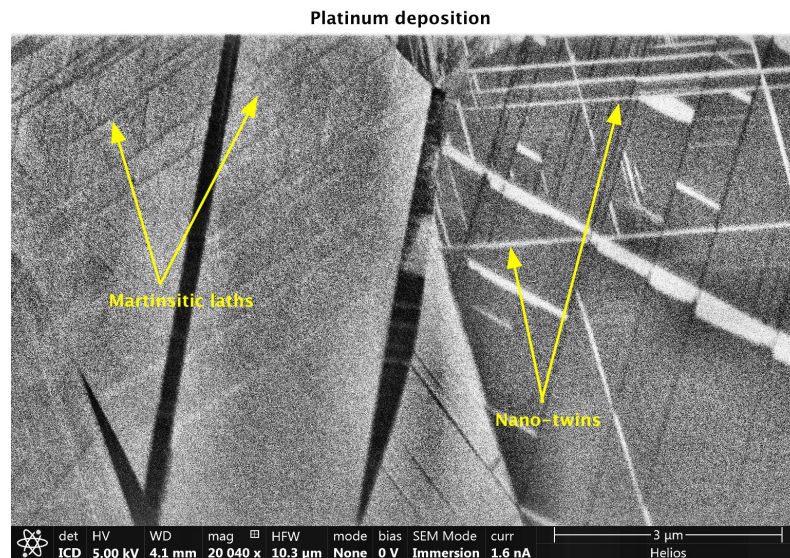


Figure 4-39 subsurface microstructure for 0V 4N worn surface. Taken by Dr Peng Zeng (Sorby centre, The university of Sheffield)

4.2.4 Sliding speed-potential effect:

Figure 4-40 shows the effect of increasing sliding speed on the sliding potential at 400 MPa, and 500 MPa initial main contact pressure. In both cases increasing sliding speed results in a reduction of sliding potential. In this work 1 GPa was chosen as the initial contact pressure in order to ensure entire removal of the protective oxide layer from the very beginning of the test at all tested sliding speeds.

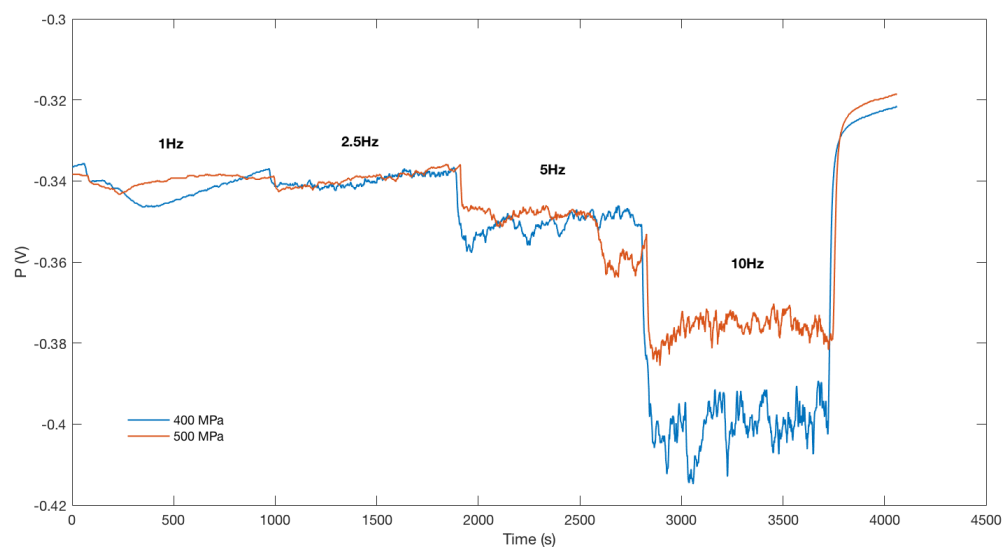


Figure 4-40 sliding speed effect on sliding potential at 400, and 500 MPa initial contact pressure

4.2.4.1 Tribological behaviour

The COF and current (or potential for OCP tests) versus time for all sliding speeds at cathodic, OCP and anodic potential are shown in Figure 4-41, Figure 4-42, and Figure 4-43 respectively. The sliding speed does not have an impact on the average COF at cathodic potential at all sliding speeds having the same value of about 0.13. However, the COF profile is a function of the sliding speed. At the intermediate speed, the cathodic current is quite noisy in comparison to slow sliding (1Hz), and with faster sliding (10 Hz). No change in cathodic current was seen after the rubbing had been stopped at slow and intermediate speeds. Nevertheless, a noticeable increase in cathodic current can be easily observed due to fast rubbing at 10 Hz sliding speed which is possibly because of the high speed resulted in significant stirring of the electrolyte. The specific wear rate K showed no change at the first three sliding speeds, but, increased up to about 1.5 times at 10 Hz (Table 4-13). Note that this increase in K comes concurrently with increasing cathodic current.

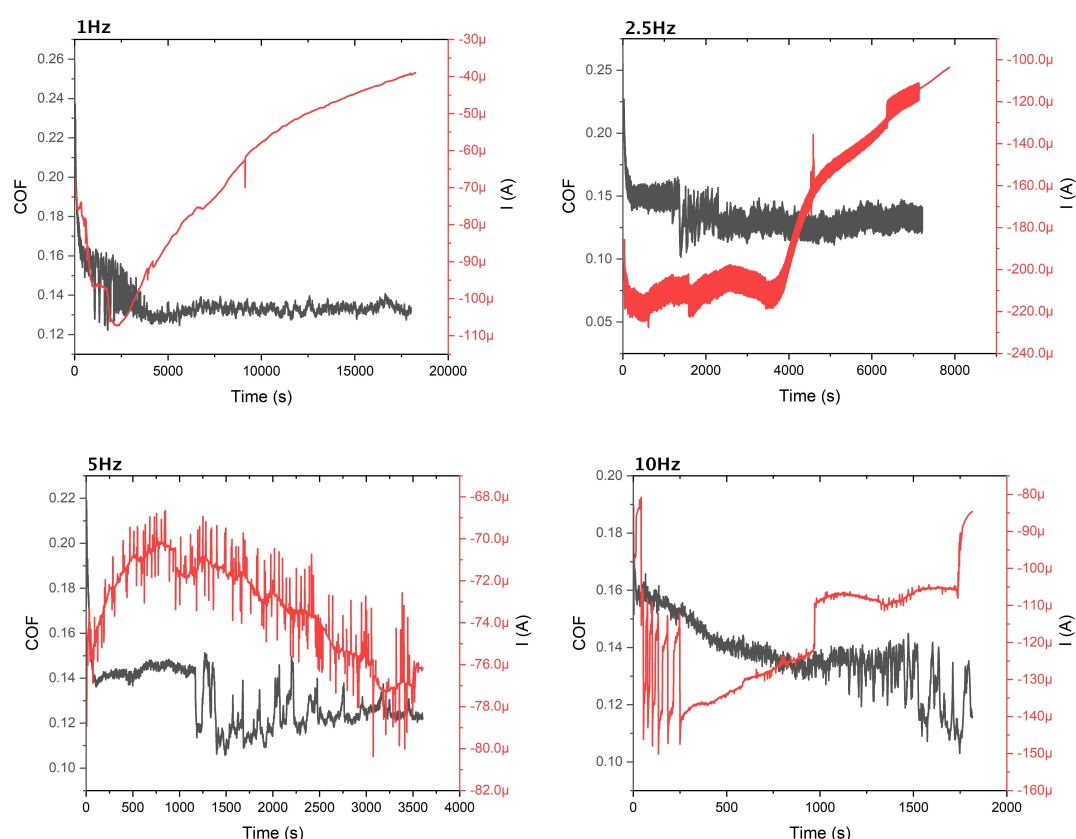


Figure 4-41 COF and the current versus time for all tested sliding speeds at cathodic potential

Figure 4-42 shows the COF and sliding potential against time for rubbing at the OCP. At sliding speeds of 1 Hz and 2.5 Hz, the sliding potential has totally been recovered to the OCP value within the first quarter of rubbing. Furthermore, the potential gets even nobler than the OCP at 1 Hz sliding speed. In contrast, at 5 Hz, and 10 Hz sliding speed, the OCP never recovered and no difference in sliding potential was observed between these two sliding speeds. The COF showed an increase with sliding distance at 5 and 10 Hz sliding speed, while, it followed the sliding potential at the other two sliding speeds. Before the transition recovery, the averaged COF was 0.24, and 0.21 for 1 Hz, and 2.5 Hz sliding speed respectively. After this transition it dropped to 0.168, and 0.174. Moreover, the COF was noisier at 2.5 Hz speed. The specific wear rate K , at 5 Hz, and 10 Hz sliding speed was double compared to that observed at 1 Hz, and 2.5 Hz, Figure 4-46 and Table 4-13.

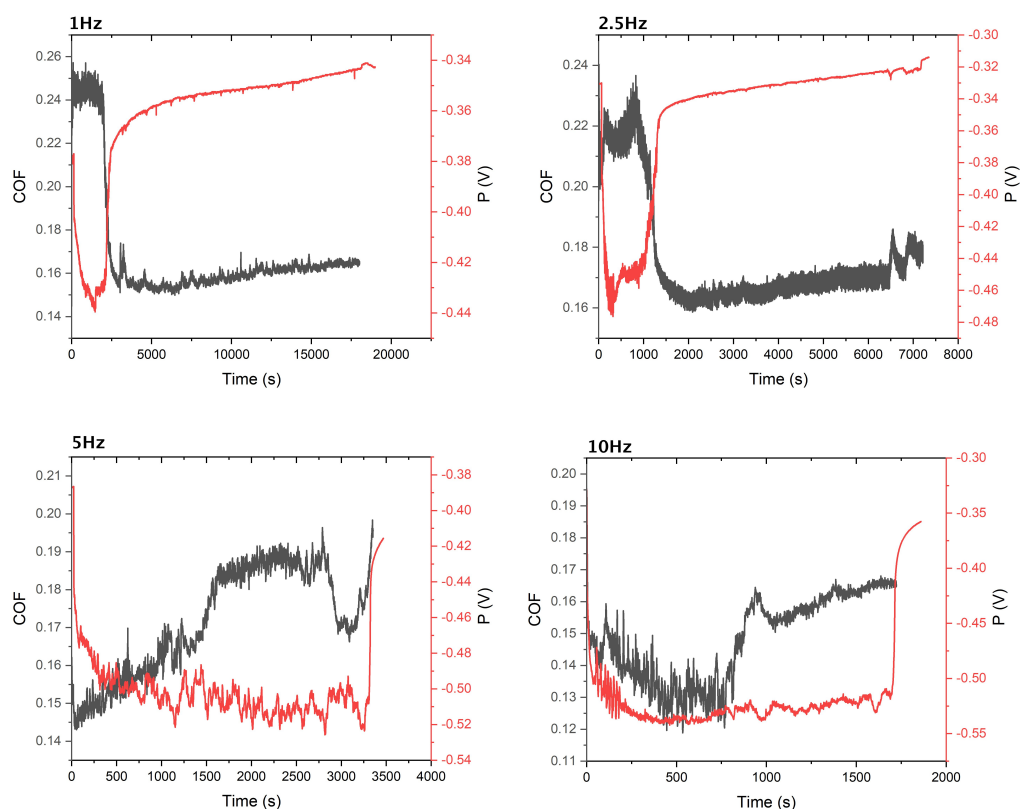


Figure 4-42 COF and sliding potential versus time for all tested sliding speeds at OCP tests

Anodically polarized surfaces generally showed as the same trend of sliding speed influence as at the OCP. Anodic current exhibited a sudden reduction within the first quarter of all tested sliding speeds (Figure 4-43). The tests at anodic potential were distinguished from the OCP in that the transition in anodic current occurred at all sliding

speeds. Again, the COF nicely follows this transition as it does at OCP. K shows a steady increase with sliding speed at the anodic potential (Figure 4-46).

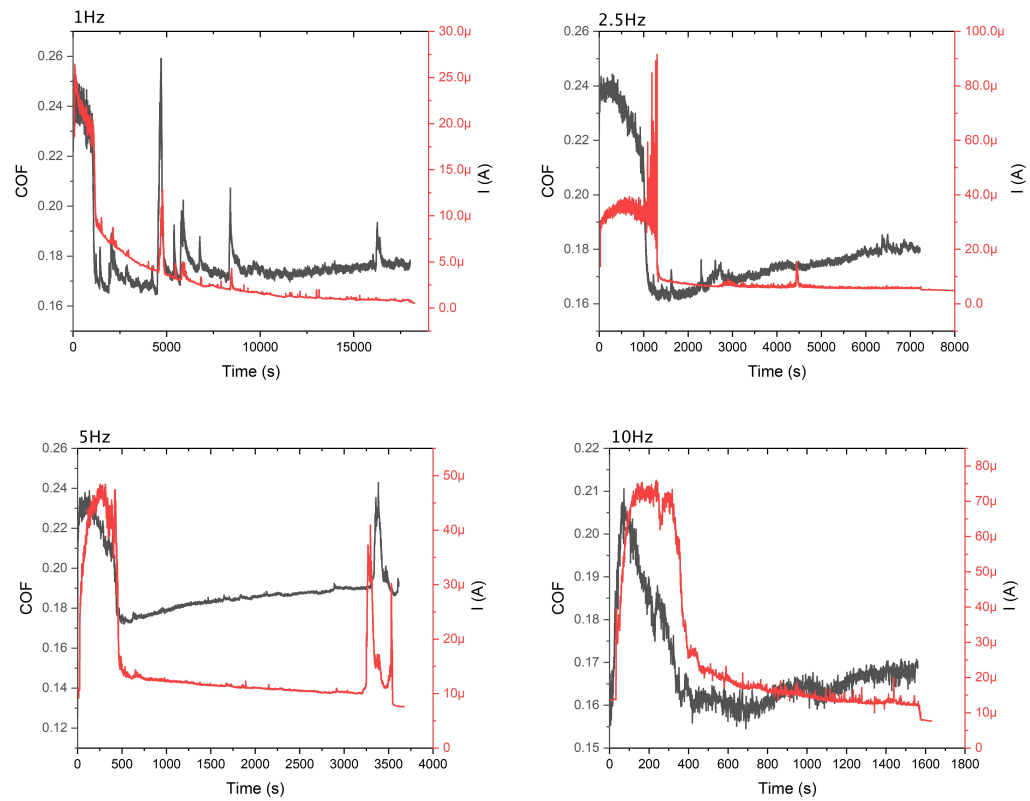


Figure 4-43 COF and anodic current versus time for all tested sliding speeds at anodic potential

Table 4-13 tribocorrosion tests results for sliding speed effect studying

Potential (V)	Sliding speed (Hz)	Sliding speed (mm/s)	COF before	COF after	K (mm ³ /N.m) ×10 ⁻⁶	SA (mm ²)	V _{total} (mm ³) ×10 ⁻⁴	V _{chem} (mm ³) ×10 ⁻⁴	V _{mech} (mm ³) ×10 ⁻⁴
-0.4 vs. OCP	1	4	0.134		1.11	0.27	3.18	----	3.18
	2.5	10	0.134		0.94	0.26	2.71	----	2.71
	5	20	0.131		0.89	0.24	2.58	----	2.58
	10	40	0.137		1.64	0.32	4.72	----	4.72
OCP	1	4	0.243	0.16	2.3	0.36	6.62	----	----
	2.5	10	0.224	0.17	2.27	0.37	6.55	----	----
	5	20	0.174		5.54	0.5	16	----	----
	10	40	0.15		5.45	0.51	15.7	----	----
0.3V vs. OCP	1	4	0.242	0.176	1.69	0.33	4.87	1.11	3.76
	2.5	10	0.235	0.152	3	0.4	8.67	7	1.66
	5	20	0.224	0.183	3.33	0.41	9.59	7.87	1.73
	10	40	0.197	0.162	4.8	0.48	13.8	13.2	0.66

The reproducibility of the data was good. An example is given in Figure 4-44 for two different tests at OCP and 1 Hz sliding speed.

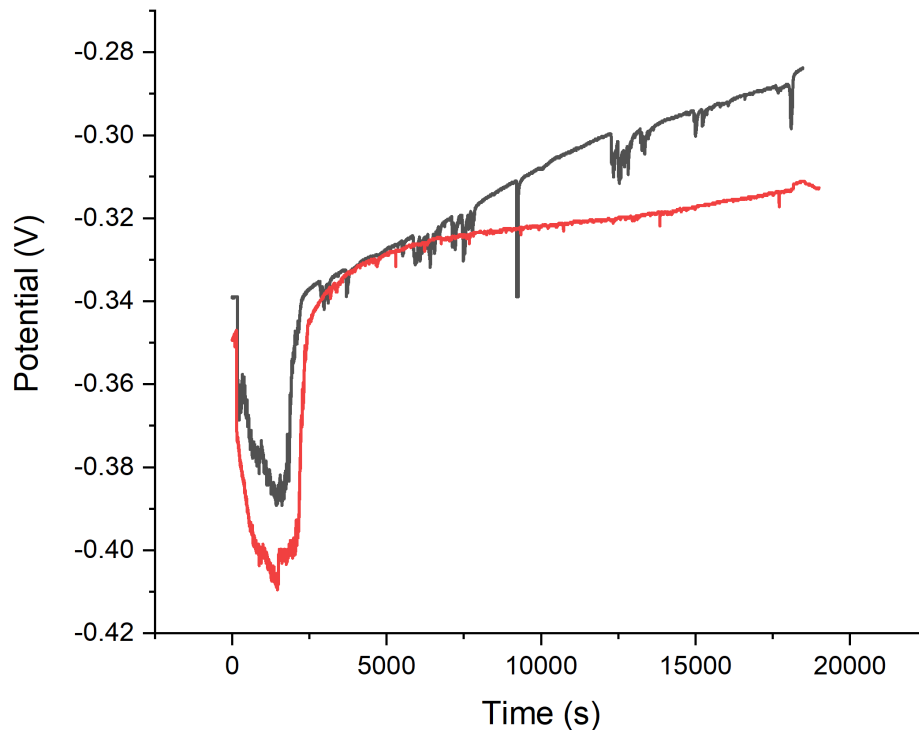


Figure 4-44 sliding potential for two different tests for 1 Hz sliding speed at OCP

Figure 4-45 shows the COF for all tested sliding speeds at cathodic, OC, and anodic potentials. The figure also shows COF before and after the transition in sliding potential or anodic current where it occurred in some tests. The COF was always the lowest at the cathodic potential for all tested sliding speeds. Repassivation with a relatively stable oxide layer on the worn surface, which can be clearly seen from the current drop down and sliding potential recovery, always reduced the COF. The issue will be discussed in detail in the discussion chapter.

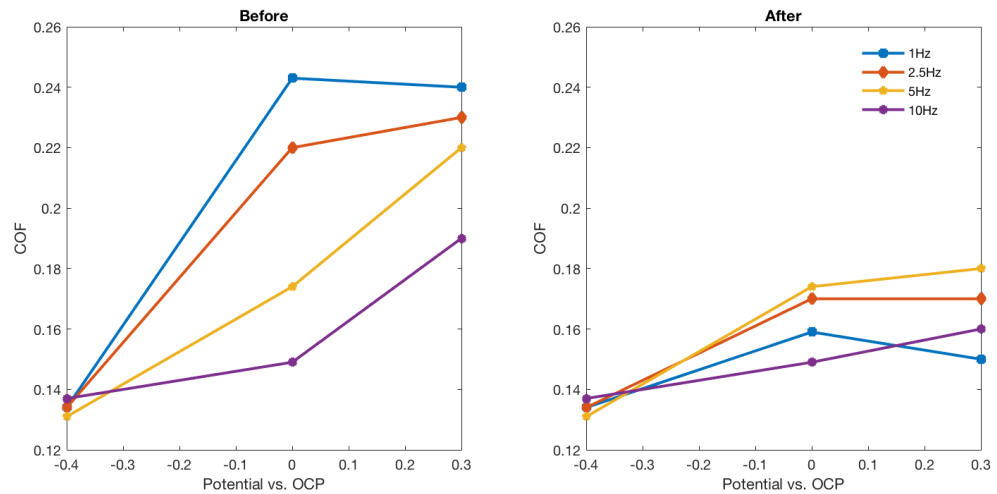


Figure 4-45 COF against potential before and after the transition in OCP or the anodic current

Figure 4-46 shows the specific wear rate K at the OCP for all potential condition. The OCP exhibited one transition in behavior at around $2.3 \times 10^{-6} \text{ mm}^3/\text{N.m}$ at 1 Hz, and 2.5 Hz which abruptly doubled at 5 Hz and 10 Hz. In contrast, K shows an approximately linear increase with sliding speed at the anodic potential. Apart from at 2.5 Hz, the anodic polarization of the surface reduced K . Sliding speed had no impact on K at cathodic potential. However, at 10 Hz and cathodic potential, K increased by 1.5 times.

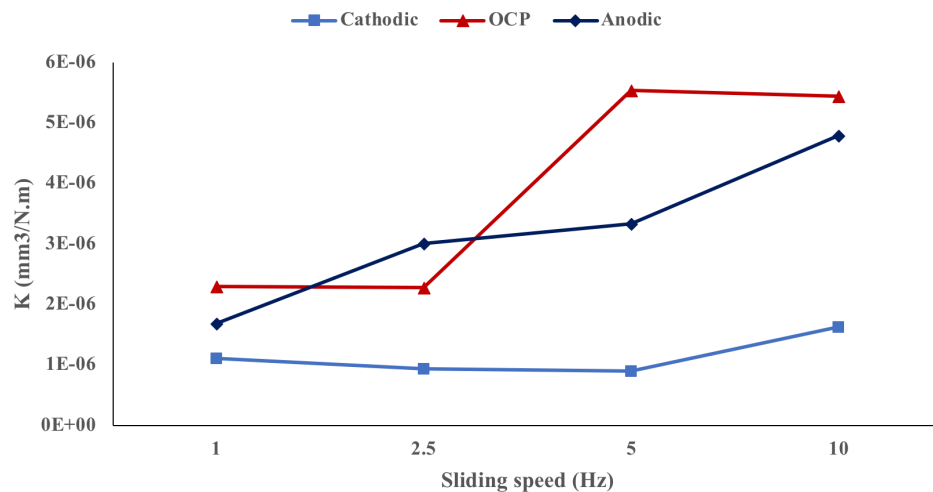


Figure 4-46 specific wear rate K at different potentials and sliding speeds

4.2.4.2 Tribocorrosion behaviour:

Table 4-14 and Figure 4-47 show the total material loss rate, T , the material loss rate due to the synergistic effect, S , the wear accelerated corrosion material loss rate, C_w , the

corrosion accelerated wear material loss rate, W_c , and the change in corrosion rate due to wear and the change in wear due to corrosion ΔC_w and ΔW_c respectively. The wear rate W_0 and corrosion rate C_0 without synergistic effect are also shown in the table.

The results of cathodic potential and OC potential have been interpreted depending on the synergistic approach [103], [118]. The mechanical related material loss rate (T , W_0 and W_c) exhibit continuous increasing with sliding speed. On the other hand, C_w shows one step jump at 5 Hz sliding speed. Note that this jump occurs alongside with the the removal of the protective oxide layer of the worn surfaces at 5 Hz and 10 Hz. At 1 Hz, the contribution of corrosion in tribocorrosion process was 44% which dropped to 19% at 2.5 Hz because of a linear increase in the mechanical part, while the corrosion rate remained the same at this range of sliding speeds. At 5 Hz, the corrosion contribution increased by 34% due to a step jump in C_w at this speed. C_w did not change at further sliding speeds, leading to a reduced contribution in the tribocorrosion process.

Table 4-14 penetration rates in tribocorrosion tests in mm/y.

Sliding speed (Hz)	W_0	T	S	C_w	W_c	ΔW_c	ΔC_w	C_w/T
1	2.06	3.19	1.11	1.39	1.80	-0.26	1.38	0.44
2.5	4.56	7.82	3.25	1.51	6.31	1.75	1.50	0.19
5	9.35	28.23	18.87	9.48	18.75	9.40	9.47	0.34
10	25.53	54.04	28.49	9.10	44.94	19.40	9.09	0.17

At anodic potential testing, a mechanistic approach was used [27]. To get an accurate V_{chem} , baselines were created and subtracted from the sliding current curves as shown in Figure 4-48. V_{chem} is the area under the curve. Figure 4-49 shows that the V_{chem} increases with sliding speeds at the expense of V_{mech} . This shows the rule of sliding speed on the dominant wear mechanism. Furthermore, V_{chem} versus number of sliding cycles is shown in Figure 4-50. The slope of the curve represents V_{chem} per cycle. It always significantly decreases after the current reduction event. V_{chem} per cycles before and after the change in anodic current for all speeds and anodic potentials are tabulated in Table 4-15 and shown in Figure 4-51.

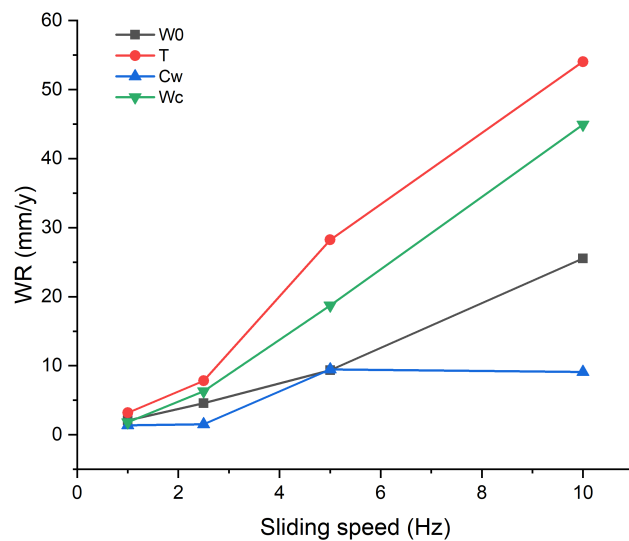


Figure 4-47 sliding speed effect on tribocorrosion material loss of CoCrMo ally in 25 vol.% BS in PBS at 37 °C

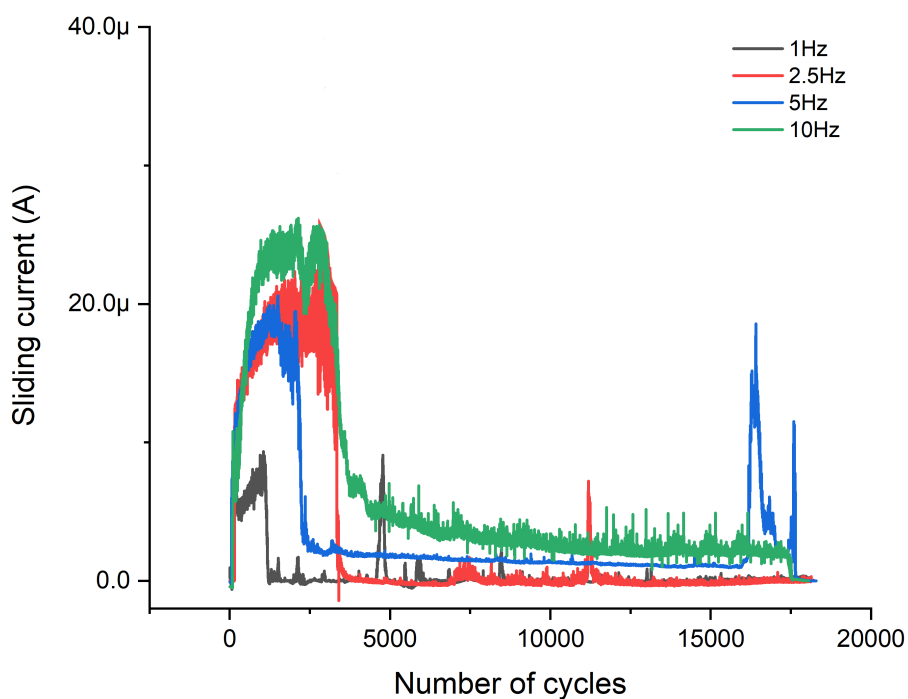


Figure 4-48 Sliding current after subtract baseline at anodic potential for CoCrMo ally in 25 vol.% BS in PBS at 37 °C

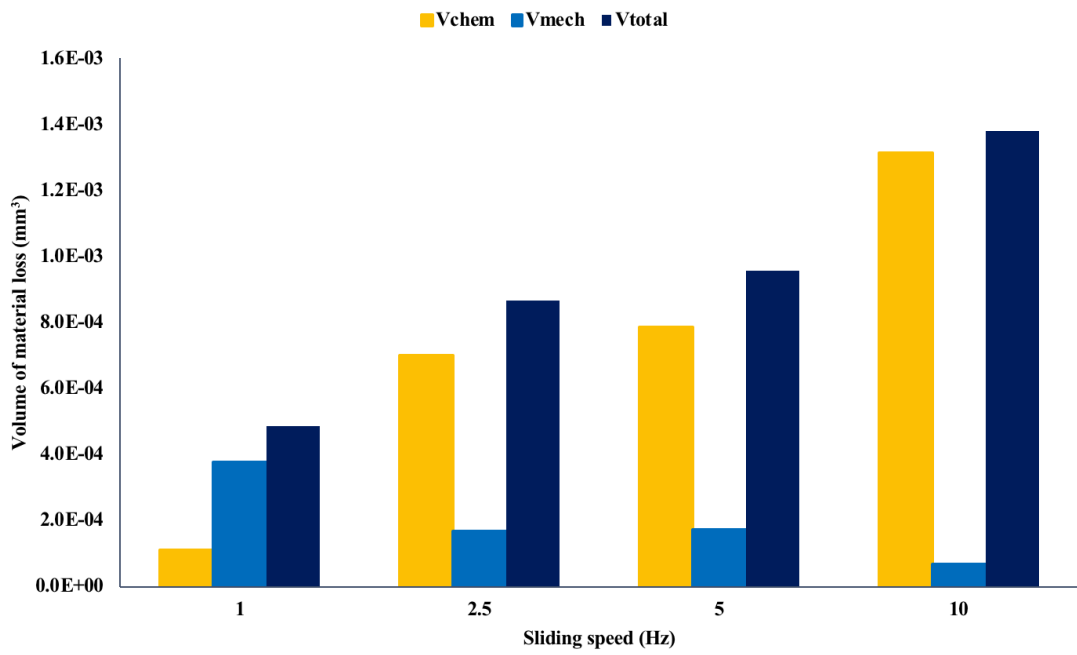


Figure 4-49 volume of material loss at anodic potential

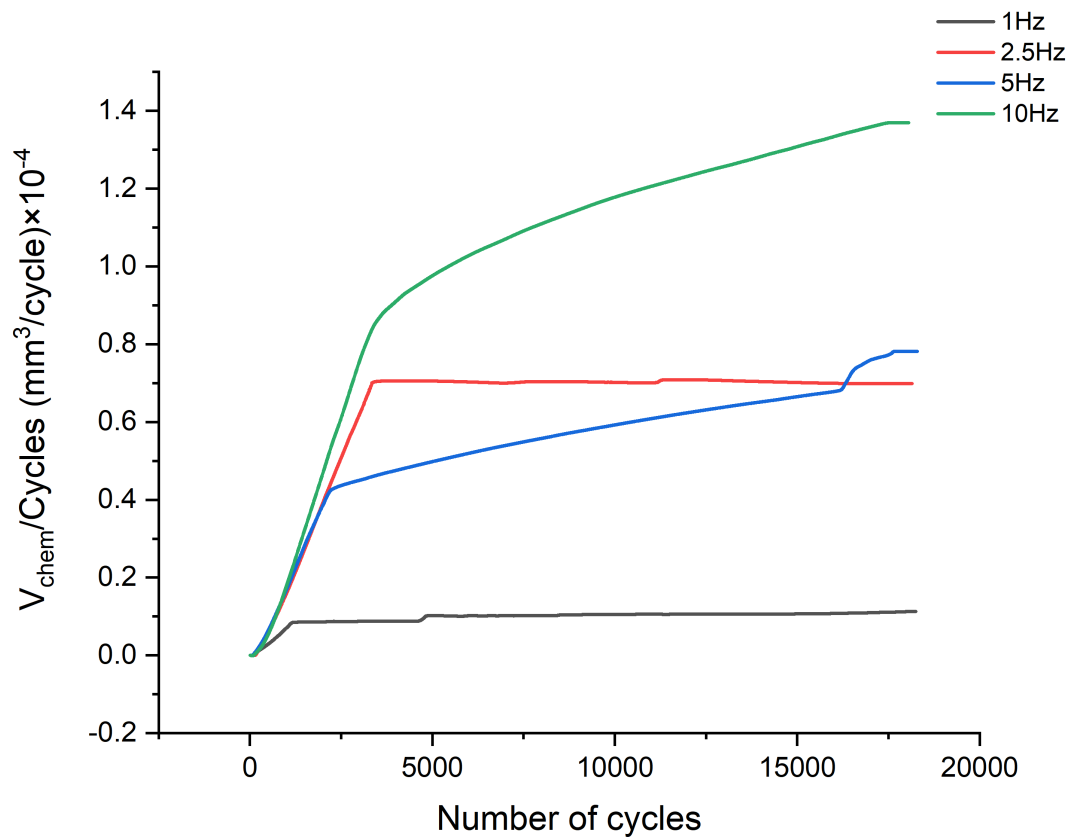


Figure 4-50 V_{chem} vs. number of cycles at anodic potential

Table 4-15 V_{chem} per cycle for anodic current at different sliding speeds. Calculated from the slope of the lines in Figure 4-50

Sliding speed	$V_{chem}/\text{cycle before}$ (mm^3/cycle) $\times 10^{-7}$	$V_{chem}/\text{cycle after}$ (mm^3/cycle) $\times 10^{-9}$
1	0.929	1.2
2.5	2.2	0.76
5	2.44	13.7
10	3	23

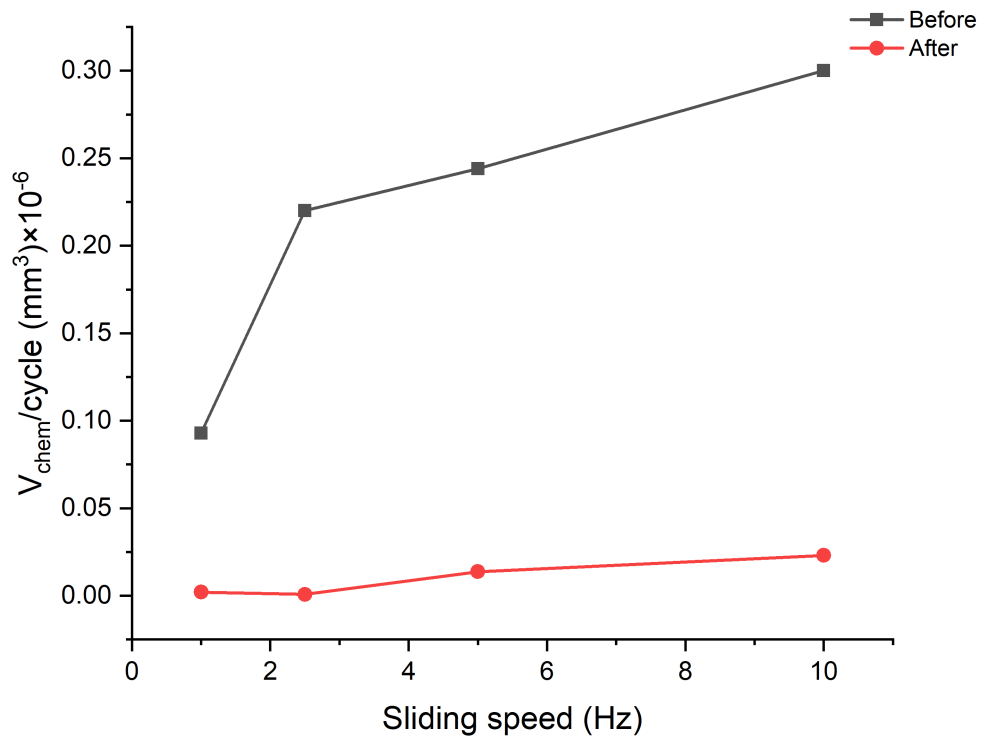


Figure 4-51 changing in V_{chem} after and before the drop down in current

4.2.4.3 Worn surfaces characterization:

Figure 4-52 shows the worn surfaces at cathodic potential with different sliding speeds. Abrasion appears to be the dominated wear mechanism as it is clear from the sharp edges grooves of the worn surfaces and the accumulation of wear debris at these sharp grooves. The sharp grooves might indicate a microcutting abrasion submechanism [49]. The sliding speed does not have a clear effect on surface morphology and wear mechanism at this potential. However, the severity of abrasion decreases with sliding speed. The surface roughness R_a for the worn surfaces at cathodic potential continuously decreases with sliding speed (Table 4-16).

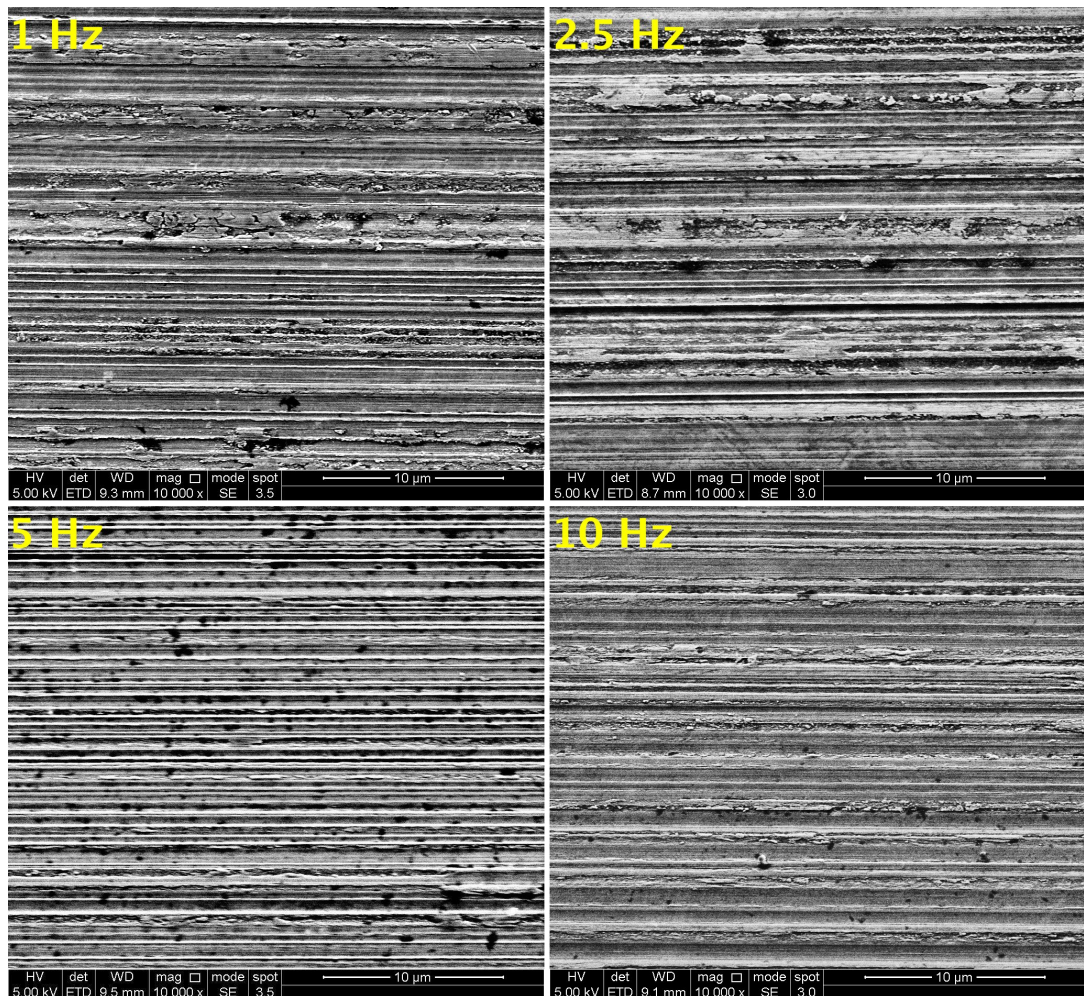


Figure 4-52 SEM images for worn surfaces at cathodic potential at different sliding speeds

Figure 4-53 is for OCP tests at different sliding speeds. Unlike cathodically polarized surfaces, sliding speed has a significant effect on the morphology of the worn surfaces and the wear mechanism. At 1 Hz sliding speed the worn surface was smooth with occasional grooves. This appearance suggests that corrosive wear was the dominant process. Mild grooving was more widespread at 2.5 Hz, but with occasional deeper grooves, indicating a small contribution from the abrasive wear mechanism. With further increase in sliding speed, the worn surface became mechanically deformed indicating the gradual increase in the mechanical wear with sliding speed. The worn surfaces at intermediate and fast sliding (5, and 10 Hz) were rougher than the ones at slower sliding (1, and 2.5 Hz). Note that the morphology of the worn surfaces where the sliding potential

exhibited a recovery (1, 2.5 Hz) were similar. Similarly, the worn surfaces where sliding potentials did not recover (5, and 10 Hz) had almost the same morphology.

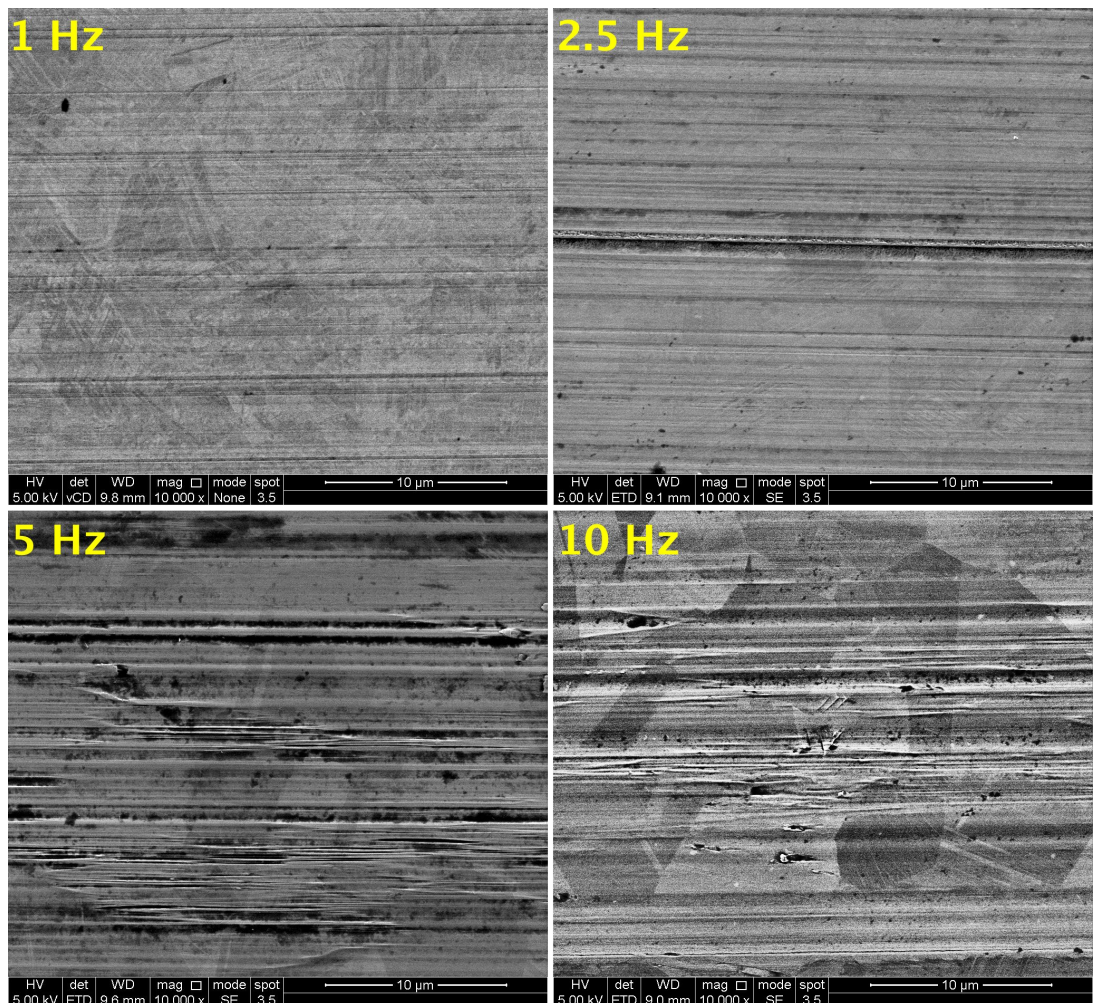


Figure 4-53 SEM images for worn surfaces at OCP at different sliding speeds

Figure 4-54 shows the worn surfaces at anodic potential at different sliding speeds. At 1, 2.5 and 5 Hz, SEM imaging shows a clear ploughing morphology for the worn surfaces. The morphology of the worn surface at 10 Hz sliding speed appeared smoother than at the other sliding speeds (Table 4-16). As with the cathodic potential, faster sliding brought about a smoother worn surfaces.

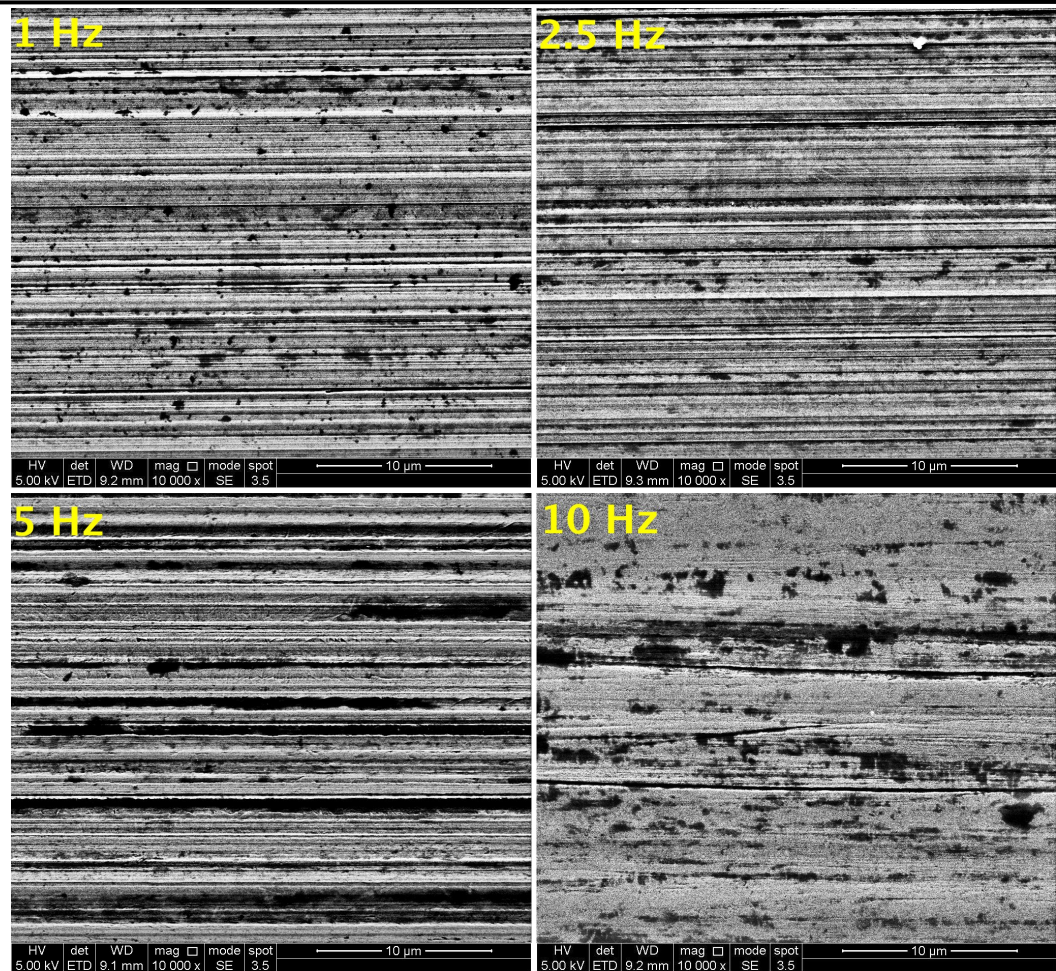


Figure 4-54 SEM images for worn surfaces at anodic potential at different sliding speeds

Table 4-16 the roughness of the worn surfaces

Potential (V)	Sliding speed (Hz)	R _a (nm)
-0.7	1	102
	2.5	74
	5	58
	10	43
OCP	1	61
	2.5	56
	5	95
	10	82
0	1	77
	2.5	72
	5	51
	10	47

The microstructure of the worn surfaces at OCP have been revealed via SEM images by enhancing the brightness and the contrast and shown in Figure 4-55. Slow sliding produced a deformed microstructure with many martensitic laths visible. In contrast, at 5 Hz and 10 Hz, the microstructure of worn surfaces looks much less deformed, which was almost free of martensitic laths. Some twins could be seen on these surfaces, but they were also present on the starting surface (Figure 4-1).

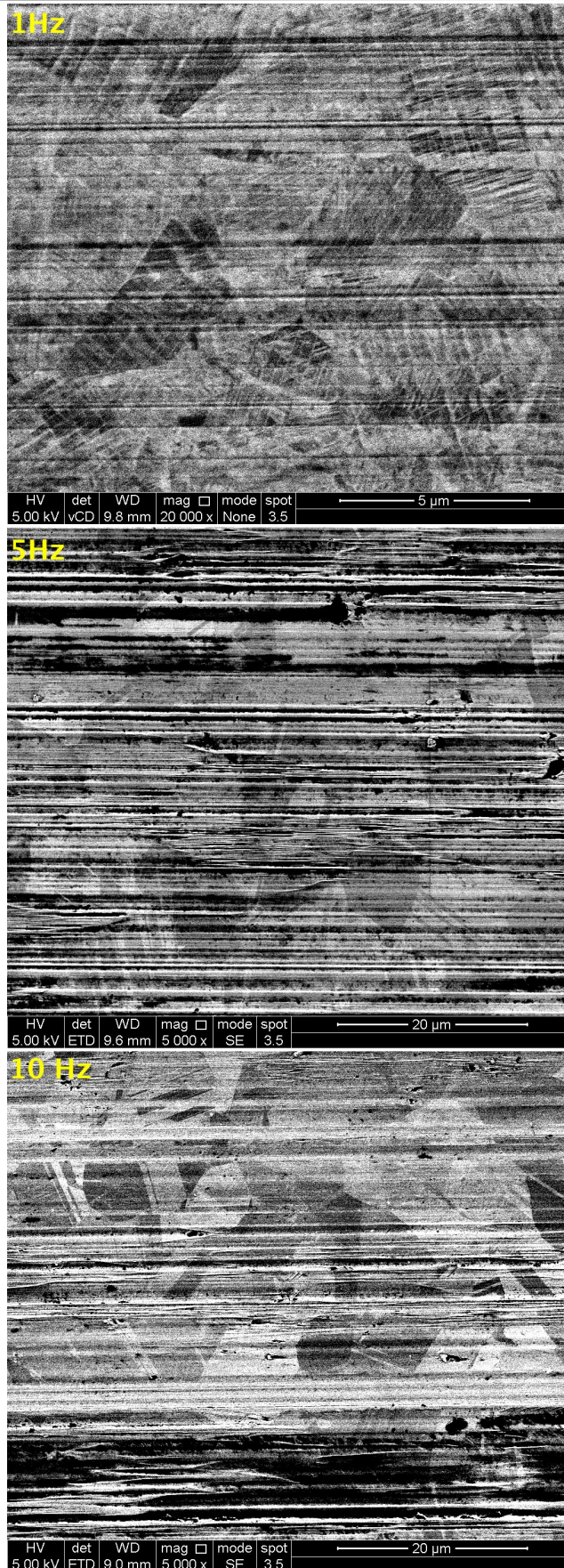


Figure 4-55 microstructure of the worn surfaces at OCP with different sliding speeds

4.2.4.4 The mechanical properties of the worn surfaces

Figure 4-56 and Table 4-17 show the mechanical properties of the worn surfaces measured by nanoindentation. The hardness of the worn surface at 1 Hz and cathodic potential was 6 GPa, which abruptly increased to more than 7.5 GPa for all faster sliding tests at this potential. At the OCP, the hardness continuously decreased with sliding speed from 8.69 GPa at 1 Hz sliding speed to 5.76 GPa at 10 Hz. The hardness of tests under anodic conditions exhibited more or less the same value of around 8 GPa.

Table 4-17 the mechanical properties as measured by Nanoindentation for the worn surfaces sor sliding speed effect studying

Potential	Speed (Hz)	E_r (GPa)	H (GPa)	h_f/h_{max}
Cathodic	1	158	6.07	0.72
	2.5	209	8.47	0.71
	5	153	7.64	0.71
	10	178	7.5	0.71
OCP	1	215	8.69	0.71
	2.5	172	7.15	0.72
	5	215	7	0.76
	10	210	5.76	0.8
Anodic	1	211	8.21	0.72
	2.5	209	7.75	0.73
	5	199	8.16	0.72
	10	181	7.48	0.71

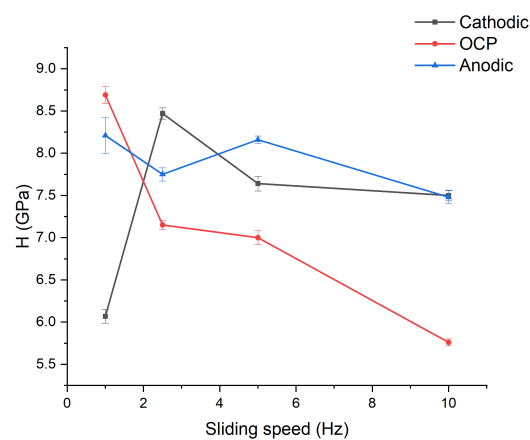


Figure 4-56 H for worn surfaces after different tested potentials and sliding speed

5 Discussion

5.1 Tribology properties:

Figure 4-2 shows that the specific wear rate decreased with load up to 60 N, but that an abrupt wear transition was observed between 60 and 80 N. Wear transitions have not been reported in the literature concerning the wear of CoCrMo alloys. Wimmer et al. [119] undertook the most detailed tests correlating the wear with the formation of an organic film. They found that there was an increase in wear with load up to approximately 32 N. The wear rate then exhibited a plateau with increasing load up to 48 N. For greater loads, wear rate again increased with load. They found that the plateau in wear rate coincided with the formation of an organic layer. This strongly suggested that the organic layer was beneficial in reducing wear rate. In the current study an organic layer was observed at 40 and 60 N, which exhibited the lowest specific wear rates. This result is therefore broadly in agreement with the work of Wimmer et al. and gives further confirmation that the formation of an organic layer reduces wear rate of CoCrMo alloys.

It is not clear why an organic film forms at some loads but not others. Wimmer et al. [119], [120] suggested that there were two possible reasons. Firstly, they suggested that low contacts stresses would not be sufficient to remove the protective oxide film. They also presented evidence that dissolution of molybdenum ions is important in the formation of these organic layers. Other researchers [121], [122] suggested that transition metals ions like cobalt, chromium, and nickel act as a catalyst to remove water and ammonia from albumin resulting a composition similar to typical hydrogenated carbon film which used to reduce friction. The presence of an oxide film would clearly limit the release of these ions. The removal of the oxide layer is possibly the most important factor for forming this carbonaceous layer. For instance, applying sufficient cathodic potential to totally remove the protective oxide layer favours the forming of this layer as will be discussed later in section 5.2.2. Other authors [123]–[127] who suggested the layer was organic material mixed with metal and oxide particles.

It is interesting to note that in the current work the formation of an organic layer coincided with the presence of a surface nanocrystalline layer. This implies low strain in the surface layer, allowing the oxide layer to be retained. It is worth exploring whether there was a correlation between surface microstructure and the formation of the organic film without

interference from the formation of an oxide layer. To do so the sliding speed was deliberately chosen to be very fast with a latent time of 50 ms (the time between each two successive contact events) and the lower limit of the load range was chosen to give a mean initial contact pressure much higher than the yield of the material (1150 MPa). For the tests at loads 5-20N, there was no uniform nanocrystalline layer covering the surface (Figure 4-10). This possibly implies that at these loads the surface structure of the metal was not conducive to the formation of a carbonaceous layer. The organic film formed at 40 and 60 N, and coincidentally, the worn surface at these loads was uniformly covered in a nanocrystalline layer. The evidence of significant surface strain suggests that the protective oxide film was continuously broken up by the contacting asperities. Thus, this would allow transition metal ion release, particularly Mo, that was evidently sufficient to promote the formation of this layer. Additionally, it is pointed out that the presence of proteins favours the formation of complexing agents for the dissolved metal ions such as iron, chromium, nickel and molybdenum which stimulates dissolution and suppresses oxide film formation [128]. The question then arises as to why an organic layer was not observed at 80N. However, the formation of such a thick (10-16 μm) nanocrystalline layer indicates that the deformation strains in the surface were very significant. This, coupled with the very high wear rate, would have led to continuous disruption of the surface, presumably making the adherence of an organic film impossible. In other words, the organic layer is formed and squeezed away under the effect of extreme contact pressure and high wear rate.

Figure 4-8 shows the mechanical properties of all the surfaces as a function of load, while Figure 4-9 shows how the hardness changed with depth below the surface. In general, the hardness and yield strength of the surface increased with the load used in the wear test. There was some correlation between the hardness and the presence and depth of the nanocrystalline layer. For example, the surface of the 80N test exhibited a thick nanocrystalline layer that contained the finest crystallite size. This had the greatest yield strength of all surfaces, as expected. However, the yield strength of the surface after testing at 20 N and 40 N were similar despite the different surface microstructures. At 20N, there was an intermittent poorly formed nanocrystalline layer, while at 40N, the surface was covered in a nanocrystalline layer which was between 60 and 130 nm thick. This suggests the hardness of the martensite/twinned region was similar to that of a thin

nanocrystalline layer, while a fully developed, thick nanocrystalline layer exhibits a much higher yield strength.

A key question is why a wear transition was observed between 60 and 80N. There has long been a debate as to whether a nanocrystalline surface layer is beneficial or detrimental to the wear resistance of CoCrMo alloys. In this case, the test at 80N exhibited the thickest nanocrystalline layer, with the finest crystallite size and the greatest yield strength, but at the same time, it suffered substantially greater wear than at the other loads. This strongly implies that the superior mechanical properties of the nanocrystalline layer do not impart superior wear resistance. This perhaps because of the interaction between the mechanical and the electrochemical aspects which cannot be avoided in any aqueous solution and will discuss in the next sections.

5.2 Tribocorrosion properties

5.2.1 Load effect:

The current work defines critical operation points at which wear accelerated corrosion C_w and corrosion accelerated wear W_c exhibited an abrupt increase. Figure 4-12 shows that at 4 N load, C_w jumps more than 5 times higher compared to previously tested load. This jump is consistent with sliding potential behaviour shown in Figure 4-13. At the load range up to 2 N, sliding potential showed a recovery to the OCP value indicating dropping in total corrosion contribution down. At this range of loads, the mechanical contribution in the total tribocorrosion process was not changed as the wear rate in the absence of corrosion W_0 was more or less equals to W_c (Table 4-4). At 4 N and further tested loads, the sliding potential of the worn surfaces did not recover to the OCP value under the effect of load. Interestingly, C_w shows a plateau at this range of loads. This defines a clear critical point before which C_w is relatively low, and beyond it, a significant increase in corrosion contribution was observed. Moreover, C_w showed a one-step jump that is consistent with the sliding potential behaviour (at least throughout the tested load range). SEM imaging for the worn surfaces at OCP at different loads (Figure 4-33) shows that the worn surface at 2 N load experienced high deformation as shown by the presence of twins and martensitic lathes. All these indicating that this deformation occurs because of having rebuilt oxide layer.

SEM imaging (Figure 4-33) also shows that at 4 and 8 N, the worn surface's microstructure was quite similar to that of the starting surface (Figure 4-1). However, at 16 N load, the worn surface was heavily deformed again with martensitic laths and twins are almost cover the entire worn surface. Total mechanical contribution W_c shows the same one-step jump behaviour as well at 8-16 N load range (Figure 4-12).

The load dependent microstructure and consequently the tribocorrosion behavior could be explained as follows:

- At low load range (up to 2 N), the worn surfaces fully (or almost) repassivated. The rebuilt surface oxide layer interferes with dislocations movement and activity during the successive contact events causing relatively higher deformed worn surfaces. The effect of the oxide film interfering with dislocation flow has been reported in the literature concerning 316L austenitic stainless steel [88], [129], 304L stainless steel [89] and CoCrMo alloy [130]. All these studies reported higher deformed microstructure for the worn surfaces at anodic potential in comparison to cathodic potential. They suggested that the oxide layer is the main mechanism attributed to this finding. In low stacking fault energy materials such as CoCrMo alloys, the dislocations move on discrete planes where neither cross slip nor climb occurs, resulting in blocking of dislocations that results in the formation of martensitic plates and twins (Figure 4-33)
- At intermediate loads of 4, and 8 N, the applied load was enough to maintain continuous removal of the surface oxide layer. Thus, there was no interference for dislocations annihilating at the surface. This leads to a microstructure of the worn surfaces (as it is shown in SEM imaging Figure 4-33) similar to that of the starting polished surface (Figure 4-1).
- At the high tested load of 16 N, the load was still enough to continuously remove the oxide layer. However, this high load caused high deformation at the worn surface with embedded martensitic lathes and twins (Figure 4-33). This microstructure work hardens the surface limiting further mechanical damage. Therefore, W_c exhibited a plateau at 8-16 N load range. It should be noted here that C_w showed a plateau at intermediate and high tested loads meaning it does not provide any further contribution in tribocorrosion process. Thus, the enhancement in specific wear rate K at 16 N load in comparison to 8 N load

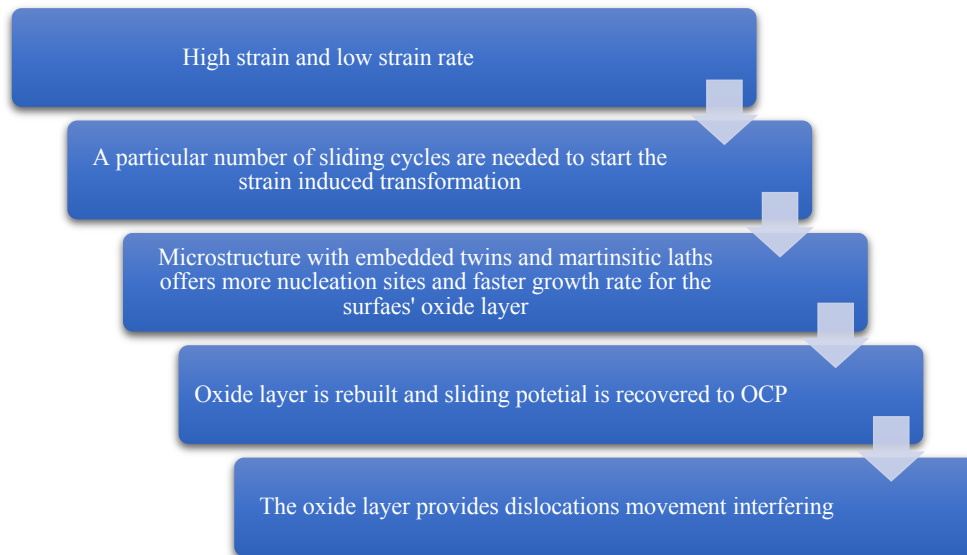
(Figure 4-21) can be pragmatically rationalized to this deformed microstructure and the improvement of the mechanical properties of the worn surface, which was demonstrated by nanoindentation testing (Figure 4-35). Despite a finer grain structure at the worn surface at 16 N load, which facilitate more oxide nucleation sites and faster growth rate for passive material [131]–[134], the mechanical effect of this high load in continuously removing the oxide layer at tested sliding speed still dominates (total removing of the oxide layer at each pass). Even with applying potential pulse equals to the OCP for 10 min in the middle of a separated test at the same load (Figure 4-14), the sliding potential could not have been recovered after this potential pulse. Applying such a pulse at 8 N load resulted in 80% recovery of the sliding potential.

It is interesting that a deformed microstructure was observed for the worn surfaces at both low and high load but not at intermediate loads. The deformation mechanism of each, however, is absolutely different as explained.

However, the important question remains as to why the oxide layer at up to 2 N load range is rebuilt abruptly after a particular number of sliding cycles. The answer of this question should be related to the microstructure changes and the effect of this on the ability of the worn surfaces to form oxide layer faster. It should be noted here that even at the lowest tested load (1N), the mean initial contact pressure is still high (650 MPa) with initial maximum contact pressure 1 GPa. It is also important to note that at the same reciprocating sliding speed, increasing the load caused an increase in both strain and strain rate. It has been pointed out in the literature that at high strains for low stacking fault energy material like austenitic stainless steel, the high strain rate sufficiently depresses strain induced martensitic transformation [135]–[137]. They attributed this to the temperature rise due to locally adiabatic heating. This might explain the differences in microstructure of the worn surfaces at 1, 2 N compared to ones at 4, and 8 N testing load. Higher load causes higher strain rate and consequently depressed strain induced transformation. The worn surfaces with less deformed microstructure cannot offer, compared to the starting surface, more nucleation sites and faster growth rate. For worn surfaces in the load range up to 2 N, the high strain and relatively low strain rate facilitate strain induced transformation which is needed to provide more nucleation sites and faster growth rate for the oxide layer. It is also possible that the local flash temperature works in the same direction that is it is higher at higher load. The microstructure of the worn

surface at 16 N, however, does have martensitic laths (Figure 4-33). The reason behind forming like this structure in spite of having high strain and strain rate (or even higher local flash temperature) is not understood for the authors. This needs further investigation.

The results suggest the following consequence for oxide rebuilding on the worn surfaces up to 2 N for CoCrMo alloy in 25 wt.% BS in PBS at 37°C and 5 Hz reciprocating speed at 2 mm stroke length:

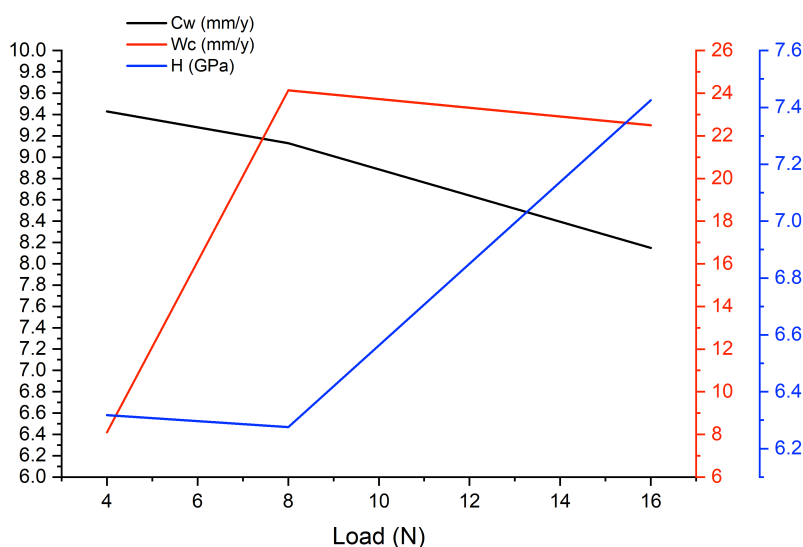


It has not been demonstrated that there is a direct relationship between the mechanical properties of the surface and the wear resistance. For example, Purcek et al [138] have shown that using equal-channel angular extrusion (ECAE) for pure titanium leads to substantially increase the mechanical properties with retaining adequate ductility, but has zero effect on wear resistance. Furthermore, negative effect of ultrafine grain on wear resistance has been observed [139], [140]. This has been attributed to tribochemical reaction and having synergistic effect between oxidative and abrasive wear which masks the superior enhance in mechanical properties. In this work, the tribological investigation of CoCrMo alloy in simulated body fluid (section 4.1) has also reported that having a thick layer nanocrystalline structure (Figure 4-10) and superior mechanical properties (Figure 4-8) for the worn surface did not protect the surface from the sharp wear transition (Figure 4-2). Some researchers [141], [142], however, have reported that using severe plastic deformation and consequently having much finer grain size resulting in improved wear resistance for commercially pure titanium [34] and Al-Cu alloy [35]. This discrepancy in wear resistance for ultrafine grains has been reviewed by Nong Gao et al.

[143]. They came to concluded that predicting the correlation between wear resistance and surface mechanical properties is restricted because of the complexity of the process. Nevertheless, they suggested a list of factors influence wear positively and negatively.

In the current work, the worn surface's microstructure at 16 N OCP tribocorrosion test (Figure 4-33) shows embedded martensitic laths and twins. The wear resistance of this microstructure significantly improved as it is shown in Figure 4-11. The results in section 4.1 ,on the other hand, showed a poor wear resistance for a microstructure that has a thick subsurface nanocrystalline layer, whereas, the worn surfaces with thin nanocrystalline or embedded martensitic laths, twins, and nanocrystalline exhibited a low specific wear rate. This strongly suggests that the microstructure with embedded harder phases, twins, and nanocrystalline might be quite beneficial for wear resistance at least for the material being tested.

Figure 5-1 shows the effect of the mechanical properties of the worn surface on C_w , and W_c at OCP. The enhancement in the hardness of the worn surface has a direct impact on the total mechanical contribution of tribocorrosion W_c . In contrast, it has a very little effect on electrochemical contribution C_w . The hardness of the worn surface did not change in the tested load range 4-8 N load, W_c rises by about three times. At 16 N load, martensitic laths formed at the worn surface and the hardness increased by about 1 GPa. This was very beneficial for the wear rate as it kept the mechanical penetration rate the same despite doubling the load. This finding might define a new insight of the relation between the mechanical properties and tribological behavior of CoCrMo alloys and possibly other similar metal alloys.

Figure 5-1 C_w, W_c, and H vs. load

5.2.2 load-potential effect:

The focus of interest of the orthopedic implants is having a local break down of the surface protective oxide layer or scratched surfaces. These events significantly re-polarize the surface. The severity of this polarization depends on the area that has lost its protective layer. Surprisingly, studying the tribological behaviour of CoCrMo over a range of cathodic and anodic potentials has not been reported in the literature. Therefore, the current work provides an extended study of the dual effect of load and potential on COF, wear behaviour, and microstructure and mechanical properties of the worn surfaces. The range of 4, 8, and 16 N load has been chosen to avoid the confusion caused by partial or total repassivation that occurs at OCP in the lower load range.

Figure 4-21 and Table 4-7 show the dependence of COF and specific wear rate K on working electrode potential. Generally, the COF at cathodically polarized surfaces is less than at the OCP and anodically polarized surfaces. At the cathodic potentials, COF gets lower with time almost for all tested loads. At the anodic potentials, it followed the anodic current. The dependence of COF on surface passivation (having an oxide covers the surface) was also observed for CoCrMo alloy [144] and for complex metallic alloys [145] immersed in PBS. In their work, the conditions were deliberately managed to maintain or remove the surface oxide layer by changing the time between each two successive contact events (latent time). They showed that the COF for the long latent time (6 s) is always

higher than that for the short one (0.5 s). Other research groups, have reported that the COF in the cathodic domain is higher than for anodic conditions for high carbon CoCrMo, low carbon CoCrMo, and 316L austenitic stainless steel in 50% serum [124], and for 316L austenitic stainless sliding against alumina ball in 0.5 M H₂SO₄ [88]. The current work, however, showed that the average COF at cathodic potential is always the lowest at the tested conditions. The work also defines COF for passivating (surfaces trying to re-passivate) and passivated (surface already got passivated) worn surfaces. The COF was always higher for passivating worn surfaces than that for passivated ones. The observation can be implicitly seen in Figure 4-18, Figure 4-19 and Figure 4-20 for anodic potentials where COF is higher at the beginning of the test (the current had not been stabilized yet). It went down and got more stable after a certain sliding time of sliding indicating that the system has reached a new thermodynamic equilibrium state. This new state of equilibrium reduced COF. It is quite challenging to compare the COF of this work with others because the COF is a system property sensitive to all system parameters like temperature, testing duration, solution chemistry, load, sliding status (bi or unidirectional, and successive contact event frequency), etc.

The specific wear rate *K* at OCP was higher than for the cathodically or anodically polarised surfaces (Figure 4-21) for all tested loads. Under cathodic conditions, partially or totally elimination of electrochemical contribution effectively reduces *K*. However, it is noticed that with decreasing cathodic potential, *K* increased. Electrochemical impedance spectroscopy EIS was employed to investigate the surface status at different cathodic potentials and shown in Figure 4-17. The polarization resistance of the surface increased with decreasing the applied cathodic potential (Table 4-6). This indicates that at -0.7 V and -0.5 V cathodic potential, the corrosion contribution was not entirely eliminated and the surface was not totally immune to corrosion. Thus, the formed galvanic couple between bare metal (wear scar) and the partially passive surface (the rest of the surface) was still working (but much less severely) at these cathodic potentials. However, the EIS results show that at -0.9 V the polarisation resistance for the surface significantly dropped down. In other words, the corrosion contribution is significantly reduced.

The cathodically polarised worn subsurfaces exhibit high deformation due to the dominance of the mechanical effect (Figure 4-38). Apparently, this is reflected on the mechanical properties of these surfaces. The hardness of them at 4 and 8 N was higher

than those at OCP and anodic potentials (Figure 4-35). Nevertheless, at 16 N load, the hardness of -0.5 V is the highest over the tested potential range. This was possibly because of the interfering of forming a carbonaceous layer on these surfaces.

Raman spectroscopy results (Figure 4-32) showed that the tribolayer deposited on the worn surfaces at cathodically polarized surfaces is a mixture of amorphous and nanocrystalline carbon [117]. The sp^2 bonding fraction has been determined from G peak position to be $> 80\%$ [117], [146]. The relative intensity (I_D/I_G) is correlated to the size of graphite cluster as follows [147], [148]:

$$\frac{I_D}{I_G} = \frac{C_\lambda}{L_a}$$

where C_λ is 4.4 nm for 515.5 nm laser, L_a is graphite domain size. With relative intensity 0.942, L_a was calculated to be 4.67 nm. Y. Liao et al [121] have investigated this layer by scratching it off by tungsten probe using a FIB and attached it to TEM grid. Their TEM work has detected short range ordered graphite material with few nanometers grain size and about 0.34 nm spacing. They used Raman spectroscopy to confirm their results and calculate the graphite domain size which reported as 4.5 nm.

The current work demonstrated a direct relation between the cathodic potential and the formation of tribolayer. At 4 N -0.9 V test, SEM image (Figure 4-29) revealed a thick carbonaceous layer (as recognized by Raman Figure 4-32) covered almost the entire worn surface. This relationship between the potential and the formation of the tribolayer has not been reported in the literature. Full mechanical characterisation of this layer has been done and shown in (Figure 4-36, and Figure 4-37). The same layer was observed at 8 and 16 N load at similar cathodic potential. Nevertheless, it has different morphology (Figure 4-30, and Figure 4-31). The formation of this layer affected the mechanical properties of the worn surfaces. For instance, the hardness of 4 N -0.9V is less than at -0.7V at the same load. At 16 N -0.9V (Figure 4-31), the worn surface was smeared by a darker color. These dark areas were examined by Raman microscopy and found to be a carbonaceous material. The hardness of these worn surfaces is less than that at the rest of cathodic potentials at the same load and the same cathodic potential at less loads at which these dark areas were not observed. Fischer [48] has pointed out that mechanical mixing can occur in the outermost layer of both laboratory and retrieval CoCrMo alloys leading to the formation of a metallo-organic nanostructure composite. Namus et al [113] have

reported that at very high load at OCP, the carbonaceous layer on the worn surfaces can be detected by Raman spectroscopy but cannot be seen by using SEM. This might be the case at the high load and high cathodic potential used here. The high load worked concurrently with sufficient cathodic potential to form tribolayer and mix it with worn surface material. The mechanical properties of like this composite is obviously less than that for the deformed metallic surface.

The enhancement in K of anodically polarized surfaces compared to surfaces tested at OCP was quite noticeable. For example, the surface anodically polarized at 8 N load had reduced K by about 50%. This clearly shows the rule of rebuilt oxide layer on the worn surfaces. Figure 4-34 reveals the deformed microstructure of the anodically polarised worn surfaces at 4 and 8 N load. The mechanism of this deformation is possibly the dislocation movement interfering by the rebuilt oxide layer that explained earlier. The influence of increasing anodic potential on the chemically and mechanically lost volume is manifested more clearly at higher load as shown in Figure 4-23. The results show an obvious load-potential interaction (Figure 4-24 and Figure 4-25). For instance, at 8 N load, increasing anodic potential led to increase in V_{chem} , while, at 16 N load the opposite occurred

The microstructure of the worn surfaces at anodic potentials at 16 N load could not have been revealed using SEM imaging perhaps because of the high deformation. Note that the two earlier explain mechanisms might work together at this load and potentials.

The effect of forming a galvanic coupling at OCP, cathodic, and anodic potentials is schematically illustrated in Figure 5-2. Polarizing the surface cathodically reduces the galvanic coupling effect significantly and eventually it totally removes this effect. At low tested load and anodic potential, rebuilding an oxide layer on the worn surfaces mitigates the galvanic effect.

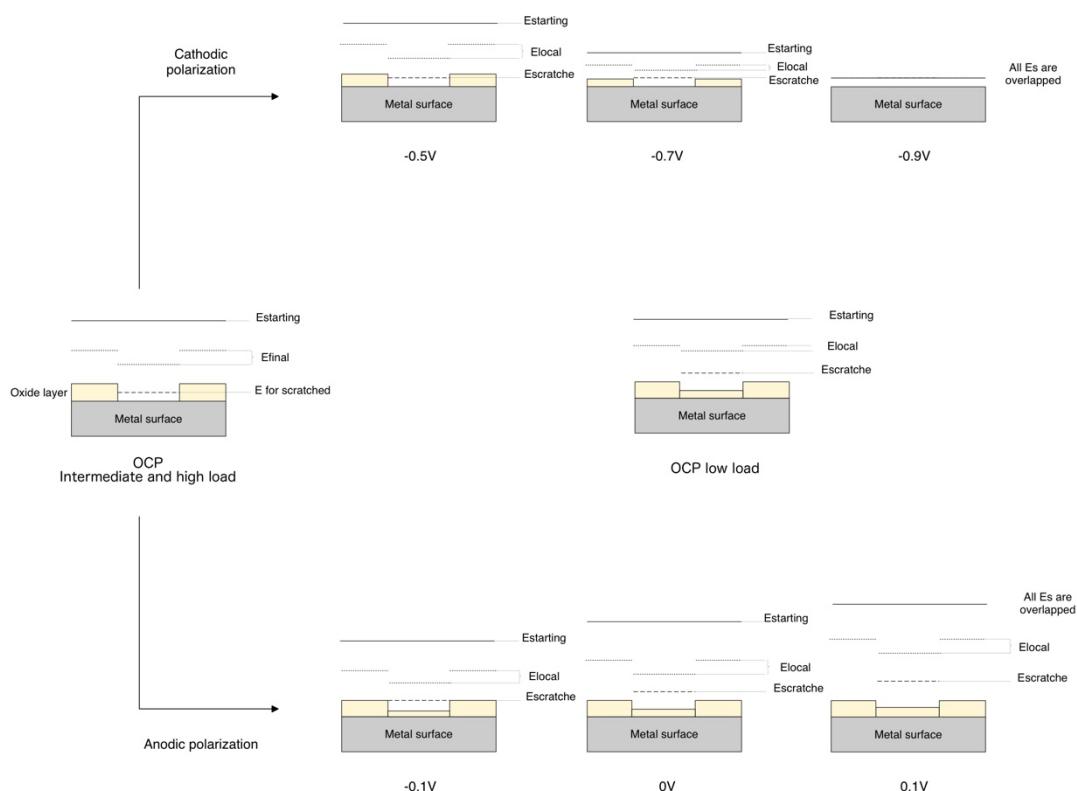


Figure 5-2 schematic diagram illustrates the impact of forming a galvanic couple at different potentials

5.2.3 Sliding speed-potential effect:

It has been shown in this work that the sliding speed has a significant effect of both mechanical and electrochemical material loss of CoCrMo biomedical grade alloy in simulated physiological body fluid. At low sliding speeds OCP and tested anodic potential, the material exhibited an electrochemical transition which has a significant effect on the mechanical properties and microstructure of the worn surfaces and consequently on tribological behaviour. The COF exhibited a noticeable decrease after this electrochemical transition (Figure 4-42 and Figure 4-43). The dependence of COF on surface passivation (having oxide covers the surface) was discussed earlier in section 5.2.2. It is again noticed that COF is defined for passivating (surfaces try to repassivate) and passivated (surface already got passivated) worn surfaces. The COF was always higher for passivating worn surfaces than ones for passivated ones. The observation can be clearly seen in Figure 4-45 for OCP and anodic potentials domain where COF is higher at the beginning of the test (the sliding potential or current has not been stabilized). They

reduce and become more stable after a certain time of sliding indicating that the system has reached a new thermodynamic equilibrium state. This new state of equilibrium reduces COF.

As far as the author is aware, the effect of sliding speed on the material loss (Figure 4-47) has not been studied well in the literature. The mechanical related material loss rate (W_0 and W_c) at OCP significantly increased with sliding speed. Electrochemical material loss, on the other hand, showed a one step jump behaviour which occurred simultaneously with having or not a drop down in potential, that is C_w is less than 1.5 mm/y when this drop down occurred and transitions to about 9 times higher when this event occurred. It has been pointed out that at high strain for low stacking fault energy material like austenitic stainless steel, the high strain rate sufficiently depresses strain induced martensitic transformation [135]–[137]. They attributed this to the temperature rise up due to adiabatic heating which is significant enough to depress this transformation. SEM imaging for worn surface at OCP tests and slow sliding (Figure 4-55) shows crossed martensitic laths cover the entire worn surface, while the worn surfaces of intermediate and fast sliding (5 and 10 Hz) were almost free of martensitic laths. The hardness of the slow sliding worn surfaces was much higher than ones of fast sliding (Figure 4-56). All this might indicate that for the material and tested conditions, the strain rate plays an important role that is low strain rate enhanced strain induced martensitic transformation. It is also possible (but not confirmed) that the local flash temperature works in the same way that is higher temperature at fast sliding depress SIT. The high density of martensitic laths on the worn surfaces at slow sliding speed facilitates more oxide nucleation sites and faster growth rate for the oxide film [131]–[134]. Thus, these worn surfaces have fully (or almost) repassivated which effectively protects the surfaces from further wear.

One of the driving force for electrochemical contribution in tribocorrosion at OCP is the formation of a galvanic couple between the wear scar and the rest of the surface. This obviously has a limit that is C_w has not changed at 5 and 10 Hz. Note that the surface area of the wear scar at these two sliding speeds is the same (Table 4-13). Note also that at 1, and 2.5 Hz sliding speed, the surface area of the wear scare remained the same. This is not the case at anodic potential because the driving force here is the external applied anodic potential. V_{chem} continuously increased with sliding speed (latent time decreases). At 1 Hz sliding speed, the latent time was enough for the oxide layer to be rebuilt. This freshly rebuilt oxide might be removed in the next contact event. It should be noted that

according to Faraday's law, V_{chem} refers to the flowing current. The removing of already rebuilt oxide is a mechanical action. Thus, V_{mech} at slow sliding is higher than that at faster sliding speeds (Figure 4-50). Moreover, the material exhibited current drop down at all tested sliding speeds (Figure 4-48). This had a direct effect on the electrochemical contribution throughout the tests (Figure 4-51). The current flow increased with sliding speed. Nevertheless, this increase was more significant before the current drop down in term of amount and time at which the drop down occurred. The current drop down can be attributed to the same reason of potential recovery at OCP tests. The decreasing in the $V_{\text{chem}}/\text{cycle}$ at 1, and 2.5 Hz to very low value (1.2×10^{-9} and 0.76×10^{-9} mm³/cycle respectively) after current drop down apparently means that the oxide layer was almost totally rebuilt. This also means that V_{mech} was decreased because if there was a mechanical abrasion, it would remove the oxide layer first. The dependence of $V_{\text{chem}}/\text{cycle}$ on the sliding speed after the current drop down might be explain in the light of reduction of strain induced martensitic transformation mechanism which was explained earlier.

M. Stemp et al [149] and Gil and Muñoz [150] have studied the sliding velocity effect at anodic potential for stainless steel in sulphuric acid and high carbon CoCrMo alloy in different simulated body fluids respectively. They have shown that the charge per stroke is independent on frequency. They rationalized this to the rapid electrochemical kinetics of the system. In the current work, however, a clear dependence of flow anodic current on the sliding speed can be seen in Figure 4-48. Nevertheless, the sliding speed that they used and consequently the latent time falls within the slow sliding domain that used in this work.

Further analysis for the effect of sliding speed on the mechanical and electrochemical wear and the relationship with the mechanical properties of the worn surfaces has been shown in Figure 5-3. At OCP, the enhancement in the worn surface hardness has zero effect on total corrosion contribution C_w . In contrast, a relationship between the worn surface hardness and the total mechanical contribution W_c can be clearly seen for softer worn surfaces where mechanical wear is easier. On the other hand, at anodic potential, this relationship does not exist. This is because the interference of the rebuilt oxide film which significantly affects both V_{chem} and V_{mech} as explained previously.

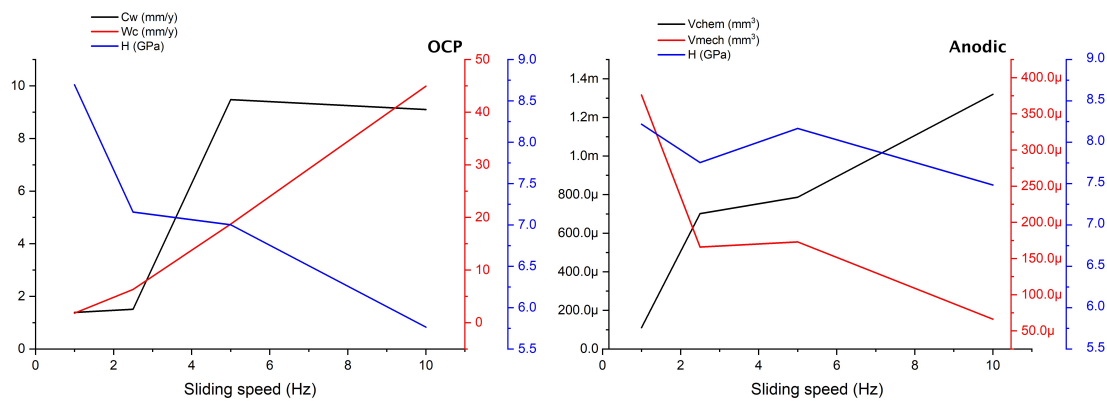


Figure 5-3 H, mechanical wear, and electrochemical wear vs. sliding speed at OCP (the left hand figure), V_{chem} and V_{mech} vs. sliding speeds at anodic potential (the right hand figure)

6 Conclusions

6.1 Tribological study

1. The work has defined a range of loads where the specific wear rate was the lowest (40-60 N) which associated to the formation of the pretentious layer which clearly indicated the beneficial effect of the formation of this layer. At 60 N the wear rate was the lowest of all that corresponded to the formation of a surface proteinaceous layer and extensive surface deformation that resulted in a uniform nanocrystalline layer which was 3–5 μm in depth.
2. At higher load, 80 N, a sharp wear transition was observed. A thicker nanocrystalline layer, of 10 and 16 μm depth, was shown by using subsurface cross section imaging. No proteinaceous layer could be detected by SEM imaging and Raman spectroscopy. All these indicate the beneficial effect of the carbonaceous layer and the formation of nanocrystalline surface structure.
3. The formation of a nanocrystalline surface structure was a function of load whereby at 20 N load; it was thin intermitted changed to continuous thin layer at 40 N. The thickness of this layer significantly increased at higher loads to be more than 10 μm at the highest tested load.
4. The mechanical properties measured by nanoindentation were a function of depth and largely scaled with the load (and therefore with surface microstructural changes). At the highest tested load, the hardness and the yield strength were approximately twice that of the starting surface. However, there was no obvious correlation between the mechanical properties of the surface and the wear rate. The lowest specific wear rate at 60 N was associated with a nanocrystalline layer that had a yield strength of 1058 MPa, while the highest specific wear rate was associated with a thick nanocrystalline layer that exhibited a yield strength of 1087 MPa, which was similar to that observed at 60 N.

6.2 Tribocorrosion study

6.2.1 Load effect

1. The specific wear rate, K , at -0.9 V cathodic potential continuously increased with load obeying Archard's equation. The COF at this potential was not sensitive to

load. In contrast, at the OCP, K exhibited an increase with the load up to 8 N followed by an abrupt decrease associated with the formation of martensitic laths and twins which occurred in the entire worn surface.

2. The mechanical and chemical material loss were successfully defined by using the synergistic tribocorrosion approach and galvanic tribocorrosion model. At low tested load, sliding potentials showed a recovery to its OCP after some time of sliding. At 4 N and further loads, this recovery of sliding potential did not occur. C_w was all the same at the range of load that did not have such a sliding potential recovery. Furthermore, W_c exhibited a plateau at 8 N and 16 N which can be pragmatically attributed to the surface microstructure changes that 16 N load worn surface experienced.
3. It was also shown that applying a potential pulse at 8 N load helped the worn surface significantly to partially re-passivated which is almost certainly important in improving our understanding of the tribocorrosion behavior of the passive metals and alloys.
4. The work successfully separated the mechanical and electrochemical contributions in tribocorrosion testing and found that there is a relationship between the mechanical wear and the mechanical properties of the surfaces at least in the testing system. However, this correlation might be shielded under the strong synergistic effect of corrosion and wear. Thus, a great deal of care should be taken, and many experiments must be conducted on different materials and systems before believing this correlation.

6.2.2 Load potential dual effect:

1. Not all cathodic potentials were able to totally damage the protective nature of the oxide layer of CoCrMo alloys. This had a major effect on the tribocorrosion behaviour of these alloys. The specific wear rate increased with decreasing the cathodic potential toward the OCP.
2. The work has defined a strong correlation between load and electrode potential on one hand and specific wear rate K on the other hand. At the tested loads, applying either cathodic or anodic potential led to a decrease in K . However, this effect significantly depended on the load.
3. COF was always the highest at the anodic electrode potentials and the lowest at cathodic electrode potentials for all tested loads.

4. The work suggested a close relationship between COF and the thermodynamic stability of the surface. At all tested anodic potentials and loads, when the current decreased the COF exhibited lower value. Therefore, a new definition of the worn surfaces in tribocorrosion is suggested whereby repassivating surfaces (the surfaces that try to repassivate) have higher COF values, and passivated surfaces (the surfaces already got passivated) have lower COF values.
5. The presence of relatively thick carbonaceous layer on the worn surfaces was only observed at -0.9 V electrode potential for all tested load. This was probably because this is the only potential that was able to almost entirely remove the oxide layer and thus helped in releasing ions that are needed to form this layer according to the mechanism suggested and widely accepted in the literature.
6. The imaging of the worn surface microstructure at anodic electrode potentials clearly showed the presence of twins and martensitic laths that covered the whole worn surface which might be the reason behind having lower values of K at these potentials.
7. The worn surfaces at cathodic potential exhibited higher nanoindentation hardness followed by those tested at anodic potential. The lowest hardness was observed at OCP. The only exception to this was at 8 N where the hardness at OCP was higher or equal to that at anodic electrode potentials.
8. Subsurface imaging showed highly deformed microstructure at cathodic potentials. At anodic potential, the deformation was less, but nanotwins and martensitic laths were seen. OCP worn surface microstructure was quite similar to that of the starting surfaces. This was consistence with the mechanical properties of these surfaces.

6.2.3 Sliding speed effect:

1. The mechanical elements of wear in tribocorrosion (W_0 , and W_c), and the wear accelerated corrosion C_w showed (in the testing system) sliding speed dependence. W_0 , and W_c exhibited continuous increase with sliding speed. Whereas, C_w showed one step jump behaviour which was associated with having or not sliding potential recovery. In another words, whereby the worn surface cannot repassivate, C_w is high.
2. At the tested anodic potential, the current flowing significantly increased with sliding speed in such a way that at fast sliding V_{chem} was more than V_{mech} . The

flowing current started high and then exhibited a sudden drop down. However, this transition in current was dependent on the sliding speed. The time needed for this transition, and the amount of current flowing after and before this transition showed a strong dependence on sliding speed.

3. Further confirmation of the strong relationship between COF and the thermodynamic stability of the system has been shown throughout the results of this work. At OCP and anodic potentials, when the system adopted a new state of stability (by recovering the sliding potential to the OCP value or the drop down in current at anodic electrode potential), the COF went down substantially.
4. As shown in load-potential dual effect, the mechanical and electrochemical contribution of tribocorrosion were separated at OCP and anodic electrode potential. At OCP a correlation between the worn surface microstructure and consequently the mechanical properties and total mechanical wear was found. The slow sliding led to a more deformed microstructure which obviously gave harder worn surface. This harder surface worn less mechanically. However, this relationship was not observed at anodic electrode potential.

7 Future work:

1. Throughout the current work, it has been shown that there is a correlation between the mechanical material loss and the mechanical properties of the worn surfaces at OCP for CoCrMo biomedical grade alloy in simulated body fluid. This correlation was shielded at anodic potentials. The concept needs further investigation on different wear systems.
2. There is a lack of understanding of the influence of protein adsorption on the surface of biomedical alloys on corrosion and tribocorrosion properties. In particular, the real protein concentration of human body fluid and its fluctuation depending on human health has never been investigated.
3. The temperature of the hip joint has been reported to rise up to 50°C. This probably has a major effect on protein adsorption on the implant's surface which in turn might influence the corrosion and tribocorrosion properties of the bio-metallic material.
4. The current work provides valuable knowledge about the tribocorrosion behaviour of CoCrMo biomedical grade alloy in simulated body fluid. The work could be repeated on other biomedical material like titanium alloys.

8 References

- [1] K. Lee and S. B. Goodman, "Current state and future of joint replacements in the hip and knee.," *Expert Rev. Med. Devices*, vol. 5, no. 3, pp. 383–93, May 2008.
- [2] R. Büscher and A. Fischer, "The pathways of dynamic recrystallization in all-metal hip joints," *Wear*, vol. 259, no. 7–12, pp. 887–897, 2005.
- [3] S. Mischler and A. I. Muñoz, "Wear of CoCrMo alloys used in metal-on-metal hip joints: A tribocorrosion appraisal," *Wear*, vol. 297, no. 1–2, pp. 1081–1094, 2013.
- [4] Y. Liao, E. Hoffman, M. Wimmer, A. Fischer, J. Jacobs, and L. Marks, "CoCrMo metal-on-metal hip replacements.," *Phys. Chem. Chem. Phys.*, vol. 15, no. 3, pp. 746–56, Jan. 2013.
- [5] J. N. Israelachvili and J. N. Israelachvili., *Intermolecular and Surface Forces*. Academic Press, An imprint of Elsevier, 2011.
- [6] I. M. Hutchings and P. Shipway, *Tribology : friction and wear of engineering materials*. Butterworth-Heinemann, An imprint of Elsevier, 1992.
- [7] E. Gnecco and E. Meyer, Eds., *Fundamentals of Friction and Wear on the Nanoscale*. Cham: Springer International Publishing, 2015.
- [8] Asm, *ASM Handbook Volume 2: Properties and Selection: Nonferrous Alloys and Special-Purpose Materials*, no. v. 3. 1986.
- [9] S. Parshorov, R. L.-J. of M. S. And, and U. 2014, "Phase Composition of Cast Nickel-Free Superalloy," *researchgate.net*, 2014.
- [10] S.-H. Lee, E. Takahashi, N. Nomura, and A. Chiba, "Effect of Heat Treatment on Microstructure and Mechanical Properties of Ni- and C-Free Co–Cr–Mo Alloys for Medical Applications," *Mater. Trans.*, vol. 46, no. 8, pp. 1790–1793, 2005.
- [11] A. Chiba, K. Kumagai, H. Takeda, and N. Nomura, "Mechanical Properties of Forged Low Ni and C-Containing Co-Cr-Mo Biomedical Implant Alloy," *Mater. Sci. Forum*, vol. 475–479, pp. 2317–2322, Jan. 2005.
- [12] S. Kurosu, N. Nomura, and A. Chiba, "Effect of Sigma Phase in Co-29Cr-6Mo Alloy on Corrosion and Mechanical Properties," *Adv. Mater. Res.*, vol. 26–28, no. 8, pp. 777–780, 2007.
- [13] L. E. Ram, "Precipitation path of secondary phases during solidification of the Co – 25 . 5 % Cr – 5 . 5 % Mo – 0 . 26 % C alloy," vol. 47, pp. 811–816, 2002.

-
- [14] T. Kilner and R. Pilliar, "Phase identification and incipient melting in a cast Co-Cr surgical implant alloy," *J. Biomed. ...*, 1982.
- [15] J. V. Giacchi, C. N. Morando, O. Fornaro, and H. a. Palacio, "Microstructural characterization of as-cast biocompatible Co-Cr-Mo alloys," *Mater. Charact.*, vol. 62, no. 1, pp. 53–61, 2011.
- [16] L. E. Ramírez-Vidaurre, M. Castro-Román, M. Herrera-Trejo, C. V. García-López, and E. Almanza-Casas, "Cooling rate and carbon content effect on the fraction of secondary phases precipitate in as-cast microstructure of ASTM F75 alloy," *J. Mater. Process. Technol.*, vol. 209, no. 4, pp. 1681–1687, 2009.
- [17] D. M. Stefanescu, "Equilibrium and non-equilibrium during solidification," in *Science and Engineering of Casting Solidification, Second Edition*, Boston, MA: Springer US, pp. 1–20.
- [18] A. Clemow and B. Daniell, "Solution treatment behavior of Co-Cr-Mo alloy," *J. Biomed. Mater. Res. - Part B Appl. Biomater.*, 1979.
- [19] H. S. Dobbs and J. L. M. Robertson, "Heat treatment of cast Co-Cr-Mo for orthopaedic implant use," *J. Mater. Sci.*, vol. 18, no. 2, pp. 391–401, 1983.
- [20] J. V. Giacchi, O. Fornaro, and H. Palacio, "Microstructural evolution during solution treatment of Co-Cr-Mo-C biocompatible alloys," *Mater. Charact.*, vol. 68, pp. 49–57, 2012.
- [21] H. Mancha *et al.*, "M₂₃C₆ carbide dissolution mechanisms during heat treatment of ASTM F-75 implant alloys," *Metall. Mater. Trans. A*, vol. 32, no. 4, pp. 979–984, 2001.
- [22] T. M. Devine, F. J. Kummer, and J. Wulff, "Wrought cobalt-chromium surgical implant alloys," *J. Mater. Sci.*, vol. 7, no. 1, pp. 126–128, Jan. 1972.
- [23] Y. Liao *et al.*, "New insights into hard phases of CoCrMo metal-on-metal hip replacements.," *J. Mech. Behav. Biomed. Mater.*, vol. 12, pp. 39–49, Aug. 2012.
- [24] a. J. Saldívar-García and H. F. López, "Microstructural effects on the wear resistance of wrought and as-cast Co-Cr-Mo-C implant alloys," *J. Biomed. Mater. Res. - Part A*, vol. 74, no. 2, pp. 269–74, Aug. 2005.
- [25] a. J. Saldívar and H. F. López, "Role of aging on the martensitic transformation in a cast cobalt alloy," *Scr. Mater.*, vol. 45, no. 4, pp. 427–433, 2001.
- [26] G. Dieter and D. Bacon, *Mechanical metallurgy*. McGraw-Hill, 1986.
- [27] H. F. López and a. J. Saldívar-García, "Martensitic transformation in a cast Co-
-

-
- Cr-Mo-C alloy,” *Metall. Mater. Trans. A Phys. Metall. Mater. Sci.*, vol. 39, no. 1, pp. 8–18, 2008.
- [28] H. R. Lashgari, S. Zangeneh, F. Hasanabadi, and M. Saghafi, “Microstructural evolution during isothermal aging and strain-induced transformation followed by isothermal aging in Co-Cr-Mo-C alloy: A comparative study,” *Mater. Sci. Eng. A*, vol. 527, no. 16–17, pp. 4082–4091, 2010.
- [29] a. Mani, Salinas-Rodriguez, and H. F. Lopez, “Deformation induced FCC to HCP transformation in a Co-27Cr-5Mo-0.05C alloy,” *Mater. Sci. Eng. A*, vol. 528, no. 7–8, pp. 3037–3043, 2011.
- [30] M. Meyers and K. Chawla, *Mechanical behavior of materials*. Cambridge University Press, 2009.
- [31] a. Azushima *et al.*, “Severe plastic deformation (SPD) processes for metals,” *CIRP Ann. - Manuf. Technol.*, vol. 57, no. 2, pp. 716–735, 2008.
- [32] N. Tsuji and T. Maki, “Enhanced structural refinement by combining phase transformation and plastic deformation in steels,” *Scr. Mater.*, vol. 60, no. 12, pp. 1044–1049, 2009.
- [33] R. D. Doherty *et al.*, “Current issues in recrystallization: A review,” *Mater. Today*, vol. 1, no. 2, pp. 14–15, 1998.
- [34] A. Rollett, F. Humphreys, G. Rohrer, and M. Hatherly, *Recrystallization and related annealing phenomena*. Elsevier, 2004.
- [35] K. Yamanaka, M. Mori, S. Kurosu, H. Matsumoto, and A. Chiba, “Ultrafine grain refinement of biomedical Co-29Cr-6Mo alloy during conventional hot-compression deformation,” *Metall. Mater. Trans. A Phys. Metall. Mater. Sci.*, vol. 40, no. 8, pp. 1980–1994, 2009.
- [36] K. Yamanaka, M. Mori, and A. Chiba, “Enhanced mechanical properties of As-forged Co-Cr-Mo-N alloys with ultrafine-grained structures,” *Metall. Mater. Trans. A Phys. Metall. Mater. Sci.*, vol. 43, no. 13, pp. 5243–5257, 2012.
- [37] K. Yamanaka, M. Mori, and A. Chiba, “Effects of nitrogen addition on microstructure and mechanical behavior of biomedical Co-Cr-Mo alloys,” *J. Mech. Behav. Biomed. Mater.*, vol. 29, pp. 417–426, 2014.
- [38] K. Yamanaka, M. Mori, and A. Chiba, “Nanoarchitected Co-Cr-Mo orthopedic implant alloys: Nitrogen-enhanced nanostructural evolution and its effect on phase stability,” *Acta Biomater.*, vol. 9, no. 4, pp. 6259–6267, 2013.
-

-
- [39] S. Kurosu, H. Matsumoto, and A. Chiba, "Grain refinement of biomedical Co-27Cr-5Mo-0.16N alloy by reverse transformation," *Mater. Lett.*, vol. 64, no. 1, pp. 49–52, 2010.
- [40] L. Rémy and A. Pineau, "Twinning and strain-induced f.c.c. → h.c.p. transformation on the mechanical properties of Co-Ni-Cr-Mo alloys," *Mater. Sci. Eng.*, vol. 26, no. 1, pp. 123–132, Nov. 1976.
- [41] S. Asgari, E. El-Danaf, S. R. Kalidindi, and R. D. Doherty, "Strain hardening regimes and microstructural evolution during large strain compression of low stacking fault energy fee alloys that form deformation twins," *Metall. Mater. Trans. A Phys. Metall. Mater. Sci.*, vol. 28, no. 9, pp. 1781–1795, Sep. 1997.
- [42] A. Rohatgi, K. S. Vecchio, and G. T. Gray, "The influence of stacking fault energy on the mechanical behavior of Cu and Cu-Al alloys: Deformation twinning, work hardening, and dynamic recovery," *Metall. Mater. Trans. A*, vol. 32, no. 1, pp. 135–145, Jan. 2001.
- [43] E. El-Danaf, S. R. Kalidindi, and R. D. Doherty, "Influence of grain size and stacking-fault energy on deformation twinning in fcc metals," *Metall. Mater. Trans. A*, vol. 30, no. May, pp. 1223–1233, 1999.
- [44] M. Umemoto, "Nanocrystallization of Steels by Severe Plastic Deformation," *Mater. Trans.*, vol. 44, no. 10, pp. 1900–1911, 2003.
- [45] K. S. Kumar, H. Van Swygenhoven, and S. Suresh, "Mechanical behavior of nanocrystalline metals and alloys," *Acta Mater.*, vol. 51, no. 19, pp. 5743–5774, 2003.
- [46] S. Takeuchi, "The mechanism of the inverse Hall-Petch relation of nanocrystals," *Scr. Mater.*, vol. 44, no. 8–9, pp. 1483–1487, 2001.
- [47] M. a. Wimmer, C. Sprecher, R. Hauert, G. Täger, and A. Fischer, "Tribocchemical reaction on metal-on-metal hip joint bearings A comparison between in-vitro and in-vivo results," *Wear*, vol. 255, no. 7–12, pp. 1007–1014, 2003.
- [48] A. Fischer, "Subsurface microstructural alterations during sliding wear of biomedical metals. Modelling and experimental results," *Comput. Mater. Sci.*, vol. 46, no. 3, pp. 586–590, Sep. 2009.
- [49] R. Büscher, G. Täger, W. Dudzinski, B. Gleising, M. A. a. Wimmer, and A. Fischer, "Subsurface microstructure of metal-on-metal hip joints and its relationship to wear particle generation," *J. Biomed. Mater. Res. - Part B Appl.*
-

-
- Biomater.*, vol. 72, no. 1, pp. 206–214, Jan. 2005.
- [50] J. Williams, *Engineering tribology*. Cambridge University Press, 2012.
- [51] R. Pourzal, R. Theissmann, S. Williams, B. Gleising, J. Fisher, and A. Fischer, “Subsurface changes of a MoM hip implant below different contact zones,” *J. Mech. Behav. Biomed. Mater.*, vol. 2, no. 2, pp. 186–191, 2009.
- [52] D. Dowson, C. Hardaker, M. Flett, and G. H. Isaac, “A hip joint simulator study of the performance of metal-on-metal joints,” *J. Arthroplasty*, vol. 19, no. 8, pp. 124–130, Dec. 2004.
- [53] D. Dowson, “Tribological principles in metal-on-metal hip joint design,” *Proc. Inst. Mech. Eng. Part H J. Eng. Med.*, vol. 220, no. 2, pp. 161–171, Jan. 2006.
- [54] S. C. Scholes and A. Unsworth, “Comparison of friction and lubrication of different hip prostheses,” *Proc. Inst. Mech. Eng. Part H J. Eng. Med.*, vol. 214, no. 1, pp. 49–57, Jan. 2000.
- [55] G. McKee, “McKee-Farrar total prosthetic replacement of the hip,” *Total Hip Replace.*, 1971.
- [56] S. Mischler, “Triboelectrochemical techniques and interpretation methods in tribocorrosion: A comparative evaluation,” *Tribol. Int.*, vol. 41, no. 7, pp. 573–583, 2008.
- [57] M. G. Shettlemore and K. J. Bundy, “Toxicity measurement of orthopedic implant alloy degradation products using a bioluminescent bacterial assay,” *J. Biomed. Mater. Res.*, vol. 45, no. 4, pp. 395–403, 1999.
- [58] A. W. E. W. E. Hodgson, S. Kurz, S. Virtanen, V. Fervel, C.-O. A. O. a Olsson, and S. Mischler, “Passive and transpassive behaviour of CoCrMo in simulated biological solutions,” *Electrochim. Acta*, vol. 49, no. 13, pp. 2167–2178, May 2004.
- [59] I. Milošev and H.-H. H. Strehblow, “The composition of the surface passive film formed on CoCrMo alloy in simulated physiological solution,” *Electrochim. Acta*, vol. 48, no. 19, pp. 2767–2774, Aug. 2003.
- [60] R. W. W. Hsu, C. C. Yang, C. A. Huang, and Y. S. Chen, “Electrochemical corrosion studies on Co-Cr-Mo implant alloy in biological solutions,” *Mater. Chem. Phys.*, vol. 93, no. 2–3, pp. 531–538, 2005.
- [61] A. . Human, B. Roebuck, and H. . Exner, “Electrochemical polarisation and corrosion behaviour of cobalt and Co(W,C) alloys in 1 N sulphuric acid,” *Mater.*
-

-
- Sci. Eng. A*, vol. 241, no. 1–2, pp. 202–210, Jan. 1998.
- [62] M. Srivastava, V. Ezhil Selvi, V. K. William Grips, and K. S. Rajam, “Corrosion resistance and microstructure of electrodeposited nickel–cobalt alloy coatings,” *Surf. Coatings Technol.*, vol. 201, no. 6, pp. 3051–3060, Dec. 2006.
- [63] X. Zhang, Y. Li, N. Tang, E. Onodera, and A. Chiba, “Corrosion behaviour of CoCrMo alloys in 2 wt% sulphuric acid solution,” *Electrochim. Acta*, vol. 125, pp. 543–555, Apr. 2014.
- [64] C. Valero Vidal and A. Igual Muñoz, “Influence of protein adsorption on corrosion of biomedical alloys,” in *Bio-Tribocorrosion in Biomaterials and Medical Implants*, Elsevier, 2013, pp. 187–219.
- [65] B. Clarke, P. Kingshott, X. Hou, Y. Rochev, A. Gorelov, and W. Carroll, “Effect of nitinol wire surface properties on albumin adsorption,” *Acta Biomater.*, vol. 3, no. 1, pp. 103–111, Jan. 2007.
- [66] K. Cai, J. Bossert, and K. D. Jandt, “Does the nanometre scale topography of titanium influence protein adsorption and cell proliferation?,” *Colloids Surfaces B Biointerfaces*, vol. 49, no. 2, pp. 136–144, May 2006.
- [67] L. D. and M. Stefano and S. Huth, *Tribocorrosion of Passive Metals and Coatings*. 2011.
- [68] C. Valero Vidal, A. Olmo Juan, and A. Igual Muñoz, “Adsorption of bovine serum albumin on CoCrMo surface: Effect of temperature and protein concentration,” *Colloids Surfaces B Biointerfaces*, vol. 80, no. 1, pp. 1–11, Oct. 2010.
- [69] N. P. Cosman, K. Fatih, and S. G. Roscoe, “Electrochemical impedance spectroscopy study of the adsorption behaviour of α -lactalbumin and β -casein at stainless steel,” *J. Electroanal. Chem.*, vol. 574, no. 2, pp. 261–271, Jan. 2005.
- [70] S. Omanovic and S. G. Roscoe, “Electrochemical studies of the adsorption behavior of bovine serum albumin on stainless steel,” *Langmuir*, vol. 15, no. 23, pp. 8315–8321, Nov. 1999.
- [71] D. R. Jackson, S. Omanovic, and S. G. Roscoe, “Electrochemical studies of the adsorption behavior of serum proteins on titanium,” *Langmuir*, vol. 16, no. 12, pp. 5449–5457, Jun. 2000.
- [72] G. C. F. Clark and D. F. Williams, “The effects of proteins on metallic corrosion,” *J. Biomed. Mater. Res.*, vol. 16, no. 2, pp. 125–134, Mar. 1982.
-

-
- [73] C. Valero Vidal and A. Igual Muñoz, “Study of the adsorption process of bovine serum albumin on passivated surfaces of CoCrMo biomedical alloy,” *Electrochim. Acta*, vol. 55, no. 28, pp. 8445–8452, Dec. 2010.
- [74] A. I. Muñoz and S. Mischler, “Interactive Effects of Albumin and Phosphate Ions on the Corrosion of CoCrMo Implant Alloy,” *J. Electrochem. Soc.*, vol. 154, no. 10, p. C562, Oct. 2007.
- [75] “ASTM G40-10b, Standard Terminology Relating to Wear and Erosion, ASTM International, West Conshohocken, PA, 2010,.”
- [76] S. Mischler, “Sliding tribo-corrosion of passive metals: mechanisms and modeling,” *Tribo-Corrosion Res. Testing, Appl., STP*, 2013.
- [77] M. Fontana, *Corrosion engineering*. McGraw Hill, 2005.
- [78] J. Stojadinović, D. Bouvet, M. Declercq, and S. Mischler, “Effect of electrode potential on the tribocorrosion of tungsten,” *Tribol. Int.*, vol. 42, no. 4, pp. 575–583, Apr. 2009.
- [79] D. Landolt, S. Mischler, and M. Stemp, “Electrochemical methods in tribocorrosion: A critical appraisal,” *Electrochim. Acta*, vol. 46, no. 24–25, pp. 3913–3929, Aug. 2001.
- [80] P. Jemmely, S. Mischler, and D. Landolt, “Electrochemical modeling of passivation phenomena in tribocorrosion,” *Wear*, vol. 237, no. 1, pp. 63–76, Jan. 2000.
- [81] A. C. C. Vieira, L. A. A. Rocha, N. Papageorgiou, and S. Mischler, “Mechanical and electrochemical deterioration mechanisms in the tribocorrosion of Al alloys in NaCl and in NaNO₃ solutions,” *Corros. Sci.*, vol. 54, no. 1, pp. 26–35, Jan. 2012.
- [82] S. Cao, S. Guadalupe Maldonado, and S. Mischler, “Tribocorrosion of passive metals in the mixed lubrication regime: theoretical model and application to metal-on-metal artificial hip joints,” *Wear*, vol. 324–325, pp. 55–63, 2015.
- [83] X. Jiang, S. Li, C. Duan, and M. Li, “A study of the corrosive wear of Ti-6Al-4V in acidic medium,” *Wear*, vol. 129, no. 2, pp. 293–301, Feb. 1989.
- [84] S. Mischler, A. Spiegel, and D. Landolt, “The role of passive oxide films on the degradation of steel in tribocorrosion systems,” *Wear*, vol. 225–229, pp. 1078–1087, Apr. 1999.
- [85] Y. Yan, A. Neville, D. Dowson, and S. Williams, “Tribocorrosion in implants-
-

-
- assessing high carbon and low carbon Co-Cr-Mo alloys by in situ electrochemical measurements,” *Tribol. Int.*, vol. 39, no. 12, pp. 1509–1517, 2006.
- [86] Y. Yan, A. Neville, and D. Dowson, “Understanding the role of corrosion in the degradation of metal-on-metal implants,” *Proc. Inst. Mech. Eng. Part H J. Eng. Med.*, vol. 220, no. 2, pp. 173–180, Jan. 2006.
- [87] M. T. Mathew, P. Srinivasa Pai, R. Pourzal, A. Fischer, and M. a. Wimmer, “Significance of tribocorrosion in biomedical applications: Overview and current status,” *Adv. Tribol.*, vol. 2009, pp. 1–12, 2009.
- [88] M. Favero, P. Stadelmann, and S. Mischler, “Effect of the applied potential of the near surface microstructure of a 316L steel submitted to tribocorrosion in sulfuric acid,” *J. Phys. D. Appl. Phys.*, vol. 39, no. 15, pp. 3175–3183, Aug. 2006.
- [89] J. Perret *et al.*, “EBSD, SEM and FIB characterisation of subsurface deformation during tribocorrosion of stainless steel in sulphuric acid,” *Wear*, vol. 269, no. 5–6, pp. 383–393, Jul. 2010.
- [90] A. Igual Muñoz and S. Mischler, “Effect of the environment on wear ranking and corrosion of biomedical CoCrMo alloys,” *J. Mater. Sci. Mater. Med.*, vol. 22, no. 3, pp. 437–450, Jan. 2011.
- [91] D. Sun, J. A. a. Wharton, and R. J. K. J. K. Wood, “Micro-abrasion mechanisms of cast CoCrMo in simulated body fluids,” *Wear*, vol. 267, no. 11, pp. 1845–1855, Oct. 2009.
- [92] D. Sun, J. a. Wharton, and R. J. K. Wood, “Micro-abrasion-corrosion of cast CoCrMo-Effects of micron and sub-micron sized abrasives,” *Wear*, vol. 267, no. 1–4, pp. 52–60, 2009.
- [93] L. Casabán Julián and A. Igual Muñoz, “Influence of microstructure of HC CoCrMo biomedical alloys on the corrosion and wear behaviour in simulated body fluids,” *Tribol. Int.*, vol. 44, no. 3, pp. 318–329, Mar. 2011.
- [94] S. Radice and S. Mischler, “Effect of electrochemical and mechanical parameters on the lubrication behaviour of Al₂O₃ nanoparticles in aqueous suspensions,” *Wear*, vol. 261, no. 9, pp. 1032–1041, Nov. 2006.
- [95] L. Wang, X. Liu, D. Li, F. Liu, and Z. Jin, “Contact mechanics studies of an ellipsoidal contact bearing surface of metal-on-metal hip prostheses under micro-lateralization,” *Med. Eng. Phys.*, vol. 36, no. 4, pp. 419–424, Apr. 2014.
-

-
- [96] R. L. Jackson, H. Ghaednia, H. Lee, A. Rostami, and X. Wang, “Contact mechanics,” in *Tribology for Scientists and Engineers: From Basics to Advanced Concepts*, vol. 9781461419, New York, NY: Springer New York, 2013, pp. 93–140.
- [97] I. Hutchings, “Tribology: friction and wear of engineering materials,” 1992.
- [98] G102 – 89 (Reapproved 2015)¹, “Standard Practice for Calculation of Corrosion Rates and Related Information from Electrochemical Measurements,” *ASTM Int.*, vol. 89, pp. 1–7, 2015.
- [99] M. E. Orazem, B. Tribollet, and Wiley, “Electrochemical impedance spectroscopy,” pp. 2–4, 2008.
- [100] N. Espallargas, R. Johnsen, C. Torres, and A. I. Muñoz, “A new experimental technique for quantifying the galvanic coupling effects on stainless steel during tribocorrosion under equilibrium conditions,” *Wear*, vol. 307, no. 1–2, pp. 190–197, Sep. 2013.
- [101] N. Papageorgiou and S. Mischler, “Electrochemical simulation of the current and potential response in sliding tribocorrosion,” *Tribol. Lett.*, vol. 48, no. 3, pp. 271–283, 2012.
- [102] J. R. (Joseph R. . Davis, *Corrosion : understanding the basics*. ASM International, 2000.
- [103] A. Igual Muñoz and N. Espallargas, “Tribocorrosion mechanisms in sliding contacts,” in *Tribocorrosion of Passive Metals and Coatings*, Elsevier, 2011, pp. 118–152.
- [104] N. Diomidis, S. Mischler, N. S. More, and M. Roy, “Tribo-electrochemical characterization of metallic biomaterials for total joint replacement,” *Acta Biomater.*, vol. 8, no. 2, pp. 852–859, 2012.
- [105] M. Dao, N. Chollacoop, K. J. Van Vliet, T. a Venkatesh, and S. Suresh, “Computational modeling of the forward and reverse problems in instrumented sharp indentation,” *Acta Mater.*, vol. 49, no. 19, pp. 3899–3918, 2001.
- [106] G. P. . Oliver, “An improved technique for determining hardness and elastic modulus values using load and depth sensing indentation experiments,” *Mater. Res.*, vol. 7, no. 7, p. 1564, 1992.
- [107] U. Ramamurty and J. -i. Jang, “Nanoindentation for probing the mechanical behavior of molecular crystals—a review of the technique and how to use it,”
-

-
- CrystEngComm*, vol. 16, no. 1, p. 12, 2014.
- [108] A. A. E. Giannakopoulos and S. Suresh, "Determination of elastoplastic properties by instrumented sharp indentation," *Scr. Mater.*, vol. 40, no. 10, pp. 1191–1198, 1999.
- [109] D. A. Lucca, K. Herrmann, and M. J. Klopstein, "Nanoindentation: Measuring methods and applications," *CIRP Ann. - Manuf. Technol.*, vol. 59, no. 2, pp. 803–819, 2010.
- [110] A. C. Fischer-Cripps, *Nanoindentation*. Springer, 2011.
- [111] X. Li and B. Bhushan, "A review of nanoindentation continuous stiffness measurement technique and its applications 10.1016/S1044-5803(02)00192-4 : Materials Characterization | ScienceDirect.com," *Mater. Charact.*, vol. 48, pp. 11–36, 2002.
- [112] T. A. Venkatesh, K. J. Van Vliet, A. E. Giannakopoulos, and S. Suresh, "Determination of elasto-plastic properties by instrumented sharp indentation: guidelines for property extraction," *Scr. Mater.*, vol. 42, no. 9, pp. 833–839, 2000.
- [113] R. Namus, P. Zeng, and W. M. Rainforth, "Correlation of the wear transition in CoCrMo alloys with the formation of a nanocrystalline surface layer and a proteinaceous surface film," *Wear*, vol. 376–377, pp. 223–231, 2017.
- [114] M. E. Orazem and B. Tribollet, "Time-Constant Dispersion," in *Electrochemical Impedance Spectroscopy*, vol. 307, no. 1–2, Hoboken, NJ, USA, 2008, pp. 233–263.
- [115] C. Valero Vidal and A. Igual Muñoz, "Electrochemical Aspects in Biomedical Alloy Characterization : Electrochemical Impedance Spectroscopy," *Biomed. Eng. Trends Mater. Sci.*, pp. 283–306, 2011.
- [116] P. H. Fang and W. S. Brower, "Dielectric constant of Cr₂O₃ crystals," *Phys. Rev.*, vol. 129, no. 4, p. 1561, Feb. 1963.
- [117] A. Ferrari and J. Robertson, "Interpretation of Raman spectra of disordered and amorphous carbon," *Phys. Rev. B*, vol. 61, no. 20, pp. 14095–14107, May 2000.
- [118] ASTM G119-93, "Standard Guide for Determining Synergism Between Wear and Corrosion," *Wear Erosion, Met. Corros.*, vol. 93, no. Reapproved, pp. 1–7, 1994.
- [119] M. a. A. Wimmer *et al.*, "The effect of contact load on CoCrMo wear and the
-

-
- formation and retention of tribofilms,” *Wear*, vol. 332–333, pp. 643–649, May 2015.
- [120] M. a. Wimmer *et al.*, “Wear mechanisms in metal-on-metal bearings: The importance of tribochemical reaction layers,” *J. Orthop. Res.*, vol. 28, no. 4, pp. 436–443, Apr. 2010.
- [121] Y. Liao, R. Pourzal, M. A. Wimmer, J. J. Jacobs, A. Fischer, and L. D. Marks, “Graphitic tribological layers in metal-on-metal hip replacements,” *Science*, vol. 334, no. 6063, pp. 1687–90, Dec. 2011.
- [122] J. L. Woodman, J. Black, and S. A. Jiminez, “Isolation of serum protein organometallic corrosion products from 316LSS and HS-21in vitro andin vivo,” *J. Biomed. Mater. Res.*, vol. 18, no. 1, pp. 99–114, Jan. 1984.
- [123] Y. Liao, E. Hoffman, M. Wimmer, A. Fischer, J. Jacobs, and L. Marks, “CoCrMo metal-on-metal hip replacements,” *Phys. Chem. Chem. Phys.*, vol. 15, pp. 746–756, 2013.
- [124] Y. Yan, A. Neville, and D. Dowson, “Biotribocorrosion of CoCrMo orthopaedic implant materials-Assessing the formation and effect of the biofilm,” *Tribol. Int.*, vol. 40, no. 10–12 SPEC. ISS., pp. 1492–1499, Oct. 2007.
- [125] M. A. Wimmer *et al.*, “Tribochemical Reactions in Metal-on-Metal Hip Joints Influence Wear and Corrosion,” in *Metal-On-Metal Total Hip Replacement Devices*, 100 Barr Harbor Drive, PO Box C700, West Conshohocken, PA 19428-2959: ASTM International, 2013, pp. 292–309.
- [126] M. Roba, M. Naka, E. Gautier, N. D. Spencer, and R. Crockett, “The adsorption and lubrication behavior of synovial fluid proteins and glycoproteins on the bearing-surface materials of hip replacements,” *Biomaterials*, vol. 30, no. 11, pp. 2072–2078, Apr. 2009.
- [127] C. Myant, R. Underwood, J. Fan, and P. M. Cann, “Lubrication of metal-on-metal hip joints: The effect of protein content and load on film formation and wear,” *J. Mech. Behav. Biomed. Mater.*, vol. 6, pp. 30–40, Feb. 2012.
- [128] A. Kocijan, I. Milošev, and B. Pihlar, “The influence of complexing agent and proteins on the corrosion of stainless steels and their metal components,” *J. Mater. Sci. Mater. Med.*, vol. 14, no. 1, pp. 69–77, 2003.
- [129] A. Bidiville, M. Favero, P. Stadelmann, and S. Mischler, “Effect of surface chemistry on the mechanical response of metals in sliding tribocorrosion
-

-
- systems,” *Wear*, vol. 263, no. 1–6 SPEC. ISS., pp. 207–217, Sep. 2007.
- [130] S. Guadalupe *et al.*, “Mechanical and chemical mechanisms in the tribocorrosion of a Stellite type alloy,” *Wear*, vol. 308, no. 1–2, pp. 213–221, Nov. 2013.
- [131] K. D. Ralston, N. Birbilis, and C. H. J. Davies, “Revealing the relationship between grain size and corrosion rate of metals,” *Scr. Mater.*, vol. 63, no. 12, pp. 1201–1204, 2010.
- [132] T. Li *et al.*, “Passive behavior of a bulk nanostructured 316L austenitic stainless steel consisting of nanometer-sized grains with embedded nano-twin bundles,” *Corros. Sci.*, vol. 85, pp. 331–342, 2014.
- [133] P. Peyre *et al.*, “Surface modifications induced in 316L steel by laser peening and shot-peening. Influence on pitting corrosion resistance,” vol. 280, no. 2, pp. 294–302, 2000.
- [134] A. Balyanov *et al.*, “Corrosion resistance of ultra fine-grained Ti,” *Scr. Mater.*, vol. 51, no. 3, pp. 225–229, 2004.
- [135] L. E. Murr, K. P. Staudhammer, and S. S. Hecker, “Effects of Strain State and Strain Rate on Deformation-Induced Transformation in 304 Stainless Steel: Part II. Microstructural Study,” *Metall. Trans. A*, vol. 13, no. 4, pp. 627–635, Apr. 1982.
- [136] J. Talonen, P. Nenonen, G. Pape, and H. Hänninen, “Effect of strain rate on the strain-induced $\gamma \rightarrow \alpha'$ -martensite transformation and mechanical properties of austenitic stainless steels,” *Metall. Mater. Trans. A Phys. Metall. Mater. Sci.*, vol. 36 A, no. 2, pp. 421–432, Feb. 2005.
- [137] S. S. Hecker, M. G. Stout, K. P. Staudhammer, and J. L. Smith, “Effects of Strain State and Strain Rate on Deformation-Induced Transformation in 304 Stainless Steel: Part I. Magnetic Measurements and Mechanical Behavior,” *Metall. Trans. A*, vol. 13, no. 4, pp. 619–626, Apr. 1982.
- [138] G. Purcek *et al.*, “Mechanical and wear properties of ultrafine-grained pure Ti produced by multi-pass equal-channel angular extrusion,” *Mater. Sci. Eng. A*, vol. 517, no. 1–2, pp. 97–104, 2009.
- [139] C. T. Wang, N. Gao, R. J. K. K. Wood, and T. G. Langdon, “Wear Behaviour of Al-1050 Alloy Processed by Severe Plastic Deformation,” *Mater. Sci. Forum*, vol. 667–669, pp. 1101–1106, Dec. 2010.
- [140] T. Kucukomeroglu, “Effect of equal-channel angular extrusion on mechanical
-

-
- and wear properties of eutectic Al-12Si alloy,” *Mater. Des.*, vol. 31, no. 2, pp. 782–789, 2010.
- [141] S. Faghihi, D. Li, and J. A. Szpunar, “Tribocorrosion behaviour of nanostructured titanium substrates processed by high-pressure torsion,” *Nanotechnology*, vol. 21, no. 48, 2010.
- [142] M. I. Abd El Aal, N. El Mahallawy, F. A. Shehata, M. Abd El Hameed, E. Y. Yoon, and H. S. Kim, “Wear properties of ECAP-processed ultrafine grained Al-Cu alloys,” *Mater. Sci. Eng. A*, vol. 527, no. 16–17, pp. 3726–3732, 2010.
- [143] N. Gao, C. T. Wang, R. J. K. Wood, and T. G. Langdon, “Tribological properties of ultrafine-grained materials processed by severe plastic deformation,” *Journal of Materials Science*, vol. 47, no. 12. Springer US, pp. 4779–4797, 26-Jun-2012.
- [144] P. Ponthiaux, R. Bayon, F. Wenger, and J. P. Celis, “Testing protocol for the study of bio-tribocorrosion,” in *Bio-Tribocorrosion in Biomaterials and Medical Implants*, 2013, pp. 372–394.
- [145] N. Diomidis, N. Göçkan, P. Ponthiaux, F. Wenger, and J. P. Celis, “Assessment of the surface state behaviour of Al71Cu10Fe9Cr10 and Al3Mg2 complex metallic alloys in sliding contacts,” *Intermetallics*, vol. 17, no. 11, pp. 930–937, 2009.
- [146] A. C. Ferrari and J. Robertson, “Raman spectroscopy of amorphous, nanostructured, diamond-like carbon, and nanodiamond,” *Philos. Trans. A. Math. Phys. Eng. Sci.*, vol. 362, no. 1824, pp. 2477–512, Nov. 2004.
- [147] P. K. Chu and L. Li, “Characterization of amorphous and nanocrystalline carbon films,” *Mater. Chem. Phys.*, vol. 96, no. 2–3, pp. 253–277, Apr. 2006.
- [148] F. Tuinstra and J. L. Koenig, “Raman Spectrum of Graphite,” *J. Chem. Phys.*, vol. 53, no. 3, pp. 1126–1130, Aug. 1970.
- [149] M. Stemp, S. Mischler, and D. Landolt, “The effect of mechanical and electrochemical parameters on the tribocorrosion rate of stainless steel in sulphuric acid,” *Wear*, vol. 255, no. 1–6, pp. 466–475, Aug. 2003.
- [150] R. Alonso Gil and A. Igual Muñoz, “Influence of the sliding velocity and the applied potential on the corrosion and wear behavior of HC CoCrMo biomedical alloy in simulated body fluids,” *J. Mech. Behav. Biomed. Mater.*, vol. 4, no. 8, pp. 2090–2102, Nov. 2011.
-